IChF
Institute of Physical Chemistry PAS

PhD Dissertation

Diffusion and reactions under crowding: Theory and simulations

Tomasz Skóra

Institute of Physical Chemistry
Polish Academy of Sciences
Kasprzaka 44/52, 01-224
Warszawa, Poland

Diffusion and reactions under crowding: Theory and simulations

Tomasz Skóra

Supervisor: **dr hab. Svyatoslav Kondrat**

December 31, 2022

It is not *how* things are in the world that is mystical, but *that* it exists.

Ludwig Wittgenstein

Contents

Funding

This research was supported by National Science Center (grant no. 2017/25/B/ST3/02456). The author thanks PLGrid for providing computational resources.

Acknowledgements

I want to express my deepest appreciation for the support and mentorship I received from my supervisor, dr hab. Svyatoslav Kondrat. His help was indispensable in the research work during these four long years. It is impossible to count how many times he gave me inspiration and motivation to work hard.

Acknowledgements of a different nature but of equal importance go to my wife, Magdalena, who endured my writing crises and eruptions and did not let me go mad. She has always motivated me to become a better man. I also want to thank my close family, without whom I would not be where I am now.

Thanks to the extraordinary networking skills of my supervisor, I had the privilege of collaborating with great researchers from all over Europe. At this point, I would like to thank prof. Jörg Fitter, dr Mathijs Janssen, dr Edyta Słyk, prof. Andreas Carlson, prof. Mihail N. Popescu, Farzaneh Vagefikia, and Christian Justus, who contributed to the research described in this Thesis.

I am highly grateful to prof. dr hab. Piotr Petelenz, my former supervisor at the Faculty of Chemistry of the Jagiellonian University, who probably had the greatest influence on how I imagine the fulfillment of my vocation to research work. He will always be an unsurpassed role model for me.

Finally, I would like to acknowledge PLGrid for providing the top-notch computational resources necessary to conduct my research.

En passant, I once read somewhere that the average number of readers of a doctoral dissertation, including its author, is 1.6. If so, I sincerely thank the remaining 0.6 readers for making this effort and I hope they will find value in it.

Abstract

Whole-cell simulations have been identified as the grand challenge of XXIst-century. Since even in the exascale computing era, first-principle atomistic whole-cell simulations are computationally prohibitive, coarse-grained reaction-diffusion models appear as essential and feasible alternatives. In such models, it is crucial to adequately describe the diffusion and reaction properties of all biologically-relevant molecules. However, as it has been known for decades, the cell interior is crowded with macromolecules occupying 20 to 40% of the cell volume. Clearly, diffusion and reactions under such crowding conditions are not the same as in test tubes. To understand these differences, in this Thesis, we explore the generic effects of how crowding affects macromolecular diffusion, chemical equilibria, and reaction kinetics.

In many simulation studies, hard spherical particles are used to model macromolecules composing the crowded intracellular milieu. However, the macromolecules inside living cells have various shapes and softness. We show with Brownian dynamics (BD) simulations that these factors can considerably affect macromolecular diffusion. For instance, we find that elongated crowders slow down diffusion more substantially than spherical ones, while soft crowders slow down diffusion less effectively than hard ones, but not in the case of elongated diffusing particles.

To minimize computational costs, many studies consider hydrodynamic interactions using the (generalized) Rotne-Prager-Yamakawa (RPY, or far-field) approximation, neglecting near-field lubrication effects. Here, we provide an open-source computer program (`pyBrown`) that includes both near-field and far-field hydrodynamic interactions. Using this program, we demonstrate that the popular RPY approximation visibly overestimates the diffusion coefficients of macromolecules in crowded environments. We find that the RPY approximation may provide even less accurate results than simulations without hydrodynamic interactions at all.

A living cell is a non-equilibrium system where many reactions continuously occur. Thus, another critical aspect of cellular modeling is to account for the coupling of diffusion and reactions. With BD simulations, we explore the effect of crowding on a catalysis-induced enhancement of enzyme diffusion, reported recently for dilute systems (*i.e.*, without crowders). We consider a model enzyme that shrinks upon binding a substrate and find that such enzymes exhibit enhanced diffusion also in crowded environments. The enhanced diffusion increases when crowding is due to enzymes but decreases when it is due to passive particles. The catalytically-active enzymes enhance the diffusion of passive crowders as well. One possibility to study such

catalysis-induced diffusion enhancements experimentally is microfluidic H-cell measurement. We perform the rational design of an H-cell experiment and investigate under which conditions such experiments are feasible to study the enhanced enzyme diffusion.

Since the seminal work by Minton, it has been known that crowding affects chemical equilibria and reaction kinetics. However, our understanding of how reactions proceed under crowding is still limited. Herein, we study the kinetics of reactions catalyzed by conformation-changing enzymes and how crowding affects them. Using scaled particle theory (SPT), we derive an expression relating the crowding-dependent reaction rates and geometrical factors describing how an enzyme changes its shape during catalytic turnover. We test these results with BD simulations of a model enzyme consisting of two beads changing their separation upon binding a substrate.

Multivalent binding reactions play an essential role in many life-sustaining and life-threatening processes, from antibody-antigen binding in the immune response to amyloid aggregation. Although such reactions often occur under crowding conditions, the effect of crowding on their equilibria is not fully understood. In this Thesis, we study the cooperativity of divalent binding – an important measure describing how the binding of one site affects the binding affinity of other sites – using SPT and combined Monte Carlo and BD simulations. We show that crowding can enhance or reduce cooperativity depending on how the conformation of a molecule changes upon subsequent binding events. In particular, we find that non-cooperative reactions can become cooperative under crowding and *vice versa*.

Streszczenie

Holistyczne symulacje komputerowe komórek żywych zostały uznane za jedno z wielkich wyzwań XXI-wiecznej nauki. Ponieważ nawet w epoce obliczeń eksaskalowych atomistyczne symulacje całych komórek są z obliczeniowego punktu widzenia nieosiągalne, gruboziarniste modele reakcji-dyfuzji wydają się być niezbędną i realną alternatywą. W takich modelach kluczowe jest poprawne opisanie dyfuzji i reakcji wszystkich biologicznie istotnych cząsteczek. Jednakże, jak wiadomo od dekad, wnętrze komórki jest zatłoczone makrocząsteczkami, które zajmują od 20 do 40% jej objętości. Jasnym jest, że dyfuzja i reakcje w warunkach takiego zatłoczenia nie są takie same jak w probówkach. Aby zrozumieć te różnice, w niniejszej rozprawie badamy jak zatłoczenie wpływa na dyfuzję makrocząsteczek, równowagi chemiczne oraz kinetykę reakcji.

W wielu symulacjach komputerowych makrocząsteczki tworzące zatłoczone środowisko wewnątrzkomórkowe reprezentowane są przez twarde kule. Jednak makrocząsteczki wewnątrz żywych komórek cechują się różnym kształtem i miękkością. Za pomocą symulacji dynamiki brownowskiej pokazujemy, że czynniki te mogą wyraźnie wpływać na dyfuzję makrocząsteczek. Na przykład, jak wynika z naszych badań, wydłużone cząsteczki zatłaczające spowalniają dyfuzję bardziej niż kuliste, a twarde bardziej niż miękkie, ale nie w przypadku wydłużonych cząstek dyfundujących.

Aby zmniejszyć koszt obliczeniowy, wiele badań uwzględnia oddziaływania hydrodynamiczne używając (uogólnionego) przybliżenia Rotne-Pragera-Yamakawy (RPY, lub dalekiego pola), zaniedbując efekty lubrykacyjne bliskiego pola. W niniejszej rozprawie przedstawiamy otwarty program komputerowy (`pyBrown`), który uwzględnia zarówno oddziaływania hydrodynamiczne bliskiego, jak i dalekiego pola. Używając tego programu pokazujemy, że popularne przybliżenie RPY wyraźnie zawyża współczynniki dyfuzji makrocząsteczek w zatłoczonym środowisku. Ponadto przybliżenie RPY może dostarczyć nawet mniej dokładnych wyników niż symulacje bez oddziaływań hydrodynamicznych w ogóle.

Żywa komórka jest układem nierównowagowym, w którym nieustannie zachodzi wiele reakcji chemicznych. Dlatego też kolejnym istotnym aspektem komputerowego modelowania komórek jest uwzględnienie sprzężenia dyfuzji i reakcji. Za pomocą symulacji dynamiki brownowskiej badamy wpływ zatłoczenia na przyspieszenie dyfuzji enzymów w wyniku katalizy, które niedawno zaobserwowano w rozcieńczonych układach (tj. bez zatłoczenia). Rozważamy model enzymu, który kurczy się po związaniu substratu i wykazujemy, że takie enzymy przeja-

wiają przyspieszoną dyfuzję również w zatłoczonym środowisku. Efekt przyspieszenia dyfuzji rośnie gdy zatłoczenie jest spowodowane przez enzymy, ale maleje gdy jest spowodowane przez nieaktywne cząsteczki. Katalitycznie aktywne enzymy przyspieszają również dyfuzję nieaktywnych cząsteczek. Jedną z metod badania takiego przyspieszenia dyfuzji może być pomiar w układach mikroprzepływowych o geometrii w kształcie litery H. Przeprowadzamy projekt takiego eksperymentu i badamy w jakich warunkach umożliwia on zbadanie przyspieszonej dyfuzji enzymów.

Od czasu przełomowych prac Mintona wiadomo, że zatłoczenie wpływa na równowagi chemiczne i kinetykę reakcji. Jednak nasze zrozumienie tego, jak przebiegają reakcje w warunkach zatłoczenia jest wciąż ograniczone. W niniejszej pracy badamy kinetykę reakcji katalizowanych przez enzymy zmieniające konformację w cyklu katalitycznym oraz wpływ zatłoczenia na te reakcje. Korzystając z teorii cząstki skalowanej (*scaled particle theory*, SPT) wyprowadzamy wyrażenie wiążące ze sobą zmianę szybkości reakcji w zatłoczeniu i czynniki geometryczne opisujące jak enzym zmienia kształt podczas obrotu katalitycznego. Wyniki te testujemy za pomocą symulacji dynamiki brownowskiej dla modelu enzymu składającego się z dwóch kulek zmieniających swoją odległość równowagową po związaniu substratu.

Reakcje multiwalentnego wiązania odgrywają istotną rolę w wielu procesach podtrzymujących życie i zagrażających mu, od wiązania przeciwciał z antygenami w odpowiedzi immunologicznej po agregację amyloidu. Chociaż takie reakcje często zachodzą w warunkach zatłoczenia, jego wpływ na ich równowagi nie jest w pełni zrozumiany. W tej rozprawie badamy kooperatywność wiązania diwalentnego – ważną miarę opisującą jak wiązanie w jednym miejscu aktywnym wpływa na powinowactwo pozostałych miejsc aktywnych – używając SPT oraz podejścia łączącego całkowanie Monte Carlo i dynamikę brownowską. Pokazujemy, że zatłoczenie może zwiększać lub zmniejszać kooperatywność w zależności od tego jak konformacja makrocząsteczki zmienia się w kolejnych etapach wiązania. W szczególności, stwierdzamy że reakcje niekooperatywne mogą stać się kooperatywne w warunkach zatłoczenia i odwrotnie.

List of Papers

Publications related to the Thesis:

1. **Skóra, T.**, Vaghefikia, F., Fitter, J. & Kondrat, S. Macromolecular Crowding: How Shape and Interactions Affect Diffusion. *The Journal of Physical Chemistry B* **124**, 7537–7543 (2020).
   Farzaneh Vaghefikia, Christian Justus, and Jörg Fitter from RWTH Aachen University performed the fluorescence correlation spectroscopy measurements and analyzed their results.
   This article has been selected by Professor Michael Feig to feature in The Journal of Physical Chemistry B Virtual Issue: Protein Crowding and Stability.

2. **Skóra, T.**, Popescu, M. N. & Kondrat, S. Conformation-changing enzymes and macromolecular crowding. *Physical Chemistry Chemical Physics* **23**, 9065–9069 (2021).

3. Słyk, E. **Skóra T.**, & Kondrat, S. How macromolecules' softness affects diffusion under crowding. *Soft Matter* **18**, 5366–5370 (2022).
   Edyta Słyk developed the immunoglobulin G model, performed all the Brownian dynamics simulations and analyzed their results. I introduced the dsDNA models, performed all the Monte Carlo integrations, and parametrized the models of soft particles

4. **Skóra, T.**, Janssen M., Carlson A. & Kondrat, S. Crowding-regulated binding of divalent biomolecules. Submitted to *Physical Review Letters*.

5. **Skóra, T.** & Kondrat, S. `pyBrown`: versatile Brownian and Stokesian dynamics package for simulations of diffusion and reactions. *In preparation*.

6. **Skóra, T.** & Kondrat, S. Hydrodynamic interactions and macromolecular crowding. *In preparation*.

Other publications:

7. Andrzejak, M., **Skóra, T.** & Petelenz, P. Is Vibrational Coherence a Byproduct of Singlet Exciton Fission? *The Journal of Physical Chemistry C* **123**, 91–101 (2018).

8. Andrzejak, M., **Skóra, T.** & Petelenz, P. Limitations of Generic Chromophore Concept for Femtosecond Vibrational Coherences. *The Journal of Physical Chemistry C* **124**, 3529-3535 (2020).

9. Andrzejak, M., Mazur, G., **Skóra, T.** & Petelenz, P. Soft Selection Rules for Femtosecond Pump–Probe Vibrational Coherence Spectroscopy. *The Journal of Physical Chemistry C* **124**, 23501-23510 (2020).

   This article has been selected to feature in The Journal of Physical Chemistry A Virtual Issue: Josef Michl Festschrift.

List of Figures

List of Tables

Glossary

BD	Brownian dynamics
BSA	bovine serum albumin
CESP	chain entanglement softened potential
cryo-EM	cryo-electron microscopy
cryo-ET	cryo-electron tomography
DLS	dynamic light scattering
DLVO	Derjaguin-Landau-Verwey-Overbeek
DS	donor stream
E. coli	*Escherichia coli*
FCS	fluorescence correlation spectroscopy
FRAP	fluorescence recovery after photobleaching
GFP	green fluorescent protein
IgG	immunoglobulin G
LD	Langevin dynamics
LDVM	lengthscale-dependent viscosity model
M. genitalium	*Mycoplasma genitalium*
MC	Monte Carlo
MD	molecular dynamics
MSAD	mean squared angular displacement
MSD	mean squared displacement

NMR	nuclear magnetic resonance
OA	orientation autocorrelation
QM/MM	quantum mechanics/molecular mechanics
RDF	radial distribution function
RPY	Rotne-Prager-Yamakawa
RS	receiver stream
SD	Stokesian dynamics
SMT	single-molecule tracking
SPT	scaled particle theory
SRFM	super-resolution fluorescence microscopy
SSE	Stokes-Sutherland-Einstein
TAMSD	time-averaged mean squared displacement
WCA	Weeks-Chandler-Andersen

Chapter 1

Introduction

> The ultimate aim of the modern movement in biology is to explain all biology in terms of physics and chemistry.
>
> Francis Crick

A central theme of the work described in this Thesis is to study macromolecular diffusion and chemical equilibria in diverse, crowded environments akin to biological cells, particularly concerning the total concentration and other, more subtle features, *e.g.*, shape, softness, and enzymatic activity of its constituents. In this introductory section, I first present the motivation for this work (Section 1.1), and then provide an overview of the proceeding chapters (Section 1.2).

1.1 Motivation

Recent decades have brought huge advances in experimental techniques such as super-resolution fluorescence microscopy (SRFM) [1], cryo-electron microscopy (cryo-EM), and cryo-electron tomography (cryo-ET), which allow for obtaining high-resolution images of living cells and observing their macromolecular constituents therein [2]. Results obtained using these cutting-edge methods provide the scientific community with data concerning not only the structure of the cells but also the dynamics of their building blocks. The number of examples grows quickly and includes, among others, visualization of endoplasmic reticulum-associated degradation in the unicellular alga [3] and cytoplasmic translational machinery in HeLa cells [4]. The major advantage of these novel methods is that in contrast to X-ray crystallography, which demands cumbersome and time-consuming protocols to isolate the macromolecules of interest and prepare their crystal samples, cryo-EM and SRFM image them directly in their native environment, with all of its extraordinary and fascinating features.

The most striking feature of biological cells is that they are overcrowded with diverse biomacromolecules (Fig. 1.1) [5–8]. For instance, approximately $34\text{-}44\%$ of *Escherichia coli* cytoplasm volume is occupied by macromolecules [9], which makes it, paraphrasing Skolnick, crowded to a similar extent to Times Square on New Year's Eve [10]. Such crowding im-

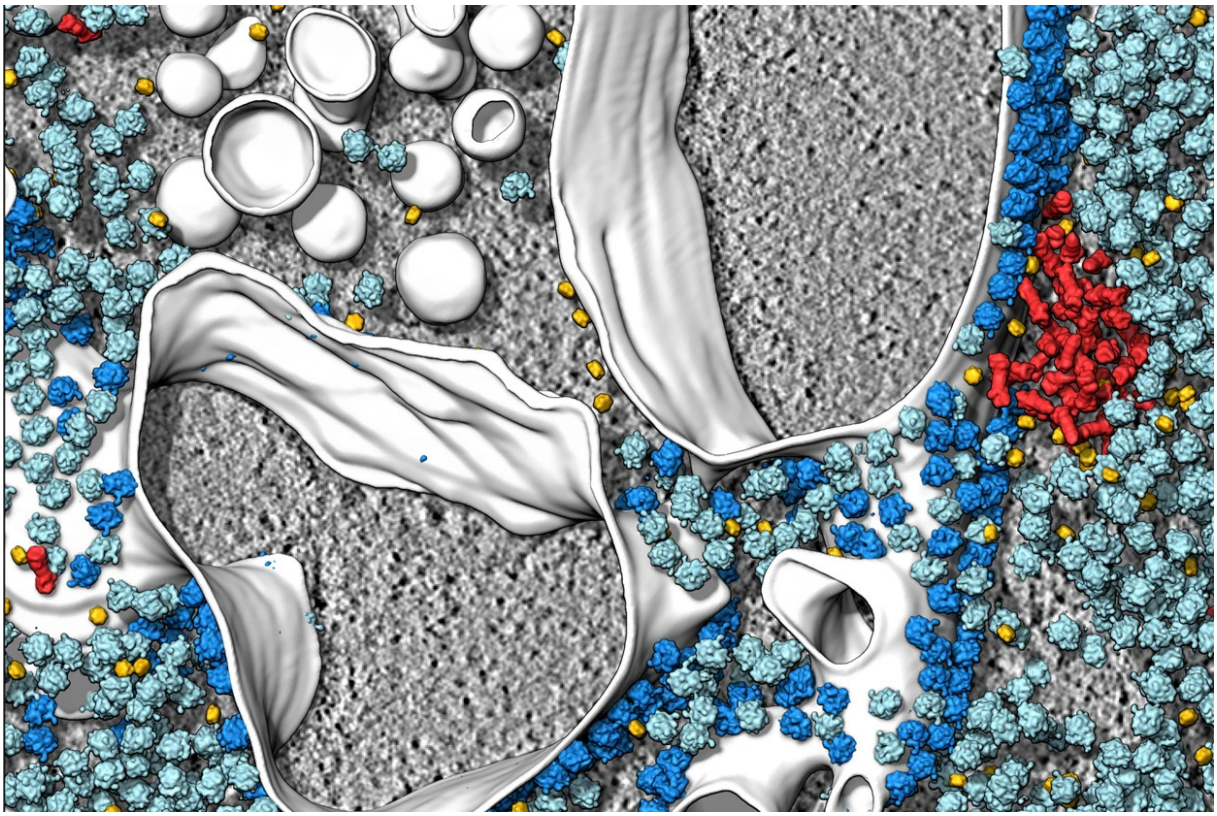

Figure 1.1: **Image of crowded intracellular environment obtained using cryo-ET.** It presents cytosolic protein degradation machinery that removes the potentially harmful, misfolded proteins from the endoplasmic reticulum. It consists of proteasomes (red) and Cdc48 proteins (yellow). Moreover, we can see cytosolic (light blue) and membrane-bound (blue) ribosomes. Figure reprinted from ref. [3].

pacts the physical chemistry of the intracellular milieu in a complex way [11–19]. Apart from macromolecular crowding, there are also other interesting features of cellular compartments. In particular, a cell is a non-equilibrium system, and changes in metabolic activity reportedly glassificate its cytoplasm [20, 21].

The aforementioned quickly growing body of high-resolution cell images leads to the emergence of a more precise picture of the biological cells at the nanoscale. In some sense, it is analogous to the accurate and solicitous astronomical observations of XVIth-century Danish astronomer Tycho Brahe, who authored the famous star catalog and noted the precise positions of planets over many years [22]. These experimental results then paved the way for his more broadly recognized successors: Johannes Kepler (assistant of Tycho Brahe) and sir Isaac Newton, who revolutionized science by finding general laws governing *celestial mechanics* (Fig. 1.2).

Nowadays, one of the grand challenges of the XXIst-century science in general, and computational biophysics in particular, is the development of computer code simulating the biological cell in a quantitative and predictive way [24–29], which we could name *"CELLestial" mechanics*. While the "stars" of cellular biophysics, *i.e.*, protein structures, are to a large extent

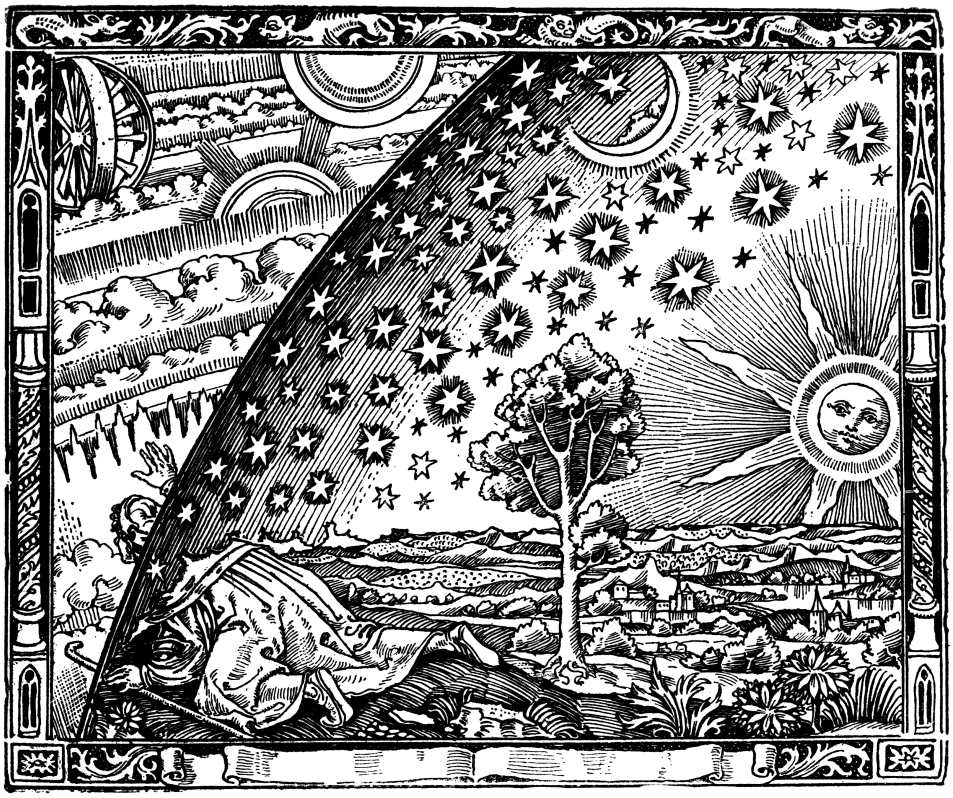

Figure 1.2: **Celestial mechanics – wood engraving.** The Flammarion engraving by unknown artist. It was originally published by Flammarion [23]. Photographic reproduction source: `https://en.wikipedia.org/wiki/File:Flammarion.jpg`.

cataloged, thanks to ambitious projects such as AlphaFold [30] and Protein Data Bank (PDB) [31], the latter of which recently celebrated its 50th birthday [32], the tracks over which the "CELLestial" bodies move are still missing. Such a piece of code, embodying our best knowledge of the laws governing the intracellular mechanics, would be a great tool in many areas of research and technology, including bioengineering, precision medicine, and the origin of life research.

Cell inner workings stem from the microscopic dynamics of the macromolecules constituting it, such as proteins, ribosomes, and nucleic acids. However, although we are undoubtedly at the dawn of the exascale computing era, the first-principle simulations of whole cells are currently unattainable and will probably remain so in the coming years. Netz & Eaton [33] estimated that it would take *ca.* 1 billion years to run such a simulation of one of the tiniest unicellular organisms, *Mycoplasma genitalium* ($\approx 3 \cdot 10^9$ atoms), for the duration of its doubling time, which is *ca.* 2 hours. Assuming that the exponential rise of computational power will continue in line with Moore's law (≈ 10-fold increase every 5 years), which is somewhat unrealistic [34], these simulations would become feasible no earlier than 50 years from now. Even the much more coarse-grained treatments, such as Brownian dynamics (BD) and Stokesian dynamics (SD), are currently at the limit of our computational capabilities when applied to small fragments of cytoplasm [35–38]. Because of that, Netz & Eaton [33] pointed out that, so

far, it is much more feasible to employ reaction-diffusion equations to these types of problems, which for equivalent systems could be solved in a month timescale.

In reaction-diffusion systems, the major bottleneck is not in computation *per se* but instead in gathering all the relevant information about diffusion and reaction properties from independent experiments and calculations. This information cannot be obtained by *in vitro* experiments or small-scale simulations unless we *understand in detail how they are affected when molecules and reactions are transferred to the intracellular environment* by, among other factors, *macromolecular crowding*. This fact motivates the research on generic effects of crowding on macromolecular diffusion, chemical equilibria, and reaction kinetics.

1.2 Outline

This Thesis is organized in the following way.

- In Chapter 2, I cover the concepts fundamental to the scope of this Thesis, which are: Brownian motion, anomalous diffusion, macromolecular crowding, and chemical equilibria.

- In Chapter 3, I present the computational methods we used to carry out the research presented in this Thesis, *viz.*, Brownian dynamics, Stokesian dynamics, and Monte Carlo integration.

- Chapter 4 is devoted to macromolecular diffusion in crowded environments. This chapter provides an extensive literature review covering the experimental measurements of diffusion *in vivo*, as well as experimental and theoretical studies aimed at elucidating the physicochemical reasons for the observed diffusion slowdown. Previous studies focused mainly on the dependence of the diffusion coefficient on the occupied volume. In this Thesis, the diffusion slowdown is decomposed into contributions from two kinds of hydrodynamic interactions, showing that the popular approach to account for them substantially overestimates the diffusion coefficients in crowded environments. Furthermore, the chapter covers the research performed in collaboration with our experimental colleagues from RWTH Aachen University. We single out the effect of crowder shape on diffusion in crowded environments and hypothesize about the role of hitherto unknown attractive interactions between the diffusing molecule and crowders in the experimentally observed unexpectedly slow diffusion. Finally, I describe the effect of crowder softness on diffusion, with particular emphasis on its dependence on the shape of diffusing molecule.

- In Chapter 5, we explore an enhanced enzyme diffusion, which is an increase in the diffusion coefficient of an enzyme in the presence of substrates of the reaction it catalyzes. Previous studies reported this phenomenon for various enzymes, but its existence is still heavily debated, and overall, the research so far has generated more heat than light. Here,

the effect of macromolecular crowding on this phenomenon is discussed, which has never been done before. Moreover, I describe the rational design of H-cell measurement for detecting enhanced enzyme diffusion, and discuss how feasible it is to realize it experimentally.

- Chapter 6 deals with the change in reaction rates and shift of chemical equilibria due to macromolecular crowding. Previous studies investigated these effects extensively with scaled particle theory. Here, the scaled particle theory formalism and Brownian dynamics are applied to conformation-changing enzymes, showing that macroscopic chemical kinetics measurements may give insight into the microscopic features of enzyme conformations. Furthermore, the influence of crowding on the cooperativity of divalent binding reactions is explored. In some cases, crowding may even lead to the emergence of cooperativity in otherwise noncooperative systems.

- Chapter 7 summarizes the results presented in this Thesis.

Appendices A–E contain technical details regarding the implementation of computational methods, applied software, and the experimental setup.

Chapter 2

Theoretical background

> A scientist would rather use someone else's toothbrush than another scientist's nomenclature.
>
> Murray Gell-Mann

2.1 Brownian motion

Brownian motion phenomenon is named after Scottish botanist Robert Brown, who in 1827 observed random, leaping movement of plant pollen suspended on the surface of water [39] (see example Brownian trajectories in Fig. 2.1). The phenomenon was rather mysterious at that time, and the explanation was provided only in the next century, independently by three scholars: Albert Einstein [40], William Sutherland [41], and Marian Smoluchowski [42].

For the sake of brevity, we will not discuss the original development of the Brownian motion theory in chronological order. Readers interested in the historical aspects are referred to comprehensive review papers published in 2005 on the occasion of the 100th anniversary of explaining the Brownian motion [43–45]. Instead, we will start from the equation proposed by another famous scholar of that time, Paul Langevin, in 1908 [46]. It is especially handy here, as it is an equation of motion, and thus adheres to the computational, mechanistic approach held throughout this Thesis.

Langevin proposed a stochastic differential equation that describes the Brownian motion in a framework of the Newtonian dynamics:

$$m\frac{d^2}{dt^2}\boldsymbol{r} = -\boldsymbol{F}_{\mathrm{drag}} + \boldsymbol{F}_{\mathrm{rand}}, \tag{2.1}$$

where t is time, m is mass of a Brownian particle, $\boldsymbol{r}$ is its position, $\boldsymbol{F}_{\mathrm{drag}}$ is drag force experienced by it, and $\boldsymbol{F}_{\mathrm{rand}}$ is fluctuating random force acting on it. For brevity, we assume that the Brownian motion is performed in $\mathbb{R}^3$, although Eq. 2.1 may be used to describe Brownian motion in $\mathbb{R}^n$ for arbitrary $n \in \mathbb{N}_+$.

Figure 2.1: **Ten example trajectories of Brownian particles starting from the same point.**

The idea behind Eq. 2.1 is a division of the degrees of freedom into two classes: fast – degrees of freedom of solvent and slow – degrees of freedom of the Brownian particle. Knowing the positions and momenta of all the particles and all the forces, it would be possible to simply solve the coupled Newton equations *explicitly* for both types of particles without any need for introducing randomness. However, the sheer number of fast degrees of freedom renders the problem practically unsolvable. Instead, the Langevin equation accounts for the fast particles *implicitly*, *via* drag and random forces exerted by them collectively. The formula for the drag force acting on a sphere moving in a viscous fluid was derived by Stokes and reads [47]:

$$\boldsymbol{F}_{\text{drag}} = 6\pi\eta a\boldsymbol{v} = \xi\boldsymbol{v}, \tag{2.2}$$

where η is a dynamic viscosity of the fluid, $\boldsymbol{v} = \frac{d}{dt}\boldsymbol{r}$ is the velocity of a sphere, and a is its radius.

2.1.1 Mean squared displacement

The nature of Brownian motion is stochastic and the random force $\boldsymbol{F}_{\text{rand}}$ does not have a preferred direction ($\langle \boldsymbol{F}_{\text{rand}} \rangle = \boldsymbol{0}$) and does not depend on the position of the particle ($\langle \boldsymbol{r}^T \boldsymbol{F}_{\text{rand}} \rangle = \boldsymbol{0}$, where superscript ^{T} denotes a transpose of a matrix). Because of that, we cannot use mean displacement $\langle \boldsymbol{r}(t) - \boldsymbol{r}(0) \rangle$ to describe the particle's mobility, as it is $\boldsymbol{0}$ regardless of the dynamics of the motion. Instead, we investigate the behavior of mean squared displacement (MSD), *i.e.*:

$$\text{MSD}(t) = \langle (\boldsymbol{r}(t) - \boldsymbol{r}(0))^T (\boldsymbol{r}(t) - \boldsymbol{r}(0)) \rangle. \tag{2.3}$$

In the course of the derivation, we assume $\boldsymbol{r}(0) = \mathbf{0}$ for simplicity.

Interesting conclusions may be drawn after few ingenious transformations of the Langevin equation proposed by Langevin himself. Firstly, Eq. 2.1 multiplied from the left by $\boldsymbol{r}^T$, with the drag force expanded using Eq. 2.2, yields:

$$m\boldsymbol{r}^T\frac{d^2}{dt^2}\boldsymbol{r} = -\xi\boldsymbol{r}^T\frac{d}{dt}\boldsymbol{r} + \boldsymbol{r}^T\boldsymbol{F}_{\mathrm{rand}}. \tag{2.4}$$

Using the following properties of derivatives:

$$\boldsymbol{r}^T\frac{d}{dt}\boldsymbol{r} = \frac{1}{2}\frac{d}{dt}\left(\boldsymbol{r}^T\boldsymbol{r}\right), \tag{2.5a}$$

$$\boldsymbol{r}^T\frac{d^2}{dt^2}\boldsymbol{r} = \frac{1}{2}\frac{d^2}{dt^2}\boldsymbol{r}^T\boldsymbol{r} - \left(\frac{d}{dt}\boldsymbol{r}^T\right)\frac{d}{dt}\boldsymbol{r}, \tag{2.5b}$$

we rewrite Eq. 2.4 as:

$$\frac{1}{2}m\frac{d^2}{dt^2}\boldsymbol{r}^T\boldsymbol{r} + \frac{1}{2}\xi\frac{d}{dt}\boldsymbol{r}^T\boldsymbol{r} = m\boldsymbol{v}^T\boldsymbol{v} + \boldsymbol{r}^T\boldsymbol{F}_{\mathrm{rand}}. \tag{2.6}$$

It is now difficult to progress without any further assumptions. However, we can use what we know from thermodynamics, as we believe that the final microscopic description for $t \to \infty$ should be consistent with the predictions for the equilibrium state. From the equipartition theorem, we know that $\langle \boldsymbol{v}^T\boldsymbol{v}\rangle = 3k_{\mathrm{B}}T/m$, where k_{B} is Boltzmann constant and T is temperature. We can then ensemble-average Eq. 2.6, knowing that $\langle \boldsymbol{r}^T\boldsymbol{F}_{\mathrm{rand}}\rangle = 0$ and using $\mathrm{MSD} = \langle \boldsymbol{r}^T\boldsymbol{r}\rangle$, to obtain:

$$\frac{1}{2}m\frac{d^2}{dt^2}\mathrm{MSD} + \frac{1}{2}\xi\frac{d}{dt}\mathrm{MSD} = 3k_{\mathrm{B}}T, \tag{2.7}$$

which after single integration gives:

$$\frac{d}{dt}\mathrm{MSD} = c\exp\left(-\frac{\xi}{m}t\right) + \frac{6k_{\mathrm{B}}T}{\xi}, \tag{2.8}$$

where c is an arbitrary constant.

For times well beyond the momentum relaxation time, *i.e.*, $t \gg m/\xi$, the solution of Eq. 2.7 is:

$$\mathrm{MSD}(t) = 6\frac{k_{\mathrm{B}}T}{\xi}t = 6Dt. \tag{2.9}$$

Thus, the Langevin equation at long times predicts a linear dependence of MSD on time. The proportionality factor D is called a diffusion coefficient (compare to Eq. 2.2) and is related to temperature T, fluid viscosity η, and sphere radius a through the Stokes-Sutherland-Einstein

(SSE) relation:

$$D = \frac{k_{\mathrm{B}}T}{6\pi\eta a}. \tag{2.10}$$

We will use Eqs. 2.9 and 2.10 frequently in this Thesis.

2.1.2 Fluctuation-dissipation theorem

Thermodynamics imposes yet another constraint on the equilibrium state ($t \to \infty$), which makes $\boldsymbol{F}_{\mathrm{rand}}$ dependent on $\xi = k_{\mathrm{B}}T/D$. To show that, for simplicity, we assume that $\boldsymbol{F}_{\mathrm{rand}}$ has no memory, meaning:

$$\langle \boldsymbol{F}_{\mathrm{rand}}(t)^T \boldsymbol{F}_{\mathrm{rand}}(t') \rangle = 3\sigma^2 \delta\left(t - t'\right), \tag{2.11}$$

where σ controls the strength of the random force, and $\delta(t - t')$ is the Dirac delta distribution. The lack of memory stems from a huge number of collisions per second with much smaller solvent molecules constituting the fluid ($\approx 10^{14}$ at room temperature) [48]. Direct integration of Eq. 2.1 leads to:

$$\boldsymbol{v} = \boldsymbol{v}_0 \exp\left(-\frac{\xi}{m}t\right) + \frac{1}{m}\int_0^t \boldsymbol{F}_{\mathrm{rand}}(t') \exp\left[-\frac{\xi}{m}\left(t - t'\right)\right] dt', \tag{2.12}$$

where $\boldsymbol{v}_0$ is $\boldsymbol{v}(0)$. Using Eq. 2.12, we find an expression for squared velocity $\boldsymbol{v}^T\boldsymbol{v}$:

$$\begin{aligned}\boldsymbol{v}^T\boldsymbol{v} = \boldsymbol{v}_0^T\boldsymbol{v}_0 \exp\left(-\frac{2\xi}{m}t\right) + \\ \frac{1}{m^2}\int_0^t\int_0^t \boldsymbol{F}_{\mathrm{rand}}(t')^T \boldsymbol{F}_{\mathrm{rand}}(t'') \exp\left[-\frac{\xi}{m}\left(2t - t' - t''\right)\right] dt'dt'' + \\ \frac{2}{m}\exp\left(-\frac{\xi}{m}t\right)\boldsymbol{v}_0^T \int_0^t \boldsymbol{F}_{\mathrm{rand}}(t') \exp\left[-\frac{\xi}{m}\left(t - t'\right)\right] dt'.\end{aligned} \tag{2.13}$$

Ensemble averaging of $\boldsymbol{v}^T\boldsymbol{v}$ (Eq. 2.13) using Eq. 2.11 and the following property of the Dirac delta:

$$\int_a^b f(x')\delta(x - x')dx' = f(x), \tag{2.14}$$

where $a < x < b$, leads to:

$$\left\langle \boldsymbol{v}^T\boldsymbol{v} \right\rangle = \left\langle \boldsymbol{v}_0^T\boldsymbol{v}_0 \right\rangle \exp\left(-\frac{2\xi}{m}t\right) + \frac{3\sigma^2}{2m\xi}\left[1 - \exp\left(-\frac{2\xi}{m}t\right)\right]. \tag{2.15}$$

Then, computing the $t \to \infty$ limit results in:

$$\lim_{t\to\infty} \langle \boldsymbol{v}^T \boldsymbol{v} \rangle = \frac{3\sigma^2}{2m\xi}. \tag{2.16}$$

To satisfy the equipartition theorem, Eq. 2.16 has to be equal to $3k_{\mathrm{B}}T/m$, which leads to an expression for σ:

$$\sigma = \sqrt{2k_{\mathrm{B}}T\xi}, \tag{2.17}$$

often referred to as the fluctuation-dissipation theorem. It constitutes the fundamental relation between $\boldsymbol{F}_{\mathrm{drag}}$ and $\boldsymbol{F}_{\mathrm{rand}}$ in the Langevin equation.

2.1.3 Concluding remarks

The essential conclusions from the derivation above are: (1) after some initial time, referred to as momentum relaxation time, the increase in MSD of an isolated Brownian particle is linear (Eq. 2.9), which is a characteristic feature of diffusion, as compared to ballistic motion for which it is quadratic; (2) the diffusion coefficient D depends on temperature, viscosity, and size of a Brownian particle, as dictated by the SSE relation (Eq. 2.10). Linear dependence means that the time τ_L needed, on average, to traverse distance L is:

$$\tau_L = \frac{L^2}{6D}. \tag{2.18}$$

In other words, in order for a Brownian particle to reach a distance 10 times larger, 100 times longer time is needed, which renders the efficiency of diffusive transport smaller and smaller when the system size increases.

2.2 Anomalous diffusion

The classical description of Brownian motion provided by Einstein, Sutherland, Smoluchowski, and Langevin, and summarized in Section 2.1, explains the motion of dilute particles suspended in simple, homogeneous fluids. However, there are physical systems driven by random forces, in which the tracked particle's MSD is not a linear function of time (compare to Eq. 2.9). Examples of such behavior are numerous and include, *e.g.*, diffusion of enzymes in lipid membranes [49] and mRNA in *Escherichia coli* cytoplasm [50].

There are two assumptions guaranteeing the linear dependence of Brownian particle's MSD on time: (1) the lack of memory, *i.e.*, consecutive steps are statistically independent (Eq. 2.11), (2) the existence of MSD for a single step, *i.e.*, the mean of the step length probability density distribution exists. If an MSD deviates from linearity, then at least one of these two assumptions does not hold. We refer to this phenomenon as anomalous diffusion.

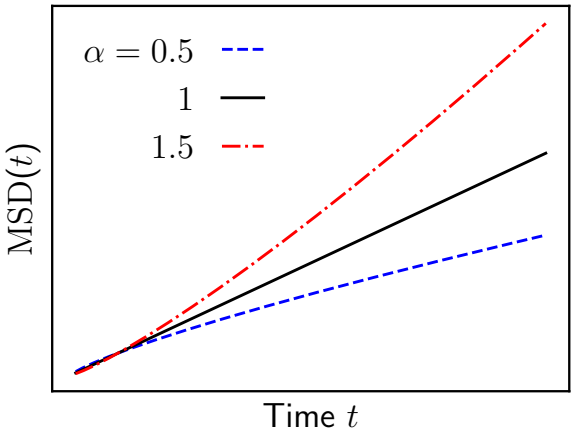

Figure 2.2: **Comparison of MSD for anomalous** ($\alpha = 0.5$**,** 1.5) **and normal** ($\alpha = 1$) **diffusion.**

A detailed discussion of the mathematical formalism used to describe anomalous diffusion is beyond the scope of this Thesis. An interested reader is referred to review papers elaborating on that topic [45, 51–54]. Below, we focus only on the behavior of MSD.

Eq. 2.9 can be generalized to a power law to account for the anomalous behavior:

$$\mathrm{MSD}(t) = 6\Gamma t \left(\frac{t}{t_0}\right)^{\alpha-1}, \tag{2.19}$$

where Γ is a generalized diffusion coefficient, t_0 is a characteristic timescale, and α is an anomalous exponent. Sometimes Eq. 2.19 is expressed with $\Gamma/t_0^{\alpha-1}$ compressed into a single constant, but then its dimension is α-dependent.

When $\alpha > 1$, the process is superdiffusive because for $t \gg t_0$ the diffusion coefficient appears to increase with time; when $\alpha < 1$, the process is subdiffusive because for $t \gg t_0$ the diffusion coefficient appears to decrease with time. For $\alpha = 1$, Eq. 2.19 reduces to Eq. 2.9, *i.e.*, normal diffusion (Brownian motion), with $D = \Gamma$. All three cases are compared in Fig. 2.2.

There are various physical mechanisms responsible for the emergence of anomalous diffusion, among others, active transport of particles by motor proteins [54], binding sites acting as traps for the diffusing particles [55], macromolecular crowding (Section 2.3) [56, 57], and viscoelastic properties of the medium [52, 58]. The overall behavior of MSD may be even more complex and impossible to express by a single power law.

2.3 Macromolecular crowding

The primary observation made through various imaging techniques, as visualized in renowned illustrations by Goodsell [6, 7], is that the cytoplasm is highly crowded by diverse macromolecules. The total macromolecular mass concentration is 17-35 % of cell's entire weight [5]. In particular, the total macromolecular concentration in *E. coli* was estimated to be 300-

$400\,\mathrm{mg\,mL^{-1}}$ [9]. The intracellular space is then approximately an order of magnitude more concentrated than, *e.g.*, typical seawater (in terms of mass concentration of salt). However, a handful of compounds are concentrated therein, as the macromolecular content is divided among thousands of different chemicals, which are often present in small copy numbers. For instance, in *E. coli*, tRNA is $\approx 500\,\mu\mathrm{M}$ (≈ 300000 copies), ribosome is $\approx 50\,\mu\mathrm{M}$ (≈ 30000 copies), RNA polymerase is $\approx 10\,\mu\mathrm{M}$ (≈ 6000 copies), and mRNA is $\approx 4\,\mu\mathrm{M}$ (≈ 2400 copies) [6]. That is why the term macromolecular crowding was coined to connect the realm of concentrated solutions to those in which no specie is necessarily concentrated *per se*, but by their multitude, in total, the solution behaves as concentrated.

2.3.1 Occupied volume

A useful but simplistic approach to describe crowded systems is to approximate all these macromolecules by hard bodies of certain sizes, *e.g.*, by hard spheres. For hard bodies, the potential energy is infinite when the bodies overlap with each other and zero otherwise (Eq. A.6). The concentration of such mixtures may be expressed by occupied volume fraction ϕ_{occ}, which is the volume occupied by all hard spheres divided by the total volume of the system $\mathcal{V}$:

$$\phi_{\mathrm{occ}} = \frac{4\pi}{3}\frac{1}{\mathcal{V}}\sum_{k=1}^{M} N_k a_k^3, \tag{2.20}$$

where k runs over all different molecule types, N_k is the number of k-th molecules in the system, and a_k is k-th molecule's radius.

2.3.2 Excluded volume

Even if two systems are characterized by equal occupied volume fraction, it does not mean that all that volume is equally accessible to the center of geometry of any particle. From the perspective of an arbitrary particle i, the volume inaccessible to its center of geometry is called excluded volume and its ratio to the total system volume $\mathcal{V}$ is excluded volume fraction $\phi_{\mathrm{ex},i}$. Concepts of occupied and excluded volume are visually presented in Fig. 2.3.

The volume excluded by a sphere of radius a_i to a sphere of radius a_j (and *vice versa*) is:

$$V_{\mathrm{ex},ij} = \frac{4}{3}\pi(a_i + a_j)^3. \tag{2.21}$$

In contrast to occupied volume, excluded volume is not additive because excluded volumes of many hard particles may mutually overlap (Fig. 2.3c). Hence, computing ϕ_{ex} in dense systems is not as straightforward as ϕ_{occ} (compare to Eq. 2.20). However, one can harness numerical methods such as Monte Carlo integration for that purpose (Section 3.3).

For a given system in a given configuration, excluded volume ϕ_{ex} depends on the size and

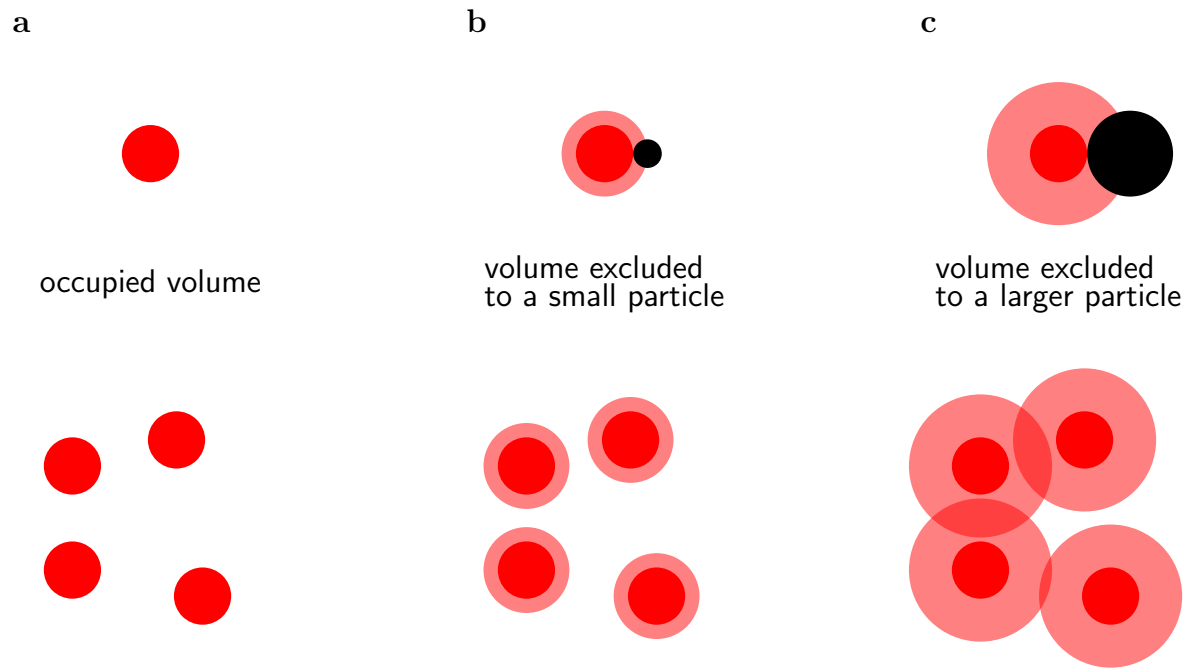

Figure 2.3: **Concepts of occupied and excluded volume.** (**a**) Volume occupied by a sphere (red, above) and an arbitrary configuration of these spheres (below). Spheres are hard and hence cannot overlap. (**b**) Volume excluded by a sphere (red, above) and an arbitrary configuration of these spheres to a small particle (black). (**c**) The same as (b) but for a larger particle.

shape of a particle to which the volume is excluded. Moreover, it depends on the sizes and shapes of the crowders. Note that the occupied volume is the volume excluded to a point particle. In the context of crowding, the distinction between occupied and excluded volume is of utmost importance, and leads to several interesting effects (Sections 4.3 and 4.5).

2.3.3 Occupied volume inside biological cells

The macromolecular content of biological cells is commonly estimated to reach 20-30 % of their total volume [8]. For *E. coli*, Zimmerman & Trach [9] found $\phi_{\text{occ}} \approx$ 34-44 % by performing composition measurements of cell extracts and then carefully accounting for differences between the extracts and the parent cytoplasm. This ϕ_{occ} is closer to a crystal than to a dilute solution, as for equally sized spheres, the phase transition from a fluid to an FCC solid is at $\phi_{\text{occ}} \approx 54\%$ [59]. CyberCell Database [60] (currently down, but the data still available at BioNumbers [61]; BNID: 100045, 100046, 100050, 100051) provides fractions of *E. coli* cell volume occupied by specific families of macromolecules (Fig. 2.4). Among these, proteins constitute the majority (17 %), followed by ribosomes (8 %) and nucleic acids (7 %).

The occupied volume is roughly three times smaller in the eukaryotic cell cytoplasm, probably because they are much larger than prokaryotic ones and in part due to compartmentalization [62]. It is worth mentioning that the analysis of electron micrographs by Gershon *et al.* [63] indicated that 16-20% of PTK (cell line derived from male long-nosed potoroo epithelial kidney

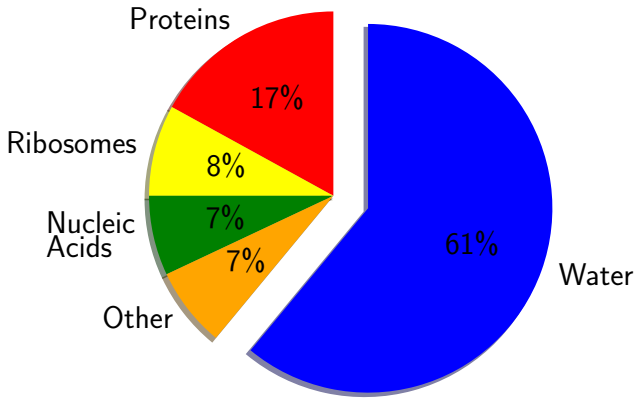

Figure 2.4: **Estimated fraction of the *E. coli*'s cytoplasm volume occupied by various families of macromolecules.** Data accessible at BioNumbers database [61]; BNID: 100045, 100046, 100050, 100051.

cells) cell volume is occupied by various elements of the cytoskeleton, which seemingly contradicts the claim about significantly smaller ϕ_{occ} in eukaryotic cells. However, this estimate is now considered incorrect as a significant fraction of the observed structures that were counted into ϕ_{occ} turned out to be merely artifacts of the preparative method [64].

One comment is worth adding here. Although it is a common practice to treat proteins and polymers as spheres of some effective radii, there is some freedom in choosing these radii, especially for significantly nonspherical entities. Nonetheless, such a treatment works reasonably well to describe the changes in thermodynamics and kinetics of proteins upon moving them to a crowded environment. For example, it leads to the correct reproduction of the experimental dependence of osmotic pressure, sedimentation equilibriumm and light scattering data of hemoglobin and serum albumin solutions over a broad range of concentrations [12]. The reason is the averaging over all mutual orientations of interacting macromolecules, which leads to canceling out subtle effects of local attractions and repulsions, leaving the steric volume exclusion as the primary effect, possibly with slightly modified radii of the hard spheres. However, this reasoning holds only if the long-range electrostatic interactions are absent or effectively screened. Ando & Skolnick [36] confirmed the validity of the effective sphere approximation in simulations of *E. coli* cytoplasm, where replacing rigid macromolecular models for the effective spheres led to only minor differences in their diffusion coefficients. For these reasons, effective sphere models have been successfully employed in so many studies. The question remains, however, whether this approximation holds for significantly nonspherical macromolecules, such as dsDNA or mRNA. We will discuss this issue in Section 4.3.

2.4 Chemical equilibria

A description of the macromolecular mobility alone is far from sufficient to understand how living cells work. Their functioning is based on chemical reactions that take place in them. It turns out that these reactions may proceed differently in the cellular environment than in a test tube [17, 18]. Although biological systems are fundamentally non-equilibrium, a description in the language of equilibrium constants, popularized by Allen Minton [12, 17, 18, 65], makes it possible to understand and quantify these differences.

Let us consider a general chemical reaction:

$$|\nu_1|\mathrm{X}_1 + |\nu_2|\mathrm{X}_2 + ... + |\nu_{N_\mathrm{r}}|\mathrm{X}_{N_\mathrm{r}} \overset{K_0}{\rightleftharpoons} \nu_{N_\mathrm{r}+1}\mathrm{X}_{N_\mathrm{r}+1} + ... + \nu_{N_\mathrm{r}+N_\mathrm{p}}\mathrm{X}_{N_\mathrm{r}+N_\mathrm{p}} \tag{2.22}$$

where ν_i is a stoichiometric coefficient of the reagent X_i (negative for reactants, positive for products), N_r is a number of reactants and N_p is a number of products. In the limit of infinite dilution, the concentrations $[i]$ of the reagents in chemical equilibrium are related *via* equilibrium constant K_0:

$$K_0(T,p) = \prod_{i=1}^{N_\mathrm{r}+N_\mathrm{p}} [i]^{\nu_i}, \tag{2.23}$$

where T and p are temperature and pressure, respectively. In turn, the equilibrium constant K_0 is related to the free energy change of reaction ΔF:

$$\Delta F = -k_\mathrm{B}T \ln K_0, \tag{2.24}$$

where k_B is a Boltzmann constant. If the assumption of a very low concentration of the reagents does not hold, Eq. 2.23 breaks down. There are two distinct approaches to correct for that.

One approach is to say that the equilibrium constant does not change, but instead of relating concentrations, it relates activities $\{i\}$ defined as follows:

$$\{i\} = \gamma_i [i], \tag{2.25}$$

where γ_i is an activity coefficient of i-th reagent in equilibrium that depends on the concentrations of all species and tends to unity in infinite dilution. Then a thermodynamic equilibrium constant is:

$$K_0(T,p) = \prod_{i=1}^{N_\mathrm{r}+N_\mathrm{p}} \{i\}^{\nu_i}, \tag{2.26}$$

regardless of the concentrations of all species.

The alternative approach is to say that the free energy of a reaction ΔF changes by a value

$\Delta\Delta F$ and, in consequence, following Eq. 2.24, the equilibrium constant of the reaction changes as well. By virtue of that, the new composition-dependent equilibrium constant $K(T, p, \{[i]\})$ remains a relation connecting concentrations, not activities. K is called an apparent equilibrium constant and reads:

$$K = K_0 \prod_{i=1}^{N_\mathrm{r}+N_\mathrm{p}} \gamma_i^{-\nu_i}. \tag{2.27}$$

Both approaches are equivalent and related *via*:

$$\Delta\Delta F = -k_\mathrm{B}T \ln \prod_{i=1}^{N_\mathrm{r}+N_\mathrm{p}} \gamma_i^{-\nu_i} = \sum_{i=1}^{N_\mathrm{r}+N_\mathrm{p}} \nu_i \Delta F_i, \tag{2.28}$$

where $\Delta F_i = k_\mathrm{B}T \ln \gamma_i$ are additive contributions to $\Delta\Delta F$ from each reagent.

2.4.1 Effect of macromolecular crowding

To study the effect of crowding, we assume that all reagents are in infinite dilution, but apart from them, there is a high concentration of inert crowders, which indirectly affect the chemical equilibrium through excluded volume. By virtue of that, in the activity-approach we can say that γ_i depend only on the concentration of the inert crowders measured by the occupied volume fraction ϕ_occ (Section 2.3.1). Similarly, we can say that the apparent equilibrium constant depends, apart from T and p, also on ϕ_occ.

To find the physical interpretation of ΔF_i (Eq. 2.28) in such scenario, we consider a thermodynamic cycle including the same reaction in a dilute solution and in a crowded environment (Fig. 2.5). Since the free energy is a function of state, it is clear that ΔF_i expresses the free energy of inserting i-th reagent into the crowded system.

To find ΔF_i, we turn to statistical mechanics, in which the apparent equilibrium constant may be expressed using molecular partition functions q_i [66]

$$K = \prod_{i=1}^{N_\mathrm{r}+N_\mathrm{p}} \left(\frac{q_i}{\mathcal{V}}\right)^{\nu_i}, \tag{2.29}$$

where $\mathcal{V}$ is the volume of the system. We consider molecule i to consist of n_i beads. Then, molecular partition function q_i in the classical limit reads:

$$q_i = h^{-3n_i} \int \ldots \int \exp\left(-\beta \mathcal{H}_i\right) \prod_{j=1}^{n_i} d\boldsymbol{p}_j d\boldsymbol{r}_j, \tag{2.30}$$

where h is Planck's constant, $\beta = 1/k_\mathrm{B}T$ is the inverse thermal energy, and $\boldsymbol{p}_j$ and $\boldsymbol{r}_j$ are the

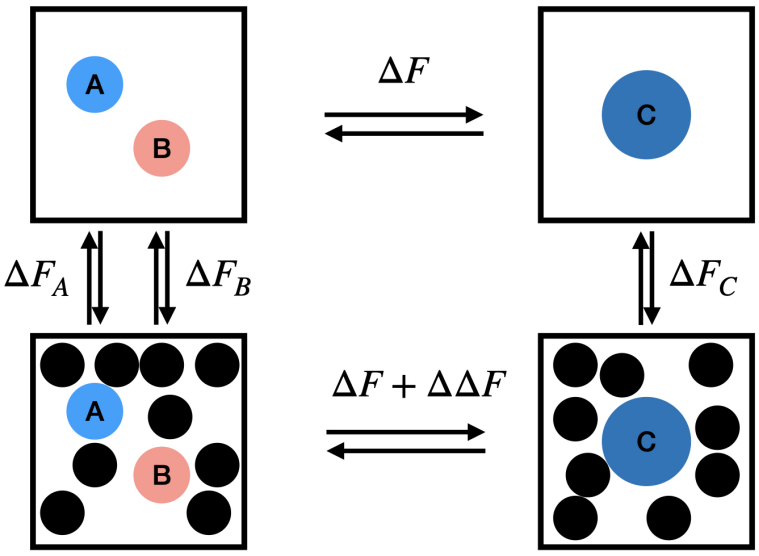

Figure 2.5: **Thermodynamic cycle of a reaction in a crowded system.** For clarity, a chemical reaction of the form A + B $\longrightarrow$ C is shown, but a similar cycle may be constructed for any reaction. Horizontal arrows denote the reaction in dilution (upper half of the cycle) and upon macromolecular crowding (lower half of the cycle). Vertical arrows denote "pseudoreactions" of inserting each reagent into a crowded system.

momentum and position of bead j. $\mathcal{H}_i$ is the molecular Hamiltonian of the molecule i:

$$\mathcal{H}_i = \sum_{j=1}^{n_i} \frac{\boldsymbol{p}_j^T \boldsymbol{p}_j}{2m_j} + U_i\left(\{\boldsymbol{r}_j\}\right), \tag{2.31}$$

with m_j being a mass of j-th bead and U_i being an intramolecular potential energy.

Upon introducing N immobile hard spheres of radii $a_{\mathrm{cr},k}$ at positions $\boldsymbol{R}_k$, the Hamiltonian changes to:

$$\mathcal{H}_i\left(\phi_{\mathrm{occ}}\right) = \mathcal{H}_i + \sum_{j=1}^{n_i}\sum_{k=1}^{N} V(\boldsymbol{r}_j - \boldsymbol{R}_k), \tag{2.32}$$

where V is the reagent-crowder interaction potential. The set of positions $\boldsymbol{R}_k$ represents a particular configuration of crowders. Thus, the molecular partition function in a crowded system is an ensemble average of $q_i(\phi_{\mathrm{occ}})$ over all crowder configurations:

$$q_i(\phi_{\mathrm{occ}}) = h^{-3n_i} \left\langle \int \ldots \int \exp\left[-\beta \mathcal{H}_i\left(\phi_{\mathrm{occ}}\right)\right] \prod_{j=1}^{n_i} d\boldsymbol{p}_j d\boldsymbol{r}_j \right\rangle_{\mathrm{cr}}. \tag{2.33}$$

For our purposes, the crucial quantity is a ratio of the apparent equilibrium constants with

and without crowders, the latter being equal to thermodynamic equilibrium constant K_0, *i.e.*:

$$\frac{K\left(\phi_{\mathrm{occ}}\right)}{K_0} = \prod_{i=1}^{N_{\mathrm{r}}+N_{\mathrm{p}}} \gamma_i^{-\nu_i} = \prod_{i=1}^{N_{\mathrm{r}}+N_{\mathrm{p}}} \left(\frac{q_i\left(\phi_{\mathrm{occ}}\right)}{q_i\left(0\right)}\right)^{\nu_i}. \tag{2.34}$$

The ratio of partition functions with and without crowding amounts to:

$$\frac{q_i\left(\phi_{\mathrm{occ}}\right)}{q_i\left(0\right)} = \frac{\left\langle \int \ldots \int \exp\left(-\beta \mathcal{H}_i\right) \exp\left[-\beta \sum_{j=1}^{n_i} \sum_{k=1}^{N} V(\boldsymbol{r}_j - \boldsymbol{R}_k)\right] \prod_{j=1}^{n_i} d\boldsymbol{p}_j d\boldsymbol{r}_j \right\rangle_{\mathrm{cr}}}{\int \ldots \int \exp\left(-\beta \mathcal{H}_i\right) \prod_{j=1}^{n_i} d\boldsymbol{p}_j d\boldsymbol{r}_j}, \tag{2.35}$$

which, upon integrating out the momentum degrees of freedom, simplifies to:

$$\frac{q_i\left(\phi_{\mathrm{occ}}\right)}{q_i\left(0\right)} = \frac{\left\langle \int \ldots \int \exp\left[-\beta U_i\left(\{\boldsymbol{r}_j\}\right)\right] \exp\left[-\beta \sum_{j=1}^{n_i} \sum_{k=1}^{N} V(\boldsymbol{r}_j - \boldsymbol{R}_k)\right] \prod_{j=1}^{n_i} d\boldsymbol{r}_j \right\rangle_{\mathrm{cr}}}{\int \ldots \int \exp\left[-\beta U_i\left(\{\boldsymbol{r}_j\}\right)\right] \prod_{j=1}^{n_i} d\boldsymbol{r}_j}. \tag{2.36}$$

For hard-sphere interactions between reagents and crowders, $V = V_{\mathrm{HS}}$ (Eq. A.6), and Eq. 2.36 has an intuitive physical interpretation. For a single-bead molecule ($n_i = 1$), Eq. 2.36 reduces to

$$\frac{q_i^{\mathrm{HS}}\left(\phi_{\mathrm{occ}}\right)}{q_i\left(0\right)} = \frac{\langle \iiint_{\mathcal{V}} \exp\left[-\beta \sum_{k=1}^{N} V_{\mathrm{HS}}(\boldsymbol{r}_1 - \boldsymbol{R}_k)\right] dx_1 dy_1 dz_1 \rangle}{\iiint_{\mathcal{V}} dx_1 dy_1 dz_1} = 1 - \phi_{\mathrm{ex},i}, \tag{2.37}$$

where $\phi_{\mathrm{ex},i}$ is the excluded volume introduced in Section 2.3. Inserting Eq. 2.37 and Eq. 2.29 into Eq. 2.34, yields:

$$\frac{K(\phi_{\mathrm{occ}})}{K_0} = \prod_{i=1}^{N_{\mathrm{r}}+N_{\mathrm{p}}} \left(1 - \phi_{\mathrm{ex},i}\right)^{\nu_i}. \tag{2.38}$$

with:

$$\gamma_i = \frac{1}{1 - \phi_{\mathrm{ex},i}}. \tag{2.39}$$

Inserting Eq. 2.39 into the definition of activity (Eq. 2.25) results in:

$$\{i\} = \gamma_i\left[i\right] = \frac{\mathcal{N}_i}{\left(1 - \phi_{\mathrm{ex},i}\right)\mathcal{V}} = \frac{\mathcal{N}_i}{\mathcal{V}_{\mathrm{acc},i}}, \tag{2.40}$$

Thus, the thermodynamic activity of a molecule of species i is given by the number of molecules $\mathcal{N}_i$ divided by the volume $\mathcal{V}_{\mathrm{acc},i}$ accessible to them. It means that hard crowders merely reduce the size of the system, but to a different extent depending on the molecule size and shape. For molecules much smaller than the crowders, $\phi_{\mathrm{ex},i} \approx \phi_{\mathrm{occ}}$ and the accessible volume approaches

the unoccupied volume.

2.4.2 Scaled particle theory

One way to approach the integral in Eq. 2.36 is to use Monte Carlo (MC) integration (Section 3.3). An alternative approach is to construct some approximations, which can be done for hard-sphere reagent-crowder interactions [67–70].

Assuming that a reagent i and crowders are hard spheres of radii a_i and a_{cr}, respectively, and ignoring overlaps between excluded volumes, to a first approximation, expressing Eq. 2.39 using Eq. 2.21 leads to:

$$\ln \gamma_i = -\ln\left(1-\phi_{\mathrm{ex},i}\right) \approx -\ln\left[1-\frac{4}{3}\pi\frac{N}{\mathcal{V}}\left(a_{\mathrm{cr}}+a_i\right)^3\right]. \tag{2.41}$$

Transforming Eq. 2.41 and expanding in MacLaurin series up to the second order in a_i and g, where

$$g = \frac{\phi_{\mathrm{occ}}}{1-\phi_{\mathrm{occ}}}, \tag{2.42}$$

leads to the following expression:

$$\ln \gamma_i = \ln\left(1+g\right) + \left(\frac{3a_i}{a_{\mathrm{cr}}} + \frac{3a_i^2}{a_{\mathrm{cr}}^2}\right) g + \frac{9a_i^2}{2a_{\mathrm{cr}}^2} g^2, \tag{2.43}$$

which is the basic result of scaled particle theory (SPT) [71]. SPT loses accuracy with increase of ϕ_{occ} and decrease of crowder size, as Eq. 2.21 breaks down when excluded volumes start to mutually overlap.

A better approximation is offered by the generalized SPT [12, 70], which includes also the third order terms and applies to crowders of various convex shapes. In the generalized SPT, the activity coefficients are [12]:

$$\begin{aligned}\ln \gamma_i = \ln\left(1+g\right) + \left(1+g\right)\left(H_i \left\langle\langle S\right\rangle\rangle + S_i \left\langle\langle H\right\rangle\rangle + V_i \left\langle\langle 1\right\rangle\rangle\right) + \\ \frac{1}{2}(1+g)^2\left(H_i^2 \left\langle\langle S\right\rangle\rangle^2 + 2V_i \left\langle\langle H\right\rangle\rangle \left\langle\langle S\right\rangle\rangle\right) + \frac{1}{3}(1+g)^3 V_i \left\langle\left\langle H^2\right\rangle\right\rangle \left\langle\langle S\right\rangle\rangle^2\end{aligned} \tag{2.44}$$

where V_i, S_i, and H_i are the i-th particle's volume, surface area, and Kihara parameter (half of the orientation-averaged projection of the particle onto a single axis), respectively. For a generic observable G,

$$\left\langle\langle G\right\rangle\rangle = \frac{1}{\mathcal{V}}\sum_{k=1}^{M} N_k G_k, \tag{2.45}$$

where M is the number of different types of crowders, and N_k is the number of crowders of type

k. Note that $\langle\langle H^2\rangle\rangle = (1/\mathcal{V})\sum_{k=1}^{M} N_k H_k^2 \neq \langle\langle H\rangle\rangle^2$ and that $\langle\langle 1\rangle\rangle = N/\mathcal{V}$ is the concentration of crowders.

When all the crowders are spheres, we can simplify Eq. 2.44 to:

$$\ln\gamma_i = \ln(1+g) + \left(\frac{3H_i}{H_{\rm cr}} + \frac{3S_i}{S_{\rm cr}} + \frac{V_i}{V_{\rm cr}}\right) g + \left(\frac{9H_i^2}{2H_{\rm cr}^2} + \frac{3V_i}{V_{\rm cr}}\right) g^2 + \frac{3V_i}{V_{\rm cr}} g^3. \tag{2.46}$$

Additionally, when i-th molecule is a sphere as well, we can fuurther simplify Eq. 2.46 by using the explicit expressions for the volumes, surface areas and Kihara parameters (for spheres $H = a$) in the following way:

$$\ln\gamma_i = \ln(1+g) + \left(\frac{3a_i}{a_{\rm cr}} + \frac{3a_i^2}{a_{\rm cr}^2} + \frac{a_i^3}{a_{\rm cr}^3}\right) g + \left(\frac{9a_i^2}{2a_{\rm cr}^2} + \frac{3a_i^3}{a_{\rm cr}^3}\right) g^2 + \frac{3a_i^3}{a_{\rm cr}^3} g^3. \tag{2.47}$$

Equation 2.47 is an improved version of Eq. 2.43. We will use generalized SPT to compute reaction rates of enzymatic reactions (Section 6.2) and the cooperativity parameters of divalent binding reactions (Section 6.3).

Chapter 3

Methods

> The inside of a computer is as dumb as hell but it goes like mad!
>
> Richard Feynman

3.1 Brownian dynamics simulations

Probably the most straightforward approach to simulations of biological systems is molecular dynamics (MD). In MD, one applies the Newtonian equations of motion to atoms and molecules. Despite huge development in this field [72, 73], demonstrated, for instance, by its role in understanding the workings of SARS-CoV-2 spike protein [74], it is still challenging to reach with that method timescales characteristic to many important biological phenomena [33].

There are various approaches to decrease the computational cost of MD simulations. One approach has been discussed in Section 2.1 and consists in implicit modeling of the solvent molecules through stochastic and drag forces (Eq. 2.1). The second approach is to coarse-grain a system, *i.e.*, represent multiple atoms, polymeric subunits or even whole biomacromolecules with single beads in order to reduce the number of degrees of freedom. The hierarchy of approximations in biomolecular modeling is shown in Fig. 3.1.

Brownian dynamics (BD) is a simulation method used specifically to study mesoscopic systems, for which it would be computationally too costly to perform quantum mechanics/-molecular mechanics (QM/MM) or MD simulations. It was devised and first used in 1978 by Ermak & McCammon [75] and since has been applied to a number of problems, most notably to simulate bacterial cytoplasm [36, 37] and cell adhesion [76]. The interested reader is referred to review papers elaborating on BD applications [77–79].

BD stems from the Langevin dynamics (LD) governed by Eq. 2.1. The additional assumption on top of the ones described in Section 2.1 is that the friction term is very large compared to the particle mass, which leads to a quick relaxation of macromolecules' momenta gained by the action of the random force. In hydrodynamic terms, this corresponds to low Reynolds numbers characteristic to small bodies (cellular and subcellular scale) in viscous fluids [80].

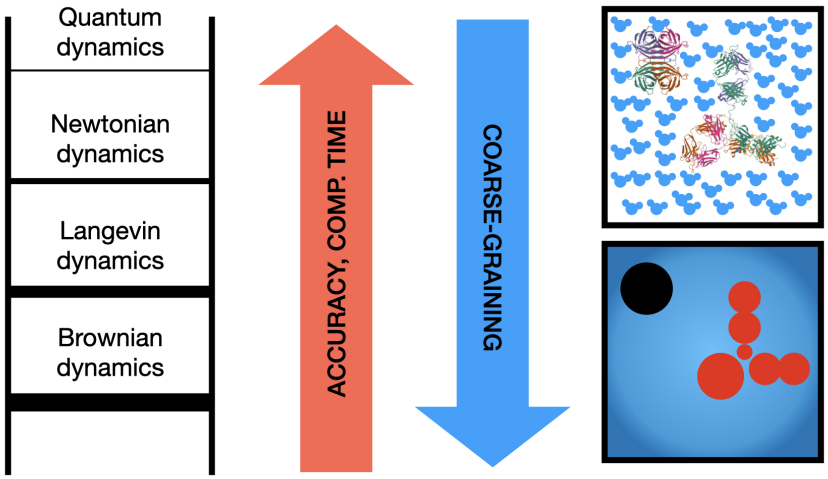

Figure 3.1: **Hierarchy of approaches used in biomolecular modeling.** Brownian dynamics (BD), Langevin dynamics (LD), molecular dynamics (MD), and quantum mechanics/molecular mechanics (QM/MM) ordered according to their computational cost, accuracy, and level of coarse-graining involved. In QM/MM and MD, particles are usually fine-grained and the water molecules are included *explicitly*. In LD and BD, particles are usually coarse-grained and the water molecules are included *implicitly*.

In such an overdamped limit, the Langevin equation reads:

$$-\xi \frac{d}{dt}\boldsymbol{r} + \boldsymbol{F} + \sqrt{2k_{\mathrm{B}}T\xi}\boldsymbol{X}(t) = \boldsymbol{0}, \tag{3.1}$$

where $\boldsymbol{F}$ is a deterministic force acting on Brownian particle (which we silently assumed $\boldsymbol{0}$ in Section 2.1), and $\boldsymbol{X}(t)$ is a 3-dimensional standard white-noise stochastic process, *i.e.*, δ-correlated process with zero mean and unit variance representing the direction of $\boldsymbol{F}_{\mathrm{rand}}$. Equation 3.1 may be reformulated as:

$$\frac{d}{dt}\boldsymbol{r} = \frac{1}{\xi}\boldsymbol{F} + \sqrt{2\frac{k_{\mathrm{B}}T}{\xi}}\boldsymbol{X} = \frac{D}{k_{\mathrm{B}}T}\boldsymbol{F} + \sqrt{2D}\boldsymbol{X}, \tag{3.2}$$

where we used Eq. 2.9 to introduce the diffusion coefficient.

For a system of N Brownian particles, with generally different diffusion coefficients, $\boldsymbol{r}$ and $\boldsymbol{F}$ are block vectors, *i.e.*, $3N$-dimensional vectors, which may be understood as N-dimensional vectors with 3-dimensional entries (sometimes called supervectors). Similarly, D becomes a block matrix $\boldsymbol{D}$, with 3×3 blocks:

$$\boldsymbol{D}_{ij} = \delta_{ij}\frac{k_{\mathrm{B}}T}{6\pi\eta a_i}\boldsymbol{I}, \tag{3.3}$$

where $\boldsymbol{I}$ is an identity matrix, a_i is a hydrodynamic radius of i-th particle, and δ_{ij} is the Kronecker delta.

The equation of motion in a matrix form reads:

$$\frac{d}{dt}\boldsymbol{r} = \frac{1}{k_{\mathrm{B}}T}\boldsymbol{D}\boldsymbol{F} + \sqrt{2\boldsymbol{D}}\boldsymbol{X}. \tag{3.4}$$

Here, $\boldsymbol{D}$ may be understood as a covariance matrix of the random force, up to a factor of 2, and its square root, in case $\boldsymbol{D}$ is diagonal, is simply a matrix of square roots of the respective elements. The BD with diagonal $\boldsymbol{D}$ is referred to as free-draining approximation [10]. Implementation of Eq. 3.4 is discussed in Appendix A.

3.2 Hydrodynamic interactions

To accurately describe systems consisting of many Brownian particles, it is necessary to take into account hydrodynamic interactions between them [10]. Hydrodynamic interactions are indirect interactions between the particles mediated by the motion of a fluid. They arise due to the fluid flows emerging as a result of particles' motion. One may understand it as follows: when two particles are close to each other, it is no longer true that their motions are statistically independent. Note that the equilibrium properties of the system are not affected by hydrodynamic interactions, as the steady-state solution of the corresponding Fokker-Planck equation is the Boltzmann distribution [75].

Hydrodynamic interactions are included in BD by modifying diffusion matrix $\boldsymbol{D}$ with respect to its free-draining form (Eq. 3.3). There are several methods to compute $\boldsymbol{D}$ accounting for them. One often considers two distinct contributions: far-field (long-range) and near-field (short-range). Originally, Ermak & McCammon [75] accounted only for the far-field hydrodynamic interactions, and the progress in including near-field ones came later [81–84].

3.2.1 Far-field hydrodynamic interactions

Far-field hydrodynamic interactions do not affect the diagonal blocks of $\boldsymbol{D}$ but give rise to off-diagonal blocks, which statistically correlate the random forces acting on particles in the close proximity and make particles experience the deterministic forces felt by the particles in their vicinity. The first approximation to off-diagonal blocks may be obtained by computing the effect of the velocity field around a point particle on the velocity field in the arbitrary point of the fluid using the Stokes equation [85]. This results in Oseen matrix or Oseen approximation ($i \neq j$):

$$\boldsymbol{D}_{ij} = \frac{k_{\mathrm{B}}T}{8\pi\eta r_{ij}}\left(\boldsymbol{I} + \frac{\boldsymbol{r}_{ij}\boldsymbol{r}_{ij}^T}{r_{ij}^2}\right) = \frac{k_{\mathrm{B}}T}{8\pi\eta r_{ij}}\left(\boldsymbol{I} + \hat{\boldsymbol{r}}_{ij}\hat{\boldsymbol{r}}_{ij}^T\right), \tag{3.5}$$

where $\boldsymbol{r}_{ij}$ is a vector pointing from i-th particle to j-th particle. r_{ij} is its length, $\hat{\boldsymbol{r}}_{ij} = \boldsymbol{r}_{ij}/r_{ij}$, and $\hat{\boldsymbol{r}}_{ij}\hat{\boldsymbol{r}}_{ij}^T$ is a projection matrix onto the axis connecting particle centers.

This approximation can be iteratively corrected to account for nonzero volume of the hydrodynamically interacting particles. The consecutive corrections take form of powers of $1/r_{ij}$ [85]. The first iteration step applied to the hydrodynamic interactions between two spheres yields the so-called Rotne-Prager-Yamakawa (RPY) matrix [86, 87]:

$$\boldsymbol{D}_{ij} = \frac{k_\mathrm{B}T}{8\pi\eta r_{ij}} \left[\left(1 + \frac{2a_i^2}{3r_{ij}^2} \right) \boldsymbol{I} + \left(1 - \frac{2a_i^2}{r_{ij}^2} \right) \hat{\boldsymbol{r}}_{ij} \hat{\boldsymbol{r}}_{ij}^T \right]. \tag{3.6}$$

The generalized RPY approximation [88, 89] additionally allows for different sphere radii and their overlaps. The formula reads:

$$\boldsymbol{D}_{ij}(r_{ij}) = \frac{k_\mathrm{B}T}{8\pi\eta r_{ij}} \left[\left(1 + \frac{a_i^2 + a_j^2}{3r_{ij}^2} \right) \boldsymbol{I} + \left(1 - \frac{a_i^2 + a_j^2}{r_{ij}^2} \right) \hat{\boldsymbol{r}}_{ij} \hat{\boldsymbol{r}}_{ij}^T \right] \tag{3.7a}$$

for $r_{ij} > a_i + a_j$ and

$$\boldsymbol{D}_{ij}(r_{ij}) = \frac{k_\mathrm{B}T}{8\pi\eta r_{ij}} \left[\frac{16r_{ij}^3(a_i + a_j) - [(a_i - a_j)^2 + 3r_{ij}^2]^2}{32r_{ij}^3} \boldsymbol{I} + \frac{3[(a_i - a_j)^2 - r_{ij}^2]^2}{32r_{ij}^3} \hat{\boldsymbol{r}}_{ij} \hat{\boldsymbol{r}}_{ij}^T \right] \tag{3.7b}$$

for $a_{ij}^M - a_{ij}^m < r_{ij} < a_i + a_j$, where $a_{ij}^M = \max(a_i, a_j)$ and $a_{ij}^m = \min(a_i, a_j)$. Finally:

$$\boldsymbol{D}_{ij} = \frac{k_\mathrm{B}T}{6\pi\eta a_{ij}^M} \boldsymbol{I}, \tag{3.7c}$$

for $r_{ij} < a_{ij}^M - a_{ij}^m$.

Note that $\boldsymbol{D}_{ij}$ in Eqs. 3.5–3.7 decays as $1/r_{ij}$, which results in long-range character and slow convergence of the hydrodynamic interactions. To account for that in simulations with periodic boundary conditions, the Ewald summation method is used, as described in Appendix B.

Due to far-field hydrodynamic interactions, the distances between particles vary more slowly. This means that two particles are repeled when approaching each other and attracted when moving apart.

3.2.2 Near-field hydrodynamic interactions

The Ewald-summated RPY diffusion matrix describes only the two-body far-field hydrodynamic interactions. Stokesian dynamics (SD) [81–84] corrects the far-field diffusion matrix for the two-body near-field and the many-body far-field effects. Here, we will focus only on the so-called F-formulation of SD, *i.e.*, we will ignore the degrees of freedom other than positions in space (in particular, orientations). This approximation, although ignoring the coupling between the rotational and translational mobilities, was demonstrated to correctly describe hard-sphere suspensions [82].

A fundamental concept in SD is a resistance matrix $\boldsymbol{\xi}$, which is related to the diffusion matrix

by the generalization of the Stokes-Sutherland-Einstein (SSE) relation (compare to Eq. 2.10):

$$\boldsymbol{D} = k_{\mathrm{B}} T \boldsymbol{\xi}^{-1}. \tag{3.8}$$

SD is based on the exact expression for the two-body resistance matrix $\boldsymbol{\xi}^{\mathrm{2B}}$ obtained by Jeffrey & Onishi [90] (Appendix C). The procedure is as follows: N-particle Ewald-summated RPY matrix is computed and then inverted to obtain the N-particle far-field many-body resistance matrix $\boldsymbol{\xi}_{\mathrm{ff}}^{\mathrm{NB}}$. While the RPY diffusion matrix involves only two-body interactions, inverting it introduces many-body components in the resistance space [81]. Then, for particle pairs one computes the 2-particle two-body Jeffrey-Onishi translation-translation resistance matrices $\boldsymbol{\xi}^{\mathrm{2B}}$, which contain both far-field and near-field effects, and the 2-particle two-body far-field resistance matrices $\boldsymbol{\xi}_{\mathrm{ff}}^{\mathrm{2B}}$. All expressions needed to compute the former are gathered in Appendix C, and the latter are computed by inverting 2-particle two-body generalized RPY diffusion matrix (Eq. 3.7). The difference between these two gives a 2-particle (6×6) near-field lubrication correction to the resistance matrix:

$$\Delta\boldsymbol{\xi}_{\mathrm{nf},0} = \boldsymbol{\xi}^{\mathrm{2B}} - \boldsymbol{\xi}_{\mathrm{ff}}^{\mathrm{2B}}. \tag{3.9}$$

At the next stage, the lubrication term is itself corrected using a method suggested by Cichocki *et al.* [91] to exclude the collective motion and avoid divergence of the diffusion matrix. The procedure is sometimes called an improved lubrication correction [36] and reads:

$$\Delta\boldsymbol{\xi}_{\mathrm{nf}} = q \Delta\boldsymbol{\xi}_{\mathrm{nf},0} q^T; \tag{3.10a}$$

where:

$$q = \frac{1}{2} \begin{bmatrix} \boldsymbol{I} & -\boldsymbol{I} \\ -\boldsymbol{I} & \boldsymbol{I} \end{bmatrix}. \tag{3.10b}$$

Then, the lubrication correction 6×6 matrices $\Delta\boldsymbol{\xi}_{\mathrm{nf}}$ are added to their corresponding blocks of the $3N \times 3N$ $\boldsymbol{\xi}_{\mathrm{ff}}^{\mathrm{NB}}$. Finally, the resistance matrix is inverted to obtain the lubrication-corrected diffusion matrix. The overall scheme may be summarized in the following expression:

$$\boldsymbol{D} = k_{\mathrm{B}} T \left[\boldsymbol{\xi}_{\mathrm{ff}}^{\mathrm{NB}} + q^T \left(\boldsymbol{\xi}_{\mathrm{nf}}^{\mathrm{2B}} - \boldsymbol{\xi}_{\mathrm{ff}}^{\mathrm{2B}} \right) q \right]^{-1}. \tag{3.11}$$

3.3 Monte Carlo integration

3.3.1 General formulation

Many problems in statistical mechanics involve multidimensional integrals. The calculation of these integrals poses a challenge, because hardly ever we can find analytical solutions. Further-

more, the straightforward approach to solving them numerically, *i.e.*, defining a grid of points and using a method like Simpson's rule, is not feasible, because the number of grid points grows exponentially with the dimensionality of the problem.

Alternative approach is drawing points in which the function is evaluated at random – the Monte Carlo (MC) approach [92]. In the simplest variant (crude MC), random numbers are drawn from a uniform random distribution over the integration volume Ω. Then the definite integral of function $f(\boldsymbol{x})$ over Ω may be approximated in a following way:

$$\int_{\Omega} f(\boldsymbol{x}) d\boldsymbol{x} \approx \frac{V_{\Omega}}{N_{\mathrm{tot}}} \sum_{\alpha=1}^{N_{\mathrm{tot}}} f(\boldsymbol{x}_{\alpha}), \tag{3.12}$$

where N_{tot} is the total number of draws of $\boldsymbol{x}_{\alpha}$ and $V_{\Omega} = \int_{\Omega} d\boldsymbol{x}$ is the volume.

More general approach, called importance sampling, allows for drawing points from a nonuniform random distribution. Then, the approximation of the integral reads:

$$\int_{\Omega} f(\boldsymbol{x}) d\boldsymbol{x} \approx \frac{1}{N_{\mathrm{tot}}} \sum_{\alpha=1}^{N_{\mathrm{tot}}} \frac{f(\boldsymbol{x}_{\alpha})}{p(\boldsymbol{x}_{\alpha})}, \tag{3.13}$$

where $p(\boldsymbol{x}_{\alpha})$ is a probability distribution from which $\boldsymbol{x}_{\alpha}$ is sampled.

3.3.2 Calculations of excluded volume

In Section 2.4, we showed that the excluded volume $\phi_{\mathrm{ex},i}$ and activity coefficient γ_i in crowded systems can be calculated through multidimensional integration (Eq. 2.36). To compute these integrals, we use Eq. 3.13 with $p(\boldsymbol{x}_{\alpha})$ being a Boltzmann distribution without crowders:

$$p\left(\{\boldsymbol{r}_j\}_{\alpha}\right) = \frac{\exp\left[-\beta U_i\left(\{\boldsymbol{r}_j\}_{\alpha}\right)\right]}{Z_i(0)}, \tag{3.14}$$

where

$$Z_i(0) = \int \ldots \int \exp\left[-\beta U_i\left(\{\boldsymbol{r}_j\}\right)\right] \prod_{j=1}^{n_i} d\boldsymbol{r}_j, \tag{3.15}$$

is a configurational integral playing a role of the normalization factor. Inserting Eq. 3.14 into Eq. 3.13 and using MC method to integrate Eq. 2.36, with

$$f(\{\boldsymbol{r}_j\}_{\alpha}) = \exp\left[-\beta U_i\left(\{\boldsymbol{r}_j\}_{\alpha}\right)\right] \exp\left[-\beta \sum_{j=1}^{n_i} \sum_{k=1}^{N} V(\boldsymbol{r}_{\alpha j} - \boldsymbol{R}_k)\right], \tag{3.16}$$

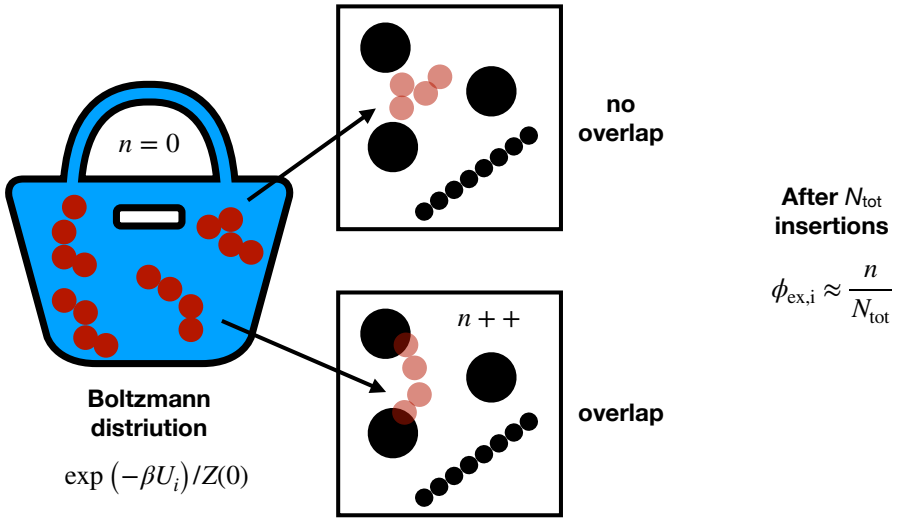

Figure 3.2: **Schematics of MC algorithm for computing excluded volume fraction $\phi_{\text{ex},i}$.** Initial configuration of crowders is loaded from a BD simulation snapshot. Then, reagent is inserted to the crowded box randomly, in a conformation drawn from Boltzmann distribution. Every insertion resulting in overlap of reagent and at least one of the crowders leads to incrementation $(n++)$ of the counter variable n. After large number of trials N_{tot}, ratio n/N_{tot} gives an estimate of the fraction of volume excluded to the selected reagent.

we obtain:

$$\frac{1}{\gamma_i} = 1 - \phi_{\text{ex},i} \approx \frac{1}{Z_i\left(0\right)} \frac{1}{N_{\text{tot}}} \sum_{\alpha=1}^{N_{\text{tot}}} \frac{\exp\left[-\beta U_i\left(\{\boldsymbol{r}_j\}_\alpha\right)\right] \exp\left[-\beta \sum_{j=1}^{n_i} \sum_{k=1}^{N} V(\boldsymbol{r}_{\alpha j} - \boldsymbol{R}_k)\right]}{\exp\left[-\beta U_i\left(\{\boldsymbol{r}_j\}_\alpha\right)\right] / Z_i\left(0\right)}$$
$$= \frac{1}{N_{\text{tot}}} \sum_{\alpha=1}^{N_{\text{tot}}} \exp\left[-\beta \sum_{j=1}^{n_i} \sum_{k=1}^{N} V(\boldsymbol{r}_{\alpha j} - \boldsymbol{R}_k)\right]. \tag{3.17}$$

For hard-sphere interactions between i-th particle and crowders (Eq. A.6), the exponential term in Eq. 3.17 has only two possible values:

- 0, if hard-sphere potential is infinite, *i.e.*, i-th particle overlaps with at least one of the crowders,
- 1, if hard-sphere potential is zero, *i.e.*, i-th particle does not overlap with any crowder.

We used the following algorithm to compute the excluded volume fraction $\phi_{\text{ex},i}$ (Fig. 3.2):

1. The positions of crowders are loaded from a BD trajectory of crowded box simulation.
2. A reagent is inserted into the system at a random position (and, for nonspherical particles, with random orientation), and in conformation drawn from the Boltzmann distribution (Eq. 3.14).
3. If the reagent overlaps with any of the crowders in the box, the counter variable n is incremented.

4. The reagent is removed from the system.

5. After N_{tot} repetitions of steps 2-4, the excluded volume fraction is approximated by n/N_{tot}.

For that purpose, I developed `ExVol` software (Appendix D.4). Reagent's conformations from BD simulation are Boltzmann-distributed, so sampling from the BD trajectory fulfills Eq. 3.14. The configurations of crowders can be sampled from BD simulation of the crowders as well.

The algorithm presented above is, in fact, the Widom insertion method applied to hard particles [93]. Qin & Zhou [94] used this method to study the effects of crowding on protein stability against denaturation and protein association equilibria. In a separate paper, the authors reported a good agreement between the results of explicit MD simulations of protein in crowded box and the MC insertion-based method [95].

The algorithm for calculating excluded volume fraction can be generalized to account for interactions V between the inserted particle and the crowders other than hard-core. To compute what we call the effective excluded volume fraction for non-hard-sphere systems, we use the modified algorithm:

1. The positions of crowders are loaded from a BD trajectory of crowded box simulation.

2. A reagent is inserted into the system at a random position (and, for nonspherical particles, with random orientation), and in conformation drawn from the Boltzmann distribution (Eq. 3.14).

3. The interaction energy V between the reagent and the crowders is computed.

4. Counter variable x is incremented by $1 - \exp(-\beta V)$.

5. The reagent is removed from the system.

6. After N_{tot} repetitions of steps 2-5, the effective excluded volume fraction is approximated by x/N_{tot}.

Note that effective occupied volume fraction may be defined as an effective volume excluded to a point particle.

Chapter 4

Diffusion in crowded media

> These motions were such as to satisfy me ... that they arose neither from currents in the fluid, nor from its gradual evaporation, but belonged to the particle itself.
>
> Robert Brown

In contrast to a physicist or chemist, a biologist usually thinks, talks about, or even sees the macromolecules composing biological cells not so much in terms of their physical properties, but rather their biological function, *i.e.*, the reasons for their occurrence in systems subject to natural selection. However, molecules, big or small, can perform their function only when they approach or are delivered to a specific location in a cell or encounter their specific counterparts. Thus, the mobility of macromolecules, although somewhat hidden deeper in the biological machinery, in fact, underlies the functioning of biological systems.

In living cells, two modes of motion exist: diffusion (thermal transport) and motor transport. Although the latter is much more effective, it is dependent on chemical energy, whereas the former is not, so the two coexist. Furthermore, prokaryotic cells lack the permanent cytoskeleton structure over which the motor proteins can transport cargo, hence they rely solely on diffusion [96]. For specific examples of reaction-diffusion systems driving biological cells, the reader is referred to a review by Soh *et al.* [97].

As noted by Netz & Eaton [33], in the near future first-principle simulations of biological cells, even as small and simple as *Mycoplasma genitalium*, will remain computationally prohibitive, hence the reaction-diffusion models for a long time will stay dominant in the field of cellular modeling. Thus, understanding intracellular diffusion is of utmost importance to the reliability of such modeling.

In this Chapter, we discuss research concerning macromolecular diffusion in crowded environments mimicking intracellular milieu. In Section 4.1, we overview an immense body of experiments, theories, and simulations concerning diffusion in crowded environments, *in vivo* as well as *in vitro*, focusing on both what is considered certain and, probably more interestingly, where there are still gaps in our understanding and what is uncertain due to contradictory results. Finally, in Sections 4.2–4.5, I present the results of our scientific inquiries into the in-

fluence of hydrodynamic and attractive interactions, shape, and softness of macromolecules on the diffusion in crowded environments.

4.1 Literature review

Macromolecular crowding (Section 2.3) is expected to visibly affect the diffusion of macromolecules in the cytoplasm, as well as nucleoplasm, membranes, and extracellular matrix. Here, I review the experiments and simulations pointing out the deviations from the normal, dilute-regime diffusion, which we discussed in section Section 2.1. Additionally, I describe theoretical models aimed at explaining these deviations.

For the rest of this Thesis, I will commonly use the distinction between a tracer, *i.e.*, the molecule the motion of which is under study, and crowders, *i.e.*, all the background molecules affecting the motion of the tracer. The distinction origins from experiments, *e.g.*, fluorescence recovery after photobleaching (FRAP), where tracers are fluorescently tagged, hence only they are visible to the experimentalist, the other macromolecules – crowders – merely creating a dark background which affects tracer motion. In simulations, the division into tracer and crowders is arbitrary.

4.1.1 Measurements *in vivo*

Studies of the macromolecular diffusion in the cytoplasm started over 40 years ago [98], and since then, the research field has grown hugely. The majority of early results were obtained with the FRAP method [99, 100]. The pioneering studies focused on diffusion in the eukaryotic cytoplasm due to the larger size of eukaryotic cells compared to prokaryotic ones, which makes them easier to investigate experimentally.

In 1981, Wojcieszyn *et al.* [98] measured translational diffusion of fluorescently labeled immunoglobulin G (IgG) and bovine serum albumin (BSA) in human fibroblast cytoplasm and reported approximately 70 times lower diffusion coefficients than in dilution. The following studies in various eukaryotic cells reported more minor diffusion slowdowns, ranging from 2- to 6-fold [101–106], apart from very large tracers [102, 103].

The differences between these results are probably not exclusively the features of various organisms but, at least in part, hallmarks of some interactions between fluorescent tracers and the cytoskeleton. For instance, tracers used by Wojcieszyn *et al.* [98] apparently interacted with the fibroblast microtubule network, as the 70-fold slowdown was reduced upon adding colchicine, the microtubule polymerization inhibiting agent.

Subsequently, technically more demanding FRAP measurements of the macromolecular diffusion in prokaryotic cytoplasm started to appear. In 1999, Elowitz *et al.* [107] reported an approximately 11 times slower diffusion of green fluorescent protein (GFP) in *Escherichia coli* than in dilution and the following studies reported similar slowdowns [108–110]. Schavemaker

et al. [96] in their review paper collected an extensive set of experimental results of diffusion coefficient measurements in bacteria cells. It seems that, ignoring the pioneering results by Wojcieszyn *et al.* [98], the diffusion in prokaryotic cells is visibly slower than in eukaryotes, mainly due to the smaller macromolecular content in eukaryotes (Section 2.3) [62, 111].

The rise of single-molecule methods, mainly single-molecule tracking (SMT) [112] and fluorescence correlation spectroscopy (FCS) (Appendix E), delivered new experimental data regarding diffusion coefficients *in vivo* [113–115]. What is particularly exciting, the data differs from the one obtained in earlier studies, predominately using FRAP method. A recent paper by Bellotto *et al.* [115] reports translational diffusion coefficients of multiple proteins of various sizes in *E. coli* using both FCS and FRAP. The FRAP measurements resulted in similar, albeit systematically smaller (5 to 30%) diffusion coefficients, but did not lead to qualitatively different conclusions. For small proteins, like GFP, the authors measured with FCS a 6-fold diffusion slowdown, which is visibly smaller than the values reported in the aforementioned prokaryotic FRAP studies [107, 116–118].

Apart from the bare values of diffusion coefficients, there are also some specific features of diffusion in cells' cytoplasm, which are worth noting here. In dilution, the dependence of diffusion coefficient D on size a of the diffusing particle is determined by the Stokes-Sutherland-Einstein (SSE) relation ($D \propto 1/a$, see Eq. 2.10). Some authors reported a faster decay of D with size *in vivo* [102, 103, 105, 109, 110, 119], which is sometimes referred to as sieving effect. However, there are also reports to the contrary, in which $D(a)$ follows the SSE relation, apart from very large tracers [104, 108, 114, 115].

Moreover, as the cytoplasm is a complex fluid, there are reports suggesting the appearance of anomalous diffusion therein (Section 2.2) [50, 57, 113, 114, 120, 121]. For instance, Golding & Cox [50] showed that diffusion of mRNA in *E. coli* is anomalous even on a timescale of minutes, with anomalous exponent $\alpha \approx 0.7$, close to the asymptotic value in dense polymer solutions [122]. Interestingly, Bellotto *et al.* [115] used anomalous diffusion model to fit FCS data and received $\alpha = 0.8$-0.86 suggesting the anomalous diffusion. However, after correctly accounting for finite volume effects, anomalous diffusion disappeared. This shows how small hidden assumptions in theoretical models used to analyze experimental data may lead to artifacts interpreted as real physical phenomena.

Leaving aside detailed physical mechanisms of the macromolecular diffusion inside the cytoplasm, the reported experimental values allow placing the macromolecules' diffusivities in the frame of cellular length scales. In order to do that, let us compare estimates of how much it would take GFP to traverse a distance equal to the respective cell size, based on Eq. 2.18. We assume that the intracellular diffusion coefficient of GFP is $14.8\,\mathrm{nm^2\,\mu s^{-1}}$, following Bellotto *et al.* [115]. Three cells are worth mentioning here: the smallest prokaryote *M. genitalium* of diameter $\approx 400\,\mathrm{nm}$, the model prokaryote *E. coli* of length $\approx 2\,\mu\mathrm{m}$, and the eukaryotic fibroblast cell of diameter $\approx 14\,\mu\mathrm{m}$. It would take GFP $\approx 1.8\,\mathrm{ms}$, $45\,\mathrm{ms}$, and $2.2\,\mathrm{s}$, respectively, to diffuse a distance equal to these cell sizes (Fig. 4.1).

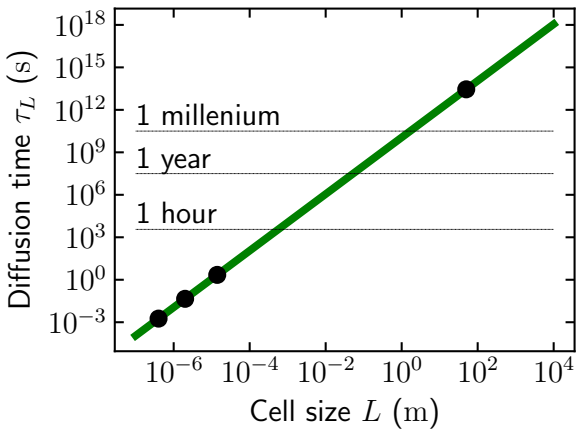

Figure 4.1: **Diffusion timescale** *vs.* **cell size** Average time τ_L needed by GFP to traverse the distance L equal to cell size, calculated with Eq. 2.18 and plotted in the form of a log-log plot. The value of GFP diffusion coefficient is taken from ref. [115]. Markers denote (in that order) *M. genitalium*, *E. coli*, fibroblast, and sauropod head-to-tail nerve cell, reportedly the most extended cell ever existing [123].

Probably the longest cells that ever existed were nerves connecting the tail and brain of the largest sauropod (clade of dinosaurs), achieving even $50\,\mathrm{m}$ [123]. The diffusion timescale for them is close to 1 million years (more precisely, 890000 years). This example is slightly extreme, but demonstrates that due to a quick, quadratic increase in the diffusion timescales, larger cells cannot depend solely on the diffusive transport. Precisely for that reason, eukaryotic cells use motor proteins which actively transport cargo along the cytoskeleton architecture. On the other hand, for the same reason the size of prokaryotic cells, which do not have a permanent cytoskeleton, is limited by the diffusion timescale [124].

Ross [19] coined a term "dark matter of biology" for a broad range of intracellular effects, including diffusion slowdown. The simile is based on the fact that in cell biophysics, likewise in astrophysics, there are deviations from fundamental theories, like, for instance, the theory of Brownian motion (Section 2.1), but it is practically impossible to isolate what their sources are, as a plethora of various effects not directly visible in experiments are all at once at play.

At least six different mechanisms may, to a different extent, account for the observed diffusion slowdown [10, 116, 125]:

1. Increased water viscosity (Section 4.1.2),
2. Excluded volume interactions (Section 4.1.3),
3. Hydrodynamic interactions (Section 4.1.4),
4. Electrostatic interactions (Section 4.1.5),
5. Nonelectrostatic attractive interactions (Section 4.1.6),
6. Confinement within polymer network (Section 4.1.7).

Experimentally, it is challenging to study each of them separately. However, it is possible to single out the mechanisms 1-3 by studying concentrated solutions of sufficiently inert polymeric crowders of high ionic strengths, assuming that the water viscosity there changes similarly as inside the cell. This approach became state-of-the-art when accounting for the effects of macromolecular crowding *in vitro* [125–127]. Then, lowering the ionic strength or adding noninert crowders, *e.g.*, proteins, may additionally introduce mechanisms 4 and 5 [128–130]. Simulations [35–38, 131, 132] and theoretical considerations are, in that respect, more flexible, as they enable isolation of each of these 6 mechanisms. Gauging the importance of each of these mechanisms is one of the major goals of the intracellular diffusion research field.

4.1.2 Increased water viscosity

The effect of increased fluid phase viscosity is straightforward from the theoretical standpoint, as it reduces to merely rescaling the value of viscosity η in the SSE relation (Eq. 2.10). However, the majority of measurements of diffusion of small molecules *in vivo* and *in vitro* show that their diffusion is weakly affected, which would suggest that the fluid viscosity increase is minor [125, 133, 134]. Furthermore, in a scenario in which the viscosity has a deciding role, the rotational diffusion of spherical molecules should be slowed down similarly to translational diffusion, which is not the case as shown by Swaminathan *et al.* [105] (only ≈ 1.5-fold decrease). Therefore, the change in the fluid viscosity is usually ignored.

4.1.3 Excluded volume interactions

4.1.3.1 Simulations: lattice models

Excluded volume effects were studied in isolation by Saxton [56, 135–140] in his important series of papers concerning random walk on the two-dimensional triangular lattice with obstacles, and later by Ellery *et al.* [141] on the two-dimensional and three-dimensional square lattice using nonstochastic method introduced by Mercier & Slater [142, 143]. Their main observation is that the total occupied volume fraction ϕ_{occ} (Section 2.3.1) is insufficient to predict tracer's diffusion coefficient. The diffusion coefficient depends in a complicated way on other features: tracer's size and crowders' sizes, shapes, and mobilities [135–137, 140, 141].

For sphere-like (on the lattice) crowders and tracers, the diffusion coefficient decreases with the tracer size and increases with the crowder size, assuming a fixed occupied volume fraction ϕ_{occ} [135, 140, 141]. There are two interesting exceptions to the former. (1) When crowders are allowed to move, the tracer-size dependence is weak, and overall, mobile crowders hinder the diffusion less effectively than immobile ones [136, 137]. (2) There is no tracer size dependence when crowders aggregate to form fractal-like structures [140]. These effects might be the reasons for ambiguous experimental results, some of which report tracer size-dependence [102, 103, 105, 109, 110, 119], while the others do not, apart from very large tracers [104, 108, 114,

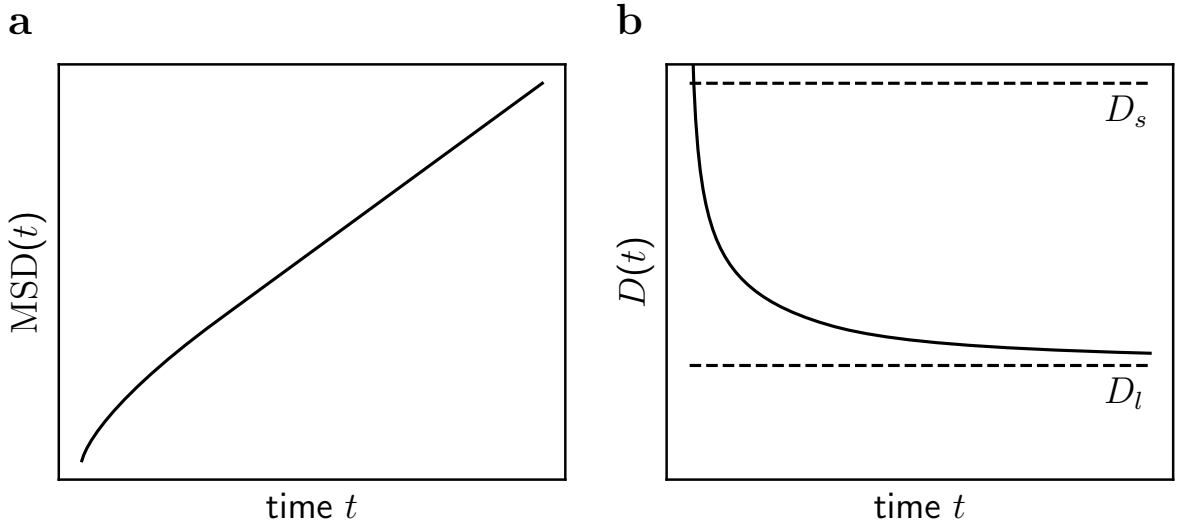

Figure 4.2: **Diffusion in crowded environments.** (**a**) Mean squared displacement (MSD) of a tracer in a crowded fluid. At short times, MSD changes nonlinearly (Eq. 2.19), following a subdiffusive power law ($\alpha < 1$). At long times, the linear normal regime is brought back. (**b**) Time-dependent diffusion coefficient $D(t) = \mathrm{MSD}(t)/6t$. Due to collisions with crowders, the diffusion coefficient gradually decreases and tends to the limit value for $t \to \infty$. We refer to $\lim_{t\to 0} D(t)$ as short-time diffusion coefficient D_s, and to $\lim_{t\to\infty} D(t)$ as long-time diffusion coefficient D_l. We neglect the initial balistic motion.

115].

Furthermore, the dependence on crowder shape is complex. For the same volume fraction, short rod-like and L-shaped crowders hinder the diffusion of sphere-like tracers more effectively than small spheres, but for longer, rod-like crowders, the difference disappears [141].

Moreover, Saxton [56] showed that in highly occupied lattices, the overall diffusive dynamics is not normal, but in contrast to anomalous diffusion (Section 2.2), it cannot be expressed by a general power law (Eq. 2.19) either. The observed motion of the tracer is subdiffusive at short times, with short-time diffusion coefficient $D_s = \lim_{t\to 0} D(t)$, but then returns to linear normal regime with long-time diffusion coefficient $D_l = \lim_{t\to\infty} D(t)$, as shown schematically in Fig. 4.2.

The studies by Saxton [56] and Ellery *et al.* [141] are limited by the fact that the authors considered the diffusion on a lattice. Nevertheless, their results successfully accounted for the excluded volume effects and brought attention to the effects beyond the total occupied volume, such as sizes and shapes of the crowders.

4.1.3.2 Theory: off-lattice models

Hanna *et al.* [144] solved the N-particle Smoluchowski equation for a system of hard spheres performing Brownian motion. The obtained long-time self-diffusion coefficient D_l up to the

first order in ϕ_{occ} reads:

$$\frac{D_l}{D_0} = 1 - 2\phi_{\mathrm{occ}}. \tag{4.1}$$

The slope of diffusion coefficient decrease agrees well with the on-lattice results by Saxton [136] observed for $\phi_{\mathrm{occ}} \leq 15\%$.

Muramatsu & Minton [145] introduced an approximate theory of excluded volume effect on the diffusion coefficient slowdown, which is based on the scaled particle theory (SPT) (Section 2.4.2). It relates the diffusion coefficient with the Gibbs displacement activation energy ΔG_t:

$$D_0 = A \exp\left[-\frac{\Delta G_t}{k_{\mathrm{B}}T}\right], \tag{4.2}$$

where A is the diffusion coefficient in the limit of infinite temperature T. In crowded environments, the Gibbs energy change is modified by a factor which can be estimated with SPT (Section 2.4.2). The relative diffusion coefficient reads:

$$\ln \frac{D}{D_0} = -\frac{\Delta\Delta G_t}{k_{\mathrm{B}}T}. \tag{4.3}$$

where $\Delta\Delta G_t$ is the Gibbs energy needed to make a cavity in the crowded fluid that allows for a movement of the particle.

In principle, it is nontrivial to calculate $\Delta\Delta G_t$ for a cavity needed for a small translation of a sphere. However, it may be roughly approximated with the difference between the insertion Gibbs energies for spherical molecules of radius a and $a+da$, and computed from the SPT [12]:

$$\Delta\Delta G_t = \Delta G\left(a + da\right) - \Delta G\left(a\right). \tag{4.4}$$

Han & Herzfeld [146] improved that approach by approximationg $\Delta\Delta G_t$ more closely, with a dfference between the insertion free energies of a spherocylinder and a sphere. For small ϕ_{occ}, this approach leads to Eq. 4.1 if the spherocylinder length is set to $2a/3$.

In contrast to the result by Hanna *et al.* [144] (Eq. 4.1), the approaches by Muramatsu & Minton [145] and Han & Herzfeld [146] allow for pinpointing the dependence of diffusion coefficient on various features of the tracer and crowders. For instance, it predicts a more substantial diffusion coefficient decrease for larger tracers at a fixed occupied volume. Moreover, the predicted crowder-size dependence is opposite, namely the larger crowders hinder the diffusion of tracers less strongly at fixed ϕ_{occ}.

4.1.4 Hydrodynamic interactions

4.1.4.1 Theory

The next level of description includes hydrodynamic interactions – indirect interactions arising because a particle moving through a fluid induces a fluid velocity field, which affects the motion of other particles (Section 3.2) [10]. Cichocki & Felderhof [147] derived expressions for short-time and long-time diffusion coefficients for a suspension of spherical Brownian particles to a first-order in ϕ_{occ}. The resulting expressions read [147]:

$$\frac{D_s}{D_0} = 1 - 1.8315\phi_{\mathrm{occ}}, \tag{4.5}$$

for short-time diffusion coefficient, and:

$$\frac{D_l}{D_0} = 1 - 2.0972\phi_{\mathrm{occ}}, \tag{4.6}$$

for long-time diffusion coefficient. The long-time diffusion coefficient decreases slightly more quickly than predicted in absence of hydrodynamic interactions by Hanna *et al.* [144] (Eq. 4.1).

Different approach was undertaken by Tokuyama & Oppenheim [148], who, starting from the fluctuating Navier-Stokes equation, derived formulas for short-time D_s and long-time D_l diffusion coefficients in suspensions of identical hard spheres in an incompressible fluid. The short-time diffusion coefficient is:

$$\frac{D_s}{D_0} = \frac{1}{1 + H(\phi_{\mathrm{occ}})}, \tag{4.7a}$$

where:

$$H(\phi_{\mathrm{occ}}) = \frac{2b^2}{1-b} - \frac{c}{1+2c} - \frac{bc(2+c)}{(1+c)(1-b+c)}, \tag{4.7b}$$

$$b(\phi_{\mathrm{occ}}) = \sqrt{\frac{9}{8}\phi_{\mathrm{occ}}}, \tag{4.7c}$$

$$c(\phi_{\mathrm{occ}}) = \frac{11}{16}\phi_{\mathrm{occ}}. \tag{4.7d}$$

For the long-time diffusion coefficient, Tokuyama & Oppenheim [148] obtained:

$$\frac{D_l}{D_0} = \frac{1 - \frac{9}{32}\phi_{\mathrm{occ}}}{1 + H(\phi_{\mathrm{occ}}) + \frac{\tilde{\phi}}{(1-\phi)^2}}, \tag{4.8a}$$

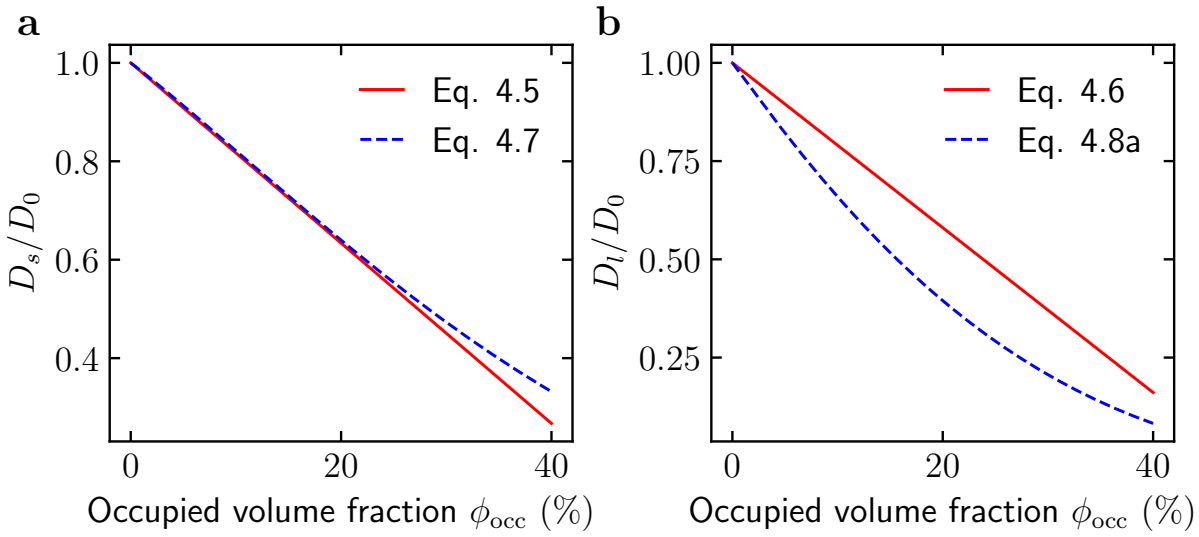

Figure 4.3: **Comparison of theoretical expressions for (a) short-time and (b) long-time diffusion coefficient in crowded environment.** (**a**) Expression due to Cichocki & Felderhof (Eq. 4.5) in red; expression due to Tokuyama & Oppenheim (Eq. 4.7a) in blue. (**b**) Expression due to Cichocki & Felderhof (Eq. 4.6) in red; expression due to (Eq. 4.8a) in blue.

where:

$$\tilde{\phi} = \frac{\phi_{\mathrm{occ}}}{\phi_0}, \tag{4.8b}$$

$$\phi_0 = \left(\frac{4}{3}\right)^3 \frac{1}{7\ln 3 - 8\ln 2 + 2} \approx 0.5718. \tag{4.8c}$$

We note that Eq. 4.8a predicts a lower D_l than Eq. 4.6 derived by Cichocki & Felderhof [147] (Fig. 4.3).

4.1.4.2 Simulations

Ando & Skolnick [36] showed using Stokesian dynamics (SD) simulations accounting for both far-field and near-field hydrodynamic interactions (Section 3.2.2) that including excluded volume effects and hydrodynamic interactions only is enough to reproduce the GFP diffusion coefficient in *E. coli* without any fitting parameters. It may, however, be argued that it holds only in one of three systems of various ϕ_{occ} they analyze, $300\,\mathrm{mg\,mL^{-1}}$, whereas the experimental estimates for ϕ_{occ} in *E. coli* are closer to $340\,\mathrm{mg\,mL^{-1}}$ [9]. Furthermore, the authors compared their results to the GFP diffusion coefficient in *E. coli* obtained by Elowitz *et al.* [107] using FRAP, which may be underestimated according to Bellotto *et al.* [115].

4.1.4.3 Experiments: artificial inert crowders

In principle, in solutions of inert, compact polymers, hydrodynamic interactions, fluid viscosity, and excluded volume are the only diffusion slowdown mechanisms at play. Of course, in practice, it is not trivial to determine how much the real polymer crowders, such as Ficoll, Dextran, poly(ethylene glycol) (PEG), poly(ethylene oxide) (PEO), *etc*., fulfill these criteria, and if yes, up to what concentrations [149]. Nevertheless, these discrepancies are beyond the scope of this Thesis.

The majority of diffusion measurements performed in artificially crowded solutions agree that there is a tracer-size dependence in crowded systems [126, 150–154], although some authors do not observe this effect [155, 156]. Based on extensive experimental studies [152, 153] and previous phenomenological equations [155, 157], Kalwarczyk *et al.* [133] proposed a single formula, called lengthscale-dependent viscosity model (LDVM), to capture the general dependence of viscosity (and by simple inversion – the diffusion coefficient, see Eq. 2.10) on the tracer size, which applies to crowded micellar and polymer solutions:

$$\frac{\eta}{\eta_0} = \exp\left[\left(\frac{R_{\text{eff}}}{\xi}\right)^B\right]; \tag{4.9a}$$

$$\frac{D_l}{D_0} = \exp\left[-\left(\frac{R_{\text{eff}}}{\xi}\right)^B\right], \tag{4.9b}$$

where B is a constant close to 1, ξ is a correlation length of the polymer network depending on its concentration and gyration radius, and the effective hydrodynamic radius R_{eff} is given by:

$$R_{\text{eff}}^{-2} = a^{-2} + R_h^{-2}, \tag{4.10}$$

where a and R_h are hydrodynamic radii of a tracer and polymeric or micellar crowder, respectively.

Eq. 4.9 predicts that the smallest tracers experience viscosity close to the water viscosity, as we discussed in Section 4.1.2, whereas large tracers experience macroscopic viscosity. Furthermore, Junker *et al.* [126] showed that polymer crowding agents exhibit positive deviation from the SSE relation, *i.e.*:

$$D_l(\phi_{\text{occ}}) > \frac{k_{\text{B}}T}{6\pi\eta a}, \tag{4.11}$$

which means that the viscosity felt by tracer particles is smaller than the macroscopic viscosity (compare to Eq. 2.10) and agrees with the LDVM [133].

Banks & Fradin [122] observed anomalous diffusion of streptavidin in crowded solutions of Dextran persisting for a few seconds. The measured anomalous exponent α depended on

the crowder size and concentration. Interestingly, its behavior was asymptotic, and approached 0.74 with increasing crowder concentration, irrespective of the crowder size.

4.1.5 Electrostatic interactions

The role of electrostatic interactions in the diffusion slowdown is still unclear. The Debye length in cells is less than $1\,\mathrm{nm}$ [158], which leads to a rapid decay of electrostatic interactions with the distance. However, some of the biomacromolecules bear huge electric charges, *e.g.*, ribosomes $\approx -4024e$ [36]. Schavemaker *et al.* [159] showed with FRAP that in *E. coli* a positively-charged GFP diffuses two orders of magnitude slower than its negatively-charged analog. The difference is probably due to the electrostatic attraction by ribosomes.

McGuffee & Elcock [37] compared the results of Brownian dynamics (BD) simulations of a coarse-grained *E. coli* cytoplasm model with and without electrostatic interactions. Apart from electrostatics, only excluded volume interactions were accounted for. The authors reported ≈ 1.3 times slower diffusion of GFP in a model with electrostatics at play.

4.1.6 Nonelectrostatic attractive interactions

4.1.6.1 Simulations

The next level of description involves attractive interactions between the macromolecules. In a random walk study on 2D lattices, Saxton [55] showed that attractive interactions between the crowders and tracer lead to a significant decrease in diffusion coefficient compared to the excluded-volume-only reference system. The magnitude of the decrease depends on the details of the interactions and their strength.

We discuss here only so-called valley models, *i.e.*, models in which the lattice points have attributed various binding energies. The probability of escape from a given binding site was computed by Saxton [55] using the Metropolis algorithm. When random walk simulations were started from positions drawn from a uniform probability distribution, the diffusion was strongly anomalous over a long timescale. However, if the starting positions were Boltzmann-distributed, the magnitude and timescale of anomalous subdiffusion were comparable to those observed in excluded-volume-only systems, however, with a smaller D_s value. In systems with binding sites but without crowding, in the case of equilibrated initial configuration, there was no anomalous diffusion.

Nawrocki *et al.* [160] argued, based on the results of all-atom molecular dynamics (MD) simulations of proteins, that the translational and rotational diffusion slowdown could be explained solely by excluded volume and transient complex formation due to attractive interactions. It is contrary to the stance held by Ando & Skolnick [36], who claim that the excluded volume and hydrodynamic interactions could explain the translational diffusion slowdown without invoking any attractive interactions. As described by Ando & Skolnick [36], precise mea-

surements of tracer-size-dependence of diffusion slowdown may, in principle, tip the balance between these two hypotheses.

4.1.6.2 Experiments: noninert crowders

As the systems with viscosity, hydrodynamic, and excluded volume interactions only are realized by artificial crowder solutions with high ionic strength, the systems which, on top of these interactions, have also electrostatic and nonelectrostatic attractive interactions are realized by crowded protein solutions. The diffusion slowdown observed in crowded protein systems is more substantial than observed in polymer crowder systems of comparable occupied volume ϕ_{occ} [129, 130]. Proteins differ from inert crowders because they are nonuniformly charged and can be engaged in a myriad of nonspecific interactions varying in strength [128].

Furthermore, in contrast to polymeric crowders, protein crowders lead to a negative deviation from the SSE relation [129, 161], *i.e.*:

$$D_l(\phi_{\mathrm{occ}}) < \frac{k_{\mathrm{B}}T}{6\pi\eta a}, \tag{4.12}$$

This means that diffusion slowdown in protein solutions is larger than what is expected based on the macroscopic viscosity (compare to Eq. 2.10).

Etoc *et al.* [114] analyzed how the intracellular diffusion of a nanoparticle with a fixed size changes upon varying its surface coating. With inert coating, the diffusion coefficient was only 2-4 times smaller than in water, whereas, with less inert, even 10-15 times. For the noninert tracers, the authors also observed a long-time subdiffusion (Section 2.2).

Interestingly, the LDVM (Eq. 4.9) allowed Kalwarczyk *et al.* [162] to obtain diffusion coefficients of the whole *E. coli* proteome based on the literature values for *ca.* 20 macromolecules in its cytoplasm [62, 162]. The physical meaning of ξ and R_h (Eq. 4.9) in cells is not clear, although in HeLa and Swiss 3T3, $\xi \approx 5$-$7\,\mathrm{nm}$ and coincides with the hydrodynamic radius of the actin filaments and water pores [62, 103, 133]. However, all papers we are aware of advocating for LDVM [133, 134, 152, 153, 162–167] reduce the mobility of macromolecules merely to its size dependence, which, as discussed above, may not apply to systems with attractive interactions [114, 129], in which the microscopic viscosity exceeds the macrocopic one.

4.1.7 Confinement within polymer network

In addition to the mobile biomacromolecules crowding the cytoplasm, the cell interior also contains biopolymeric networks, such as cytoskeleton [168] and nucleoid [169], which affect its physicochemical properties. In some sense, such cytoplasm is similar to a concentrated polymer solutions such as hydrogels, in which thin channels bridge separate cages of various sizes.

Such a porous environment is known to affect the diffusion of particles therein in a complex

way. First and foremost, the effect depends strongly on the size of a tracer relative to the mesh size ξ of the polymeric network, which is determined by its total concentration and degree of cross-linking. When tracers are significantly smaller than the mesh size, their diffusion is only slightly affected by it, whereas when tracers are significantly larger, they become trapped and virtually immobile [170, 171]. In the intermediate regime, when $2a \approx \xi$, the diffusion of tracers is transiently anomalous. It is because the molecules diffuse inside individual cages of the network and relatively rarely hop between them. In the long-time regime, the normal diffusion is recovered, and its rate is determined by the frequency of such hops.

Moreover, tracer diffusion in a polymeric network becomes coupled with the dynamics of the network. It was observed that even the particles a few times larger than the mesh size are not entirely trapped and are able to diffuse, albeit slowly [171]. As shown by BD simulations, it is due to cooperative mesh fluctuations, which can dynamically change the local mesh size and facilitate the release of a tracer from the cage [172, 173]. Interestingly, the effect is the opposite for smaller tracers, which diffuse faster in nonfluctuating networks, owing to their smaller effective size [172].

Finally, as with mobile crowders, the immobile ones may also interact with tracers through interactions other than the excluded volume [174, 175].

4.1.8 Concluding remarks

Ellis [8] suggested editors to reject papers reporting *in vitro* experiments that have not controlled macromolecular crowding, as they may be of little or no relevance to *in vivo* conditions. However, the emerging picture seems to be very complex, as macromolecular crowding is not characterized by a single, easy to control value, *e.g.*, occupied volume fraction ϕ_{occ}. Due to conflicting results, there is currently no consensus on whether hydrodynamic or attractive interactions or their combination account for the diffusion slowdown observed *in vitro*, and the influence of the crowder shape has not been completely understood. We address these problems in the following sections of this chapter.

4.2 Effect of hydrodynamic interactions

The works by Ando & Skolnick [36] and Roosen-Runge *et al.* [130] have attracted much attention to the role of hydrodynamic interactions (Section 4.1.4) in the slowdown of diffusion *in vivo*. Although it is widely accepted that accounting for far-field hydrodynamic interactions only is not sufficient to correctly describe the diffusion in crowded environments [10, 77], surprisingly, to our knowledge, there is no work comparing directly the effect of far-field and near-field hydrodynamics for simple systems of various occupied volume fractions ϕ_{occ}.

Blanco *et al.* [176] compared BD simulations (1) without hydrodynamic interactions, (2) with hydrodynamic interactions in the Rotne-Prager-Yamakawa (RPY) approximation (although with-

Table 4.1: **Compositions of systems studied with BD and SD simulations to assess the role of hydrodynamic interactions in diffusion slowdown.** ϕ_{occ} is the occupied volume fraction and N_{F} is a number of particles in the simulation box.

ϕ_{occ}	N_{F}
5.5%	42
11.1%	84
22.1%	168

out accounting for their long-range character *via* Ewald summation), and (3) with a mean-field method based on the Tokuyama & Oppenheim [148] formula for rescaling the short-time diffusion coefficients (Eq. 4.7a). However, their trajectories ($1\,\mu\mathrm{s}$) are likely too short to reach the long-time diffusion, and the timestep ($100\,\mathrm{ps}$) was probably too large in this context.

The purpose of our study was to compare three different approaches to hydrodynamic interactions for a simple system of identical, spherical crowders:

1. No hydrodynamic interactions (free draining).
2. Far-field hydrodynamic interactions with the Ewald-summated generalized RPY approximation (Section 3.2.1).
3. Far-field and near-field hydrodynamic interactions with F-formulation of SD (Section 3.2.2).

We used the hydrodynamic radius $a = 5.1\,\mathrm{nm}$, mimicking Ficoll70, frequently used artificial polymer crowder [126]. However, the results do not depend on the size of particles. We studied systems of occupied volume fraction $\phi_{\mathrm{occ}} = 5.5$, 11.1, and 22.1% (Fig. 4.4a).

4.2.1 Simulation details

In our BD and SD simulations, we placed the model macromolecules in cubic boxes of $75\,\mathrm{nm} \times 75\,\mathrm{nm} \times 75\,\mathrm{nm}$ and applied periodic boundary conditions in all three directions. Precise numbers of particles in each studied system are presented in Table 4.1. The time step Δt was $0.5\,\mathrm{ps}$, and simulations lasted for $20\,\mu\mathrm{s}$ ($10\,\mu\mathrm{s}$ for $\phi_{\mathrm{occ}} = 20\%$). BD was propagated with the Ermak-McCammon scheme (Eq. A.3), and SD with the midpoint scheme with $m = 100$ (Eq. A.5). The temperature T was $293.15\,\mathrm{K}$, and dynamic viscosity $\eta = 1.005\,\mathrm{cP}$.

The particles interacted only *via* hard-sphere potential (Eq. A.6). We performed Ewald-summation of the diffusion matrix with $\alpha = \sqrt{\pi}$, $m_{\mathrm{cutoff}} = n_{\mathrm{cutoff}} = 2$ (Appendix B). We followed Ando & Skolnick [36] and performed the Choleski decomposition every 100 steps (instead of every step) for computational efficiency. In the SD, we used the generalized lubrication correction approach (Eq. 3.11) with cutoff on near-field hydrodynamic interactions equal to $6a$. Since there was no open-source software, allowing for simulations using lubrication-corrected RPY approximation, we developed and used our own `pyBrown` package (Appendix D.2).

We computed time-averaged mean squared displacement (TAMSD) (Eq. A.14) with a window length equal to $5\,\mathrm{ns}$ for each system under study. The long-time diffusion coefficients D_l were obtained by a linear fit to TAMSD with weights equal to $\sqrt{N_{\mathrm{steps}} - i - 1}$ to account for the fact that the i-th element of TAMSD vector is a time average of $N_{\mathrm{steps}} - i - 1$ squared displacements of a single particle. For fitting TAMSD with Eq. 2.9, we used only datapoints for $t > 10\,\mu\mathrm{s}$ ($t > 2.5\,\mu\mathrm{s}$ for $\phi_{\mathrm{occ}} \approx 20\%$). Uncertainty of the D_l due to sampling error was estimated by dividing the simulations into five subsets and computing the standard deviation of the mean while treating the subsets as independent "measurements".

Short-time diffusion coefficients D_s were obtained by computing the mean diagonal elements of the diffusion matrix at consecutive timesteps and averaging them:

$$D_s = \frac{1}{3N} \left\langle \mathrm{Tr}\left[\boldsymbol{D}\right] \right\rangle , \tag{4.13}$$

where N is the number of particles and $\mathrm{Tr}\left[\boldsymbol{D}\right]$ denotes a trace of diffusion matrix $\boldsymbol{D}$, *i.e.*, a sum of its diagonal elements. Nesting expression inside the angle brackets ($\langle\rangle$) represents averaging over timesteps.

4.2.2 Short-time diffusion

Short-time diffusion coefficients obtained from SD simulations decrease with increasing occupied volume fraction ϕ_{occ} (Fig. 4.4b). Linear fit to $D_s(\phi_{\mathrm{occ}})/D_0$ leads to an equation $1 - 1.9\phi_{\mathrm{occ}}$, close to the theoretical result obtained by Cichocki & Felderhof [147] (Eq. 4.5). and the F-version SD results by Phillips *et al.* [82]. The far-field hydrodynamic interactions do not affect the short-time diffusion coefficients, because they change only the off-diagonal blocks of diffusion matrix $\boldsymbol{D}$ (Section 3.2.1).

4.2.3 Long-time diffusion

The long-time diffusion is established after a few microseconds, faster for higher ϕ_{occ}. The long-time diffusion coefficients computed with all three approaches decrease upon increasing the occupied volume fraction ϕ_{occ} (Fig. 4.4c). Results accounting for a full range of hydrodynamic interactions are in perfect agreement with the Cichocki & Felderhof [147] formula (Eq. 4.6). Results not accounting for hydrodynamic interactions overestimate the long-time diffusion coefficients, conforming to a $1 - 1.8\phi_{\mathrm{occ}}$ trend, which is close to the theoretical result by Hanna *et al.* [144] (Eq. 4.1), albeit slightly higher. Diffusivities calculated accounting only for far-field hydrodynamic interactions are significantly higher than those obtained without hydrodynamic interactions at all. The linear fit gives a slope of decay between 1.0 and 1.2, depending on whether we include a point $\phi_{\mathrm{occ}} = 0.0$ into the fitting, which indicates that, at least for small ϕ_{occ}, the relation is nonlinear.

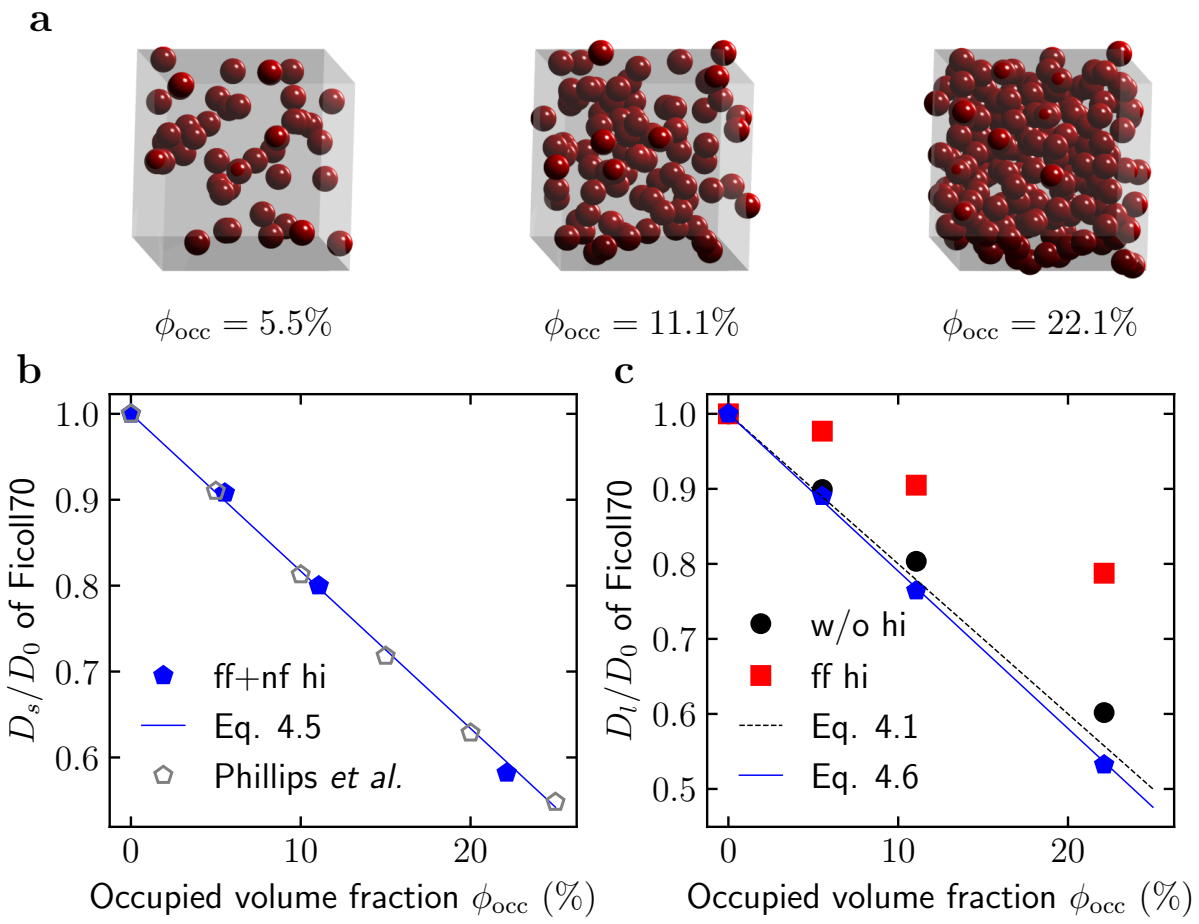

Figure 4.4: **Diffusion coefficient of Ficoll70 obtained with BD and SD on various levels of description of hydrodynamic interactions.** (**a**) Snapshots of simulated systems of hard spheres with increasing ϕ_{occ}. (**b**) Relative short-time diffusion coefficient D_s/D_0 of Ficoll70 from simulations with far-field and near-field hydrodynamic interactions (ff+nf hi, blue) as a function of ϕ_{occ}. Results are compared with the theoretical expression by Cichocki & Felderhof (Eq. 4.5, blue line) [147] and simulation results by Phillips *et al.* [82] (gray symbols). Note that $D_s = D_0$ when we do not account for near-field hydrodynamic interactions. (**c**) Relative long-time diffusion coefficient D_l/D_0 of Ficoll70 as a function of ϕ_{occ} from simulations without hydrodynamic interaction (w/o hi, black), with far-field hydrodynamic interactions (ff hi, red) and with far-field and near-field hydrodynamic interactions. Results are compared with the theoretical expressions by Hanna *et al.* [144] (Eq. 4.1, black line) and Cichocki & Felderhof [147] (Eq. 4.6, blue line). D_0 is computed from the SSE relation.

4.2.4 Discussion

The major difference between the BD simulations with far-field RPY hydrodynamic interactions and SD simulations with far-field and near-field hydrodynamic interactions is the decrease in short-time diffusion coefficient in the latter. For occupied volume fraction $\phi_{\mathrm{occ}} = 22.1\,\%$, lying in the lower end of the physiological range, the decrease in short-time diffusion coefficient is 42%. For the same ϕ_{occ}, the long-time diffusion coefficient obtained with BD without hydrodynamic interactions overestimates the one obtained with full hydrodynamics only by 13%,

while the RPY approximation overestimates it by 48%.

The interparticle correlations induced by the Ewald-summated RPY diffusion matrix lead to a visible underestimation of the decrease in the diffusion coefficient for the whole range of the studied occupied volume fractions, approximately by a factor of 2. Similarly, D_l/D_s in SD is much higher than D_l/D_0 without hydrodynamic interactions. It is because correlations make collisions less probable. The overall effect of the far-field hydrodynamic interactions is then an increase, not decrease, of D_l.

In quantum chemistry, there is a notion of a "Pauling point", brilliantly described in a quote by Vålådalen: "a characteristic feature of quantum chemistry was that even a fairly simple theory could sometimes give excellent agreement with experimental experience, but that this agreement may disappear whenever one tries to improve the theory" [177]. This seems to be the case in the description of diffusion in crowded environments as well. Long-time diffusion coefficients in dense hard-sphere systems obtained without accounting for hydrodynamic interactions are closer to the exact values than those which account for it only on the far-field level.

In principle, it is straightforward, although computationally rather cumbersome, to systematically improve the results of F-version SD. One should include the angular degrees of freedom with their coupling to the translational ones on the level of resistance and diffusion matrices, and possibly incorporate more terms in multipole expansion of far-field hydrodynamic interactions. However, it is unclear whether this computationally demanding procedure will systematically improve the reproduction of experimental diffusion coefficients of biologically relevant macromolecules. The equations describe the behavior of hard spheres, and the proteins, ribosomes, *etc*., rarely have either of these features. It would be interesting to verify how more realistic models of macromolecules affect the behavior of explicit water molecules in MD simulations, and by these means, possibly validate the RPY and SD approaches to hydrodynamic interactions.

4.3 Effect of macromolecule's shape

4.3.1 Experimental results

In our joint work [127], the experimental group of Jörg Fitter performed FCS measurements (Appendix E) of the diffusion coefficient of fluorescently-tagged streptavidin in buffer solutions containing mixtures of Ficoll70 and $16\text{-}\mathrm{nm}$-long double-stranded DNA (dsDNA) of various molar and occupied volume fraction, x_{dsDNA} and ϕ_{occ}, respectively (Fig. 4.5a). The results are gathered in Tables E.1–E.4. In all experiments the concentration of streptavidin was orders of magnitude lower than that of Ficoll70 and dsDNA. To our knowledge, dsDNA has never been used as a crowder before.

In systems containing only one crowder (Ficoll70 or dsDNA), the diffusion coefficient of

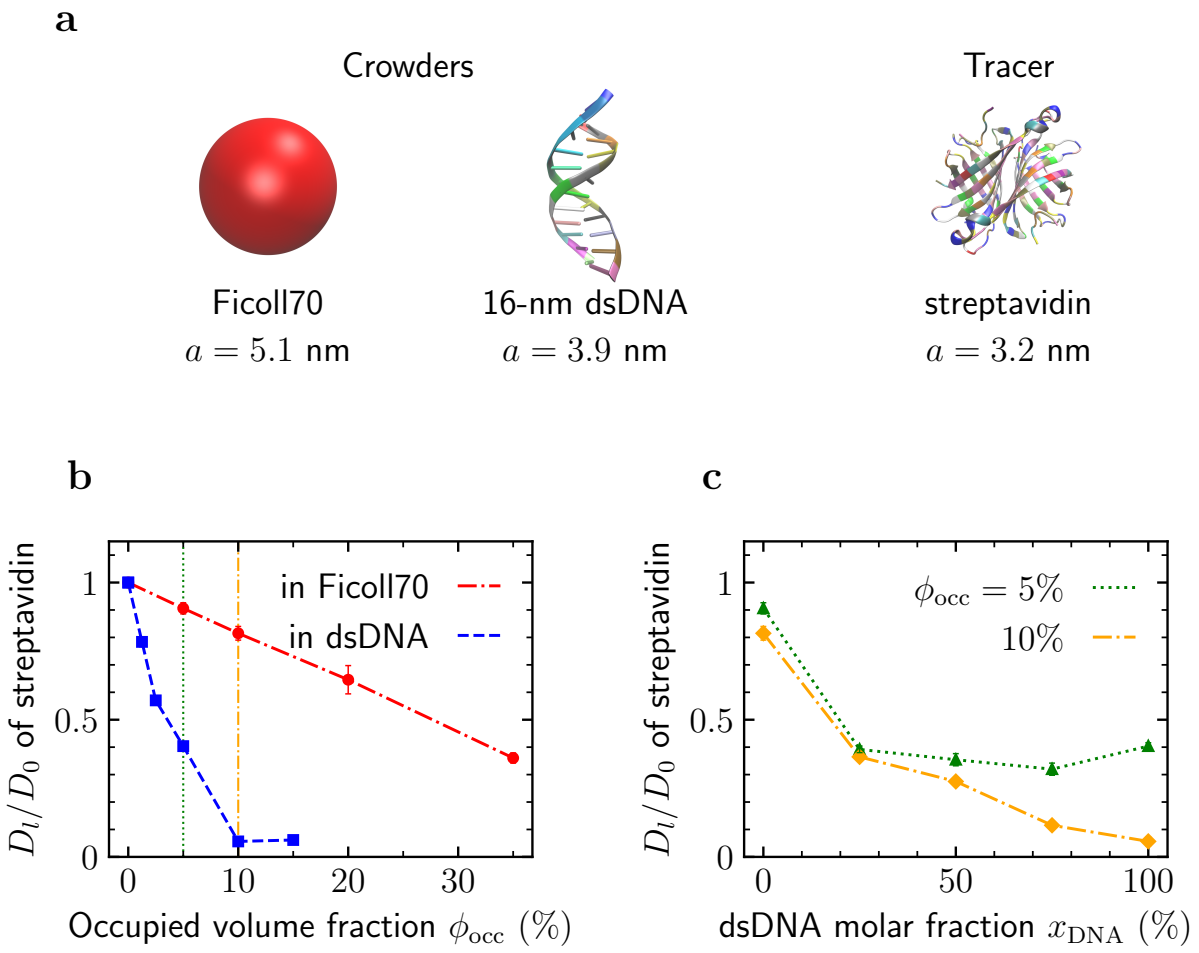

Figure 4.5: **Diffusion of streptavidin in solutions crowded with Ficoll70 and/or dsDNA measured with FCS.** (**a**) We studied diffusion of fluorescently-labeled streptavidin in buffer solutions containing Ficoll70 – chemically inert polymeric crowder and 16-nm-long dsDNA of various occupied volume fractions ϕ_{occ} and dsDNA molar fractions x_{dsDNA}. (**b**) Diffusion coefficient of streptavidin in one-crowder systems – either Ficoll70 (red) or dsDNA (blue). Vertical lines denote the ϕ_{occ} values for which mixtures of various x_{dsDNA} are plotted in panel c. (**c**) Diffusion coefficient of streptavidin in two-crowder systems of various x_{dsDNA} and $\phi_{\mathrm{occ}} = 5$ (green), 10% (orange). Lines on the plot do not represent experimental data but serve only as a guide to the eye. Figure adapted from ref. [127].

streptavidin relative to its value in dilution decreased with ϕ_{occ} in both cases (Fig. 4.5b). However, the slope of the decrease differs considerably between the two cases. Namely, the solutions of the elongated dsDNA crowders hinder the diffusion of streptavidin much more than the solutions of the spherical Ficoll70 crowders. The linear fit to the results for Ficoll70 crowders yields $1 - 1.81\phi_{\mathrm{occ}}$. The slope is $\approx 14\%$ smaller than what we obtained in our SD simulations (Fig. 4.4). Note, however, that the streptavidin tracer is smaller than Ficoll70, so the slope might be smaller than for Ficoll70-only system (Section 4.1.3).

The results obtained for mixtures reflect the trend observed in the one-component systems (Fig. 4.5c). Increasing x_{dsDNA} while keeping ϕ_{occ} fixed leads to a substantial decrease in the

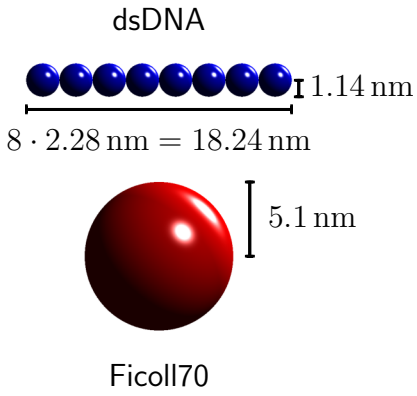

Figure 4.6: **Models representing Ficoll70 and dsDNA used in BD simulations.** Ficoll70 macromolecule is modeled using a sphere with hydrodynamic radius $a = 5.1\,\mathrm{nm}$. 16-nanometer-long dsDNA macromolecule is modeled using an 8-bead-long chain, with all beads of the same radius $1.14\,\mathrm{nm}$.

streptavidin diffusion coefficient. Interestingly, the majority of the drop is observed already at the lowest studied x_{dsDNA} (25%). It seems that even small concentration of dsDNA affects the mobility of streptavidin substantially, while further addition of dsDNA changes the diffusion coefficient only slightly.

4.3.2 Ficoll70 and dsDNA models

To understand the origin of the observed effect, we performed BD simulations of systems similar to the experimental ones. However, for computational reasons, we have chosen not to include streptavidin and focus on binary systems. In the experiments, the concentration of streptavidin was a few orders of magnitude smaller than the concentration of Ficoll70 and dsDNA, as it is needed for a good accuracy of FCS measurements. It means that we would have to perform a huge number of simulations, in which we would place a single streptavidin tracer in a crowded system, in order to gather satisfying statistics. We estimated that given the computational resources attained for this project (Intel Xeon E5-2680 v3, 48 CPU/job, 480 CPU in total), it would take approximately two years to obtain satisfactory results, which we found prohibitive. The dsDNA and Ficoll70 models used in BD simulations are presented in Fig. 4.6.

4.3.2.1 Ficoll70 model

We modeled Ficoll70 macromolecule as an electrically neutral sphere with a hydrodynamic radius of $5.1\,\mathrm{nm}$ [126]. Ficoll70 interacted with other particles only through short-range repulsive, integrated Weeks-Chandler-Andersen (WCA) interaction [178] (Eq. A.7). The diffusion coefficient of Ficoll70 in dilution at $T = 293.15\,\mathrm{K}$ computed from the SSE relation is $41.89\,\mathrm{nm}^2\,\mu\mathrm{s}^{-1}$, which means that the model macromolecule, on average, needs approximately $0.1\,\mu\mathrm{s}$ to traverse a distance equal to its radius.

4.3.2.2 dsDNA model

We modeled the 16-nm-long dsDNA fragment used in the experiments with eight linearly connected beads of radius $1.14\,\mathrm{nm}$ each. Thus, the dsDNA was slightly longer but the volume occupied by eight beads was equal to the volume occupied by a cylinder with a diameter of $2\,\mathrm{nm}$ and length of $16\,\mathrm{nm}$, as previously assumed by experimentalists [126]. Here, every bead represented six base pairs. We set the force constant for bonds (Eq. A.12) to $k_r = 9.866\,\mathrm{kcal\,mol^{-1}\,nm^{-2}}$, which gives $\approx 10\%$ of thermal fluctuations in the bond length, according to a simple estimate $k_\mathrm{B}T/k_r$. Force constant for angles (Eq. A.13) was $k_\alpha = 12.086\,\mathrm{kcal\,mol^{-1}\,rad^{-2}}$, which gives $\approx 12.6°$ of thermal fluctuations in the bond angle ($k_\mathrm{B}T/k_\alpha$). As with Ficoll70, a dsDNA interacted with other particles through the integrated repulsive WCA potential (Eq. A.7); in addition every bead had an electric charge of $-2.4e$ and interacted through the screened electrostatic potential due to Derjaguin-Landau-Verwey-Overbeek (DLVO) theory (Eq. A.11). In reality, every base pair has a charge of $-2e$ and amounts to approximately $0.33\,\mathrm{nm}$ of length, so the charge should be even higher ($-12e$ per bead). However, we followed ref. [36] and renormalizad the charges by a factor of 0.2, as suggested by Levin [179].

The hydrodynamic radius (Fig. 4.7a) and diffusion coefficient of the dsDNA model were calculated from 500 independent BD simulations of single dsDNA particle in a box. We fitted the TAMSD (Eq. A.14) of its center of geometry with a linear function $6D_0t$. It is worth noting that on short timescales, the outmost beads diffuse the fastest due to the coupling of geometric center translation and end-to-end vector rotation (Fig. 4.7b) [180].

We divided the trajectories into five subsets and estimated the uncertainty of the obtained result by computing standard deviation of the mean (Fig. 4.7c). We obtained the diffusion coefficient (at $T = 293.15\,\mathrm{K}$) $D = 57.8 \pm 1.4\,\mathrm{nm^2\,\mu s^{-1}}$, which, using the SSE relation, translates to a hydrodynamic radius $a = 3.70 \pm 0.09\,\mathrm{nm}$. This value is in a reasonable agreement with the experimental result ($a = 3.90 \pm 0.14\,\mathrm{nm}$) obtained with FCS, and with the value obtained using `PyGRPY` software for computing diffusion coefficients of rigid bead structures ($3.5\,\mathrm{nm}$) [181, 182] (Appendix D.5). The difference between BD and `PyGRPY` results is probably due to the fact that the rigid linear geometry does not represent the hydrodynamic properties of a dynamic structure, which can bend and elongate.

We used the same simulations to compute the rotational diffusion coefficient D_r by fitting an exponentially decaying function of time to OA of the end-to-end vector (Eqs. A.18 and A.19 and Fig. 4.7d). We obtained $D_r = 1.225 \pm 0.006\,\mathrm{rad^2\,\mu s^{-1}}$.

To quantify the relation between rotational and translational movement, we introduce a parameter:

$$k = \sqrt{\frac{2D_r}{3D_t}}. \tag{4.14}$$

It describes how much the chain rotates after traversing a particular distance. In the case of our dsDNA model, $k \approx 6.8\,^\circ\,\mathrm{nm^{-1}}$, which means that a dsDNA rotates, on average, by $25°$ moving

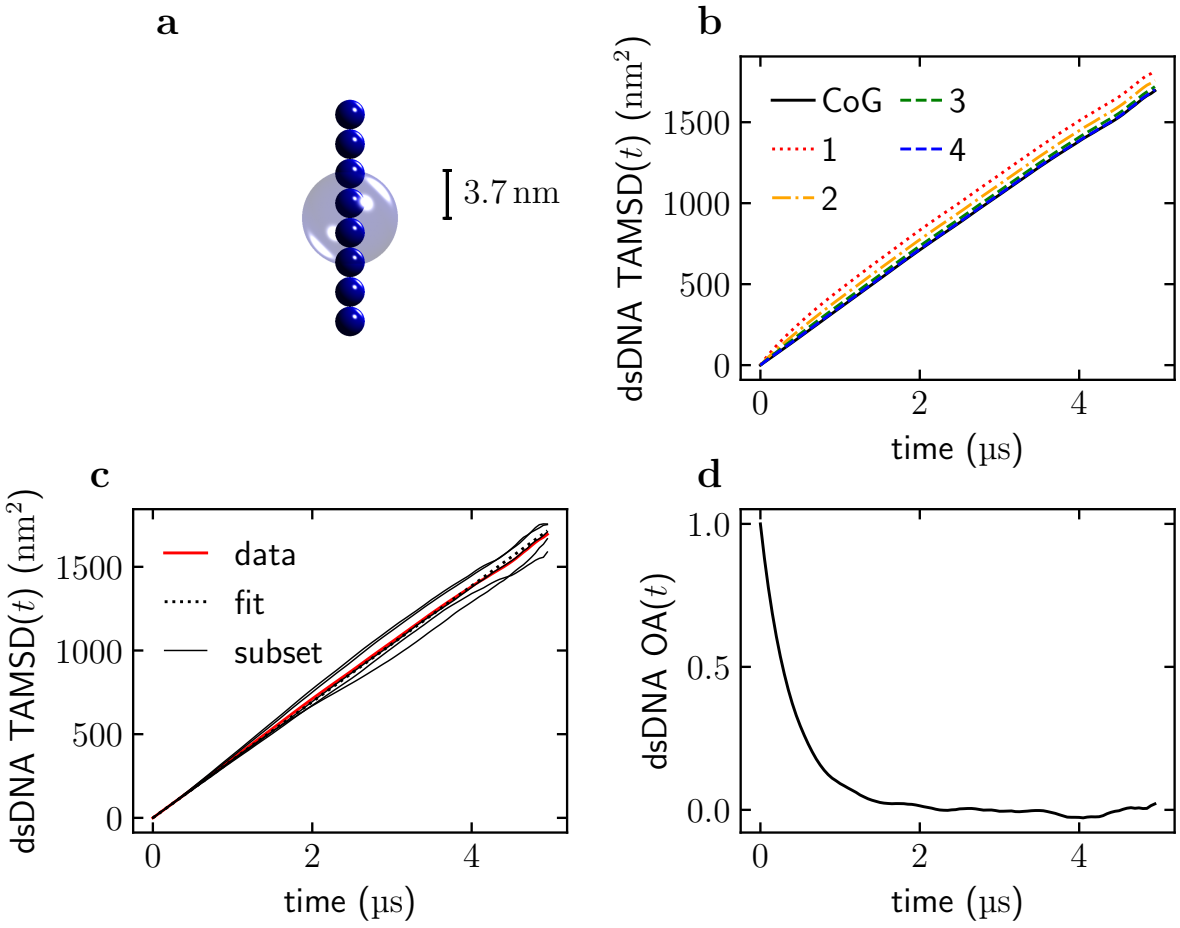

Figure 4.7: **Properties of dsDNA model used in BD simulations.** (**a**) Model of dsDNA used in BD simulations compared to the sphere of the same hydrodynamic radius $a = 3.7\,\mathrm{nm}$. (**b**) TAMSD of separate dsDNA beads and of its center of geometry (CoG). (**c**) TAMSD of the total sample (500 trajectories) and of 5 subsamples of 100 trajectories each, visualizing the uncertainty of the dsDNA diffusion coefficient. (**d**) Orientation autocorrelation (OA) of the end-to-end vector of the dsDNA model.

a distance equal to its hydrodynamic radius and by $124.5°$ moving a distance equal to its length.

Since the SD was not available to us at the time of the project, we performed BD simulations in the far-field (RPY) approximation. In Section 4.2, we show that far-field hydrodynamic interactions underestimate the slowdown of the diffusion upon crowding. A natural question is if one needs to include the far-field hydrodynamic interactions in our simulations. However, without far-field hydrodynamic interactions, the description of translational (Fig. 4.8a) and rotational (Fig. 4.8b) diffusion of bead chains is unreliable. Hydrodynamic radius of dsDNA without accounting for hydrodynamic interactions amounts to $9.1\,\mathrm{nm}$, which is approximately 2.5 times larger than the value obtained with far-field hydrodynamic interactions (≈ 2.3 times larger than the value obtained experimentally). Frembgen-Kesner & Elcock [183] previously reported a similar effect in BD simulations of 11 different proteins. The rotational diffusion coefficient without hydrodynamic interactions is underestimated as well (0.871 *vs.* $1.225\,\mathrm{rad^2\,\mu s^{-1}}$).

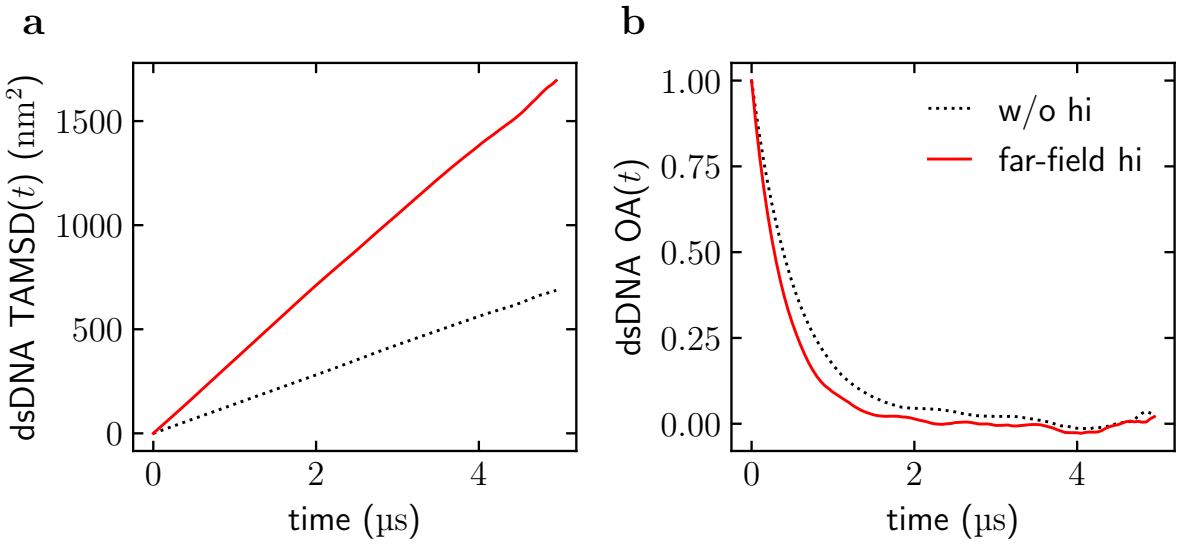

Figure 4.8: **Dependence of dsDNA model on hydrodynamic interactions in BD simulations.** Comparison of (**a**) TAMSD and (**b**) OA obtained with (red) and without (black) far-field hydrodynamic interactions.

4.3.3 Simulation details

We performed BD simulations with a customized version of the `BD_BOX` software (Appendix D.1). The model macromolecules were placed in cubic boxes of $75\,\mathrm{nm} \times 75\,\mathrm{nm} \times 75\,\mathrm{nm}$, and we applied periodic boundary conditions in all three directions. The time step Δt was $0.5\,\mathrm{ps}$, and simulations lasted for $20\,\mu\mathrm{s}$ (5 for $x_{\mathrm{dsDNA}} = 75\%$). We accounted for far-field hydrodynamic interactions with the Ewald-summated generalized RPY approximation and, following Ando & Skolnick [36], performed Choleski decomposition every 100 steps to speed up simulations. We performed Ewald-summation of the diffusion matrix with $\alpha = \sqrt{\pi}$, $m_{\mathrm{cutoff}} = n_{\mathrm{cutoff}} = 2$ (Appendix B). We used the Iniesta-Garcia de la Torre propagation scheme [184] (Eq. A.4). Simulations were performed at room temparature $T = 293.15\,\mathrm{K}$, using the Debye screening length $\kappa^{-1} = 2.3\,\mathrm{nm}$, dynamic viscosity $\eta = 1.005\,\mathrm{cP}$, and relative dielectric constant $\epsilon = 80.36$ (corresponding to the viscosity and dielectric constant of water at room temperature). Parameters for repulsive and attractive interactions (Eqs. A.7 and A.8) were: $\varepsilon_{\mathrm{LJ}} = 0.37\,\mathrm{kcal\,mol^{-1}}$, $\sigma = 0.15\,\mathrm{nm}$. To avoid large forces causing numerical problems, for separations between the macromolecules' surfaces below $r_{\mathrm{min}} = 0.1\,\mathrm{nm}$, we kept the magnitude of force fixed and equal to $\boldsymbol{F}(r_{\mathrm{min}})$. We also set the upper cutoff for the repulsive interactions to $15\,\mathrm{nm}$ and for the DLVO electrostatic interactions to $25\,\mathrm{nm}$. We accounted for macromolecules' roughness with the corresponding parameters (Eq. A.10) h equal to 0.8, 0.34, and 0.6, for Ficoll70, dsDNA and dsDNA-S, respectively. Since we did not have the data for the radii of gyration, we have chosen h in such a way that h/a is the same as for macromolecules with the similar size taken from ref. [36] (Ribonuclease for dsDNA, Phosphoglycerate dehydrogenase for Ficoll70 and dsDNA-S).

Table 4.2: **Compositions, occupied volume fractions ϕ_{occ} and molar fractions x of simulated Ficoll70-dsDNA(-S) mixtures.** N_{F}, N_{dsDNA}, and $N_{\mathrm{dsDNA-S}}$ are the numbers of Ficoll70, dsDNA, and dsDNA-S, respectively, in the simulation system.

N_{dsDNA}	N_{F}	ϕ_{occ} (%)	x_{dsDNA} (%)
0	42	5.1	0.0
14	41	5.0	25.4
39	39	5.0	50.0
104	35	5.0	74.8
$N_{\mathrm{dsDNA-S}}$	N_{F}	ϕ_{occ} (%)	$x_{\mathrm{dsDNA-S}}$ (%)
59	20	5.03	74.68

We obtained diffusion coefficients from TAMSD with a window length equal to $50\,\mathrm{ns}$. The long-time diffusion coefficients were obtained by evaluating $D(t)$ at $t = 5\,\mu\mathrm{s}$. Uncertainty of the D_l due to sampling error was estimated by dividing the simulations into 5 subsets and computing standard deviation of the mean, while treating the subsets as independent "measurements".

We used Ficoll70-dsDNA mixtures with volume fractions of 5% and molar fractions of 0, 25, 50, and 75% (Fig. 4.9a and Table 4.2). Since every dsDNA consists of eight beads, going to a higher dsDNA molar fraction on that level of description is not feasible. Note that due to the radius shift in the repulsive WCA potential (Eq. A.9), we computed occupied volumes assuming that the bead hard-core radii are smaller by σ than the hydrodynamic radii.

4.3.4 Diffusion in Ficoll-dsDNA mixtures

Motivated by the experimental results (Fig. 4.5), we considered Ficoll70-dsDNA mixtures of various composition. BD simulations show that the decrease in the diffusion coefficient is more substantial in systems with a higher molar fraction of dsDNA particles (Fig. 4.9b). This behavior is in qualitative agreement with the experimental results and previous on-lattice simulations [141, 185]. The drop in diffusivity in the system with $x_{\mathrm{dsDNA}} = 75\%$ is over three times larger than in the Ficoll70-only system with the same ϕ_{occ}. However, quantitatively the BD results still differ from the FCS results. Judging by the orders of magnitude of hydrodynamic effects (Section 4.2), the discrepancy is unlikely to arise from the absence of the near-field hydrodynamic interactions. Moreover, the curvature of $D_l(\phi_{\mathrm{occ}})$ predicted by BD is different from the observed experimentally. In FCS, the decrease in the diffusion coefficient with x_{dsDNA} is initially strong, and then the slope becomes less steep. In BD, it is the other way round (compare Fig. 4.5c *vs.* Fig. 4.9b). Despite these differences, our results prove the existence of the shape effects by virtue of which dsDNA crowders hinder the diffusion more effectively than Ficoll70.

To better understand that shape effect, we calculated volumes excluded to Ficoll70 in the systems under study (Fig. 4.9c). We estimated the total excluded volumes by summing the volumes excluded by crowder to tracer (Eq. 2.21) over all crowders, assuming their additivity. We also computed it more accurately with MC method (Section 3.3); the values are gathered in

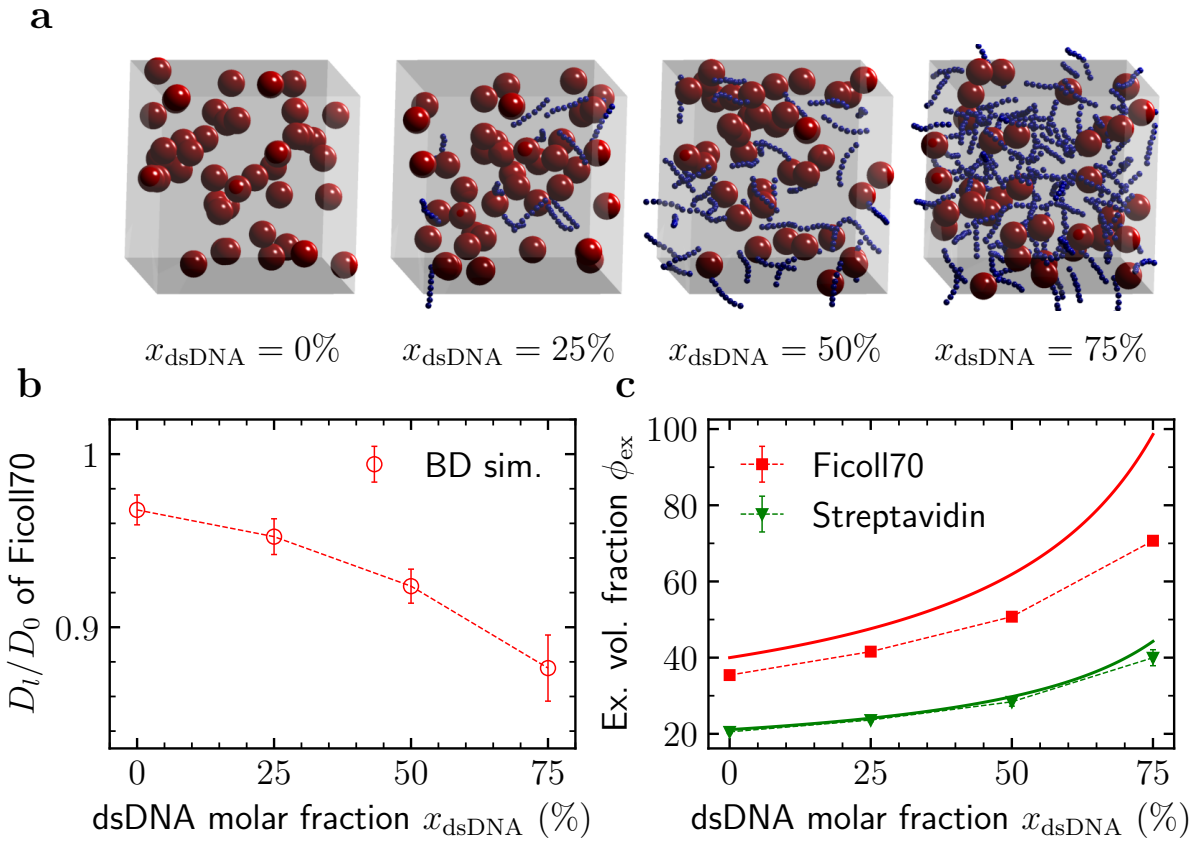

Figure 4.9: **Diffusion of Ficoll70 in Ficoll70-dsDNA mixtures from BD simulations.** (**a**) Simulated systems of $\phi_{\mathrm{occ}} \approx 5\%$ and $x_{\mathrm{dsDNA}} = 0$, 25, 50, and 75%. (**b**) Diffusion coefficient of Ficoll70 in mixtures of Ficoll70 and dsDNA as a function of x_{dsDNA} from BD simulations with far-field hydrodynamic interactions. (**c**) Volumes excluded to Ficoll70 (red) and Streptavidin (green) as a function of molar fraction of x_{dsDNA}. The solid line is a rough estimate assuming that the total excluded volume fraction is a sum of individual crowder contributions (Eq. 2.21). The values denoted by markers were computed using Monte Carlo (MC) method (Section 3.3) and account for the mutual overlaps between the individual excluded volumes. Dashed lines on the plot do not represent data but serve as a guide to the eye. Figure adapted from ref. [127].

Table 4.3: **Volume fraction ϕ_{ex} excluded to Ficoll70 tracer in mixtures of Ficoll70 and dsDNA/dsDNA-S.** x_{dsDNA} and $x_{\mathrm{dsDNA-S}}$ are molar fractions ot dsDNA and dsDNA-S, respectively. Uncertainties were computed as standard deviations of a mean.

x_{dsDNA} (%)	ϕ_{ex} (%)
0	35.4 ± 0.7
25	41.6 ± 0.5
50	50.8 ± 0.9
75	70.7 ± 0.8
$x_{\mathrm{dsDNA-S}}$ (%)	ϕ_{ex} (%)
75	45.2 ± 0.6

Table 4.3. Here, unlike in other sections, we withdrawn one tracer particle from the simulation box before each insertion, so that after the insertion the system had the same composition as in

Table 4.4: **Volume fraction excluded to dsDNA/dsDNA-S tracer in a mixture of Ficoll70 and dsDNA/dsDNA-S of $x_{\mathrm{dsDNA}} = 75\%$.** x_{dsDNA} and $x_{\mathrm{dsDNA-S}}$ are molar fractions ot dsDNA and dsDNA-S, respectively. Uncertainties were computed as standard deviations of a mean.

	ϕ_{ex} (%)
$x_{\mathrm{dsDNA}} = 75\,\%$	42.4 ± 0.5
$x_{\mathrm{dsDNA-S}} = 75\,\%$	32.1 ± 0.3

the simulations. Although this slightly shifts down the obtained values, it does not affect the results qualitatively, so for simplicity we resigned from that procedure in other sections. We found that for both streptavidin and Ficoll70, the excluded volume fraction increases upon an increase of the dsDNA molar fraction while keeping the ϕ_{occ} fixed. This increase is because the long dsDNA chains exclude more volume relative to what they occupy compared with the Ficoll70 crowders.

4.3.5 Spherical *vs.* elongated crowders

One may argue that a dsDNA differs from Ficoll70 not only in shape but also in size (hydrodynamic radius of 3.7 *vs.* 5.1 nm), which can also affect particle's diffusion [186]. To single out the shape effects, we performed additional simulations with dsDNA particles exchanged for spheres with radius equal to the dsDNA hydrodynamic radius, which we refer to as dsDNA-S, S stands for sphere (Fig. 4.10a,b). We assumed the total electric charge the same as dsDNA, but we also performed the same simulations without electrostatic interactions and excluded their influence on the discussed effect. Note that since the volume of dsDNA is smaller than dsDNA-S, keeping ϕ_{occ} and x_{dsDNA} fixed does not imply a one-to-one exchange of dsDNA for dsDNA-S (Table 4.2).

The diffusion coefficient of Ficoll70 in the system with dsDNA was decreased three times more strongly than in the system with dsDNA-S (12 *vs.* 4%, see Fig. 4.10c), both with and without electrostatics. We also computed the volumes excluded to Ficoll70 in the studied systems (Table 4.3). As expected, the fraction of volume excluded to Ficoll70 is substantially smaller in systems with spherical dsDNA-S (45.2 *vs.* 70.7%). However, in Fig. 4.10d, we see that the difference in the diffusion coefficients is much smaller when we treat dsDNA/dsDNA-S as tracers. Without electrostatic interactions, both curves slightly shift up, but the difference between them is even smaller. The diffusion coefficients of dsDNA and dsDNA-S in the corresponding systems are similar, although the difference in the excluded volumes is relatively high (Table 4.4), similar to the one obtained for Ficoll70. It seems that excluded volume-based argument works when we compare systems with the same tracer and different crowding media, but not in the case of two different tracers.

Thus, we showed, using experiments (FCS) and simulations (BD), that specifying the occupied volume fraction of binary mixtures of dsDNA (elongated) and Ficoll70 (spherical) crowders does not suffice to predict the diffusion coefficient of tracers therein. Elongated crowders

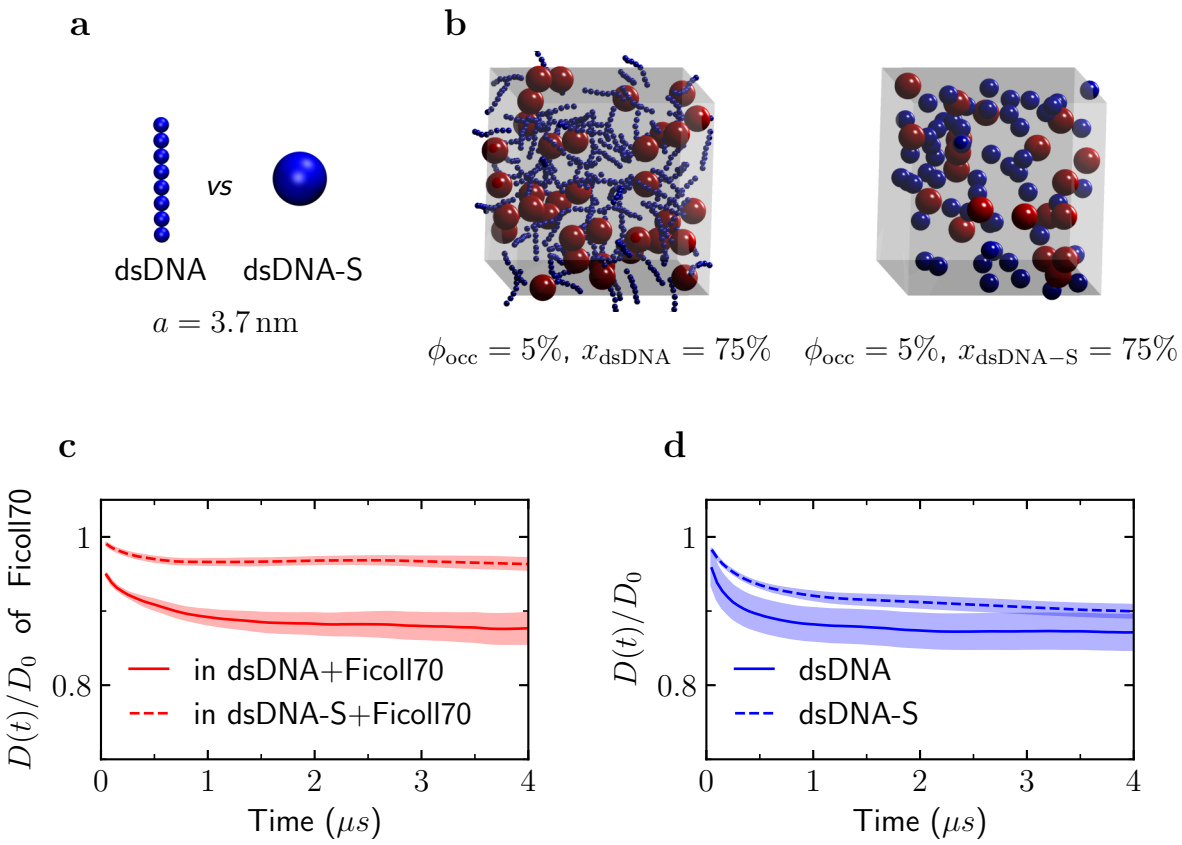

Figure 4.10: **Spherical** *vs.* **elongated crowders: results of BD simulations.** (**a**) Comparison of dsDNA polymer chain model and a sphere of equal hydrodynamic radius, which we refer to as dsDNA-S. (**b**) Simulation snapshots of Ficoll70-dsDNA and Ficoll70-dsDNA-S mixtures. Note that we keep the molar fraction of dsDNA x_{dsDNA} and occupied volume fraction ϕ_{occ} constant, so the number of dsDNA is not equal to the number of dsDNA-S. (**c**) Time-dependent diffusion coefficient of Ficoll70 in a mixture with dsDNA-S (dashed) and dsDNA (solid). (**d**) Time-dependent diffusion coefficient of dsDNA/dsDNA-S in a mixture of Ficoll70 with dsDNA-S (dashed) and dsDNA (solid). The shadowed areas denote the uncertainties due to the sampling error. Figure reprinted from ref. [127].

hinder the diffusion more efficiently than spherical ones.

A similar effect was reported previously by Ellery *et al.* [141] (Section 4.1.3.1) and Balbo *et al.* [185]. Using BD and FCS, Balbo *et al.* [185] observed that in mixtures of heart-shaped BSA and Y-shaped IgG, the latter lead to a higher slowdown of tracer diffusion and that the crowder shape has a more substantial influence on diffusion coefficient than the tracer shape. However, the authors used rigid protein models and accounted for hydrodynamic interactions using the mean-field approach based on rescaling short-time diffusion coefficients [148] (Eq. 4.7a), which, on the one hand, accounts better for the diffusion slowdown by directly rescaling diagonal elements of the diffusion matrix, but, on the other hand, does not introduce offdiagonal elements, which are responsible for correlations between the motions. Furthermore, in our study, the difference in shape is more prominent, and we pinpoint the very shape effect by exchanging nonspherical models for their spherical "equivalents" (*i.e.*, the spherical particles with

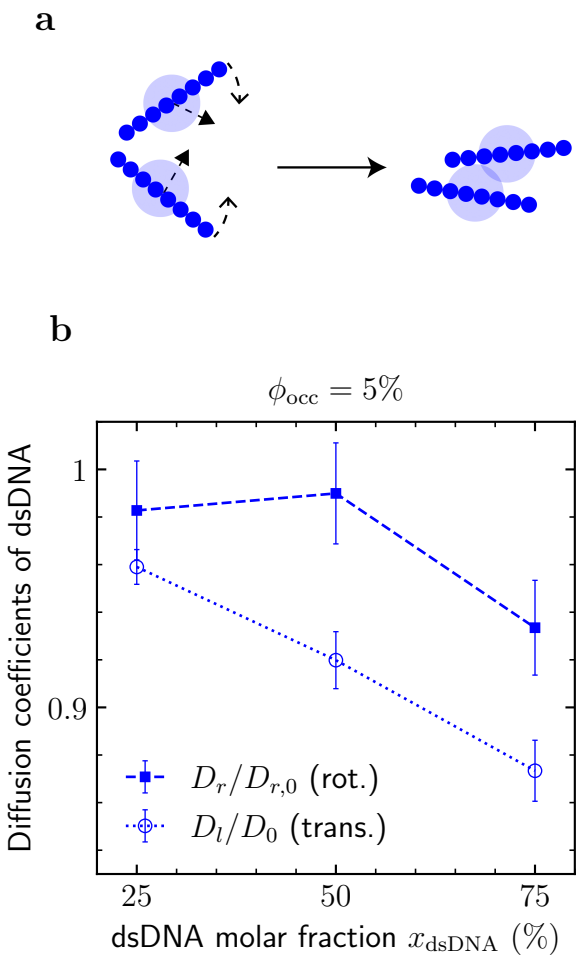

Figure 4.11: **Translational and rotational diffusion of dsDNA in Ficoll70-dsDNA mixtures: results of BD simulations.** (**a**) Schematics presenting the motion of dsDNA as a combination of Brownian motion of its center of geometry and rotational Brownian motion of its end-to-end vector. The shaded area denotes the hydrodynamically equivalent sphere. (**b**) Long-time rotational and translational diffusion coefficients of dsDNA in mixtures with Ficoll70 obtained from BD simulations with far-field hydrodynamic interactions. Lines on the plot do not represent data but serve only as a guide to the eye. Figure adapted from ref. [127].

the same hydrodynamic radius).

4.3.6 dsDNA rotational diffusion

Apart from translational diffusion of Ficoll70, we also analyzed translational and rotational diffusion of dsDNA in the same systems (Fig. 4.11a). We computed rotational diffusion using two approaches: fitting an exponential function to OA and fitting a linear function to a short-time mean squared angular displacement (MSAD). The results presented in Fig. 4.11b were obtained using the OA approach. The conclusion is that the translational diffusion is more sensitive to macromolecular crowding than the rotational diffusion. This result is in line with previous works [37, 105, 185], although the opposite was also reported [160]. Mean rotation per

traversed distance (Eq. 4.14) decreases with crowding. Additionally, the shape effect reported for translational diffusion is present in rotational motion as well.

4.4 Effect of attractive interactions

Although we observe the shape effects in our BD simulations with short-range repulsion (Fig. 4.9), in qualitative agreement with FCS results (Fig. 4.5), the BD and FCS do not agree quantitatively. The question remains what may be the reason for such a behavior. The most enigmatic feature of the observed drop of streptavidin diffusion in dsDNA-Ficoll70 mixtures is that the majority of the drop happens at the minimal dsDNA molar fraction x_{dsDNA} used in the study (Fig. 4.5c). It seems that a relatively small concentration of dsDNA changes something important in the system, and then the further slowdown upon increasing x_{dsDNA} is much slower. We hypothesized that it might be due to an attractive interaction between dsDNA and streptavidin. In experiments, streptavidin is added to the sample at nanomolar concentration, much lower than dsDNA and Ficoll70. If there is some preferential attraction between a dsDNA and streptavidin, even at small x_{dsDNA} we may observe the majority of streptavidin tracers forming transient complexes with dsDNA. The complexes would be less mobile than isolated streptavidin, which can lead to a further decrease in the diffusion coefficient.

To quantify this possibility, we performed additional BD simulations with attractive Lennard-Jones (LJ) interactions (Eq. A.8). Following Ando & Skolnick [36], we used the LJ energy $\varepsilon_{\mathrm{LJ}} = 0.37\,\mathrm{kcal\,mol^{-1}}$, as it allowed for reproducing the GFP translational diffusion coefficient in the model *E. coli* cytoplasm. We focused on the system with $x_{\mathrm{dsDNA}} = 25\%$ and considered two possibilities: attractive interactions between Ficoll70 and ds-DNA only and attractive interactions between all particles (Fig. 4.12a). The differences are noticeable in Ficoll70-dsDNA RDF (Fig. 4.12b). Without attractions, there are no signs of Ficoll70-dsDNA aggregation. With attractions between dsDNA and Ficoll70 only, we see a single maximum — a signature of the formation of dsDNA-Ficoll70 complexes. When Ficoll70-Ficoll70 and dsDNA-dsDNA attractions are turned on as well, we see an aggregation of bigger Ficoll70-dsDNA complexes resembling a solid-like structure with consecutive maxima in the dsDNA-Ficoll70 RDF plot (see also the snapshots in Fig. 4.12a). The diffusion coefficient of Ficoll70 predictably decreases when attractions are at play (Fig. 4.12c). We note that the $D(t)$ for attractions between all particles is not based on TAMSD, but on MSD, as the system is out of equilibrium and moves to the aggregated state (nonergodicity). However, the case with Ficoll70-dsDNA attractions only does not show significant differences between MSD and TAMSD.

These BD results do not directly correspond to the experimental results because, in FCS, streptavidin is present at a much lower concentration than dsDNA, whereas in BD simulations there is more Ficoll70 than dsDNA. To relate the FCS and BD results, we proceed as follows. In BD simulations in which Ficoll70 and dsDNA attract each other, we observe two different populations of Ficoll70 particles — free and bound to dsDNA. Then, the apparent diffusion

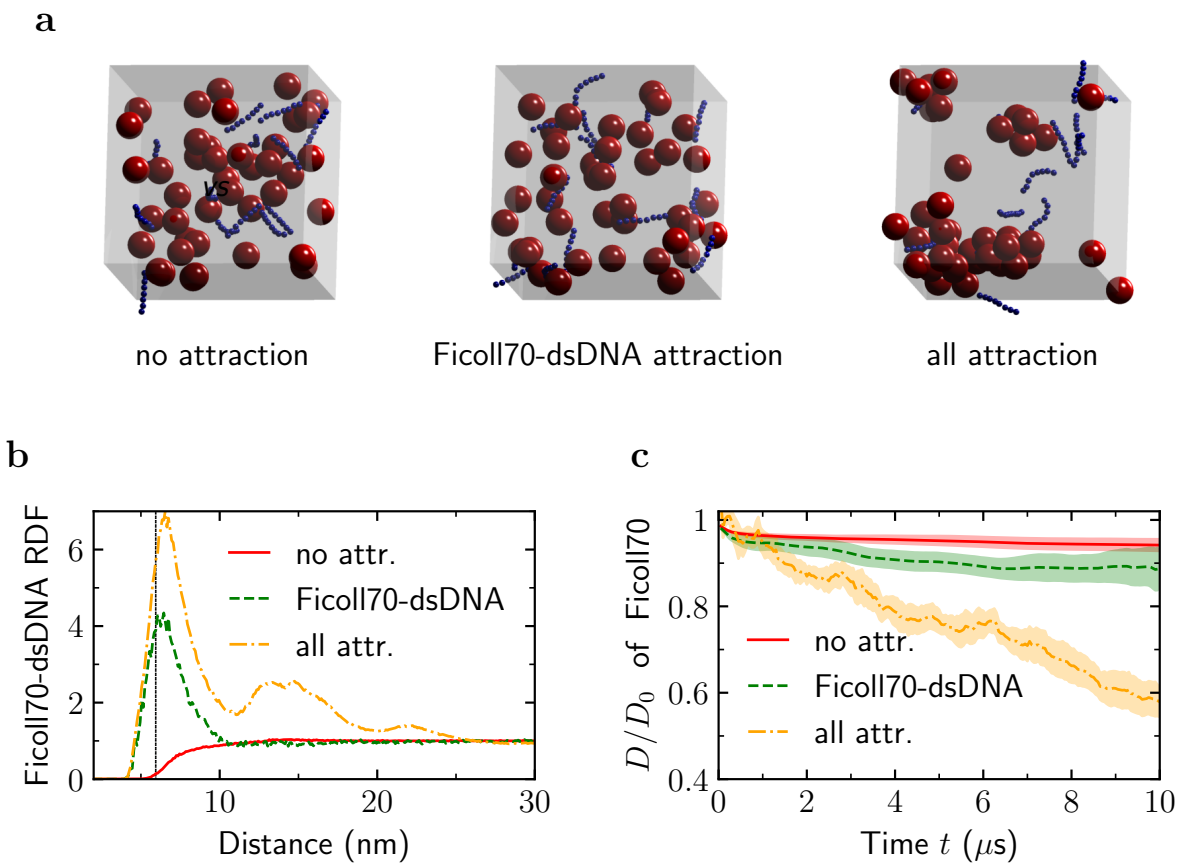

Figure 4.12: **Effect of attractive interactions on macromolecular diffusion.** (**a**) Comparison of BD snapshots of systems with no attractive interactions, attractive interactions only between dsDNA and Ficoll70, and attractive interactions between all macromolecules in systems of $\phi_{\text{occ}} = 5\%$ and $x_{\text{dsDNA}} = 25\%$. (**b**) Radial distribution function (RDF) between Ficoll70 and dsDNA center of geometry in three cases introduced above. The vertical dotted line denotes the sum of Ficoll70 and dsDNA bead radii. (**c**) Time-dependent diffusion coefficient of Ficoll70 in three introduced cases. The curve for attraction among all macromolecules is obtained from ensemble-averaged MSD (without time-averaging) as the system is not in equilibrium and Ficoll70 spheres aggregate. The shadowed areas denote the uncertainties due to the sampling error. Figure adapted from ref. [127].

coefficient is an average of the bound D_{bound} and free D_{free} diffusion coefficients weighted by the fraction of bound Ficoll70, f, *i.e.*:

$$D = fD_{\text{bound}} + (1 - f)D_{\text{free}}. \tag{4.15}$$

Note that this equation neglects the higher order complexes between Ficoll70 and dsDNA. We analyzed the time-dependent distance matrix to estimate the fraction of Ficoll70 macromolecules in close contact with dsDNA beads. We set a distance threshold at the position of the first maximum at the RDF plot (Fig. 4.12b) and obtained $f \approx 0.085$ in the system with attractive interactions between Ficoll70 and dsDNA, and $f \approx 0.003$ in the system without attractions. After plugging it into Eq. 4.15, we obtained $D_{\text{bound}} = 0.35 \pm 0.29$. The resulting

uncertainty is high due to sampling error, but it covers the experimental result, which supports the hypothesis of streptavidin-dsDNA attraction. We note, however, that attractive interactions between streptavidin and dsDNA have not been reported before, thus more work needs to be done to fully rationalize the FCS results.

4.5 Effect of macromolecules' softness

4.5.1 Previous studies

The majority of simulations assume that polymeric crowders closely resemble hard spheres, either explicitly using hard-sphere potential, or using very steep, WCA potential. However, as pointed out by Luby-Phelps *et al.* [102] and Junker *et al.* [126], this assumption is not always justified. Some polymers, like Ficoll, exist in a compact form, which in dilute and semi-dilute regimes is reasonably well approximated with a hard-sphere model. On the opposite side of the spectrum, there are expanded and soft polymers, *e.g.*, Dextran, PEG, and PEO, which behave differently both as tracers [102, 103] and crowders [126, 187].

In 2018, Blanco *et al.* [187] proposed to account for the macromolecules' softness *via* a shoulder-shaped chain entanglement softened potential (CESP) in the following form:

$$U(r) = U_s(r;\ell_c) + \frac{U_0}{2}\left[1 - \tanh\left(\frac{\mathfrak{a}\ell_c}{\ell_e - \ell_c}(r - [\ell_e + \ell_c])\right)\right], \tag{4.16}$$

where U_s is a short-range potential (WCA, hard-sphere, r^{-n}, *etc.*), ℓ_c is a hard-core distance below which U_s steeply increases, ℓ_e is an entanglement distance setting the extension of CESP shoulder, U_0 is the energy cost of chain entanglement, and $\mathfrak{a}$ is a lengthscale-setting parameter (set to $1\,\mathrm{nm}$ by Blanco *et al.* [187]). CESP definition requires every marcomolecule to be defined with two separate sizes: hard-core radius a_c and entanglement radius a_e. Then, parameters ℓ_c and ℓ_e are computed as sums of the corresponding radii a_c and a_e. The authors of ref. [187] fitted U_0 to reproduce the concentration-dependence of streptavidin diffusion coefficient in Dextran50; the BD simulations with the CESP potential (Eq. 4.16) correctly predicted the respective dependence in Dextran10, Dextran400, and Dextran700.

Junker *et al.* [126] investigated with FCS the translational diffusion of various biologically-relevant tracers differing in size and shape, among others: $16\text{-}\mathrm{nm}$-long dsDNA, streptavidin, GFP, and IgG, in artificially crowded media composed of Ficoll (hard) and PEG/PEO (soft) crowders of various molecular masses. The authors reported a stronger diffusion slowdown in PEG/PEO crowders at the same occupied volume fraction ϕ_{occ} [126]. However, the volumes of the crowders used to convert between the concentrations and occupied volume fractions were different from the values resulting from the assumption that they are spheres of volume $4\pi a^3/3$, where a is the hydrodynamic radius. The authors of ref. [126] used specific volumes of Ficoll and PEG/PEO of $0.65\,\mathrm{mL\,g^{-1}}$ and $0.83\,\mathrm{mL\,g^{-1}}$, respectively. Instead, one can compute ϕ_{occ}

Table 4.5: **Specific volumes $1/\rho$ recalculated based on hydrodynamic radii a and molecular masses m, assuming that polymeric crowders are spherical.**

	$1/\rho$ (mL g^{-1}) [126]	a (nm) [126]	m (kDa)	$1/\rho(a,m)$ (mL g^{-1})
Ficoll70	0.65	5.1	70	4.78
Ficoll400	0.65	10	400	6.30
PEG35	0.83	5.7	35	13.34
PEO100	0.83	10.4	100	28.36
PEO200	0.83	15.4	200	46.05
PEO300	0.83	19.4	300	61.37

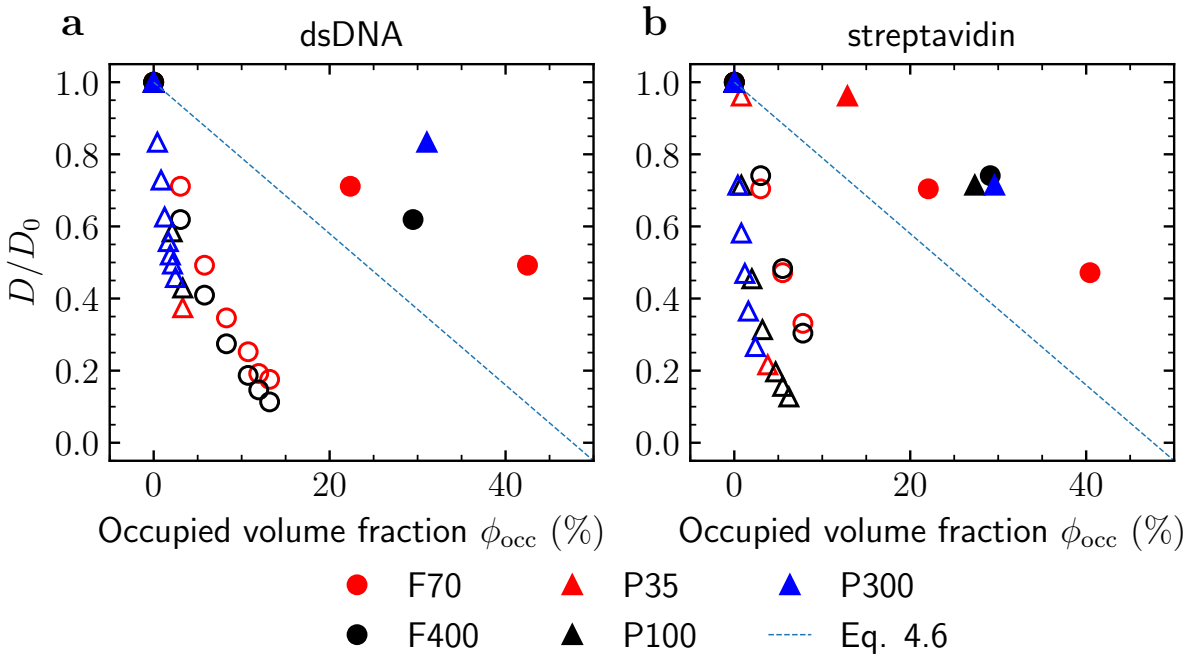

Figure 4.13: **Translational diffusion in crowders of different softness measured with FCS.** Values for two tracers are shown: (**a**) dsDNA and (**b**) streptavidin. The open symbols denote the data originally reported by Junker *et al.* [126]. The filled symbols denote the data recalculated by assuming that the specific volumes of polymeric crowders are equal to specific volumes of spheres having the same molecular mass and radius equal to the polymer's hydrodynamic radius. F in legend stands for Ficoll, P stands for PEG/PEO. Dashed line represents theoretical result for identical spheres by Cichocki & Felderhof [147] (Eq. 4.6).

from the molecular masses and hydrodynamic radii, assuming that all crowders are spherical (Table 4.5). The specific volumes computed this way are between one and two orders of magnitude larger than those used by Junker *et al.* [126]. As shown in Fig. 4.13, after recalculating, the differences between the diffusion coefficient decrease in hard and soft crowders become much smaller and do not lead to any definite conclusion. After the recalculation, the majority of datapoints fall closer to the theoretical predictions of Cichocki & Felderhof [147] for identical spheres (Eq. 4.6). However, both streptavidin and dsDNA are smaller than the crowders, so it agrees that the slope of $D(\phi_{occ})$ is less steep than in Eq. 4.6. Note that the resulting volume

Table 4.6: **CESP parameters for models of hard and soft macromolecules.**

	a_c (nm)	a_e (nm)	βU_0	a (nm)
hard	5.1	5.1	1.2	5.1
soft	3.35	6.85	1.2	5.1
hard	5.1	5.1	0.8	5.1
soft	2.5	7.7	0.8	5.1

fractions become high, suggesting that polymers might entangle and form a polymeric meshwork.

4.5.2 Model

As it emerges from the short survey above, the studies of the effect of crowder softness on tracer diffusion appeared only recently and are rather scarce. The existing studies do not single out the effect of softness systematically, either adding softness on top of hard particles to obtain a better reproduction of experimental data like Blanco *et al.* [187], or using crowders which differ not only in softness but also in size, and in very high concentrations, like Junker *et al.* [126]. The aim of our study was to isolate the effect of crowder softness on diffusion in crowded environments, including answering the question of whether the result is dependent on the size and shape of the tracer.

We approached the problem by comparing the crowding by electrically-neutral macromolecules, which differ in their softness but are otherwise equivalent. To this end, we used the CESP (Eq. 4.16) and set $a_c = a_e = a = 5.1\,\mathrm{nm}$ for hard particles (the same as for Ficoll70 in Sections 4.2 and 4.3) and $(a_c + a_e)/2 = a$ for soft particles. Thus, we introduced the softness by shrinking a_c and expanding a_e by the same amount (Fig. 4.14a). For the particles to be equivalent, we introduced a constraint on the a_c and a_e, such that they lead to the effective volume v_{occ} occupied by soft and hard particles being equal. For a hard particle, v_{occ} is a volume of the sphere with radius a. For a soft particle, we computed v_{occ} with the following integral:

$$v_{\mathrm{occ}} = 4\pi \int_0^\infty r^2 (1 - \exp[-\beta U(r; a_c, a_e, U_0)]) dr. \tag{4.17}$$

We found a_e and a_c for a given entanglement energy U_0 by equating Eq. 4.17 to the hard-sphere volume, using the bisection method with additional condition of $(a_c + a_e)/2 = a$. Results are presented in Fig. 4.14b as a dependence of U_0 on the relative splitting $(a_e - a_c)/a_c$. The extent of the entanglement decreases with the increase of the entanglement energy U_0. This kind of soft-hard correspondence is equivalent to equating the second virial coefficients for hard and soft particles [189]. For BD simulations, we picked two points from Fig. 4.14b (Table 4.6), corresponding to $\beta U_0 = 0.8$ and 1.2 ($\beta = 1/k_{\mathrm{B}}T$). Note that the entanglement energy U_0 corresponds to the height of the respective potential shoulder (Fig. 4.14c).

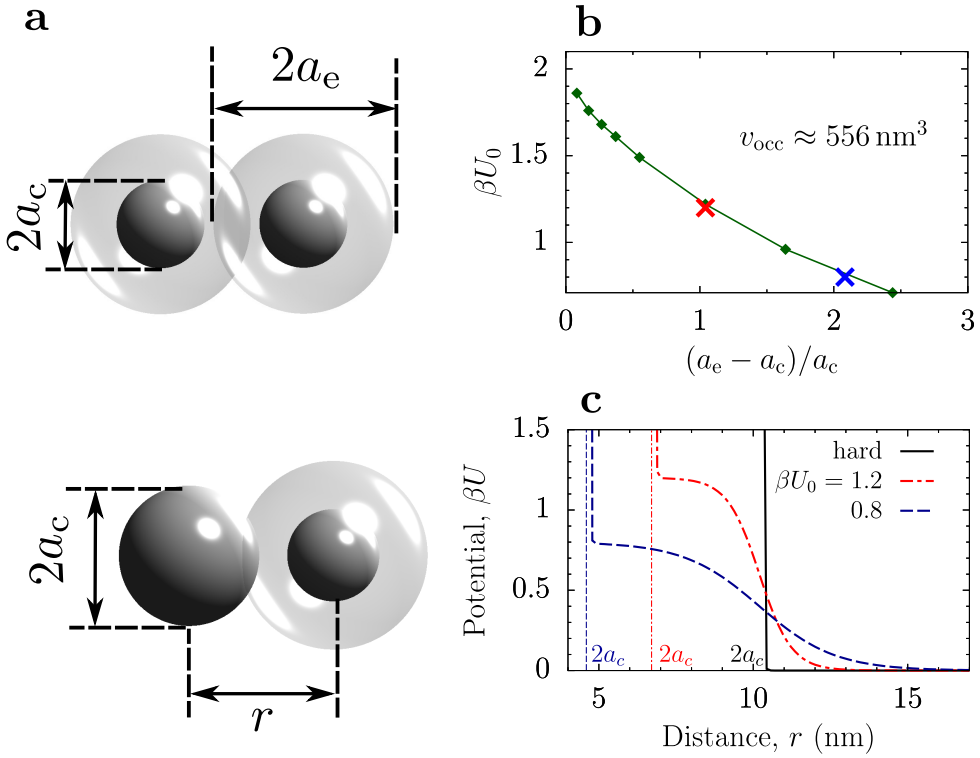

Figure 4.14: **Models of hard and soft particles.** (**a**) Juxtaposed models of two soft particles (above) and one soft and one hard particle (below). The opaque, dark-grey sphere denotes the volume restricted by a hard-core radius (impenetrable) a_c, whereas the partially transparent, light-grey pictures the extension of the CESP shoulder – entanglement radius a_e (Eq. 4.16). (**b**) Relation between the extension of soft interactions $(a_e - a_c)/a_c$ and the entanglement energy U_0, assuming constant effective occupied volume $555.6\,\mathrm{nm}^3$ equal to the occupied volume of the hard particle. The crossmarks denote the values of parameters used in simulations (Figs. 4.15, 4.17, and 4.18). (**c**) CESP between two soft particles parametrized by the values indicated by crossmarks in panel b (the same color code). For comparison, the hard-sphere potential is also plotted. The vertical dotted lines mark the hard-core diameter $2a_c$. Figure reprinted from ref. [188].

4.5.3 Simulation details

We performed BD simulations with a customized version of the `BD_BOX` software (Appendix D.1). We placed the model macromolecules in cubic boxes of $85\,\mathrm{nm} \times 85\,\mathrm{nm} \times 85\,\mathrm{nm}$, and applied periodic boundary conditions in all three directions. The time step Δt was $0.5\,\mathrm{ps}$, and simulations lasted for at least $10\,\mu\mathrm{s}$. We accounted for far-field hydrodynamic interactions with the Ewald-summated generalized RPY approximation and, following Ando & Skolnick [36], performed Choleski decomposition every 100 steps to speed up simulations. We performed Ewald-summation of the diffusion matrix with $\alpha = \sqrt{\pi}$, $m_{\mathrm{cutoff}} = n_{\mathrm{cutoff}} = 2$ (Appendix B). We propagated the BD with the Iniesta-Garcia de la Torre propagation scheme [184] (Eq. A.4). The temparature T was $298.15\,\mathrm{K}$, the Debye screening length $\kappa^{-1} = 0.96\,\mathrm{nm}$, dynamic viscosity $\eta = 1.02\,\mathrm{cP}$, and relative dielectric constant $\epsilon = 78.54$. Parameters for repulsive potential (Eq. A.7) were: $\varepsilon_{\mathrm{LJ}} = 0.37\,\mathrm{kcal\,mol}^{-1}$, $\sigma = 0.15\,\mathrm{nm}$. To avoid large forces causing numerical

Table 4.7: **Compositions, occupied volume fractions ϕ_{occ} and molar fractions x_{dsDNA} of simulated mixtures of hard and soft macromolecules.**

ϕ_{occ} (%)	x_{H} (%)	x_{S} (%)	N_{H}	N_{S}
10	100	0	111	0
10	72	28	81	30
10	28	72	31	80
10	0	100	0	111
30	100	0	333	0
30	0	100	0	333

Table 4.8: **Volumes excluded by a single hard/soft particle to another hard/soft particle.**

	$V_{\mathrm{ex}}(H-H)$	$V_{\mathrm{ex}}(H-S)$	$V_{\mathrm{ex}}(S-S)$
$\beta U_0 = 0.8$	$8v_{\mathrm{occ}}$	$6.14v_{\mathrm{occ}}$	$5.85v_{\mathrm{occ}}$
$\beta U_0 = 1.2$	$8v_{\mathrm{occ}}$	$7.20v_{\mathrm{occ}}$	$6.92v_{\mathrm{occ}}$

problems, for separations between the macromolecules' surfaces below $r_{\mathrm{min}} = 0.08\,\mathrm{nm}$, we kept the magnitude of force fixed and equal to $\boldsymbol{F}(r_{\mathrm{min}})$. We also set the upper cutoff for the repulsive interactions to $15\,\mathrm{nm}$ and for electrostatic interactions to $25\,\mathrm{nm}$. Compositions of the simulated systems are shown in Table 4.7.

We obtained diffusion coefficients from TAMSD (Eq. A.14) with a window length equal to $5\,\mathrm{ns}$. The long-time diffusion coefficients were obtained by averaging $D(t)$ around $t = 5\,\mu\mathrm{s}$. Uncertainty of the D_l due to sampling error was estimated by dividing the simulations into 5 subsets and computing the standard deviation of the mean, while treating the subsets as independent "measurements".

4.5.4 Diffusion in soft and hard crowders

We simulated mixtures of soft and hard particles (Fig. 4.15a) with effective occupied volume fraction $\phi_{\mathrm{occ}} = 10\%$ and molar fraction of hard particles $x_{\mathrm{H}} = 27\%$ (Table 4.7) for two different sets of CESP parameters (Table 4.6 and crossmarks in Fig. 4.14b). Diffusion coefficients of hard and soft particles increase with increase of the crowder softness controlled by the entanglement extension $(a_e - a_c)/a_c$ (Fig. 4.15b). The effect is similar, no matter whether we consider hard or soft particles as tracers, but the diffusion coefficients of soft particles are higher.

We also computed effective volumes excluded by soft and hard crowders using MC simulations (Section 3.3). Hard particle excludes $8v_{\mathrm{occ}}$ (v_{occ} being its volume) to another hard particle, whereas a soft particle with $\beta U_0 = 1.2$ excludes only $\approx 7.2v_{\mathrm{occ}}$ to a hard particle and $\approx 7v_{\mathrm{occ}}$ to another soft particle. Corresponding values for a soft particle with $\beta U_0 = 0.8$ are even lower (Table 4.8). Thus, soft crowders hinder diffusion of other particles less strongly because they exclude less volume to a tracer, either hard or soft.

Next, we studied diffusion in mixtures of hard and soft ($\beta U_0 = 1.2$) particles. We considered occupied volume fraction $\phi_{\mathrm{occ}} = 10\%$ and various molar fractions of hard particles x_{H}

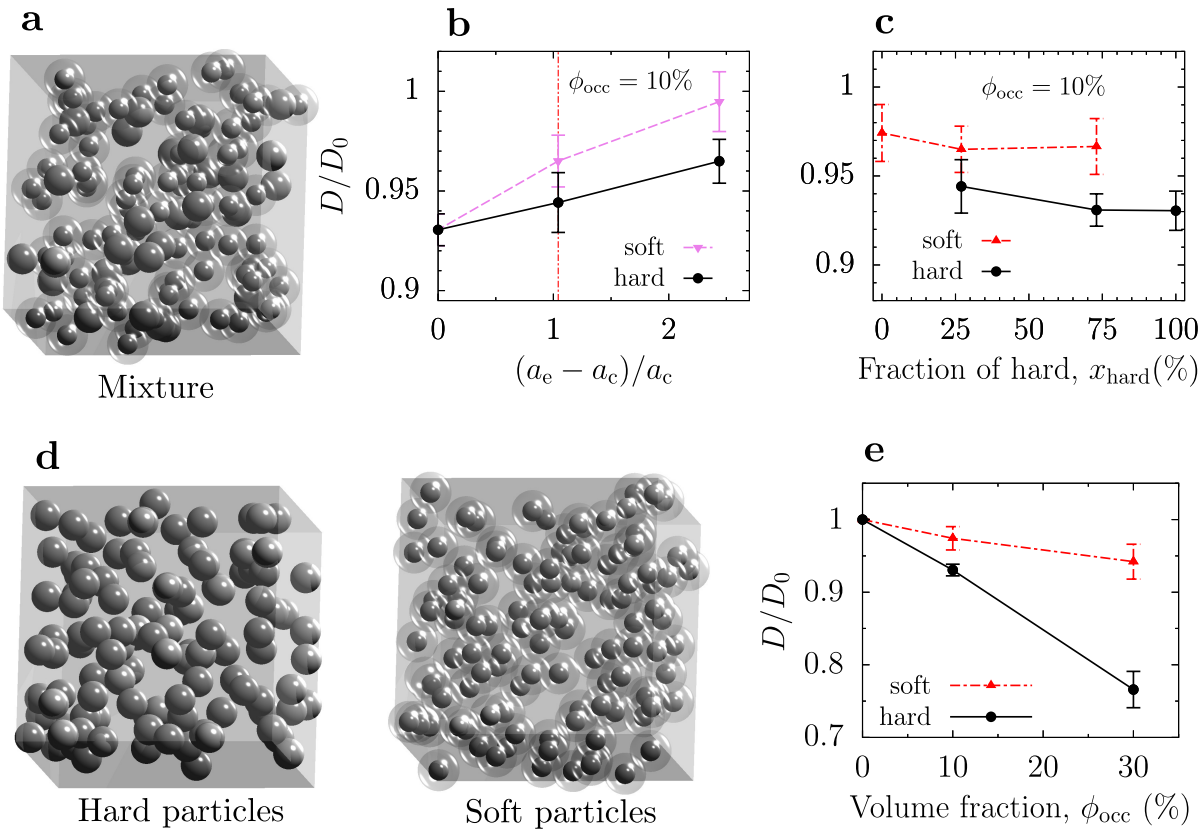

Figure 4.15: **Diffusion in systems of hard and soft macromolecules.** (**a**) Snapshot of a mixture composed of soft and hard particles used in BD simulations. (**b**) Dependence of diffusion coefficient of soft and hard tracer in hard-soft mixtures of $x_H = 27\%$ on the extent of the soft interaction, keeping the effective occupied volume fraction $\phi_{occ} = 10\%$. The value $(a_e - a_c)/a_c = 0$ corresponds to a hard particle. (**c**) Dependence of diffusion coefficient of soft ($\beta U_0 = 1.2$) and hard tracer in hard-soft mixtures on the molar fraction of hard particles, keeping the effective occupied volume fraction $\phi_{occ} = 10\%$. (**d**) Snapshots of example 1-component systems of hard/soft particles used in BD simulations. (**e**) Dependence of diffusion coefficient of soft and hard tracer in 1-component systems on the occupied volume fraction ϕ_{occ}. Figure reprinted from ref. [188].

Table 4.9: **Excluded volume fractions in simulated mixtures of occupied volume fraction $\phi_{occ} = 10\,\%$.**

$\phi_{occ} = 10\,\%$, $\beta U_0 = 1.2$			
Tracer	$x_S = 100\,\%$	$x_S = 73\,\%$	$x_S = 27\,\%$
$a_c = 0\,\text{nm}$ $a_e = 0\,\text{nm}$	$9.90 \pm 0.02\%$	$9.95 \pm 0.03\%$	$9.99 \pm 0.03\%$
$a_c = 5.1\,\text{nm}$ $a_e = 5.1\,\text{nm}$	$56.2 \pm 0.5\%$	$58.9 \pm 0.7\%$	$61.1 \pm 0.7\%$
$a_c = 3.35\,\text{nm}$ $a_e = 6.85\,\text{nm}$	$54.4 \pm 0.4\%$	$56.1 \pm 0.6\%$	$57.3 \pm 0.5\%$

(Fig. 4.15c). The diffusion coefficient in these systems gradually decreases upon increasing the number of hard particles, which reflects the trend in the volume exclusion (Table 4.8). However, since the excluded volume is not an additive property, we computed effective excluded volume fractions in the simulated systems using the MC method (Section 3.3). The MC results support our reasoning (Table 4.9).

Table 4.10: **Excluded volume fractions in simulated mixtures of occupied volume fraction** $\phi_{\mathrm{occ}} = 30\,\%$**.**

$\phi_{\mathrm{occ}} = 30\,\%, \beta U_0 = 1.2$			
Tracer		$x_{\mathrm{S}} = 100\,\%$	$x_{\mathrm{S}} = 0\,\%$
$a_c = 0\,\mathrm{nm}$	$a_e = 0\,\mathrm{nm}$	$27.6 \pm 0.2\%$	$30.10 \pm 0.10\%$
$a_c = 5.1\,\mathrm{nm}$	$a_e = 5.1\,\mathrm{nm}$	$95.40 \pm 0.12\%$	$99.1 \pm 0.2\%$
$a_c = 3.35\,\mathrm{nm}$	$a_e = 6.85\,\mathrm{nm}$	$94.00 \pm 0.14\%$	$98.1 \pm 0.3\%$

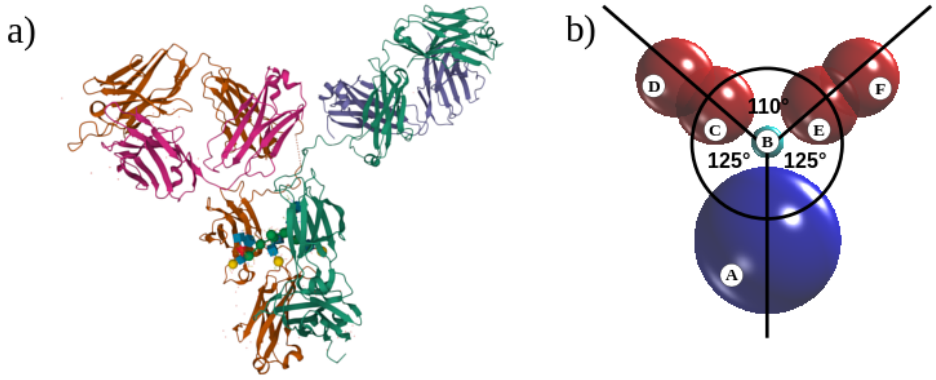

Figure 4.16: **IgG bead model.** (**a**) Crystal structure of human IgG [190] taken from Protein Data Bank (PDB ID: 1HZH) [31] and visualized using Mol* Viewer [191]. (**b**) Bead model of IgG correctly reproducing its hydrodynamic radius ($5.8\,\mathrm{nm}$) and angle distributions [192]. Figure reprinted from Supplementary Information of ref. [188].

Figure 4.15e shows the dependence of the long-time diffusion coefficient on the effective occupied volume fraction for one-component systems of hard and soft macromolecules. The slope of the line representing hard particle systems is substantially larger than for soft particles. For $\phi_{\mathrm{occ}} \approx 30\%$, the crowding by hard particles leads to approximately four times larger diffusion slowdown than in the case of soft crowders. Again, we see the same trends in the excluded volume data (Table 4.10), but the differences in excluded volume are relatively small, as compared to the differences in the diffusion coefficients. This is because the values are close to 100%, so the possible differences are somewhat limited in such a concentrated regime.

4.5.5 Tracer shape effect

We next studied how the crowder softness ($\beta U_0 = 1.2$) influences the diffusion of nonspherical tracers. We chose an elongated 16-nm-long dsDNA, the same as in Section 4.3, and a Y-shaped model of IgG (Fig. 4.16). The IgG model is characterized by a hydrodynamic radius $a_{\mathrm{IgG}} = 5.8 \pm 0.2\,\mathrm{nm}$, close to the experimental value of $6.0\,\mathrm{nm}$ [126]. Moreover, its angle distrbutions are similar to the experimental ones [192]. The model consists of 6 beads of various hydrodynamic radii (Table 4.11) with harmonic bond (Eq. A.12 and Table 4.12) and angle interactions (Eq. A.13 and Table 4.13) between the beads.

Table 4.11: **Sizes of the subunits of IgG model.**

Subunit	$a = a_c = a_e$ (nm)
A	4.5
B	1.0
C	2.42
D	2.42
E	2.42
F	2.42

Table 4.12: **Values of equilibrium bond lengths and force constants in IgG model.**

Subunit	Bond length (nm)	Force constant ($\mathrm{kcal\,mol^{-1}\,nm^{-2}}$)
A - B	6.0	1909.86595
B - C B - E	3.9	1909.86595
C - D E - F	3.0	1909.86595

Table 4.13: **Values of equilibrium angles and force constants in IgG model.**

Subunit	Angle value	Force constant ($\mathrm{kcal\,mol^{-1}\,rad^{-2}}$)
A - B - C A - B - E	125.0°	0.05
B - C - D B - E - F	180.0°	10.00
C - B - E	110.0°	0.05

Table 4.14: **Compositions, occupied volume fractions and molar fractions of simulated mixtures of hard and soft macromolecules with IgG and dsDNA.**

Tracer	ϕ_{occ} (%)	$x_{\mathrm{IgG}}/x_{\mathrm{dsDNA}}$ (%)	$x_{\mathrm{H}}/x_{\mathrm{S}}$ (%)	$N_{\mathrm{IgG}}/N_{\mathrm{dsDNA}}$	$N_{\mathrm{H}}/N_{\mathrm{S}}$
IgG	10	28	72	30	79
dsDNA	10	25	75	36	107

To understand whether the difference between the diffusion in hard and soft crowders presented in Fig. 4.15 remains similar irrespectively of the tracer size and shape, we simulated systems containing dsDNA and IgG tracers (Fig. 4.17a) with compositions shown in Table 4.14. Consistently with the previous results (Fig. 4.15), we find that the diffusion of IgG is visibly less hindered by soft crowders (Fig. 4.17b). However, for dsDNA, the difference between the diffusion coefficients in hard and soft crowders is much smaller than for larger tracers. We used the MC method (Section 3.3) to compute the effective volumes excluded by soft and hard crowders to dsDNA and IgG tracers (Fig. 4.17c). Although the respective differences are relatively small, they reflect the behavior of the diffusion coefficients, *i.e.*, soft crowders exclude less volume to hard and IgG tracers; conversely, soft crowders exclude more volume to dsDNA tracers. This behavior suggests that, for some macromolecular shapes, the diffusion might be faster in hard

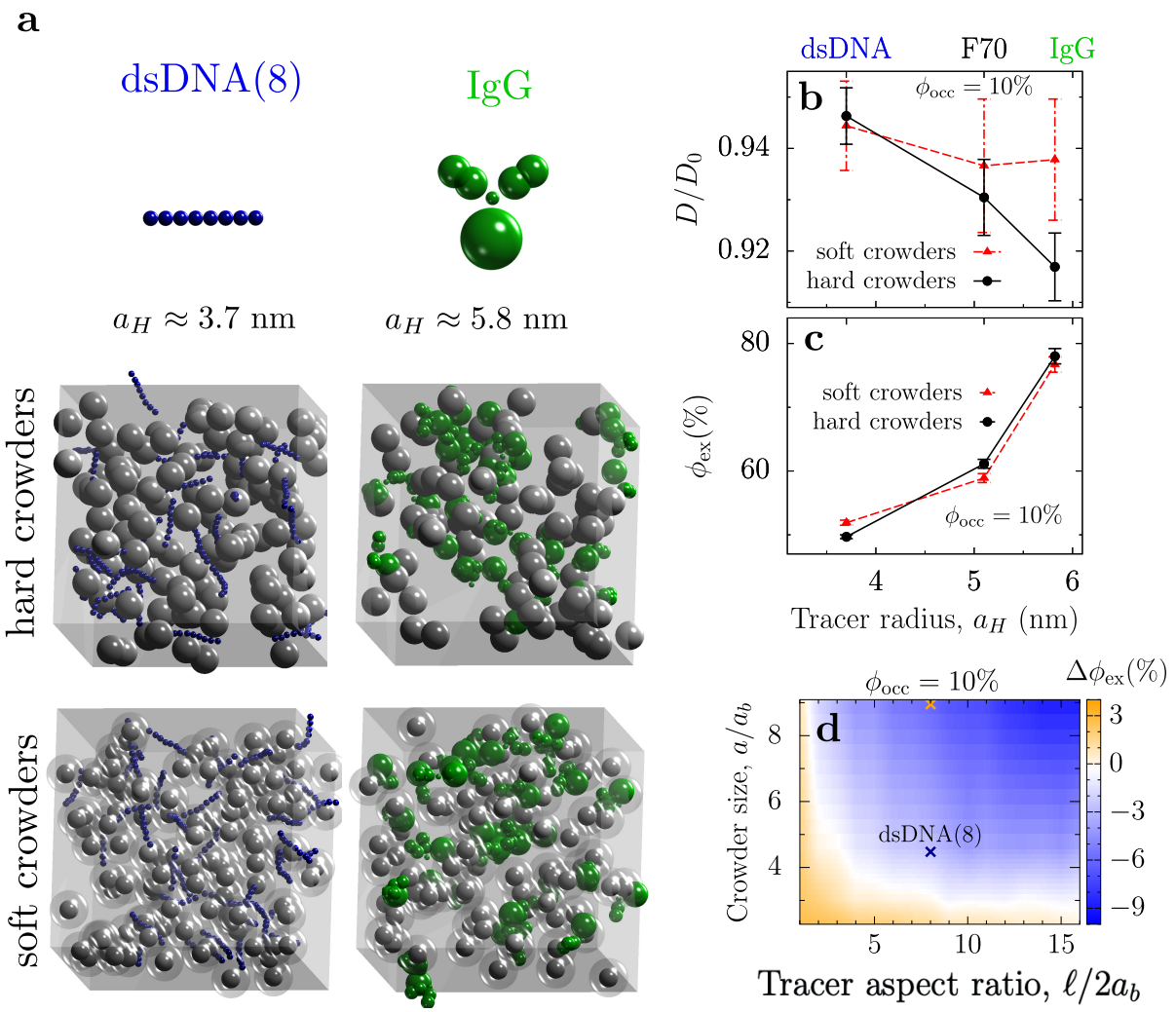

Figure 4.17: **Effect of the tracer shape on the diffusion in systems with soft and hard crowders.** (**a**) Models of nonspherical tracers, dsDNA and IgG, used in BD simulations (top) and snapshots of them mixed up with hard/soft crowders (bottom). (**b**) Diffusion coefficient of tracers in hard and soft ($\beta U_0 = 1.2$) crowder systems of $\phi_{occ} \approx 10\%$ as a function of their hydrodynamic radius. Hydrodynamic radii of dsDNA and IgG were obtained in separate BD simulations of isolated particles. (**c**) Volume excluded by hard and soft crowder systems of $\phi_{occ} = 10\%$ to various tracers as a function of their hydrodynamic radius. (**d**) Heat map presenting the difference between volume excluded by hard and soft crowders $\Delta\phi_{ex} = \phi_{ex}^{hard} - \phi_{ex}^{soft}$ to a dsDNA-like chain of various crowder size a/a_b and aspect ratio $\ell/2a_b$. Figure adapted from ref. [188].

crowders.

Because the difference of the diffusion coefficients and excluded volumes of the dsDNA were rather small, to investigate this relation more systematically, we computed volumes excluded to dsDNA-like chains as a function of the chain length $\ell/2a_b$ and crowder-to-bead radius ratio a/a_b (Fig. 4.17d). Depending on $\ell/2a_b$ and a/a_b, $\Delta\phi_{ex} = \phi_{ex}^{hard} - \phi_{ex}^{soft}$ may be positive (hard crowders exclude more volume to the chain) or negative (soft crowders exclude more volume to the chain). Thus, the volume excluded to a polymer chain by soft crowders exceeds the

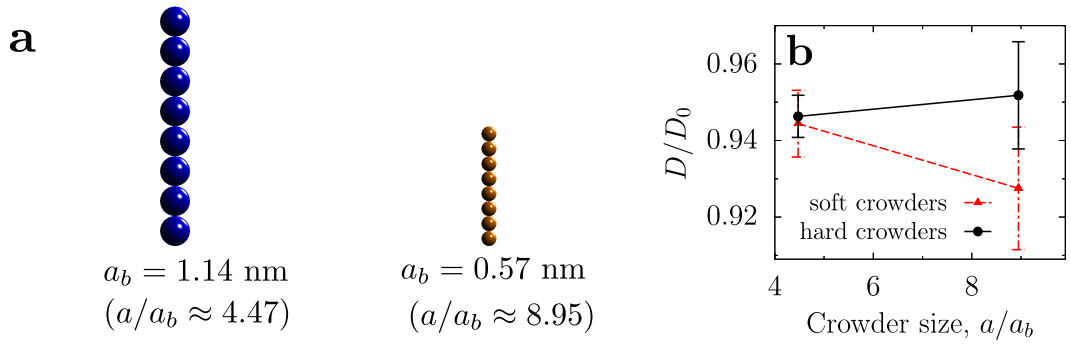

Figure 4.18: **Thin and long crowders diffuse faster in systems with hard crowders.** (**a**) Comparison of dsDNA model and its rescaled version with two times smaller bead radius a_b. (**b**) Diffusion coefficient of dsDNA models in hard and soft crowder systems of $\phi_{\text{occ}} = 10\%$ in a function of crowder size a/a_b. Figure adapted from ref. [188].

volume excluded by hard crowders for sufficiently long and thin chains.

To verify whether the behavior of the excluded volume entails a similar behavior of diffusion coefficients, we prepared a rescaled dsDNA model with two times smaller bead radius a_b (Fig. 4.18a). BD simulations with such rescaled dsDNA particles indeed show that thinner chains diffuse faster in hard crowders than in soft crowders, in agreement with the predictions based on the excluded volumes (Fig. 4.18b). This behavior is in contrast to the behavior of more spherical particles, like hard and soft macromolecules and IgG.

Chapter 5

Enhanced enzyme diffusion

> One can best appreciate, from a study of living things, how primitive physics still is.
>
> Albert Einstein

In Chapter 4, I covered self-diffusion of macromolecules in thermodynamic equilibrium. However, biological cells are not in equilibrium, unless dead. In some sense, their existence is a sheer resistance to equilibration, as energy and matter fluxes are essential features of life at the cellular level [193, 194].

It is natural that diffusive properties of macromolecules in the cytoplasm affect the chemical kinetics of reactions happening therein, therefore affecting the metabolic networks driving life [96, 97]. However, a growing body of evidence shows that the opposite might also be the case, *i.e.*, that the metabolic activity affects the diffusion of macromolecules immersed in "active" cytoplasm [20, 21, 115, 194, 195]. For instance, Parry *et al.* [20] reported that the cytoplasm of *Caulobacter crescentus* becomes glassified when its metabolic activity is halted by glucose starvation, rendering it more viscous for macromolecules. In another work, Li *et al.* [195] showed that the diffusivity of macromolecules in cells undergoing necroptosis increases in its initial stages. Understanding the coupling between the metabolic activity and macromolecular mobility is essemtial for a reliable simulation of living cells.

A possible explanation for the coupling of activity and mobility in living cells is the phenomenon of enzyme diffusion enhancement [196–198], which is an enhancement of the enzyme diffusion in systems containing substrates of the reaction it catalyzes. Moreover, Zhao *et al.* [199] reported that active enzymes could affect the diffusion of passive particles. Although the existence of enzyme diffusion enhancement is still debated [200, 201], and its studies are limited to dilute solutions, there are indications that it might be related to the observed cytoplasmic glassification [194].

In this Chapter, we discuss enzyme diffusion enhancement, focusing on crowded systems. After reviewing the literature in Section 5.1, in Section 5.2, I introduce a model enzyme that exhibits a diffusion enhancement upon binding a substrate [202]. In Section 5.3, I describe

its behavior in various crowded systems akin to intracellular environments. In Section 5.4, we will see if and how microfluidic H-cell experiment, a versatile tool for, among others, diffusion measurements, can be applied to measure enzyme diffusion enhancement.

5.1 Literature review

As already mentioned above, one of the reasons for metabolism-mobility coupling in cells may be enhanced enzyme diffusion [196–198]. The effect was communicated by various authors for a broad class of enzymes [203–214]. The experimental results are gathered in Table 5.1.

Table 5.1: **Enzyme diffusion enhancements observed experimentally.**

Enzyme	Substrate	D_0 ($\mathrm{nm}^2\,\mu\mathrm{s}^{-1}$)	δD (%)	Method
Acetylcholinesterase	acetylcholine	22 [211]	20 [211]	FCS
Alkaline phosphatase	p-nitrophenyl phosphate	23.1 [215]	80 [208]	FCS
Catalase	hydrogen peroxide	60 [206]	45 [206]	FCS
			30 [208]	FCS
DNA polymerase	ATP	122 [207]	46 [207]	FCS
F_1-ATPase	ATP	33 [203]	15-24 [203]	FCS
Fructose Bisphosphate Aldolase	Fructose-1,6-bisphosphate	42.6 [209]	30 [209]	FCS
		41.3 [200]	0 [200]	DLS
		42.5 [212]	35 [212]	FCS
		47 [201]	0 [201]	NMR
Hexokinase	D-glucose	73 [212]	38 [212]	FCS
T7 RNA polymerase	nucleoside triphosphate	15.3 [204]	25.2 [204]	FRAP
Triose phosphatase	D-glyceraldehyde 3-phosphate		5 [208]	FCS
Urease	urea	31.8 [205]	28 [205]	FCS
			25 [208]	FCS
		30 [210]	30-80 [210]	FCS
		30 [211]	50 [211]	FCS
		0.169 [213]	200 [213]	SMT

The magnitude of the enzyme diffusion enhancement varies between studies and enzymes. The enhancement ranges from just 5% for triose phosphatase reported by Riedel *et al.* [208] to even 200% for urease claimed by Xu *et al.* [213], the majority falling somewhere between 10 and 40% [203, 205, 208–212]. However, some authors claim that the effect is merely an artifact of the applied experimental methods [200, 201, 216] or a result of dissociation of oligomeric enzymes [217, 218].

The two most probable mechanisms that may lead to the enzyme diffusion enhancement are phoresis and conformational changes [194]. Phoresis is a movement driven by a gradient of some material property, *e.g.*, of the electric field in the case of electrophoresis, temperature in the case of thermophoresis, and the concentration in the case of diffusiophoresis. Within this mechanism, an enzymatic reaction is the source of such gradient itself, so one refers to the effects as a self-electrophoresis [205], self-thermophoresis [219], and self-diffusiophoresis [196, 220], respectively. In turn, conformational changes include size decrease [202, 203], active swimming [216, 221], damping conformational fluctuations [209], and chemoacoustic effects [208].

The most straightforward mechanism which may lead to an enhanced enzyme diffusion is the change of the enzyme size upon binding a substrate. The size decrease, if lasting long enough, would lead to an increase in the enzyme's diffusion coefficient according to the Stokes-Sutherland-Einstein (SSE) relation (Eq. 2.10). Such size changes are ubiquitous among enzymes. For instance, the radius of *Escherichia coli* H^+-ATPase F_1 subunit decreases by *ca.* 15% in the presence of its substrate analog, AMP-PNP [222]. Indeed, Börsch *et al.* [203] observed the enhancement of the H^+-ATPase F_1 subunit's diffusion in the presence of AMP-PNP.

Oyama *et al.* [223] performed Brownian dynamics (BD) simulations of binary mixtures in which small spheres modeled water, and large spheres, with fluctuating radii, modeled metabolically active enzymes. They observed that even small radii fluctuations ($\approx 4\%$) might lead to glass-fluid transition, which could be a size-decrease mechanism for the metabolism-driven cytoplasm fluidization observed by Parry *et al.* [20] and Nishizawa *et al.* [21]. Clearly, the same size changes could also lead to the enzyme diffusion enhancement, as described above.

All the aforementioned experiments were performed *in vitro*, in dilute solutions. As we extensively discussed in Chapter 4, such an approach does not give answers to the most intriguing question: how the macromolecular transport behaves inside biological cells, which are crowded by diverse macromolecules. To address this question, we study the dynamics of conformation-changing enzymes (Section 5.2) in crowded environments with BD simulations (Section 5.3).

5.2 Fluctuating-dumbbell model

Illien *et al.* [224] introduced a dumbbell model of an enzyme that is composed of two subunits fluctuating around an equilibrium separation. They showed that suppression of the separation fluctuations upon binding a substrate might lead to an increase in enzyme diffusion coefficient,

which they claimed to be consistent with the aldolase diffusion enhancement observed experimentally [209], along with its Michaelis-Menten-like [225] substrate concentration dependence.

A similar model was analyzed with BD simulations by Kondrat & Popescu [202]. They showed that, contrary to the results obtained by Illien *et al.* [209, 224], the suppression of internal fluctuations leads only to a minor enhancement of the diffusion coefficient ($\leq 5\%$). Nevertheless, they showed that the bare size decrease upon binding a substrate, if sufficiently large, could lead to a diffusion enhancement comparable to the one observed experimentally for such enzymes.

Following ref. [202], we consider a fluctuating dumbbell composed of two spherical beads of hydrodynamic radius $a = 1\,\mathrm{nm}$ each (Fig. 5.1a). This model enzyme can adopt two distinct conformations: open and closed, characterized by different bead-bead separations: $\ell_o = 2.5\,\mathrm{nm}$ and $\ell_c = 1.1\,\mathrm{nm}$, respectively. To compute the enzyme diffusion enhancement, we performed two sets of BD simulations, corresponding to two extreme substrate concentration values: when an enzyme can be in an open or closed conformation ($[\mathrm{S}] = 0$) and when it is only in the closed state ($[\mathrm{S}] \to \infty$).

$[\mathrm{S}] = 0$ regime is modeled implicitly by setting a double-well potential U, which has two minima with equal depth at $\ell = \ell_c$ and $\ell = \ell_o$ and a potential barrier between them (Fig. 5.1b, solid line):

$$U(\ell) = \frac{16 k_\ell}{(\ell_o - \ell_c)^4} (\ell_c - \ell)^2 (\ell_o - \ell)^2, \tag{5.1}$$

where the characteristic energy k_ℓ is the height of the energy barrier separating the two states, which we set to $7 k_\mathrm{B} T$ in all simulations below. The potential U allows for fluctuations between the two states, which mimicks the enzyme's behavior in the absence of substrates. The populations of open and closed enzymes follow the Boltzmann distribution, their imbalance being due to the higher entropy of the open state (Fig. 5.1c, solid line). This aspect of fluctuating-dumbbell enzymes is discussed more extensively in Section 6.2.

$[\mathrm{S}] \to \infty$ regime is modeled implicitly too by setting a single-well potential U_c, with a minimum at $\ell = \ell_c$ (Fig. 5.1b, dashed line):

$$U_c(\ell) = \frac{16 k_\ell}{(\ell_o - \ell_c)^4} (\ell_c - \ell)^2 g_c(\ell), \tag{5.2}$$

where:

$$g_c(\ell; \ell_c, \ell_o) = \begin{cases} (\ell_o - \ell)^2, & \text{if} \quad \ell < \ell_c \\ (\ell - 2\ell_c + \ell_o)^2, & \text{if} \quad \ell \geq \ell_c. \end{cases} \tag{5.3}$$

In this regime, all enzymes are in the closed state (Fig. 5.1c, dashed line).

The diffusion coefficients for $[\mathrm{S}] = 0$ and $[\mathrm{S}] \to \infty$ were extracted by fitting the $\mathrm{MSD}(t)$

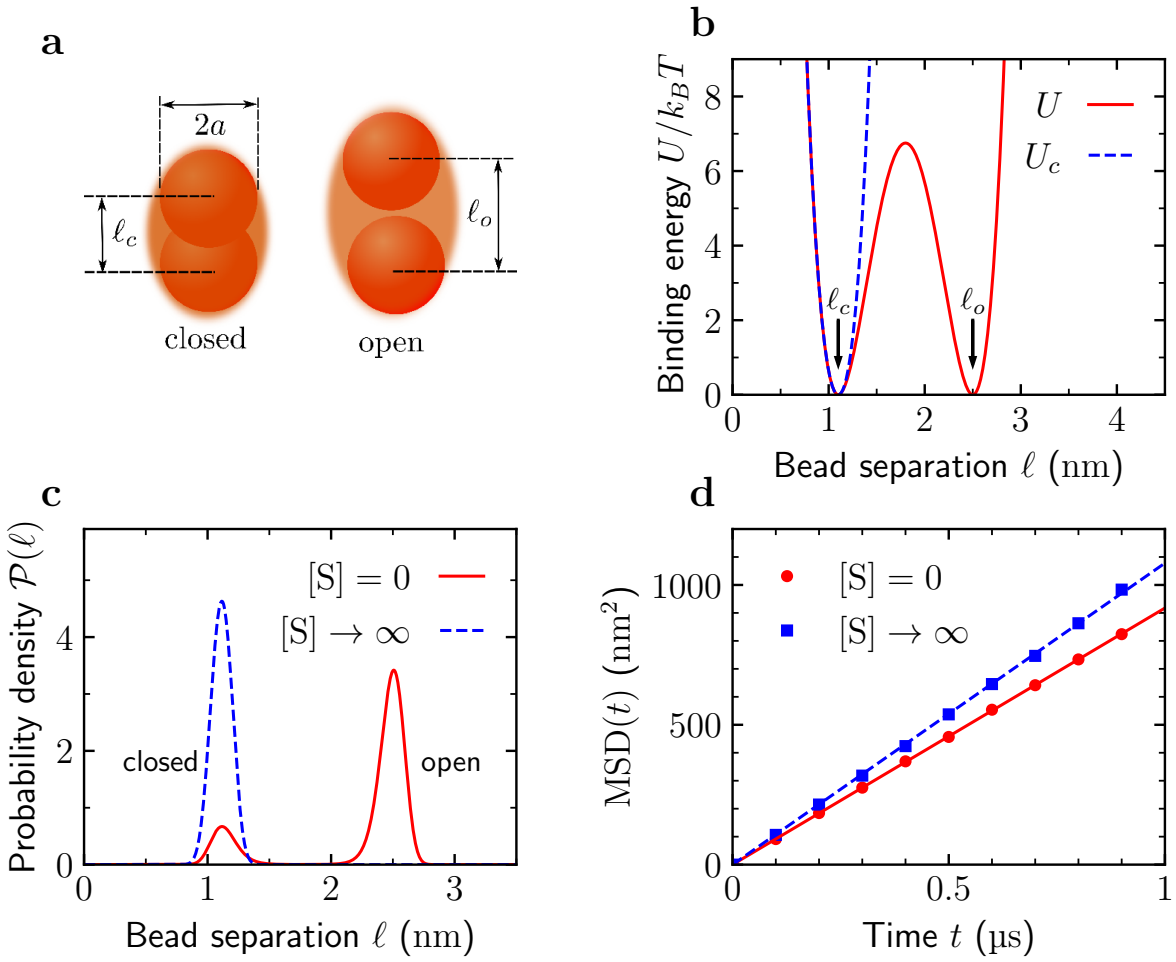

Figure 5.1: **Fluctuating-dumbbell enzyme model.** (**a**) Two possible conformations of fluctuating-dumbbell enzyme model, differing in equilibrium distance between the subunits ($\ell_c < \ell_o$ for closed; ℓ_o for open). When there is no substrate ([S] $= 0$), there is a dynamic equilibrium of enzymes in the open and closed conformations. When substrate is in abundance ([S] $\to \infty$), all enzymes are closed. (**b**) Enzyme bonded potentials: U (red) with two equienergetic minima for [S] $= 0$ case and U_c (blue) with a single minimum for [S] $\to \infty$ case. (**c**) Equilibrium probability density of bead separation ℓ for potentials U and U_c. (**d**) The mean squared displacement (MSD) obtained by 4000 independent BD simulations. Figure adapted from ref. [226].

data from BD simulations with a linear function $f(t) = 6Dt$ (Fig. 5.1d). The resulting diffusion coefficients ($T = 298.15\,\mathrm{K}$, $\eta = 1.02\,\mathrm{cP}$) are $D([\mathrm{S}] = 0) = 153\,\mathrm{nm^2\,\mu s^{-1}}$ and $D([\mathrm{S}] \to \infty) = 180\,\mathrm{nm^2\,\mu s^{-1}}$, which translate to hydrodynamic radii 1.40 and 1.19 nm, respectively. This amounts to $\approx 17.6\%$ of enzyme diffusion enhancement in infinite dilution (*i.e.*, without crowders, $\phi_{\mathrm{occ}} = 0$), comparable to the experimental results for F_1 ATP-ase [203] (Table 5.1). Hydrodynamic radii obtained from our BD simulations are also very close to the results of `GRPY` algorithm (Appendix D.5) for computing the hydrodynamic radii of rigid bead structures: 1.44 for open and 1.20 nm for closed conformation.

5.3 Effect of crowding

In this section, we discuss the interplay between the enzyme diffusion enhancement and the diffusion slowdown due to macromolecular crowding. Moreover, we discuss the influence of enzymatic activity on the diffusion of passive spheres mixed with the enzymes. To this end, we performed BD simulations of systems composed of fluctuating-dumbbell enzymes (Section 5.2) and passive spherical macromolecules.

5.3.1 Simulation details

We performed BD simulations with a customized version of the `BD_BOX` software (Appendix D.1). We placed the fluctuating-dumbbell enzymes and passive spheres in cubic boxes of $25\,\mathrm{nm} \times 25\,\mathrm{nm} \times 25\,\mathrm{nm}$, and applied periodic boundary conditions in all three directions. The time step Δt was $0.5\,\mathrm{ps}$, and simulations lasted for $10\,\mu\mathrm{s}$ or more. We accounted for far-field hydrodynamic interactions with the Ewald-summated ($\alpha = \sqrt{\pi}$, $m_{\mathrm{cutoff}} = n_{\mathrm{cutoff}} = 2$, see Appendix B) generalized Rotne-Prager-Yamakawa (RPY) approximation. Following ref. [36], to decrease the computational cost we performed Choleski decomposition every 100 steps instead of doing so in every step. We propagated the BD with the Iniesta-Garcia de la Torre scheme [184] (Eq. A.4). The temperature $T = 298.15\,\mathrm{K}$, and dynamic viscosity $\eta = 1.02\,\mathrm{cP}$. Parameters for repulsive interactions (Eq. A.7) were: $\varepsilon_{\mathrm{LJ}} = 0.37\,\mathrm{kcal\,mol^{-1}}$, $\sigma = 0.15\,\mathrm{nm}$. To avoid large forces causing numerical problems, for separations between the beads' surfaces below $r_{\mathrm{min}} = 0.1\,\mathrm{nm}$, we kept the magnitude of force fixed and equal to $\boldsymbol{F}(r_{\mathrm{min}})$. We also set the upper cutoff for the repulsive interactions to $15\,\mathrm{nm}$. We accounted for roughness of macromolecules (Eq. A.10) setting $h = \sigma$ for all beads.

We obtained diffusion coefficients from time-averaged mean squared displacement (TAMSD) (Eq. A.14) with a window length equal to $5\,\mathrm{ns}$. The long-time diffusion coefficients were obtained by averaging $D(t)$ between 2.5 and $5\,\mu\mathrm{s}$. Uncertainty of the D_l due to sampling error was estimated by dividing the simulations into 5 subsets and computing standard deviation of the mean, while treating the subsets as independent "measurements". We quantified diffusion enhancement $\delta D_l^{\mathrm{max}}$ in the following way:

$$\delta D_l^{\mathrm{max}} = \frac{D_l\left([\mathrm{S}] \to \infty\right) - D_l\left([\mathrm{S}] = 0\right)}{D_l\left([\mathrm{S}] = 0\right)}. \tag{5.4}$$

We prepared multiple mixtures of fluctuating-dumbbell enzymes and passive spheres ($a = 1\,\mathrm{nm}$) of various occupied volume fraction ϕ_{occ} and composition (Table 5.2), grouping them into two categories. In enzyme crowding (Fig. 5.2a), we kept the number of passive spheres constant ($\phi_{\mathrm{occ}} \approx 3\%$), and added enzymes to yield the total $\phi_{\mathrm{occ}} = 8$, 13, and 18%. In sphere crowding (Fig. 5.2b), we kept the number of enzymes constant ($\phi_{\mathrm{occ}} \approx 5\%$), and added passive spheres to reach the same ϕ_{occ} as in the case of enzyme crowding.

Table 5.2: **Compositions and occupied volume fractions of simulated mixtures of enzymes and passive spheres.** N_{enz} and N_{pass} are numbers of enzymes and passive spheres in a simulated system, respectively.

ϕ_{occ} (%)	N_{enz}	N_{pass}
Enzyme crowding		
8	100	100
13	200	100
18	300	100
Sphere crowding		
3	0	100
8	100	100
13	100	296
18	100	492

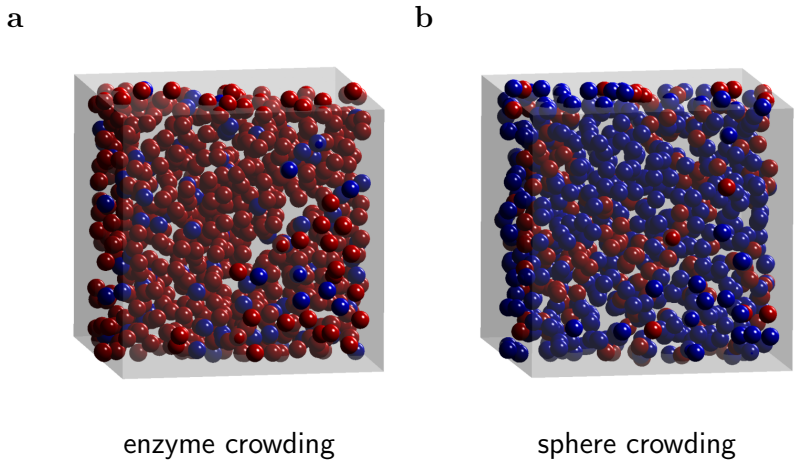

Figure 5.2: **Sphere and enzyme crowding.** The snapshots show an example of (**a**) enzyme and (**b**) sphere crowding for the total occupied volume fraction $\phi_{\text{occ}} = 18\%$. In enzyme crowding, the number of passive spheres (blue) is kept fixed, while the number of enzymes increases (red). In sphere crowding, the number of enzymes is kept fixed, while the number of passive spheres increases.

5.3.2 Enhanced diffusion of enzymes

As already mentioned, in the absence of crowders the enzyme diffusion enhancement exhibitted by our fluctuatng-dumbbell model amounts to $\approx 17.6\%$, similar to the value reported for F_1 ATP-ase by Börsch *et al.* [203]. We found that crowding decreases the diffusion coefficient in the case of both $[S] = 0$ and $[S] \to \infty$ (Fig. 5.3a). The decrease for enzyme and sphere crowding is similar in the substrate abundance case ($[S] \to \infty$). However, when there is no substrate ($[S] = 0$), the decrease is more substantial when crowding is due to enzymes.

This behavior is due to the fact that when $[S] \to \infty$, the enzymes are exclusively in the closed conformation, resembling spherical particles owing to the significant overlap of the beads composing them. This means that enzyme crowding and sphere crowding become qualitatively similar. In turn, when $[S] = 0$, most enzymes are elongated, so they hinder diffusion more than

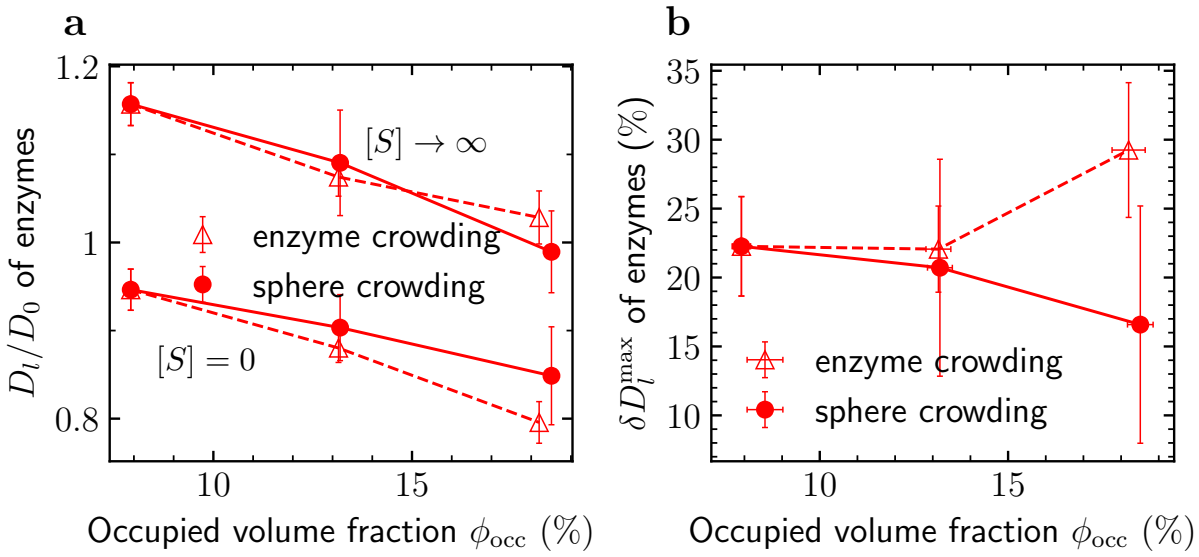

Figure 5.3: **Diffusion enhancement of fluctuating-dumbbell enzyme model in BD simulations.** (**a**) Diffusion coefficient of enzyme in two substrate concentration regimes and in two different crowding media: sphere-dominated and enzyme-dominated, plotted as a function of total occupied volume fraction ϕ_{occ}. (**b**) Diffusion enhancement in two aforementioned crowding media, plotted as a function of ϕ_{occ}. Lines on the plot do not represent neither experimental data nor theory but serve only as a guide to the eye. Figure adapted from ref. [226].

the spheres with the same occupied volume (Section 4.3).

Irrespective of the occupied volume and type of crowding, we observed the diffusion enhancement, *i.e.*, a higher diffusion coefficient for $[\mathrm{S}] \to \infty$. However, perhaps surprisingly, the enhancement increased for the enzyme crowding and decreased for the sphere crowding (Fig. 5.3b). This means that subtle features of the macromolecules composing the crowded milieu, such as their shape, can affect the enzyme diffusion enhancement not only quantitatively, but also qualitatively.

5.3.3 Enhanced diffusion of passive tracers

Zhao *et al.* [199] showed with fluorescence correlation spectroscopy (FCS) and dynamic light scattering (DLS) that inert tracers of various sizes, ranging from $0.57\,\mathrm{nm}$ (Rhodamine B) to $100\,\mathrm{nm}$ (Fluorescent Polymer Microspheres), experience the diffusion enhancement, when mixed with urease or aldolase and their respective substrate. The authors interpreted it as a transfer of diffusion enhancement between the active enzymes and passive tracers. To explore this possibility, we analyzed the diffusion of passive spheres in mixtures with active enzymes modeled by fluctuating dumbbells (Section 5.2).

Our results show that passive tracer diffusion enhancement is indeed present in concentrated systems of conformation-changing enzymes (Fig. 5.4). Moreover, the diffusion enhancement of passive spheres increases with increasing the enzyme concentration $[\mathrm{E}]$. However, the mag-

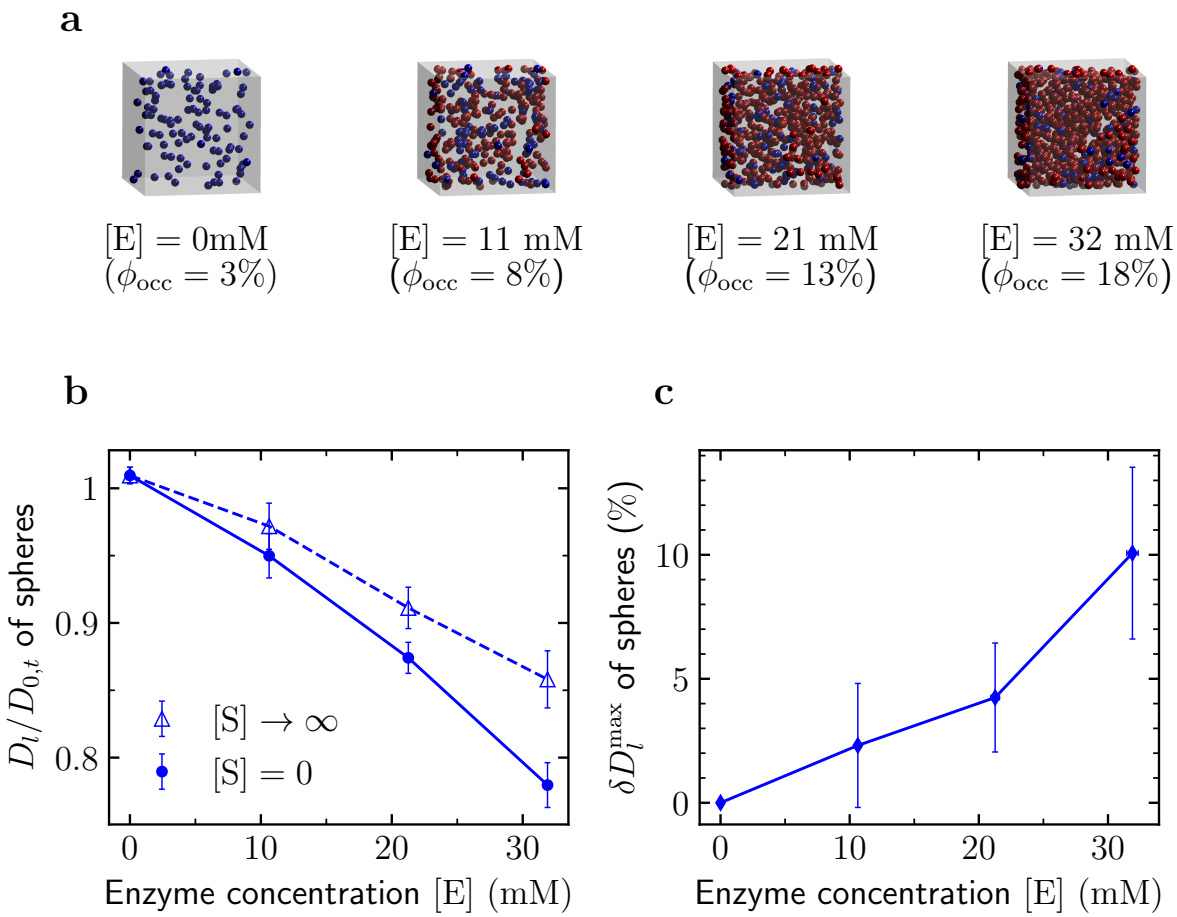

Figure 5.4: **Enhanced diffusion of passive tracers in BD simulations.** (**a**) Snapshots of BD systems with increasing concentration of enzymes [E], while keeping the number of passive spheres fixed. (**b**) Diffusion coefficient of passive sphere as a function of concentration of fluctuating-dumbbell enzymes [E] for two substrate concentrations: [S] = 0 and [S] → ∞. (**c**) Passive sphere diffusion enhancement plotted as a function of enzyme concentration [E]. Lines on the plot do not represent neither simulation data nor theory but serve only as a guide to the eye. Figure adapted from ref. [226].

nitude of the enhancement is smaller than in the case of enzyme enhanced diffusion, *e.g.*, for $\phi_{occ} = 18\%$, we observe 10% enhancement for spheres *vs.* 30% for enzymes.

We converted the occupied volume fraction ϕ_{occ} to enzyme molar concentrations [E] to compare them with the experimental data [199]. The values for $\phi_{occ} = 8$, 13, and 18% correspond to 11, 21, and 32 mM, respectively. While the passive sphere diffusion enhancement in BD simulations is qualitatively consistent with the experimental results by Zhao *et al.* [199], in the experiments the enzymes were present in nanomolar concentration, whereas in our simulations – millimolar. Therefore, the size change of the enzymes alone cannot explain the experimentally observed passive tracer diffusion.

5.4 H-cell microfluidics and enhanced enzyme diffusion

As discussed in Section 5.1, FCS experiments indicate the existence of the enzyme diffusion enhancement in systems containing substrate, while some other, nonfluorescent methods, such as DLS and nuclear magnetic resonance (NMR), do not detect it. It is natural to ask whether the existence of this phenomenon can be tested with alternative techniques that have not been used for this purpose so far, *e.g.*, H-cell microfluidics, which has recently been introduced as a versatile and robust method to measure diffusion coefficients [227, 228]. The following section attempts to answer this question.

5.4.1 Principles of H-cell diffusion measurement

H-cell microfluidics diffusion coefficient measurement is based on the mass transport between two concurrent laminar fluid streams *via* the interface between them [227, 228] (Fig. 5.5). One of the flows, called donor stream (DS), initially contains a higher concentration of an analyte. As the two streams meet and travel in parallel for a finite length of the H-cell channel L, the analyte diffuses from the DS to the receiver stream (RS). For a fixed L, the total amount of the analyte transferred from the DS to the RS depends on its transport diffusion coefficient $\mathcal{D}$.

Yu *et al.* [228] used this method to measure diffusion coefficients of proteins such as lysozyme and bovine serum albumin (BSA), varying the initial concentration in DS and RS, as well as the ionic strength, buffer type, and viscosity. The obtained results are in reasonable agreement (up to $\approx 20\%$) with the values obtained using alternative methods for protein diffusion measurement. However, one has to realize that the measured transport diffusion coefficient, denoted here by $\mathcal{D}$ to distinguish it from the self-diffusion coefficient D, is not the same property as D elaborated on in Section 2.1 and defined using MSD. The transport diffusion coefficient is defined by Fick's diffusion law:

$$\frac{\partial c}{\partial t} = \mathcal{D}\nabla^2 c, \tag{5.5}$$

and describes the time evolution of the analyte concentration c in a system with a concentration gradient. In general, these two diffusion coefficients are not the same [229, 230], and equal only for low analyte concentrations.

5.4.2 Mathematical description of H-cell diffusion measurement

Häusler *et al.* [227] showed that the problem of diffusion between DS and RS could be described mathematically using a one-dimensional diffusion equation with position-dependent diffusion coefficient $\tilde{\mathcal{D}}(y)$:

$$\frac{\partial c}{\partial x} = \frac{\mathcal{D}}{\tilde{v}(y)}\frac{\partial^2 c}{\partial y^2} = \tilde{\mathcal{D}}(y)\frac{\partial^2 c}{\partial y^2}, \tag{5.6}$$

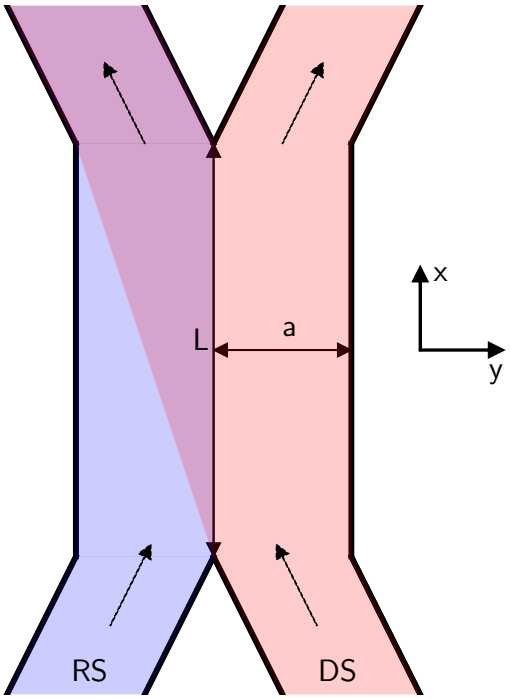

Figure 5.5: **Schematic of an H-cell microfluidic device.** Two laminar flows of fluid enter the H-cell through the inlets (bottom of the scheme). The flow containing a higher concentration of the analyte is referred to as a DS, and the other one is referred to as a RS. The two streams meet on a finite length of the H-cell channel L, and the analyte diffuses from the DS to RS. Finally, the DS and RS exit the H-cell through the outlets (top of the scheme), so their final composition can be analyzed. The z-direction is perpendicular to the plane of the scheme, and the extension of rectangular channels in that direction is denoted as $2b$.

where x coordinate, parallel to the fluid flow, acts as a time. The diffusion in the x direction can be neglected due to a much higher advective transport rate (Peclet number $Pe > 100$). $\tilde{v}(y)$ is a y-dependent flow velocity in the x-direction averaged over z coordinate [227]

$$\tilde{v}(y) = \frac{m+1}{m} v \left[1 - \left(\frac{y}{a}\right)^m\right], \tag{5.7}$$

where $2a$ is the channel width and $2b$ is the channel height, $m = 1.7 + 0.5(\frac{b}{a})^{-1.4}$, and v is a macroscopic flow velocity. The position-dependent effective diffusion coefficient $\tilde{\mathcal{D}}$ is the lowest at the center of the flow and goes to infinity when approaching the edges (when $|y|$ increases).

The concentration $c(y)$ smoothes out with x and, assuming that two streams do not diverge ($L \to \infty$), reaches an equal value at every point:

$$\lim_{x\to\infty} c(y,x) = \frac{c_0}{2}. \tag{5.8}$$

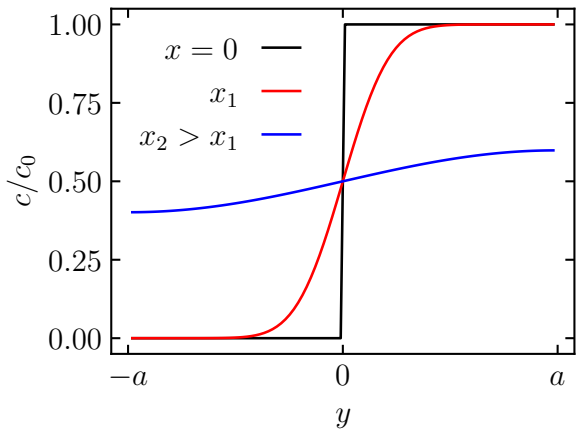

Figure 5.6: **Example of the evolution of the analyte concentration along the H-cell channel.**

For a finite value of L, the total concentrations in the DS and RS outlets are given by:

$$c_{\mathrm{DS}}(L) = \int_0^a c(y, L)dy; \tag{5.9a}$$

$$c_{\mathrm{RS}}(L) = \int_{-a}^0 c(y, L)dy, \tag{5.9b}$$

and encode the value of transport diffusion coefficient $\mathcal{D}$.

5.4.3 Simulation of H-cell diffusion measurements

We denote the initial concentration of the analyte in DS with c_0, and assume that initially there is no analyte in RS, *i.e.*:

$$\begin{cases} c = 0, \text{ for } y < 0; \\ c = c_0, \text{ for } y \geq 0; \\ \frac{\partial c}{\partial y} = 0, \text{ for } y = -a \text{ and } y = a \end{cases} . \tag{5.10}$$

We use a simple Euler discretization of Eq. 5.6 that leads to the following propagation scheme:

$$c_i^{n+1} = c_i^n + \tilde{\mathcal{D}}_i \frac{\Delta x}{(\Delta y)^2} \left(c_{i+1}^n - 2c_i^n + c_{i-1}^n \right), \tag{5.11}$$

where the upper indices enumerate discrete points in time, and lower indices – discrete points in space along the y axis. Δx and Δy denote the integration step in the x and y directions, respectively. The values of c at the edges are not propagated with Eq. 5.11, and instead are always kept equal to the values of their neighbors in order to satisfy no flux boundary conditions (Eq. 5.10). An example of the evolution of the concentration profile is shown in Fig. 5.6.

Table 5.3: **Michaelis-Menten parameters and diffusion coefficients of catalase, urease, and aldolase used in calculations.**

	catalase	urease	aldolase
K_M (mM)	96	32	13
k_{cat} (s^{-1})	$6.1 \cdot 10^5$	$5.913 \cdot 10^3$	5
$D([\mathrm{S}] = 0)$ ($\mathrm{nm}^2\,\mu\mathrm{s}^{-1}$)	60	31.8	42.6
$D([\mathrm{S}] \to \infty)$ ($\mathrm{nm}^2\,\mu\mathrm{s}^{-1}$)	87	40.7	55.4

5.4.4 Application for the diffusion enhancement measurement

Two separate H-cell diffusion measurements must be compared to obtain the diffusion enhancement using H-cell microfluidics. In one, the measurement is executed exactly like in ref. [228] and described above, with c denoting the concentration of enzyme $[\mathrm{E}]$. In the other one, substrate excess has to be added to both DS and RS. Suppose an enzyme experiences the diffusion enhancement due to the presence of substrate. In this case, the concentration of enzyme in the RS outlet $[\mathrm{E}]_{\mathrm{RS}}$ shall differ between the two measurements, *i.e.*:

$$\Delta\,[\mathrm{E}]_{\mathrm{RS}} = [\mathrm{E}]_{\mathrm{RS}}\,([\mathrm{S}] \to \infty) - [\mathrm{E}]_{\mathrm{RS}}\,([\mathrm{S}] = 0) > 0. \tag{5.12}$$

To keep the enzymatic reaction rate constant throughout the experiment, the substrate concentration has to be much higher than the enzyme concentration. We assume that the evolution of substrate concentration follows the Michaelis-Menten equation [225], which gives:

$$\frac{d\,[\mathrm{S}]}{dt} = V(t) = -\frac{k_{\mathrm{cat}}\,[\mathrm{E}]_0\,[\mathrm{S}]}{K_M + [\mathrm{S}]}, \tag{5.13}$$

where k_{cat} is the enzyme's turnover number, K_M is its Michaelis constant, $[\mathrm{S}]$ is the substrate concentration, and $[\mathrm{E}]_0$ is the initial enzyme concentration.

According to Michaelis-Menten kinetics, the reaction rate V relative to the initial (maximal) value V_0, is given by the following equation:

$$\frac{V}{V_0} = \frac{[\mathrm{S}]}{[\mathrm{S}]_0}\frac{[\mathrm{S}]_0 + K_M}{[\mathrm{S}] + K_M}. \tag{5.14}$$

$[\mathrm{S}]\,/\,[\mathrm{S}]_0$ may be computed by solving Eq. 5.13 numerically. From Eq. 5.14, we see that, initially, the reaction rate is kept virtually constant by the multiplicative factor counteracting the linear decrease of concentration.

5.4.5 Example

We consider three enzymes for which the diffusion enhancement was reported, *viz.*, catalase [206], urease [205], and aldolase [209]. The Michaelis-Menten parameters k_{cat} and K_M were taken from the Brenda database [231] (Table 5.3).

Table 5.4: **H-cell parameters used in calculations.**

a (mm)	b (μm)	v (cm min^{-1})
0.5	5	0.1

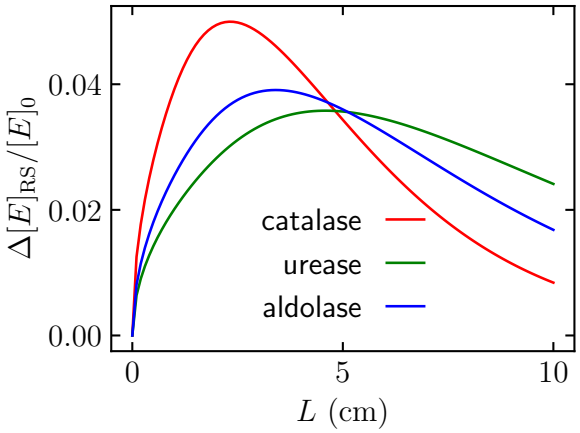

Figure 5.7: **Optimizing H-cell for diffusion enhancement measurement.** Differences between the enzyme concentration in the RS with and without substrate $\Delta\,[\mathrm{E}]_{\mathrm{RS}}$ as a function of the H-cell channel length L The optimal H-cell length corresponds to the maximum of $\Delta\,[\mathrm{E}]_{\mathrm{RS}}$.

To optimize the value of H-cell channel length L for each enzyme, we propagated the enzyme concentration using Eq. 5.11, with the H-cell parameters shown in Table 5.4 and with step sizes $\Delta x = 1\,\mu\mathrm{m}$ and $\Delta y = 10\,\mu\mathrm{m}$ for both values of diffusion coefficient – standard $D([\mathrm{S}] = 0)$ and enhanced $D([\mathrm{S}] \to \infty)$. For each enzyme, we chose the H-cell channel length L that provides the largest difference in the enzyme concentration in the outlets for systems with and without substrate $\Delta\,[\mathrm{E}]_{\mathrm{RS}}$ (Eq. 5.12). The values are $2.3\,\mathrm{cm}$ for catalase, $4.6\,\mathrm{cm}$ for urease, and $3.4\,\mathrm{cm}$ for aldolase (Fig. 5.7).

Optimal H-cell channel length L and the flow velocity v determine the total time for which we need to keep the reaction rate approximately constant – $23\,\mathrm{min}$ for catalase, $46\,\mathrm{min}$ for urease, and $34\,\mathrm{min}$ for aldolase. To gauge how to fulfill this condition, we compare the relative reaction rates at these times (Eq. 5.14) for various enzyme and substrate concentrations (Fig. 5.8). In each case, enzyme concentration has to be orders of magnitude smaller than the substrate concentration to keep the reaction rate unchanged throughout the experiment. Assuming substrate concentration to be $1\,\mathrm{M}$, which is considered concentrated, the enzyme concentration has to be in the nanomolar regime for catalase and urease, and in the micromolar regime for aldolase.

Results presented in Fig. 5.7 and Fig. 5.8 can be combined to show what differences in the concentrations between the two experiments are expected to confirm the reported enzyme diffusion enhancement. The predicted absolute enzyme concentration changes in the RS are plotted in Fig. 5.9. Results show that the changes in enzyme concentration needed to confirm the diffusion enhancement are relatively small, nanomolar for catalase and urease, and micromolar

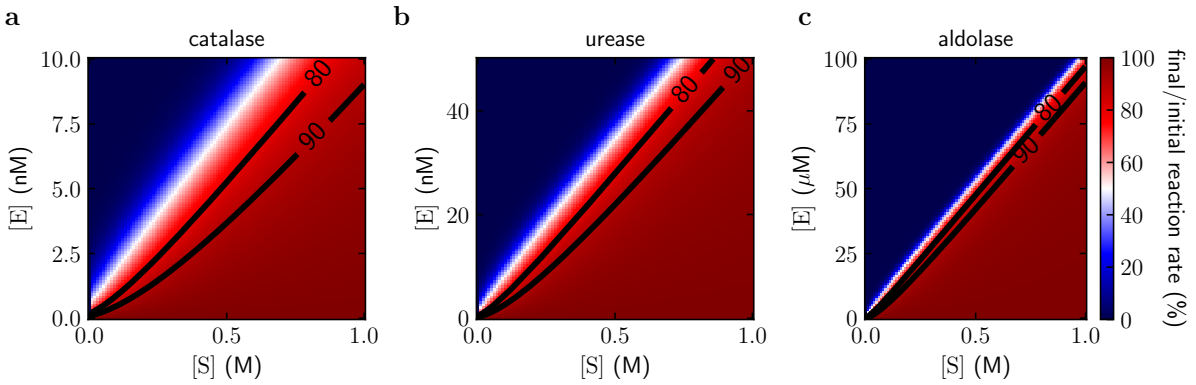

Figure 5.8: **Enzymatic reaction rate throughout the diffusion measurement in optimal H-cell.** Heat maps showing the reduction of the reaction rate at the end of the H-cell channel for (**a**) catalase, (**b**) urease, and (**c**) aldolase. The plots are drawn in the space of the initial substrate and enzyme concentrations ($[\mathrm{S}]$ and $[\mathrm{E}]$). Contours indicate the concentrations at which the reaction rate is equal to 90 and 80% of the initial value.

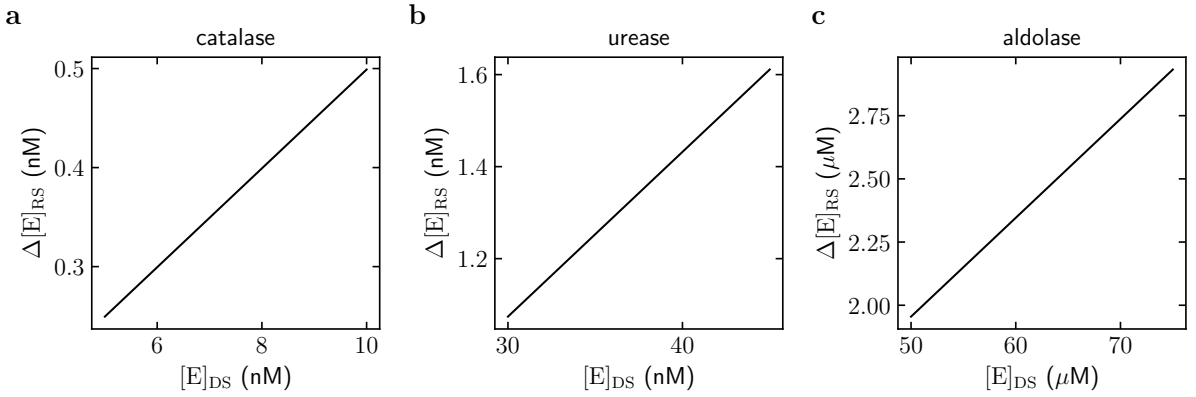

Figure 5.9: **Difference between the enzyme concentration in RS with and without substrate for enzyme concentration ensuring constant reaction rate.** Dependence of the (**a**) catalase, (**b**) urease, and (**c**) aldolase concentration in the RS outlet on its concentration in the DS inlet with and without substrate, assuming the enzyme diffusion enhancement. The substrate concentration is $1\,\mathrm{M}$. The H-cell channel length is optimized to maximize the concentration difference $\Delta\,[\mathrm{E}]_{\mathrm{RS}}$ for a given enzyme. These differences are denotes by shadowed areas.

for aldolase. Thus, highly accurate concentration measurements are required to capture the reported enhanced enzyme diffusion with H-cell measurements.

Chapter 6

Reactions under crowding

> The non-physicist finds it hard to believe that really the ordinary laws of physics, which he regards as the prototype of inviolable precision, should be based on the statistical tendency of matter to go over into disorder.
>
> Erwin Schrödinger

6.1 Literature review

Much of the scientific knowledge on biochemical reactions taking place in living systems, *e.g.*, in biological cells, comes from *in vitro* experiments. However, biologically-relevant reactions studied in test tubes may proceed differently than in their natural environment, which is crowded with various macromolecules [15, 17, 18] (Section 2.3). Although these issues are rarely covered in classical biochemistry textbooks, the attention given to them is gradually growing.

Important experiments in this field concerned the properties of hemoglobin. It was observed that the solubility of deoxy sickle hemoglobin decreases in solutions with a high concentration of other proteins [65, 232–234]. The reason for that was not a coprecipitation but rather an indirect effect of other proteins on hemoglobin precipitation equilibrium. The conclusion is then that even if some proteins do not participate in a particular reaction, they can still affect it indirectly [233].

Similar effects have been found to be omnipresent in biochemistry by multiple experiments, theories and simulations [12, 235–247] and accounting for them is now considered crucial in attempts to describe the behavior of biological systems. In the limit of ideally inert crowders acting as hard solids, the effects of macromolecular crowding on chemical reactions are solely due to entropic in origin depletion forces [59]. Depletion forces can be accounted for using statistical mechanics with scaled particle theory (SPT) [67–70] (Section 2.4); the reader is referred to classic reviews [11, 12, 14, 16–18, 248–250] for an exhaustive discussion. Below I summarize the most important conclusions.

The main effects of macromolecular crowding on the reactions involving biomacromolecules

may be summarized as follows [65]:

1. Compact, spherical conformations are favored over extended and anisotropic conformations [16, 238, 239, 242, 243, 245, 246],

2. Association processes are enhanced [12, 235–237, 240, 241, 244],

3. Reaction kinetics depends on the details of the reaction mechanism and can be enhanced or slowed down [251–255].

As a result, macromolecular crowding affects biological processes like cellular senescence [256], gene regulation [163], cell growth [257], and aggregation of synuclein into amyloid fibers observed in Parkinson's disease [244, 258, 259].

The predictions for reaction kinetics are less evident as compared to thermodynamic ones, because they depend on the details of the underlying mechanism. Slow protein association reactions, which are transition-state limited, are accelerated by macromolecular crowding, whereas diffusion-limited reactions slow down. The effect on reactions with mixed character is expected to be more complex, even involving maxima of activity with respect to the occupied volume. In the case of enzymatic reactions, the additional complexity emerges from the effect of macromolecular crowding on the structure of enzyme, *i.e.*, its conformation and oligomerization.

The crowding effects are also sensitive to the size and shape of macromolecular crowders. Smaller crowders affect the activity coefficients more significantly than large ones [94, 260]. This is explained by the fact that to occupy the same volume, a smaller number of large crowders is needed and thus the occupied volume elements are clustered together, leaving large regions of the system unoccupied. In contrast, smaller crowders tend to be more dispersed and leave much smaller cavities for macromolecules to enter. Qin *et al.* [95] observed that the flap dynamics of the HIV protease is affected more strongly by small crowders. Pastor *et al.* [254] analyzed the effect of macromolecular crowding by Dextrans of two sizes on three enzymatic reactions. They found that the reaction catalyzed by the largest enzyme considered depends not only on the total occupied volume fraction, but also on the crowder size, which is not the case for the reactions catalyzed by smaller enzymes. Gomez *et al.* [246] showed with simulations that elongated, polymeric crowders enhance protein folding more substantially than spherical crowders.

A growing body of research suggests that restricting the macromolecular crowding effects to purely entropic, excluded volume contributions is overly simplistic [149, 261, 262]. The crowders present in biological cells, such as, proteins, RNA, *etc*. (Fig. 2.4), are not inert, and thus engage in miscellaneous interactions ranging in energy from weak and transient quinary interactions [263] to stronger electrostatic and specific attractions. Moreover, in reality even the seemingly inert crowders like Ficoll, Dextran or poly(ethylene glycol) (PEG)/poly(ethylene oxide) (PEO) are complex chemical entities with various chemical groups which may interact specifically and nonspecifically (electrostatically, hydrophobically, *via* hydrogen bonding, *etc*.)

with the biomacromolecules. Thus, SPT-like theories have to be then taken with caution, as describing only the limiting behavior due to entropic interactions.

Additional complexity lies in the fact that in crowded multicomponent system such as cytoplasm, its ingredients may phase-separate and form droplets of diffrent composition and physicochemical properties [264–268]. In each of such membraneless microcompartments, the effects of macromolecular crowding may, in principle, differ.

Still, the strength of purely entropic approach exemplified by SPT lies in the fact that the part of free energy change described by it is universal, *i.e.*, independent of atomic details, and the range of predicted effects is rich. For this reason, in the following chapters, we apply it to gain new insights into the generic phenomena governing reactions upon crowding in the limit of negligible interactions between crowders and reagents. In Section 6.2, we discuss the activity change of model conformation-changing enzymes (introduced in Section 5.2) due to crowding. In Section 6.3, we explore crowding-regulated allosteric cooperativity of divalent binding.

6.2 Conformation-changing enzyme kinetics

6.2.1 Crowding-controlled reaction rate

In Michaelis-Menten kinetic model of enzymatic reaction [225], the reaction rate is proportional to the concentration of an enzyme. However, often only one particular conformation of an enzyme is catalytically active. For instance, for some conformation-changing enzymes, only enzyme in certain (open) conformations can bind a substrate and thus act as catalysts (Section 5.2). Therefore, the maximum reaction rate is proportional to the concentration of active enzymes, which in equilibrium is determined by the free energies of all possible conformations. As discussed in Section 2.4, these free energies depend, among other factors, on the macromolecular crowding.

For instance, the HIV-1 protease has two mobile flaps that cover its active site. These flaps need to open to let the substrate in and then close, and, as shown by molecular dynamics (MD) simulations, the equilibrium of flap opening is affected by macromolecular crowding [95, 269]. This effect was suggested to be responsible for the observed decrease of the HIV-1 protease activity in crowded solutions [255]. Similarly, glucose-6-phosphate dehydrogenase exists in three forms: monomeric, dimeric, and tetrameric, but only dimers are catalytically active. Macromolecular crowders affect its activity in a complex way, *e.g.*, by changing the populations of these forms [252].

We consider here enzymes with two conformations: open and closed, of which only the open one is catalytically active. To quantify the changes in the populations of open and closed states, we relate them to the values of the free energy of opening ΔF_o (Eq. 2.24):

$$\frac{p_o}{1-p_o} = \exp\left[-\beta \Delta F_o\right], \tag{6.1}$$

where $\beta = 1/k_{\mathrm{B}}T$, k_{B} is Boltzmann constant, T is temperature, p_o is fraction of open enzymes, and $1 - p_o$ is, correspondingly, the fraction of closed enzymes. The ratio of the fraction of open enzymes in crowded environment $p_o(\phi_{\mathrm{occ}})$ to the fraction of open enzymes in dilution $p_o(0)$ gives an estimate of the change in enzyme activity due to crowding $k(\phi_{\mathrm{occ}})/k(0)$. Assuming that the only effect of crowding is the population shift, we get:

$$\frac{k(\phi_{\mathrm{occ}})}{k(0)} = \frac{p_o(\phi_{\mathrm{occ}})}{p_o(0)} = \frac{\exp\left[-\beta\Delta\Delta F_o\right]}{1 - p_o(0) + p_o(0)\exp\left[-\beta\Delta\Delta F_o\right]}, \tag{6.2}$$

where $\Delta\Delta F_o = \Delta F_o(\phi_{\mathrm{occ}}) - \Delta F_o(0)$. This equation is general and depends only on the population of the open enzymes in dilution $p_o(0)$ and the free energy change induced by crowding $\Delta\Delta F_o$, which needs to be calculated in each specific case. We now use SPT to calculate $\Delta\Delta F_o$ in the case when crowding induces only entropic effects.

6.2.2 Scaled particle theory results

Assuming that all crowders are spherical and using Eq. 2.46 and Eq. 2.28, we express $\Delta\Delta F_o$ as:

$$\Delta\Delta F_o = k_{\mathrm{B}}T \sum_{k=1}^{3} h_k g^k, \tag{6.3a}$$

where function $g(\phi_{\mathrm{occ}})$ is defined in Eq. 2.42, and coefficients h_k encode the geometric features of an enzyme in the open and closed conformations (Section 2.4):

$$h_1 = \frac{3\Delta H}{a_{\mathrm{cr}}} + \frac{3\Delta S}{4\pi a_{\mathrm{cr}}^2} + \frac{3\Delta V}{4\pi a_{\mathrm{cr}}^3}; \tag{6.3b}$$

$$h_2 = \frac{9\Delta H^2}{2a_{\mathrm{cr}}^2} + \frac{9\Delta V}{4\pi a_{\mathrm{cr}}^3}; \tag{6.3c}$$

$$h_3 = \frac{9\Delta V}{4\pi a_{\mathrm{cr}}^3}. \tag{6.3d}$$

Here, for a generic variable X, $\Delta X = X_{\mathrm{o}} - X_{\mathrm{c}}$ is the difference between its value in the open and closed state.

Combining Eqs. 6.2 and 6.3 bridges the microscopic characteristics of enzymes with the macroscopic chemical kinetics measurements. Fitting experimental data to Eq. 6.2 and extracting parameters $h_{1,2,3}$ and $p_o(0)$ allows for gaining insight into the changes of enzyme conformations. To do so, at least four experimental datapoints are needed.

Equation 6.3 is general and can be simplified in some cases. For instance, for enzymes that are spherocylinders of radius a and lengths ℓ_o and ℓ_c in the open and closed states, respectively,

Eq. 6.3(b-d) simplify to [12]:

$$h_1 = \frac{3\Delta\ell}{4a_{\rm cr}}\left(1 + \frac{2a}{a_{\rm cr}} + \frac{a^2}{a_{\rm cr}^2}\right), \tag{6.4a}$$

$$h_2 = \frac{9a\Delta\ell}{4a_{\rm cr}^2}\left(1 + \frac{a}{a_{\rm cr}}\right) + \frac{9\Delta\ell^2}{32a_{\rm cr}^2}, \tag{6.4b}$$

$$h_3 = \frac{9a^2\Delta\ell}{4a_{\rm cr}^3}, \tag{6.4c}$$

where $\Delta\ell = \ell_o - \ell_c$ and $\Delta\ell^2 = \ell_o^2 - \ell_c^2$. In this case, the parameters to fit to experimental data are: $a/a_{\rm cr}$, $\Delta\ell/a_{\rm cr}$ and $\Delta\ell^2/a_{\rm cr}^2$.

Note that the activity reduction considered in our simple model is solely due to the enzyme closing caused by macromolecular crowding with inert crowders. Other effects may be at play as well, such as hindering of the enzyme's active site in the open state or change in the reagent and enzyme diffusion coefficients. We do not consider these effects in this Thesis.

6.2.3 Application to fluctuating-dumbbell model

In Section 5.2, we introduced a fluctuating-dumbbell model of size-changing enzymes, which we used in Brownian dynamics (BD) simulations to quantify the diffusion of such enzymes under various crowding conditions (Section 5.3). Here, we investigate how the activity of such enzymes is affected by macromolecular crowding. Furthermore, to check the validity of the SPT (Section 6.2.2), we compare its predictions with the results of BD simulations.

To divide enzymes into open and closed, we introduce the following criterion: an enzyme is considered open if the bead-bead separation $\ell > (\ell_o + \ell_c)/2$, and it is closed otherwise. In the dilute regime, *i.e.*, for $\phi_{\rm occ} = 0$, the fraction of open enzymes depends solely on the intramolecular potential. In the case of our model, both minima of the potential have the same depth, thus the difference in the open and closed populations stems purely from the differences in the entropy of the closed and open states, *i.e.*, $\Delta F_o = -T\Delta S_o$.

The entropy of enzyme opening may be estimated using simple geometric arguments. The number of states corresponding to the open (closed) enzyme is proportional to the surface area of a sphere of radius ℓ_o (ℓ_c). Thus, the equilibrium constant of the opening process may be approximated as:

$$\frac{p_o}{p_c} \approx \left(\frac{\ell_o}{\ell_c}\right)^2. \tag{6.5}$$

Such an estimate leads to $p_o \approx 0.84$.

Integrating the separation probability density distribution $\mathcal{P}(\ell)$, which is Boltzmann distri-

bution with the potential U (Eq. 5.1), *i.e.*:

$$p_c = \frac{\int_0^{(\ell_o+\ell_c)/2} \ell^2 \exp\left[-\beta U\left(\ell\right)\right] d\ell}{\int_0^{\infty} \ell^2 \exp\left[-\beta U\left(\ell\right)\right] d\ell}; \tag{6.6a}$$

$$p_o = \frac{\int_{(\ell_o+\ell_c)/2}^{\infty} \ell^2 \exp\left[-\beta U\left(\ell\right)\right] d\ell}{\int_0^{\infty} \ell^2 \exp\left[-\beta U\left(\ell\right)\right] d\ell}. \tag{6.6b}$$

gives $p_o = 0.83$, which is close to our simple estimate given by Eq. 6.5.

We next compared the separation probability density distributions $\mathcal{P}(\ell)$ in infinite dilution and in crowded mixtures of enzymes and passive spheres (Table 5.2). The latter were obtained by interpolating the histograms of bead separations from the BD trajectories. Results show that macromolecular crowding decreases the fraction of open enzymes (Fig. 6.1b). For the largest ϕ_{occ} used in this study ($\approx 18\%$), Eq. 6.6 yields $p_o = 0.7$, which is 84% of the dilute regime value.

Using Eq. 2.24, we computed the free energies of opening from our BD simulations (Fig. 6.1c). We compare them with the predictions of SPT, assuming that enzymes are spherocylinders of radius $a = 1\,\mathrm{nm}$ and length ℓ_c in the closed and ℓ_o in the open conformation. Thus, we used the general formula Eq. 2.44 and applied it to the case of 3 crowder types: open enzymes, closed enzymes, and passive spheres. The number of open and closed enzymes depends on ΔF_o and *vice versa*, so we solved Eq. 2.24 iteratively. The SPT curve predicts that the free energy of opening crosses 0 at $\phi_{\mathrm{occ}} \approx 25\%$, which is in the physiological range of concentrations [8]. This means that for $\phi_{\mathrm{occ}} \approx 25\%$, the enzyme population is divided evenly among open and closed enzymes.

Using the values of ΔF_o, we computed the relative rate constants of the enzymatic reaction (Eq. 6.2) from BD simulations and SPT (Fig. 6.1d). Both approaches give similar decrease in the activity upon macromolecular crowding. The SPT curve gets steeper with increase in ϕ_{occ}. and for $\phi_{\mathrm{occ}} \approx 30\%$ relative activity drops to ≈ 0.4.

In summary, we observe a reasonable agreement between the SPT and BD results, but the SPT slightly overestimates the change in the opening free energy ΔF_o and rate constant k/k_0. One reason is that in the SPT approach we approximated the dumbbells with spherocylinders, which are slightly larger. Another reason is that the SPT assumes that the excluded volumes due to individual crowders do not overlap (Eq. 2.21), which inevitably overestimates the crowding effect.

More experimental studies are needed to verify whether the assumptions of our simple model correspond to the biological reality of enzymes with their highly complex potential energy surfaces. The data available so far is insufficient to carry out the fitting to SPT [252, 255]. Apart from that, the paper on HIV-1 protease by Maximova *et al.* [255] for high ϕ_{occ} reports deviation from the Michaelis-Menten kinetics, which complicates matters even more.

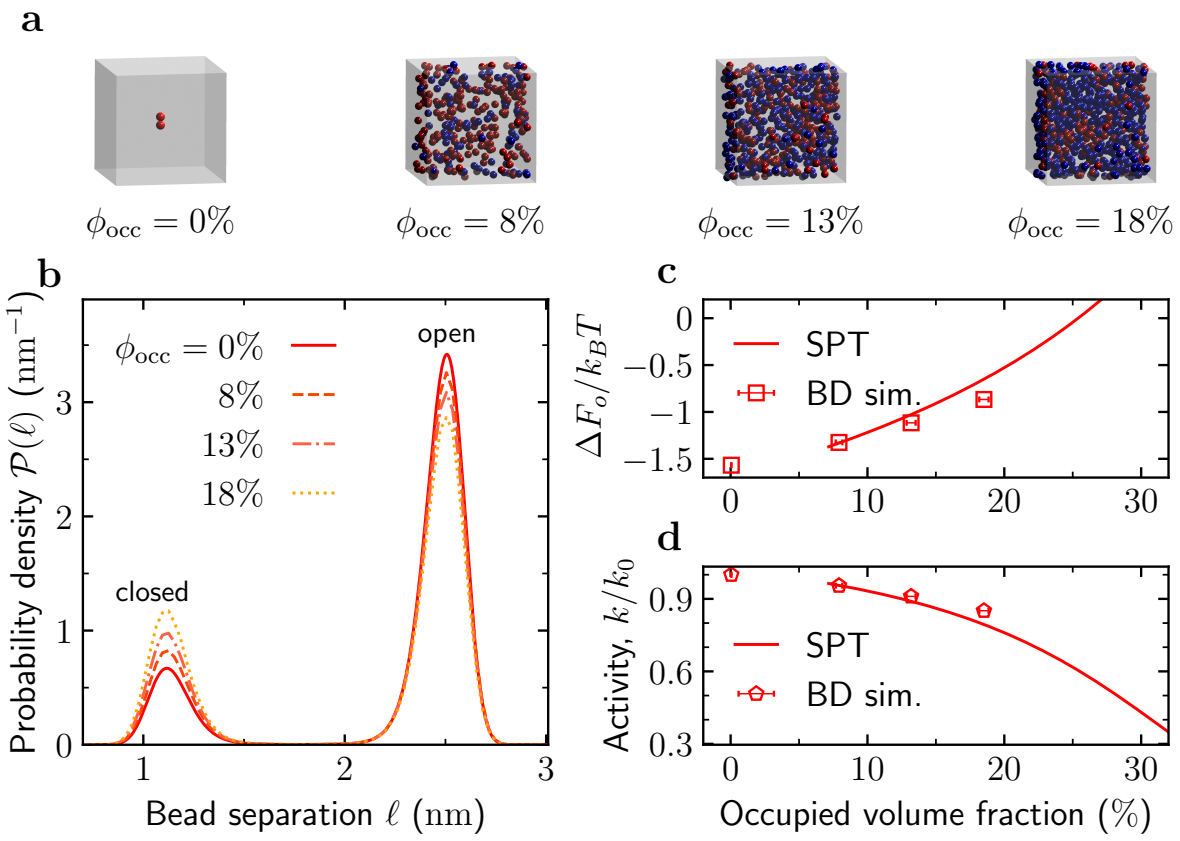

Figure 6.1: **Fluctuating-dumbbell enzyme model under macromolecular crowding.** (**a**) Snapshots of a single conformation-changing enzyme model and BD systems with the increasing concentration of passive spheres, while keeping the number of enzymes fixed. (**b**) Probability density distribution of the bead-bead separation in systems with various occupied volume fraction ϕ_{occ}. (**c**) Free energy of model enzyme opening as a function of the occupied volume fraction ϕ_{occ} computed from BD simulations based on the fraction of open enzymes. BD results (symbols) are compared with the SPT prediction (line). (**d**) Relative enzymatic reaction rate k/k_0 as a function of the occupied volume fraction ϕ_{occ} from BD simulations and SPT. The rates were computed with Eq. 6.2 based on the fraction of open enzymes in BD simulations. Figure adapted from ref. [226].

6.3 Binding of divalent molecules

Some biochemical reactions, such as binding oxygen by hemoglobin [270, 271], antigen-antibody binding [272], and condensation of intrinsically disordered proteins [273, 274], consist of multiple binding steps and are referred to as multivalent binding [275–277]. There are also attempts to artificially bind natively monovalent active sites by polymer linkers to turn them into multivalent macromolecules [66, 278, 279]. Because these reactions are multistep, the influence of crowding on them can be more difficult to predict.

To study such reactions, we consider the minimal example: a divalent binding reaction in a

form of binding of two identical monovalent molecules B to a divalent AA molecule:

$$\mathrm{AA} + \mathrm{B} \overset{K_1}{\rightleftharpoons} \mathrm{AA \cdot B}, \tag{6.7a}$$

$$\mathrm{AA \cdot B} + \mathrm{B} \overset{K_2}{\rightleftharpoons} \mathrm{AA \cdot B_2}, \tag{6.7b}$$

where K_1 and K_2 are the apparent equilibrium constants of the individual binding events. If the above binding reaction happens in an environment filled with chemically inert crowders with the volume fraction occupied by crowders ϕ_{occ}, and assuming very small concentrations of the reagents. Using Eq. 2.27, we can write:

$$K_1\left(\phi_{\mathrm{occ}}\right) = \frac{[\mathrm{AA \cdot B}]}{[\mathrm{AA}][\mathrm{B}]} = K_1\left(0\right)\frac{\gamma_{\mathrm{AA}}\gamma_{\mathrm{B}}}{\gamma_{\mathrm{AA \cdot B}}}, \tag{6.8a}$$

$$K_2\left(\phi_{\mathrm{occ}}\right) = \frac{[\mathrm{AA \cdot B_2}]}{[\mathrm{AA \cdot B}][\mathrm{B}]} = K_2\left(0\right)\frac{\gamma_{\mathrm{AA \cdot B}}\gamma_{\mathrm{B}}}{\gamma_{\mathrm{AA \cdot B_2}}}, \tag{6.8b}$$

$$K\left(\phi_{\mathrm{occ}}\right) = \frac{[\mathrm{AA \cdot B_2}]}{[\mathrm{AA}][\mathrm{B}]^2} = K\left(0\right)\frac{\gamma_{\mathrm{AA}}\gamma_{\mathrm{B}}{}^2}{\gamma_{\mathrm{AA \cdot B_2}}}, \tag{6.8c}$$

where γ_i and $[i]$ are the activity coefficient and the equilibrium concentration of i-th species, respectively (Section 2.4).

6.3.1 Binding cooperativity

Some multivalent binding reactions proceed in such a way, that each consecutive binding step is promoted by the previous ones. Such reactions are called cooperative [275, 276, 280]. Thermodynamically, it means that the equilibrium constants fulfill the following inequality: $K_1 < K_2 < ....$ As a result, for a strongly cooperative system at equilibrium, the intermediate complexes are scarce, and the population of macromolecules is either completely unbound or completely bound. Transition between these two states due to changes in some external parameters, *e.g.*, temperature, pressure, salt or ligand concentration, is sharp. Thus, the cooperative systems exhibit "all-or-nothing" or "on-off" behavior.

One distinguishes two mechanisms of cooperativity [275, 276]:

1. Allosteric – binding of a monovalent ligand to one site enhances the affinity of a separate ligand molecule for binding at another site.

2. Chelate – binding of a multivalent ligand to one site spatially constrains the ligand's remaining sites to the vicinity of their respective partner sites.

In contrast to allosteric cooperativity, chelate cooperativity depends on the ligand concentration, *i.e.*, for very high concentrations of the ligands, the concentration of completely bound

complexes drops, rendering the system "off-on-off" rather than "on-off" [276].

On the one hand, the mere presence of inert crowders may shift the equilibrium constants in the direction of more compact entities. On the other hand, ligand binding may expand [281, 282] or contract [222, 283–291] the multivalent macromolecule, depending on the specific reaction. Thus, the change in the AA size upon consecutive binding events may affect and even cause the binding cooperativity.

For the reaction defined in Eq. 6.7, the cooperativety may be quantified with the cooperativity parameter α defined as [275]:

$$\alpha = \frac{K_2}{K_1} = \frac{{\gamma_{\mathrm{AA\cdot B}}}^2}{\gamma_{\mathrm{AA}}\gamma_{\mathrm{AA\cdot B_2}}}\alpha_0, \tag{6.9}$$

where α_0 is the cooperativity parameter with no crowders ($\phi_{\mathrm{occ}} = 0$). We speak of cooperative binding when $\alpha > 1$, anticooperative binding when $\alpha < 1$, and noncooperative binding when $\alpha = 1$. Note that α can be viewed as the equilibrium constant of the following reaction:

$$2\,\mathrm{AA\cdot B} \rightleftharpoons \mathrm{AA\cdot B_2} + \mathrm{AA}. \tag{6.10}$$

Note also that the cooperativity parameter does not depend on the activity coefficient γ_{B} of species B, as this specie does not appear explicitly in Eq. 6.10.

Computing α is beyond the scope of this Thesis. Instead, we focus on the ratio α/α_0, which quantifies the change of cooperativity parameter induced by macromolecular crowding. In Section 6.3.2, we discuss the results obtained with the SPT for simplistic, spherical models of macromolecules (Section 2.4). In Section 6.3.3, we explore the results for bead chains investigated using BD simulations and Monte Carlo (MC) integration (Section 3.3).

6.3.2 Scaled particle theory

For simplicity, we assume that all crowders are spheres of the same radius a_{cr} and AA, AA $\cdot$ B, AA $\cdot$ B$_2$ are spheres of radii a_0, $a_1 = a_0 + \delta a_1$, and $a_2 = a_0 + \delta a_1 + \delta a_2$, respectively. In crowded environments, using Eqs. 2.47 and 6.9, we obtain the expression for the cooperativity parameter:

$$\begin{aligned}\ln\frac{\alpha}{\alpha_0} &= 2\ln\gamma_{\mathrm{AA\cdot B}} - \ln\gamma_{\mathrm{AA\cdot B_2}} - \ln\gamma_{\mathrm{AA}} \\ &= -g\left(\frac{3\Delta a}{a_{\mathrm{cr}}} + \frac{3\Delta a^2}{a_{\mathrm{cr}}^2} + \frac{\Delta a^3}{a_{\mathrm{cr}}^3}\right) - \frac{g^2}{2}\left(\frac{9\Delta a^2}{a_{\mathrm{cr}}^2} + \frac{6\Delta a^3}{a_{\mathrm{cr}}^3}\right) - 3g^3\frac{\Delta a^3}{a_{\mathrm{cr}}^3};\end{aligned} \tag{6.11a}$$

where:

$$\Delta X = X_{\mathrm{AA\cdot B_2}} + X_{\mathrm{AA}} - 2X_{\mathrm{AA\cdot B}} \tag{6.11b}$$

with ($X \in \{a, a^2, a^3\}$).

The ratio α/α_0 depends on four parameters: a_0/a_{cr}, $\delta a_1/a_0$, $\delta a_2/a_0$ and ϕ_{occ}. Figure 6.2 shows two-dimensional color maps of $\log_{10}\alpha/\alpha_0$ obtained with Eq. 6.11 for $\phi_{\mathrm{occ}} = 10$ and 40%. In Fig. 6.2a,b crowders are assumed to have radius $a_{\mathrm{cr}} = a_0$. Both maps are similar and may be divided into three distinct regions. The diagonal region ($\delta a_1 \approx \delta a_2$) represents a monotonic change in the size of the macromolecule, *i.e.*, either contraction or expansion in both steps of the binding. In this part of the plot, the cooperativity remains virtually unchanged. The top-left region represents a contraction-expansion behavior – AA contracts upon binding a first B and then expands after binding a second one. In this case, the cooperativity decreases. Finally, the bottom-right region represents an expansion-contraction behavior – AA expands upon binding first B and then contracts after binding a second one. Here, the model predicts an increase in cooperativity. The magnitude of the predicted changes grows with the occupied volume fraction ϕ_{occ}. For physiologically-relevant $\phi_{\mathrm{occ}} = 40\%$. the SPT predicts cooperativity change of up to a few orders of magnitude for size changes $\delta a_1 = -\delta a_2 = \pm 0.2 a_0$.

Figure 6.2c,d and Fig. 6.2e,f show the results for crowders smaller and larger than the reagents, respectively. The magnitude of the predicted changes increases drastically with the increase in the reagent-to-crowder size ratio a_0/a_{cr}. This means that α becomes more sensitive to the macromolecular crowding when the reactive macromolecules are larger than inert crowders. When the crowders are larger than the reagents, *i.e.*, $a_0/a_{\mathrm{cr}} = 0.5$, even for ϕ_{occ} as high as 40%, the cooperativity changes less than two orders of magnitude for $\delta a_1 = -\delta a_2 = \pm 0.2 a_0$. For $a_0/a_{\mathrm{cr}} = 2$, the change exceeds two orders of magnitude even for $\phi_{\mathrm{occ}} = 5\%$.

6.3.3 Polymer-based models

Polymer bead chains are simplistic models of macromolecules, in which end-to-end connections may represent folding of protein or single-stranded DNA [292]. We used such simple models to mimick the expansion-contraction behavior, which is predicted by SPT to yield large crowding-induced increase in cooperativity (Section 6.3.2). We modeled AA, AA · B and AA · B_2 as linear or cyclic polymer chains of n beads, with $1 \leq n \leq 32$ ($3 \leq n \leq 32$ for rings). Cyclic chains are more compact, and thus transformation from linear to cyclic structures mimicks the contraction behavior, and *vice versa*: transformation from cyclic to linear mimicks expansion.

6.3.3.1 Details of calculations

To calculate the cooperativity parameters, we needed the activity coefficients γ_i of bead chains and rings in various crowded environments. To obtain them, we combined three approaches:

1. BD simulations (Section 3.1), from which we obtain representative samples of bead chain conformation distribution,

2. BD simulations, from which we obtain configurations of crowders,

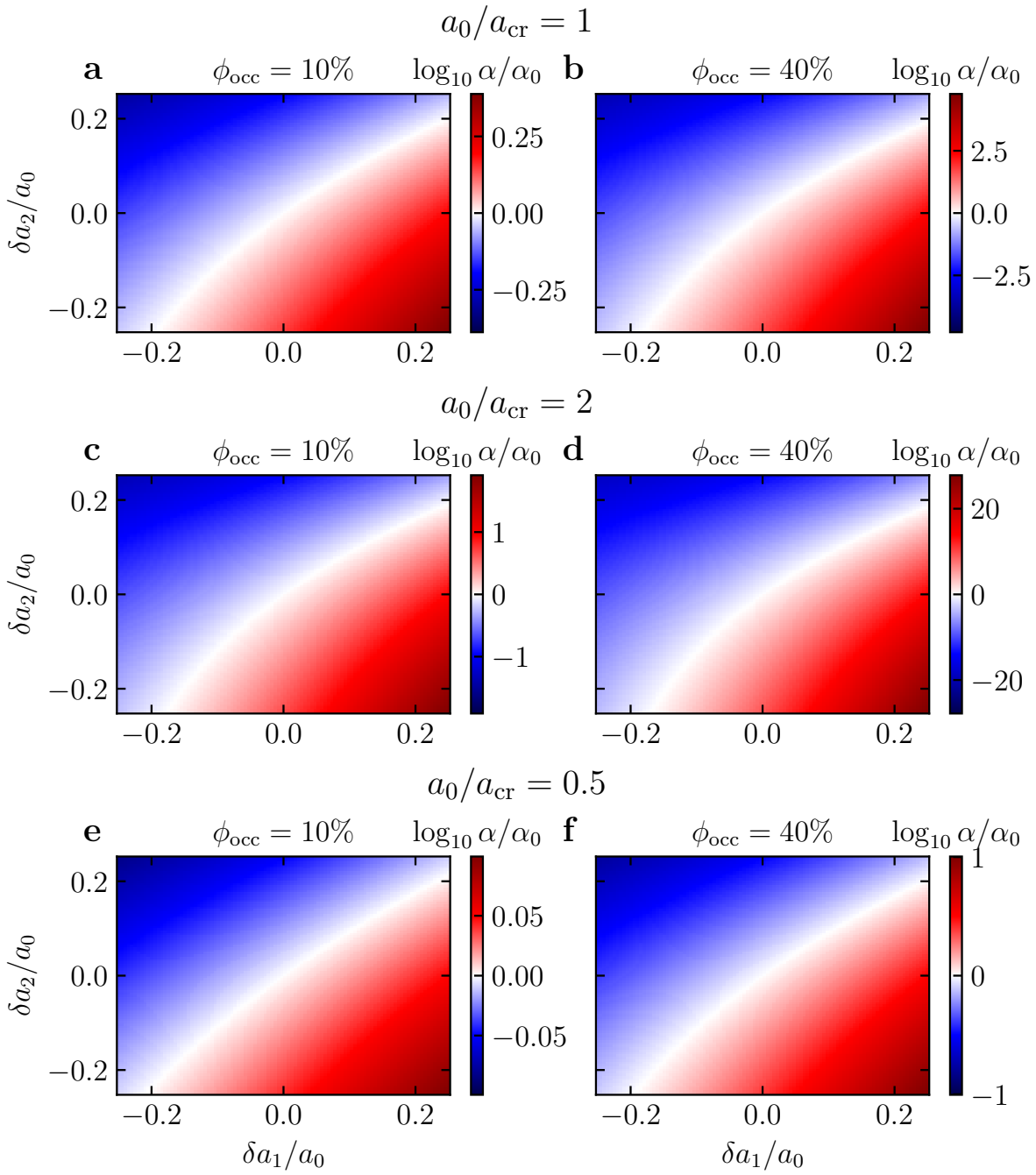

Figure 6.2: **Cooperativity of divalent binding from SPT.** Heat maps of decimal logarithm of α/α_0 plotted in the plane of $\delta a_1/a_0$ and $\delta a_2/a_0$ for: (**a,b**) crowders and reagents of equal size ($a_0/a_{\mathrm{cr}} = 1$), (**c,d**) crowders smaller than reagents ($a_0/a_{\mathrm{cr}} = 2$), (**e,f**) crowders larger than reagents ($a_0/a_{\mathrm{cr}} = 0.5$), and occupied volume fraction (**a,c,e**) $\phi_{\mathrm{occ}} = 10\%$; (**b,d,f**) $\phi_{\mathrm{occ}} = 40\%$.

3. Integration of Eq. 2.36 which we perform with MC method (Eq. 3.17), from which we obtain the activity coefficient of a given bead chain in a given crowded environment.

To gather a representative sample of the polymer chains' Boltzmann distribution, we performed BD simulations with a custom `pyBrown` software (Appendix D.2). We set the bead radius to $a_{\mathrm{bead}} = 1\,\mathrm{nm}$ and connected the neighbouring beads with a harmonic potential of force

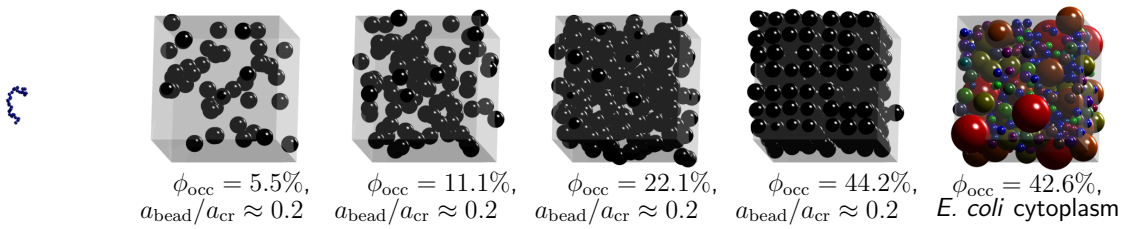

Figure 6.3: **Crowded systems used in MC calculations of activity coefficients.** The linear chain for $n = 32$ is presented to show its size relative to the size of crowders and simulation boxes.

constant $k_r = 1000\,\mathrm{kcal\,mol^{-1}\,nm^{-2}}$ and equilibrium distance $r_{\mathrm{eq}} = 2a_{\mathrm{bead}}$. Only bound beads could overlap with each other; unbound beads interact *via* a hard-sphere potential (Eq. A.6). The positions of beads were propagated using the forward Euler method (Eq. A.1). We neglected hydrodynamic interactions between beads, as they do not affect the equilibrium distribution [75]. Thus, the diffusion matrix $\boldsymbol{D}$ was diagonal, with entries given by the Stokes-Sutherland-Einstein (SSE) relation (Eq. 2.10). The hard sphere potential was taken into account by repeating steps which lead to an overlap of unconnected beads.

We placed the bead chains in a cubic box of $75\,\mathrm{nm} \times 75\,\mathrm{nm} \times 75\,\mathrm{nm}$ and applied periodic boundary conditions in all three directions. Simulations lasted for $20\,\mu\mathrm{s}$. The temperature T was set to $293.15\,\mathrm{K}$, and dynamic viscosity to $\eta = 1.005\,\mathrm{cP}$.

In separate BD simulations, chemically inert crowders were modeled as hard spheres of $a_{\mathrm{cr}} = 5.1\,\mathrm{nm}$, corresponding to Ficoll70, a typical artificial crowder. We consider systems with occupied volume fraction $\phi_{\mathrm{occ}} = 5.5$, 11.1, 22.1 and 44.2%. In addition, we considered heterogeneous *Escherichia coli* cytoplasm model of $\phi_{\mathrm{occ}} = 42.6\%$, taken from ref. [36]. A few snapshots from BD simulations of crowders are shown in Fig. 6.3. To gather configurations of crowders, we used the results from Section 4.2, with additional results for system of $\phi_{\mathrm{occ}} = 42.6\%$ and cytoplasm model obtained with the same BD setup.

We performed MC integration with a custom `ExVol` software (Appendix D.4). In MC insertions, each complex i was represented by 10000 Boltzmann-distributed conformations and inserted into 10000 (10 for $\phi_{\mathrm{occ}} = 44.2\%$) different configurations of the crowded box. 5000 insertions were performed for each of 10000 chain-box pairs. Uncertainties in γ_i^{-1} and $\phi_{\mathrm{ex},i}$ were computed based on these 10000 independent values as the standard error of the mean, and then propagated into uncertainties of the cooperativity parameters α/α_0.

6.3.3.2 Gyration radii

To connect the polymer bead simulations with the SPT results, we first computed the gyration radii R_g of various bead chains. The gyration radii of the analyzed structures were obtained

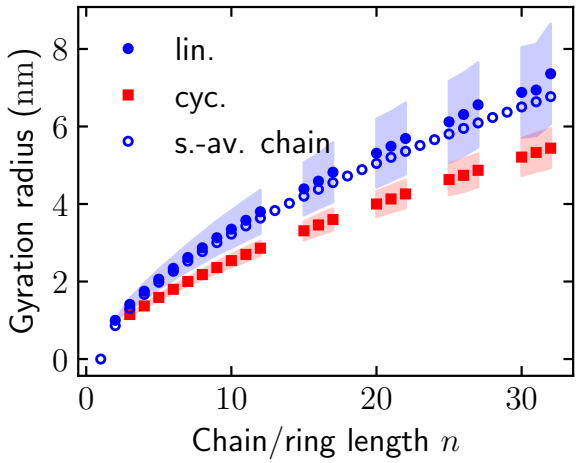

Figure 6.4: **Gyration radii of linear and cyclic bead chains from BD simulations.** Dependence of the gyration radius on the numer of beads constituting a linear (blue) and cyclic (red) chain. The shadowed areas denote the standard deviation. Empty symbols are the results for a self-avoiding random walk [293, 294].

from BD trajectories using the following formula:

$$R_g = \sqrt{\frac{1}{n}\sum_{j=1}^{n}\left(\boldsymbol{r}_j - \langle \boldsymbol{r} \rangle\right)^T \left(\boldsymbol{r}_j - \langle \boldsymbol{r} \rangle\right)}, \tag{6.12}$$

where n is a number of beads that make up the chain, $\boldsymbol{r}_i$ is a position of i-th bead, and $\langle \boldsymbol{r} \rangle$ is an average of $\boldsymbol{r}_i$. We see that the larger the chain length n, the larger the contraction of the cyclic molecule as compared to the linear one of the similar size (Fig. 6.4). The gyration radii of the linear chains are in reasonable agreement with the results of three-dimensional self-avoiding random walk on a BCC lattice [293, 294]:

$$R_g = \sqrt{0.186 r_{\mathrm{eq}}^2 (n-1)^{6/5}}, \tag{6.13}$$

where r_{eq} is a bond length.

6.3.3.3 Activity coefficients

The volumes excluded to the bead chains $\phi_{\mathrm{ex},i}$ and corresponding activity coefficients γ_i computed with Eq. 3.17 are shown in Fig. 6.5. Both $\phi_{\mathrm{ex},i}$ and γ_i increase with ϕ_{occ} and chain length n and are larger for the linear chain than for the ring chain of the same length, in accordance with the behavior of gyration radii (Fig. 6.4). The slope of $\phi_{\mathrm{ex},i}$ decreases, reflecting the fact that the volumes excluded by individual crowders start to overlap. Activity coefficients γ_i increase exponentially with the chain length. Interestingly, we observe a crossing of $\phi_{\mathrm{ex},i}$ and γ_i curves as functions of the AA length for homegeneous system with $\phi_{\mathrm{occ}} = 44.2\%$ and heterogeneous cytoplasm model with similar ϕ_{occ}. Shorter chains are excluded more strongly from

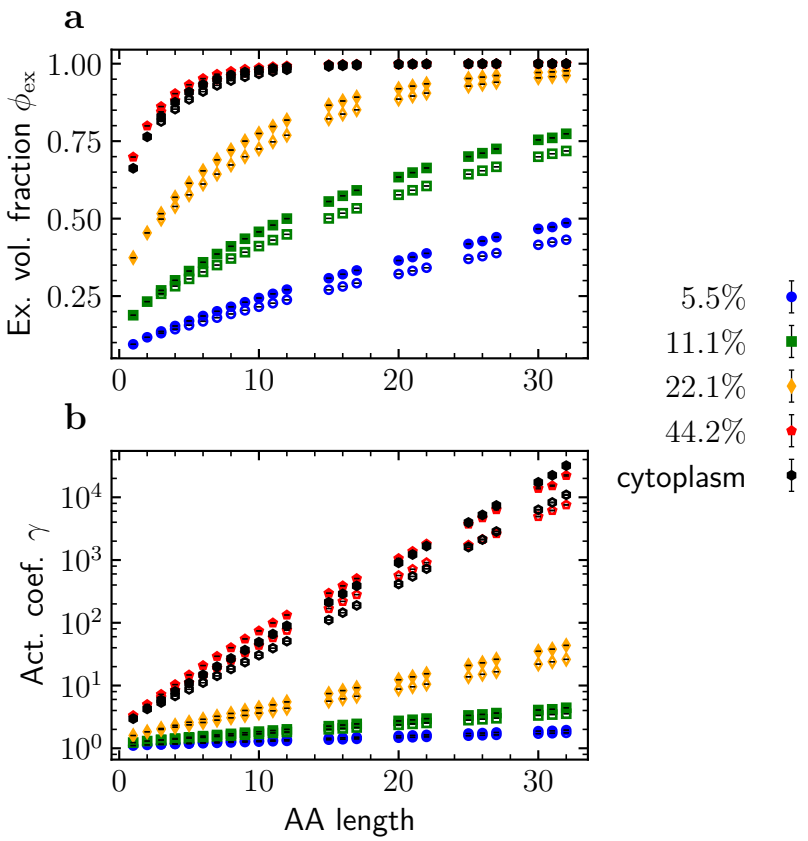

Figure 6.5: **Volumes excluded to bead chains of increasing length and the resulting activity coefficients from MC integration.** (**a**) Excluded volume $\phi_{\mathrm{ex},i}$ computed with MC integration of Eq. 2.36 by inserting bead chains of length n to crowded systems shown in Fig. 6.3. (**b**) Activity coefficients γ_i calculated using Eq. 2.39. The solid symbols denote the values for linear chains, and empty – for cyclic ones.

the homogeneous systems, whereas longer – from the heterogeneous systems.

6.3.3.4 Cooperativity

Chains and rings of various sizes n can be attributed to AA, AA $\cdot$ B and AA $\cdot$ B$_2$ reagents (Eq. 6.7). We consider two models:

1. *Model 1:* AA is an n-bead chain, AA $\cdot$ B is an $n+1$-bead chain, and AA $\cdot$ B$_2$ is an $n+2$-bead ring, that is AA expands upon binding a first B and contracts upon binding a second B.

2. *Model 2:* AA is an n-bead ring, AA $\cdot$ B is an $n+1$-bead chain, and AA $\cdot$ B$_2$ is an $n+2$-bead ring, that is AA unfolds upon binding a first B and folds back into a ring when binding a second B.

The resulting cooperativity parameters are shown in Figs. 6.6 and 6.7. We observe the increase of α/α_0 with the increase of the AA length, reflecting the trend of the gyration radius difference

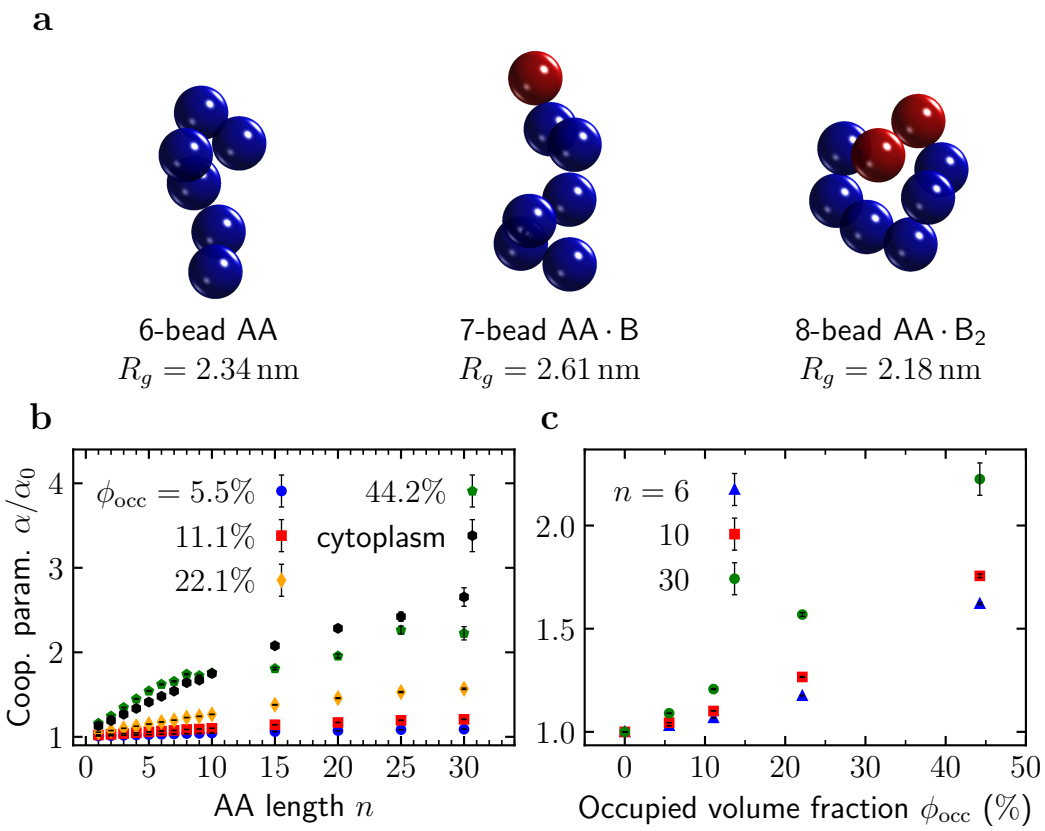

Figure 6.6: **Cooperativity for n-chain:$n+1$-chain:$n+2$-ring model.** (**a**) Bead-chain models of macromolecules involved in the divalent binding reaction. Example AA (AA · B) consist of 6 (7) identical spherical beads of radius 1 nm. The final product AA · B$_2$ is an 8-bead ring. Gyration radii R_g of the respective polymers are provided below their structures. (**b**) Dependence of cooperativity parameter α/α_0 on the number of beads n in the chain. (**c**) Dependence of cooperativity parameter α/α_0 on occupied volume fraction ϕ_{occ}.

between the linear and cyclic chains (Fig. 6.4). Yet, the increase of α/α_0 for a given crowder size is not as high as predicted by the SPT for spherical models (Fig. 6.2). For a given n, the cooperativity increases with the occupied volume fraction ϕ_{occ}. The increase in Model 2 (Fig. 6.7) is more substantial than in Model 1 (Fig. 6.6), owing to smaller, cyclic AA in Model 2.

With the values of $\gamma_i = 1/(1-\phi_{\mathrm{ex},i})$ for linear and cyclic chains, one can construct other models, in addition to the two discussed in this section. In Table 6.1, we present the excluded volumes for all studied polymer chains.

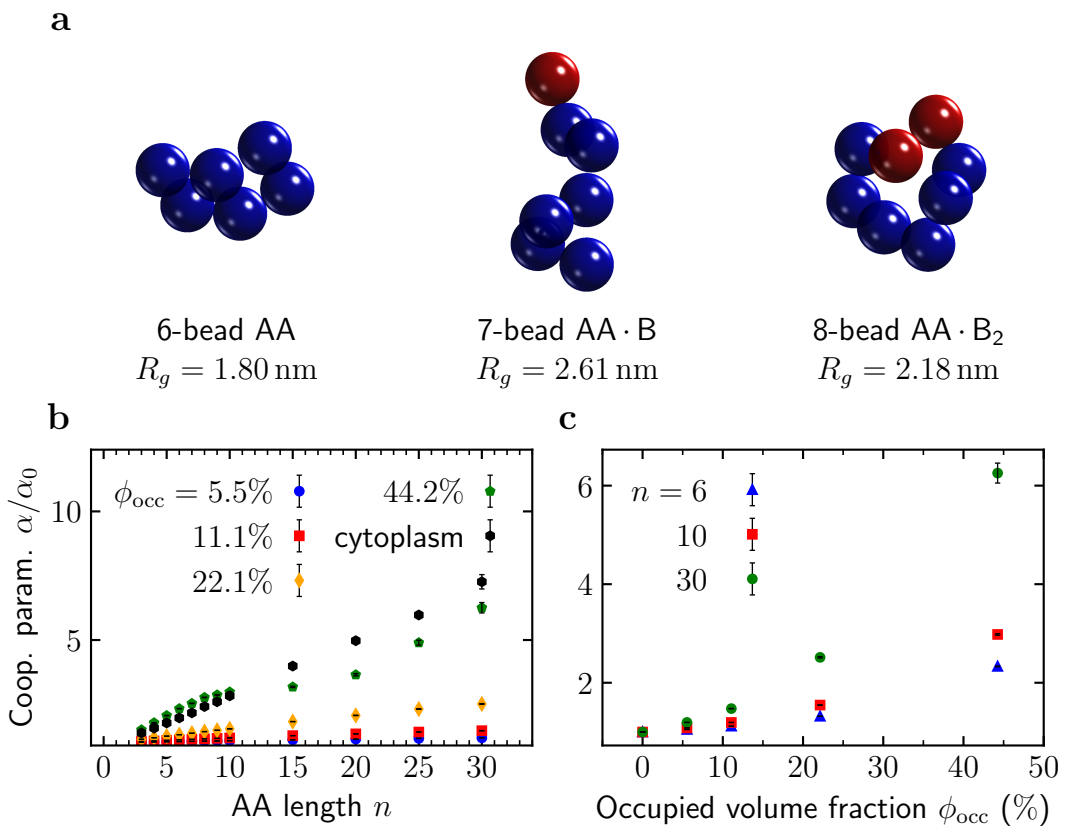

Figure 6.7: **Coperativity for n-ring:$n+1$-chain:$n+2$-ring model.** (**a**) Bead-chain models of macromolecules involved in the divalent binding reaction. Example AA (AA · B) ring (chain) consist of 6 (7) identical spherical beads of radius 1 nm. The final product AA · B$_2$ is an 8-bead ring. Gyration radii R_g of the respective polymers are provided below their structures. (**b**) Dependence of cooperativity parameter α/α_0 on the number of beads n in the chain. (**c**) Dependence of cooperativity parameter α/α_0 on occupied volume fraction ϕ_{occ}.

Table 6.1: **Volumes excluded to linear and cyclic bead chains in various crowded systems from MC integration.** These values are plotted in Fig. 6.5a.

n	$\phi_{\text{occ}} = 5.5\%$		$\phi_{\text{occ}} = 11.1\%$		$\phi_{\text{occ}} = 22.1\%$		$\phi_{\text{occ}} = 44.2\%$		cytoplasm	
	linear	ring	linear	ring	linear	ring	linear	ring	linear	ring
1	0.09445	–	0.18830	–	0.37392	–	0.69873	–	0.66240	–
2	0.11703	–	0.23219	–	0.45400	–	0.79936	–	0.76398	–
3	0.13598	0.13024	0.26831	0.25757	0.51614	0.49824	0.86166	0.84499	0.82955	0.81338
4	0.15350	0.14314	0.30078	0.28189	0.56866	0.53920	0.90345	0.88120	0.87550	0.85324
5	0.16989	0.15572	0.33071	0.30554	0.61412	0.57691	0.93215	0.90924	0.90842	0.88479
6	0.18573	0.16828	0.35898	0.32811	0.65430	0.61169	0.95197	0.93092	0.93249	0.90997
7	0.20090	0.18035	0.38568	0.35014	0.68995	0.64362	0.96574	0.94755	0.95009	0.92976
8	0.21549	0.19240	0.41051	0.37128	0.72123	0.67320	0.97507	0.96038	0.96292	0.94543
9	0.23018	0.20395	0.43508	0.39159	0.75009	0.70004	0.98192	0.96994	0.97272	0.95755
10	0.24369	0.21553	0.45733	0.41137	0.77481	0.72480	0.98654	0.97716	0.97963	0.96706
11	0.25724	0.22698	0.47894	0.43075	0.79726	0.74795	0.98995	0.98273	0.98487	0.97458
12	0.27088	0.23804	0.50006	0.44914	0.81795	0.76891	0.99248	0.98683	0.98880	0.98034
15	0.30758	0.27036	0.55519	0.50065	0.86584	0.82200	0.99662	0.99407	0.99529	0.99096
16	0.32041	0.28111	0.57374	0.51733	0.87969	0.83729	0.99742	0.99543	0.99654	0.99310
17	0.33277	0.29156	0.59113	0.53319	0.89195	0.85122	0.99803	0.99644	0.99742	0.99471
20	0.36477	0.32126	0.63389	0.57689	0.91933	0.88556	0.99905	0.99824	0.99889	0.99759
21	0.37583	0.33141	0.64854	0.59146	0.92748	0.89559	0.99927	0.99860	0.99918	0.99817
22	0.38776	0.34160	0.66348	0.60537	0.93527	0.90493	0.99944	0.99890	0.99940	0.99862
25	0.41824	0.36989	0.70028	0.64330	0.95214	0.92749	0.99973	0.99942	0.99975	0.99938
26	0.42756	0.37885	0.71111	0.65466	0.95662	0.93364	0.99979	0.99953	0.99981	0.99953
27	0.44010	0.38874	0.72503	0.66721	0.96177	0.93986	0.99984	0.99962	0.99986	0.99965
30	0.46696	0.41545	0.75430	0.69970	0.97153	0.95435	0.99993	0.99980	0.99994	0.99984
31	0.47286	0.42387	0.76061	0.70942	0.97363	0.95824	0.99993	0.99984	0.99996	0.99988
32	0.48618	0.43174	0.77381	0.71842	0.97706	0.96168	0.99996	0.99987	0.99997	0.99991

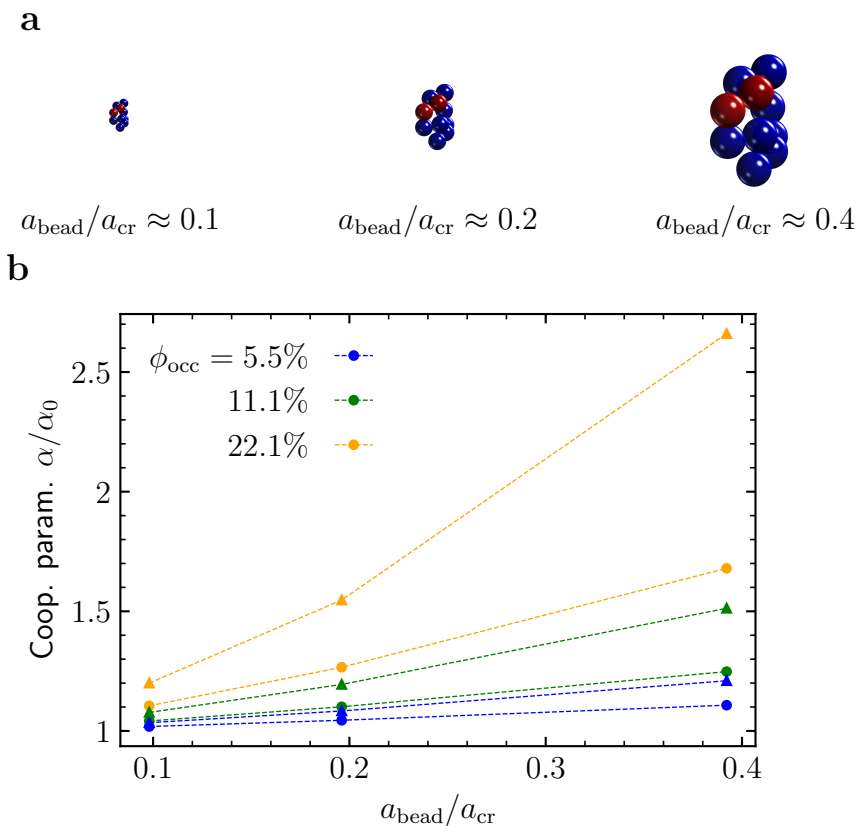

Figure 6.8: **Crowder-size effect on the crowding-regulated cooperativity from MC integration.** (**a**) Bead-chain models of an example macromolecule involved in the divalent binding reaction upscaled and downscaled two times. (**b**) Various symbols denote the cooperativity parameter α/α_0 for Model 1 (circle) and Model 2 (triangle) for $n = 10$. Lines on the plot serve only as a guide to the eye.

6.3.3.5 Crowder-size effect

To study how the crowder-size affects the cooperativity, we used the conformations of bead chains participating in the binding reaction for $n = 10$. We sampled them from exactly the same BD trajectories as above, but we rescaled their sizes prior to each insertion. The results for upscaling and downscaling 2 times are shown in Fig. 6.8. Similarly as predicted by the SPT (Section 6.3.2), the cooperativity changes are higher in systems with small crowders in both considered reaction models. Moreover, Model 2 is more sensitive to the change of crowder size than model 1.

6.3.4 Concluding remarks

Our SPT and MC results show that the change in cooperativity of divalent binding reactions depends on conformational changes at each binding step. If the size of the AA divalent molecule increases upon binding a first B and decreases upon binding a second B, then the cooperativity increases. Moreover, crowding can induce the cooperativity of originally noncooperative or

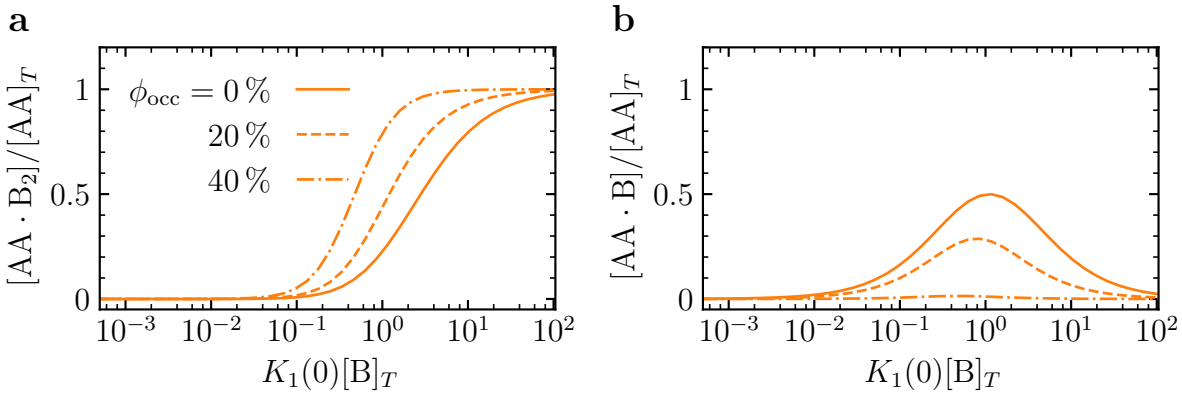

Figure 6.9: **Effect of the macromolecular crowding on the equilibrium of divalent binding reactions.** Dependence of (**a**) $[\mathrm{AA}\cdot\mathrm{B}_2]$ and (**b**) $[\mathrm{AA}\cdot\mathrm{B}]$ on the concentration of B at constant $[\mathrm{B}]_T/[\mathrm{AA}]_T = 10$ for occupied volume fraction $\phi_{\mathrm{occ}} = 0$, 20, and 40%. $\delta a_1/a_0 = -\delta a_2/a_0 = 0.1$ and $a_0/a_{\mathrm{cr}} = 1.18$. The cooperativity parameter α/α_0 was computed using SPT.

anticooperative reactions.

Although neither the SPT nor MC method used in this section accounts for the enthalpic component of the crowder-reagent interactions, they can still capture noteworthy and generic physical phenomena in biological systems. For instance, Grimaldo *et al.* [295] showed experimentally that the diffusion of small proteins is slowed down less in heterogeneously than in homogeneously crowded systems, and, *vice versa*, the diffusion of large proteins is slowed down more in systems with polydisperse crowders. We observe a similar behavior of the volume excluded to the bead chains $\phi_{\mathrm{ex},i}$. Shorter chains have larger $\phi_{\mathrm{ex},i}$ in homogeneous systems and longer – in heterogeneous ones (Fig. 6.5 and Table 6.1). This behavior seems important in the context of highly heterogeneous, intracellular environments.

The equilibria of the divalent binding reactions were extensively studied by Janssen *et al.* [277]. The authors developed an analytical model describing their dependence on equilibrium constants K_1 and K_2 and the total concentrations $[\mathrm{AA}]_T = [\mathrm{AA}] + [\mathrm{AA}\cdot\mathrm{B}] + [\mathrm{AA}\cdot\mathrm{B}_2]$ and $[\mathrm{B}]_T = [\mathrm{B}] + [\mathrm{AA}\cdot\mathrm{B}] + 2[\mathrm{AA}\cdot\mathrm{B}_2]$. Our results discussed in Sections 6.3.2 and 6.3.3 enable one to include macromolecular crowding as an additional parameter in that model. To illustrate its role, we calculated the equilibrium concentrations in the process of diluting AA and B at constant $[\mathrm{B}]_T/[\mathrm{AA}]_T$, accounting for crowding effects *via* SPT (Eqs. 2.47 and 6.8), assuming that crowders and reagents are spheres, $\delta a_1/a_0 = -\delta a_2/a_0 = 0.1$, and $a_0/a_{\mathrm{cr}} = 1.18$. The curve denoting $\mathrm{AA}\cdot\mathrm{B}_2$ concentration gets steeper with increasing the occupied volume fraction ϕ_{occ}, which is a hallmark of cooperativity (Fig. 6.9a). Furthermore, the bell-shaped maximum of $[\mathrm{AA}\cdot\mathrm{B}]$ gradually vanishes with increasing ϕ_{occ} (Fig. 6.9b).

In an influential review paper, Whitty [280] concluded that "cooperativity is a key organizing principle in chemistry and biology without which the complex molecular systems required for life could not function". Thus, understanding the processes that lead to gaining or losing that feature in biological environments is vital to get physical insight into the "on-off"-behaving sys-

tems in living organisms. The results presented in this Section are a small step in that direction, which, we hope, motivate further theoretical and experimental work.

Chapter 7

Conclusions

> So [easy to understand] are all truths, once they are discovered; the point is in being able to discover them.
>
> Galileo Galilei

The goal of this Thesis was to investigate the generic effects of macromolecular crowding on diffusion, chemical equilibria, and reaction rates. To do that, we applied relatively simple, coarse-grained models and approaches such as Brownian dynamics (BD), Stokesian dynamics (SD), and scaled particle theory (SPT).

On the one hand, as pointed out by Elcock [262], we are reaching the limit of what simple theories can produce in the field of cell biophysics. These theories usually provide intuitions that qualitatively agree with the experimental observations, but quantitative agreement is out of their reach. Sometimes there is even no qualitative agreement. As we enter the exascale computing era, we are tempted to focus on large-scale multimillion-atom simulations and leave the "spherical cows" behind.

On the other hand, as shown in this Thesis, there are still many phenomena that can be approached with simple models, keeping the number of particles and parameters involved relatively small and focusing on generic effects. Below, I present a brief summary of the main results of this Thesis.

Simulations with only far-field hydrodynamic interactions overestimate the diffusion coefficients in crowded environments. Hydrodynamic interactions, which arise due to fluid flow induced by moving particles, are considered one of the main factors determining diffusion coefficients in crowded environments [36]. It was previously claimed that the standard approach of considering only far-field (long-range) hydrodynamic interactions breaks down in crowded environments, where the average distance between macromolecules becomes comparable to their sizes [10, 77]. However, the quantitative description of that breakdown was missing. Using coarse-grained BD and SD simulations, we showed that such an approximation significantly overestimates the diffusion coefficients in crowded hard-sphere systems to such an extent that not accounting for hydrodynamic interactions at all gives better results (Fig. 4.4). However, the

far-field hydrodynamic interactions are essential to correctly describe the diffusion of structures composed of many beads connected with harmonic bonds (Fig. 4.7). Although it is well known how to systematically correct for near-field hydrodynamic interactions of hard spheres, it is not clear whether this computationally demanding procedure will systematically improve the description of biomacromolecules that, in fact, are neither entirely hard nor spherical.

Elongated crowders slow down diffusion more substantially than spherical ones. Although the dependence of diffusion on the occupied volume in systems of spherical particles is well understood (Sections 4.1.3 and 4.1.4), relatively little is known about this behavior in the case of nonspherical crowding agents. Since the shapes of the macromolecules crowding living cells are diverse, for instance, triangular (aspartate carbamoyltransferase), V-shaped (tRNA), and elongated (tyrosyl-tRNA synthetase), the knowledge of how the crowder shape affects diffusion is of great importance. Using BD simulations, we showed that elongated crowders hinder the diffusion of spherical particles more effectively than spherical crowders at the same occupied volume (Fig. 4.10), which qualitatively agrees with the fluorescence correlation spectroscopy (FCS) results (Fig. 4.5). However, the effect observed in the FCS experiment is much stronger. Thus, we hypothesized that some hitherto unknown attractive interactions between the tracer used experimentally (streptavidin) and dsDNA crowder might account for these differences (Section 4.4). In contrast to artificial crowders, protein crowders engage in a multitude of interactions and thus hinder diffusion to a larger extent (Section 4.1.6), and it may apply to nucleic acid crowders as well. In the future, a more comprehensive analysis, *e.g.*, varying radius and aspect ratio of elongated crowders and the treatment of near-field hydrodynamic interactions (here only far-field), may be crucial to develop a complete physical picture of the shape effects in crowded systems.

Soft crowders generally slow down diffusion less effectively, but not for elongated tracers. Not all macromolecules are well described by hard-sphere models. For instance, Dextran particles can allegedly entangle their chains and partially overlap at a certain energy cost [187]. To investigate the consequences of this fact, we performed BD simulations of the mixtures composed of macromolecules of various softness (Section 4.5). We modeled softness with a more expanded and less steep potential and singled out its effect by deliberately constructing the soft particles to effectively occupy the same volume as the hard crowders. In mixtures of hard and soft spherical particles of various compositions, the latter diffuse faster and hinder diffusion to a lesser extent (Fig. 4.15), which coincides with the soft crowders excluding less volume. Surprisingly, however, we found an opposite relation for dsDNA-like elongated bead-chain tracers in the same hard-soft mixtures, *i.e.*, such tracers diffuse faster in hard crowders than in soft ones (Fig. 4.17). We related this behavior to the volume excluded to them, as it is higher in soft than in hard particle systems. Artificial crowders, frequently used in *in vitro* experiments, are polymers that can interact more softly than biomacromolecules. In the future, understanding these differences even better can help avoid prematurely translating the results of experiments with artificial crowders into intracellular reality.

Activity-induced enhancement of enzyme diffusion depends on the type of crowders. Enzyme diffusion enhancement is an increase in the diffusion coefficient of an enzyme actively engaged in a catalytic turnover. Although the very existence of this phenomenon is still debated [200, 201, 216], understanding its potential origin and behavior is important as it may explain glassification of the cytoplasm under the influence of halting metabolic activity [20, 21]. Advocating for or against its existence was beyond the scope of this Thesis. Instead, we considered enzymes that decrease their size upon binding a substrate, thus naturally showing enhanced diffusion, which is consistent with experiments [203, 222]. The enhancement we observed in crowded systems differed from the dilute regime and depended on the type of a crowder (Fig. 5.3). It is larger in magnitude when crowding is due to enzymes and weaker if it is due to passive crowders. Moreover, we also observed diffusion enhancement of passive spheres in mixtures with active enzymes, albeit only for high enzyme concentrations (Fig. 5.4). To our knowledge, this is the first study of this phenomenon taking into account crowding. Since the biological environment in which enzymes operate is crowded, more research in that direction is needed.

H-cell measurements can test the existence of enzyme diffusion enhancement, but only if they are highly accurate. As mentioned above, a consensus is not yet reached on whether enzyme diffusion enhancement exists, owing to various experimental methods producing inconsistent results (Table 5.1). H-cell microfluidic experiments allow for accurate and robust measurement of protein diffusion coefficient [228] and thus might help resolve these debates. We performed the rational design of H-cell diffusion enhancement measurements for three enzymes (Fig. 5.7). In each case, we have found that very accurate enzyme concentration measurements are needed to capture the change in diffusion coefficient (Fig. 5.9). Although this accuracy requirement prevented us from performing such experiments, in the future improved H-cell measurements can be used for that purpose based on our optimization results.

Chemical kinetics measurements can help obtain information on the conformation changes of some enzymes during a reaction. For some enzymes, such as an HIV-1 protease, the reaction rate depends on the probability that they adopt a particular, catalytically active conformation [95, 269]. This probability, and therefore the reaction rate, can vary significantly between the *in vitro* and *in vivo* conditions, particularly but not exclusively due to macromolecular crowding. We quantified the contribution from crowding for model enzymes using BD simulations and SPT calculations based on how crowding affects the conformation of an enzyme. Our results show that macroscopic chemical kinetics measurements in crowded systems encode the information about the microscopic conformational states of such enzymes (Section 6.2). This information may be decoded by fitting the theoretical SPT curve (Eq. 6.2) to the experimental data. However, the literature data was insufficient to perform such an analysis in this Thesis [255]. Thus, it remains to be seen how accurate this approach is and whether reducing the crowding effects merely to changing the fraction of active enzymes can reliably describe the enzyme kinetics under crowding. This is a special case of a broader question un-

derlying "CELLestial mechanics" (Section 1.1), namely whether it is possible to predict *in vivo* rate constants using only the results obtained *in vitro*.

Macromolecular crowding can cause multivalent binding reactions to become cooperative. Some biologically relevant chemical reactions, such as the binding of oxygen to hemoglobin and antibody-antigen binding, involve molecules with more than one binding site, which are called multivalent. These reactions may exhibit cooperativity, *i.e.*, each subsequent binding step may have a larger equilibrium constant [275]. Cooperativity is considered essential to the functioning of life [280], but little is known about its interplay with macromolecular crowding. To bridge that gap, we investigated the equilibria of divalent binding reactions in crowded systems using SPT calculations (Fig. 6.2). We demonstrated that crowding might even induce cooperativity in otherwise noncooperative systems and *vice versa*. The direction of the shift depends on the details of the changes in the macromolecule's shape and size upon consecutive binding events. In particular, expansion upon the first and contraction upon the second binding step leads to an increased cooperativity. Moreover, we explored this effect in reactions of linear and cyclic bead chains, which are simplistic models of unfolded and folded macromolecular structures [292], obtaining similar results (Figs. 6.6 and 6.7). We hope these theoretical results motivate experimentalists to investigate such crowding-regulated multivalent binding both *in vitro* and *in vivo*.

Developed open-source software. In the course of this research, I developed `pyBrown` software (Appendix D.2) for BD and SD (F-version) simulations. Unlike existing alternatives, such as `BD_BOX` (Appendix D.1) and `Brownmove` [296], it accounts for near-field hydrodynamic interactions *via* improved lubrication correction (Section 3.2.1). In addition, `pyBrown` includes functionalities not covered in this Thesis, such as calculating reaction rate constants with the Northrup-Allison-McCammon (NAM) algorithm algorithm [297] or user-defined chemical interactions and reactions between particles. I also developed `ExVol` software (Appendix D.4) for computing excluded volume by Monte Carlo (MC) integration (Section 3.3). This software is released under GPL-3.0 license and is freely available at `https://tskora.github.io/pyBrown/` and `https://tskora.github.io/ExVol/`, respectively.

Appendix A

Brownian dynamics implementation details

A.1 Propagation schemes

A.1.1 Forward Euler scheme

Forward Euler method leads to the following propagation scheme for Eq. 3.4:

$$\boldsymbol{r}(t+\Delta t) = \boldsymbol{r}(t) + \frac{1}{k_{\mathrm{B}}T}\boldsymbol{D}\boldsymbol{F}\Delta t + \sqrt{2\Delta t}\boldsymbol{B}\boldsymbol{X}, \tag{A.1}$$

where $\boldsymbol{r}$ is vector of positions, t is time, Δt is propagation step, k_{B} is Boltzmann constant, T is temperature, $\boldsymbol{F}$ is force vector, $\boldsymbol{X}$ is standard white-noise vector, $\boldsymbol{D}$ is diffusion matrix, and $\boldsymbol{B}$ is a Choleski factor of $\boldsymbol{D}$, *i.e.*:

$$\boldsymbol{D} = \boldsymbol{B}^T\boldsymbol{B}. \tag{A.2}$$

The factor of $\sqrt{\Delta t}$ originates from the fact that the variance of the integral of white noise is equal to the length of the integration range, here Δt. Similarly, a sum of N normally distributed variables with unit variance has a variance equal to N.

A.1.2 Ermak-McCammon scheme

The propagation scheme for Eq. 3.4 accounting for hydrodynamic interactions (Section 3.2) derived by Ermak & McCammon [75] reads:

$$\boldsymbol{r}(t+\Delta t) = \boldsymbol{r}(t) + (\boldsymbol{\nabla}^T\boldsymbol{D})^T\Delta t + \frac{1}{k_{\mathrm{B}}T}\boldsymbol{D}\boldsymbol{F}\Delta t + \sqrt{2\Delta t}\boldsymbol{B}\boldsymbol{X}, \tag{A.3}$$

where $\boldsymbol{\nabla}$ denotes a vector of partial derivative operators over position $\boldsymbol{r}$. Ermak & McCammon [75] also performed the first simulations using that scheme and coined the term Brownian

dynamics (BD) for them.

The diffusion matrix in Oseen (Eq. 3.5) and Rotne-Prager-Yamakawa (RPY) (Eqs. 3.6 and 3.7) approximations is sourceless, *i.e.*, $\boldsymbol{\nabla}^T \boldsymbol{D} = \mathbf{0}^T$. Thus, in these approximations, the Ermak-McCammon propagation scheme (Eq. A.3) simplifies to Eq. A.1.

A.1.3 Iniesta-Garcia de la Torre scheme

Iniesta & García de la Torre [184] proposed a second order BD propagation scheme that divides the propagation step into two substeps: predictor and corrector. The scheme reads:

$$\boldsymbol{r}(t+\Delta t) = \boldsymbol{r}(t) + \frac{1}{2}\frac{\Delta t}{k_{\mathrm{B}}T}\left[\boldsymbol{D}(t)\boldsymbol{F}(t) + \boldsymbol{D}\left(t+\frac{1}{2}\Delta t\right)\boldsymbol{F}\left(t+\frac{1}{2}\Delta t\right)\right] + \sqrt{\Delta t\left[\boldsymbol{D}\left(t\right) + \boldsymbol{D}\left(t+\frac{1}{2}\Delta t\right)\right]}\boldsymbol{X}, \quad \text{(A.4)}$$

where $\boldsymbol{D}$ and $\boldsymbol{F}$ for $t+\frac{1}{2}\Delta t$ are computed using the Ermak-McCammon propagation scheme, and square root of a matrix is defined by Choleski decomposition (Eq. A.2). The purpose of such division is to better account for the changes in $\boldsymbol{F}$ and $\boldsymbol{D}$ along a single propagation step.

A.1.4 Midpoint scheme

The lubrication-corrected diffusion matrix of Stokesian dynamics (SD) (Eq. 3.11) is no longer sourceless, and the divergence term in Eq. A.3 cannot be neglected. A possible way to avoid the explicit differentiation of the diffusion matrix, which would be computationally exhaustive, is to use a midpoint propagation scheme [36]. In the midpoint algorithm, initially, beads are translated only by a $1/m$ fraction of a precalculated translation vector. Then, the diffusion matrix $\boldsymbol{D}(t+\Delta t/m)$ is calculated at that point, and the remaining part of the translation is performed (with forces $\boldsymbol{F}(t)$ and diffusion tensor $\boldsymbol{D}(t)$) but with an additional drift term. The overall scheme reads:

$$\boldsymbol{r}(t+\Delta t) = \boldsymbol{r}(t) + \frac{\Delta t}{k_{\mathrm{B}}T}\boldsymbol{D}(t)\boldsymbol{F}(t) + \sqrt{2\Delta t}\boldsymbol{B}(t)\boldsymbol{X} + \frac{m}{2}\left[\frac{\Delta t}{k_{\mathrm{B}}T}\left(\boldsymbol{D}\left(t+\frac{\Delta t}{m}\right) - \boldsymbol{D}(t)\right)\boldsymbol{F}(t) + \sqrt{2\Delta t}\left(\boldsymbol{D}\left(t+\frac{\Delta t}{m}\right)\left(\boldsymbol{B}(t)^T\right)^{-1} - \boldsymbol{B}(t)\right)\boldsymbol{X}\right]. \quad \text{(A.5)}$$

A.2 Interactions

Apart from the hydrodynamic interactions, BD simulations account for regular interactions as well. Force $\boldsymbol{F}$ appearing in the BD propagation schemes (Eqs. A.1 and A.3–A.5) is defined

as a gradient of interaction potential energy $V(\boldsymbol{r})$. Below, the interactions that we used in the research described in this Thesis are introduced.

A.2.1 Hard-sphere potential

The simplest interaction potential that we use in our studies is the hard-sphere potential:

$$\frac{V_{\mathrm{HS}}(\boldsymbol{r}_{ij})}{k_{\mathrm{B}}T} = \begin{cases} 0, \text{ for } r_{ij} > a_i + a_j; \\ \infty, \text{ else }. \end{cases} \tag{A.6}$$

where r_{ij} is distance between i-th and j-th particle of hydrodynamic radii a_i and a_j, respectively. Hard-sphere potential is included in BD and SD simulations simply by not allowing particle overlaps; if two or more particles overlap, the simulation step is withdrawn and repeated by drawing new random displacements.

A.2.2 Short-range repulsive potential

Sometimes repeating steps leading to overlaps can cause substantial computational overhead. To avoid this, one uses short-range repulsive continuous potentials approximating the hard-sphere potential. For two large spheres composed of small particles interacting with standard Weeks-Chandler-Andersen (WCA) potential – repulsive component of the Lennard-Jones (LJ) potential – with energy $\varepsilon_{\mathrm{LJ}}$, the total potential is an integral of the WCA potential over the volumes of the two spheres. The polynomial expression for it was derived by Henderson *et al.* [178] and for small separations reads [36]:

$$V_{\mathrm{rep}}\left(r_{ij}\right) = \frac{64\varepsilon_{\mathrm{LJ}}\pi^2}{315}\left(\frac{a_i a_j}{a_i + a_j}\right)\frac{\sigma^6}{\left[r_{ij} - (a_i + a_j)\right]^7}, \tag{A.7}$$

where σ is a radius of the small WCA-interacting particle.

A.2.3 Attractive potential

Similar integration for the attractive part of the LJ interaction was performed by Hamaker [300]. The resulting potential reads:

$$V_{\mathrm{attr}}\left(r_{ij}\right) = -\frac{4\varepsilon_{LJ}\pi^2}{3}\left[\frac{a_i a_j}{r_{ij}^2 - (a_i + a_j)^2} + \frac{a_i a_j}{r_{ij}^2 - (a_i - a_j)^2} + \frac{1}{2}\ln\left(\frac{r_{ij}^2 - (a_i + a_j)^2}{r_{ij}^2 - (a_i - a_j)^2}\right)\right]. \tag{A.8}$$

Note that to fit the small particles interactiong with WCA or LJ potential below the macromolecule's surface at radius a_i, the radii used in the Eqs. A.7 and A.8 must be reduced by σ,

i.e.:

$$a_i \to a_i - \sigma. \tag{A.9}$$

A.2.4 Roughness correction

Eqs. A.7 and A.8 are correct, provided the particles are perfect spheres with ideally smooth surfaces. However, this is often not the case, and the roughness of their surfaces significantly decreases the magnitude of interactions [301, 302]. It may be taken into account by introducing a multiplicative roughness correction [36]:

$$A = \frac{r_{ij} - (a_i + a_j)}{r_{ij} - (a_i + a_j) + 0.5\,(h_i + h_j)}, \tag{A.10}$$

where h_i and h_j are the roughnesses of the macromolecules.

A.2.5 Electrostatic potential

The electrostatic interactions between macromolecules are described by Derjaguin-Landau-Verwey-Overbeek (DLVO) theory of screened electrostatics in electrolytes:

$$V_{\text{elec}}\,(r_{ij}) = \frac{\Theta_i \Theta_j e^2}{4\pi\varepsilon_0\varepsilon\,(1 + \kappa a_i)\,(1 + \kappa a_j)} \frac{\exp\left[-\kappa\,(r_{ij} - a_i - a_j)\right]}{r_{ij}}, \tag{A.11}$$

where ε is relative dielectric constant of a fluid, κ is inverse of the Debye length, ε_0 is the vacuum permittivity, e is the proton charge, and Θ_i is molecular charge in elementary charge units.

A.2.6 Harmonic bond potential

The bonded potentials act only between beads connected with bonds. Harmonic bond potential is:

$$V_{\text{bond}}\,(r_{ij}) = \frac{1}{2} k_r\,(r_{ij} - r_{ij,0})^2\,, \tag{A.12}$$

where k_r is the Hooke constant describing the stiffness of the bond, and $r_{ij,0}$ is an equilibrium bond length.

A.2.7 Harmonic angle potential

The harmonic angle potential is:

$$V_{\text{angle}}\,(\alpha_{ijk}) = \frac{1}{2} k_\alpha\,(\alpha_{ijk} - \alpha_{ijk,0})^2\,, \tag{A.13}$$

where k_α is an angle force constant and $\alpha_{ijk,0}$ is the equilibrium angle value.

A.3 Trajectory analysis

A.3.1 Translational diffusion

The trajectories from BD and SD simulations encode translational diffusion coefficients that may be obtained from time-averaged mean squared displacement (TAMSD), computed by averaging squared displacements not only over the separate trajectories, but also by sliding an observation window along the trajectories:

$$\mathrm{TAMSD}(m\Delta t) = \frac{1}{N_{\mathrm{traj}}}\sum_{i=1}^{N_{\mathrm{traj}}}\frac{1}{N_{\mathrm{steps}}-m}\sum_{k=0}^{N_{\mathrm{steps}}-m-1}\{\boldsymbol{r}_i\left[(k+m)\Delta t\right]-\boldsymbol{r}_i\left[k\Delta t\right]\}^T\{\boldsymbol{r}_i\left[(k+m)\Delta t\right]-\boldsymbol{r}_i\left[k\Delta t\right]\}, \tag{A.14}$$

where Δt is a window length, N_{traj} is the number of trajectories, and N_{steps} is the number of steps in a trajectory. For nonergodic systems, the diffusion coefficient is obtained from ensemble-averaged-only mean squared displacement (MSD):

$$\mathrm{MSD}(m\Delta t) = \frac{1}{N_{\mathrm{traj}}}\sum_{i=1}^{N_{\mathrm{traj}}}\{\boldsymbol{r}_i\left[m\Delta t\right]-\boldsymbol{r}_i\left[0\right]\}^T\{\boldsymbol{r}_i\left[m\Delta t\right]-\boldsymbol{r}_i\left[0\right]\}. \tag{A.15}$$

Then, the time-dependent apparent translational diffusion coefficient is:

$$D(t) = \frac{\mathrm{TAMSD}(t)}{6t}; \tag{A.16a}$$

$$D(t) = \frac{\mathrm{MSD}(t)}{6t}. \tag{A.16b}$$

Throughout this Thesis, for both MSD and TAMSD, we used a custom analysis software `pyBrown-tools` (Appendix D.3).

A.3.2 Rotational diffusion

The trajectories of nonspherical particles encode also rotational diffusion coefficients that may be obtained from orientation autocorrelation (OA) [185, 303]:

$$\mathrm{OA} = \langle\boldsymbol{\ell}(t)^T\boldsymbol{\ell}(0)\rangle, \tag{A.17}$$

where $\boldsymbol{\ell}$ is the orientation vector. OA is computed by averaging not only over the separate trajectories, but also by sliding an observation window along the trajectories

$$\mathrm{OA}(m\Delta t) = \frac{1}{N_{\mathrm{traj}}} \sum_{i=1}^{N_{\mathrm{traj}}} \frac{1}{N_{\mathrm{steps}} - m} \sum_{k=0}^{N_{\mathrm{steps}}-m-1} \boldsymbol{\ell}_i \left((k+m)\, \Delta t \right) \cdot \boldsymbol{\ell}_i \left(k \Delta t \right). \tag{A.18}$$

OA is an exponentially decaying function of time, with the rate constant related to the rotational diffusion coefficient D_r as follows [303]:

$$\mathrm{OA}(t) = \exp\left(-2 D_r t\right). \tag{A.19}$$

Throughout this Thesis, to compute OA we used a custom analysis software `pyBrown-tools` (Appendix D.3).

Appendix B

Ewald summation of Rotne-Prager-Yamakawa diffusion matrix

In Brownian dynamics (BD) simulations, periodic boundary conditions are often used to eliminate the problem of system boundaries. However, hydrodynamic interactions decay slowly with distance ($\propto \frac{1}{r_{ij}}$), so the Ewald summation method is applied to attain their convergence. It is a similar problem to the Ewald summation of electrostatic interactions.

The Ewald summation method divides the expressions for the diffusion matrix elements into two contributions. The short-range contributions are calculated in the real space and the long-range in the reciprocal space. The Ewald-summation scheme of the generalized Rotne-Prager-Yamakawa (RPY) diffusion matrix described in this appendix was introduced by Smith *et al.* [304].

We assume that the finite simulation cubic box is $L \times L \times L$. Then, periodic boundary conditions mean that each particle with position $\boldsymbol{r}_i$ has an infinite number of replicas at coordinates $\boldsymbol{r}_i + L\boldsymbol{m}$, where $\boldsymbol{m}$ is an arbitrary vector of integers. The periodic RPY matrix is expressed as follows:

$$\boldsymbol{D}_{ij} = \frac{k_{\mathrm{B}}T}{6\pi\eta a_i}\left\{\delta_{ij}\boldsymbol{I} + \left[\frac{3a_i}{4L}\boldsymbol{O}_{\mathrm{PBC}}\left(\frac{\boldsymbol{r}_{ij}}{L}\right) + \frac{a_i^3}{2L^3}\boldsymbol{Q}_{\mathrm{PBC}}\left(\frac{\boldsymbol{r}_{ij}}{L}\right)\right]\right\}, \tag{B.1}$$

where, k_{B} is a Boltzmann constant, T is temperature, η is dynamic viscosity of a fluid, a_i hydrodynamic radius of i-th particle, δ_{ij} is the Kronecker delta, and $\boldsymbol{r}_{ij}$ is vector pointing from i-th to j-th particle.

Below we will use a distance relative to the box size $\boldsymbol{\sigma}_{ij}$ defined as follows:

$$\boldsymbol{\sigma}_{ij} = \frac{\boldsymbol{r}_{ij}}{L}, \tag{B.2}$$

and we will denote unit vectors with a hat, *e.g.*:

$$\hat{\boldsymbol{v}} = \frac{\boldsymbol{v}}{v}, \tag{B.3}$$

where:

$$v = \sqrt{\boldsymbol{v}^T \boldsymbol{v}}. \tag{B.4}$$

For $\boldsymbol{\sigma}_{ij} \notin \{\boldsymbol{m}\}$, *i.e.*, interactions between different particles (off-diagonal blocks of diffusion matrix $\boldsymbol{D}$):

$$\begin{aligned}\boldsymbol{O}_{\mathrm{PBC}}\left(\boldsymbol{\sigma}_{ij}\right) = \sum_{\boldsymbol{m}} \Bigg[& \operatorname{erfc}\left(\alpha \sqrt{\left(\boldsymbol{m}+\boldsymbol{\sigma}_{ij}\right)^T \left(\boldsymbol{m}+\boldsymbol{\sigma}_{ij}\right)}\right) \boldsymbol{O}\left(\boldsymbol{m}+\boldsymbol{\sigma}_{ij}\right) + \\ & \frac{2\alpha}{\sqrt{\pi}} \exp\left(-\alpha^2 \left(\boldsymbol{m}+\boldsymbol{\sigma}_{ij}\right)^T \left(\boldsymbol{m}+\boldsymbol{\sigma}_{ij}\right)\right) \frac{\left(\boldsymbol{m}+\boldsymbol{\sigma}_{ij}\right)\left(\boldsymbol{m}+\boldsymbol{\sigma}_{ij}\right)^T}{\left(\boldsymbol{m}+\boldsymbol{\sigma}_{ij}\right)^T \left(\boldsymbol{m}+\boldsymbol{\sigma}_{ij}\right)} \Bigg] + \\ & \sum_{\boldsymbol{n}\neq\boldsymbol{0}} \frac{2}{\pi \boldsymbol{n}^T \boldsymbol{n}} \exp\left(-\frac{\pi^2 \boldsymbol{n}^T \boldsymbol{n}}{\alpha^2}\right) \exp\left(2\pi i \boldsymbol{n}^T \boldsymbol{\sigma}_{ij}\right) \left[\boldsymbol{I} - \left(1 + \frac{\pi^2 \boldsymbol{n}^T \boldsymbol{n}}{\alpha^2}\right) \hat{\boldsymbol{n}} \hat{\boldsymbol{n}}^T\right]; \end{aligned} \tag{B.5a}$$

$$\begin{aligned}\boldsymbol{Q}_{\mathrm{PBC}}\left(\boldsymbol{\sigma}_{ij}\right) = \sum_{\boldsymbol{m}} \Bigg[& \operatorname{erfc}\left(\alpha \sqrt{\left(\boldsymbol{m}+\boldsymbol{\sigma}_{ij}\right)^T \left(\boldsymbol{m}+\boldsymbol{\sigma}_{ij}\right)}\right) + \\ & \frac{2\alpha}{\sqrt{\pi}} \sqrt{\left(\boldsymbol{m}+\boldsymbol{\sigma}_{ij}\right)^T \left(\boldsymbol{m}+\boldsymbol{\sigma}_{ij}\right)} \exp\left(-\alpha^2 \left(\boldsymbol{m}+\boldsymbol{\sigma}_{ij}\right)^T \left(\boldsymbol{m}+\boldsymbol{\sigma}_{ij}\right)\right) \Bigg] \boldsymbol{Q}\left(\boldsymbol{m}+\boldsymbol{\sigma}_{ij}\right) - \\ & \sum_{\boldsymbol{m}} \frac{4\alpha^3}{\sqrt{\pi}} \exp\left(-\alpha^2 \left(\boldsymbol{m}+\boldsymbol{\sigma}_{ij}\right)^T \left(\boldsymbol{m}+\boldsymbol{\sigma}_{ij}\right)\right) \frac{\left(\boldsymbol{m}+\boldsymbol{\sigma}_{ij}\right)\left(\boldsymbol{m}+\boldsymbol{\sigma}_{ij}\right)^T}{\left(\boldsymbol{m}+\boldsymbol{\sigma}_{ij}\right)^T \left(\boldsymbol{m}+\boldsymbol{\sigma}_{ij}\right)} + \\ & 4\pi \sum_{\boldsymbol{n}\neq\boldsymbol{0}} \exp\left(-\frac{\pi^2 \boldsymbol{n}^T \boldsymbol{n}}{\alpha^2}\right) \exp\left(2\pi i \boldsymbol{n}^T \boldsymbol{\sigma}_{ij}\right) \hat{\boldsymbol{n}} \hat{\boldsymbol{n}}^T, \end{aligned} \tag{B.5b}$$

and for $\boldsymbol{\sigma}_{ij} \in \{\boldsymbol{m}\}$, *i.e.*, interactions with self-images (diagonal blocks of diffusion matrix $\boldsymbol{D}$):

$$\begin{aligned}\boldsymbol{O}_{\mathrm{PBC}}\left(\boldsymbol{m}'\right) = \sum_{\boldsymbol{m}\neq\boldsymbol{0}} \Bigg[& \operatorname{erfc}\left(\alpha \sqrt{\boldsymbol{m}^T \boldsymbol{m}}\right) \boldsymbol{O}(\boldsymbol{m}) + \frac{2\alpha}{\sqrt{\pi}} \exp\left(-\alpha^2 \boldsymbol{m}^T \boldsymbol{m}\right) \hat{\boldsymbol{m}} \hat{\boldsymbol{m}}^T \Bigg] - \\ & \frac{3\alpha a_i}{2\sqrt{\pi} L} \boldsymbol{I} + \sum_{\boldsymbol{n}\neq\boldsymbol{0}} \frac{2}{\sqrt{\pi} \boldsymbol{n}^T \boldsymbol{n}} \exp\left(-\frac{\pi^2 \boldsymbol{n}^T \boldsymbol{n}}{\alpha^2}\right) \left[\boldsymbol{I} - \left(1 + \frac{\pi^2 \boldsymbol{n}^T \boldsymbol{n}}{\alpha^2}\right) \hat{\boldsymbol{n}} \hat{\boldsymbol{n}}^T\right]; \end{aligned} \tag{B.6a}$$

$$\begin{aligned}\boldsymbol{Q}_{\mathrm{PBC}}\left(\boldsymbol{m}'\right) = \sum_{\boldsymbol{m}\neq\boldsymbol{0}} \Bigg[& \operatorname{erfc}\left(\alpha \sqrt{\boldsymbol{m}^T \boldsymbol{m}}\right) + \frac{2\alpha}{\sqrt{\pi}} \sqrt{\boldsymbol{m}^T \boldsymbol{m}} \exp\left(-\alpha^2 \boldsymbol{m}^T \boldsymbol{m}\right) \Bigg] \boldsymbol{Q}(\boldsymbol{m}) - \\ & \sum_{\boldsymbol{m}\neq\boldsymbol{0}} \frac{4\alpha^3}{\sqrt{\pi}} \exp\left(-\alpha^2 \boldsymbol{m}^T \boldsymbol{m}\right) \hat{\boldsymbol{m}} \hat{\boldsymbol{m}}^T - \frac{1}{3\sqrt{\pi}} \left(\frac{\alpha a_i}{L}\right)^3 \boldsymbol{I} + 4\pi \sum_{\boldsymbol{n}\neq\boldsymbol{0}} \exp\left(-\frac{\pi^2 \boldsymbol{n}^T \boldsymbol{n}}{\alpha^2}\right) \hat{\boldsymbol{n}} \hat{\boldsymbol{n}}^T. \end{aligned} \tag{B.6b}$$

The auxiliary matrices $\boldsymbol{O}$ and $\boldsymbol{Q}$ are defined in the following way:

$$\boldsymbol{O}(\boldsymbol{v}) = \frac{1}{v}\left(\boldsymbol{I} + \hat{\boldsymbol{v}}\hat{\boldsymbol{v}}^T\right); \tag{B.7a}$$

$$\boldsymbol{Q}(\boldsymbol{v}) = \frac{1}{v^3}\left(\boldsymbol{I} - 3\hat{\boldsymbol{v}}\hat{\boldsymbol{v}}^T\right). \tag{B.7b}$$

Symbol erfc stands for the complementary error function, and α is an arbitrary constant governing the division of the summation among real and reciprocal space components.

In practice, number of $\boldsymbol{m}$ and $\boldsymbol{n}$ vectors included in sums in Eqs. B.5 and B.6 has to be limited. Cutoffs on these lattice vectors are defined by parameters m_{cutoff} and n_{cutoff}. The $\boldsymbol{m}$, $\boldsymbol{n}$ vectors are included, if their entries fulfill following inequalities:

$$|m_1| + |m_2| + |m_3| \leq m_{\mathrm{cutoff}}; \tag{B.8a}$$

$$|n_1| + |n_2| + |n_3| \leq n_{\mathrm{cutoff}}. \tag{B.8b}$$

As shown by Beenakker, [305] the same equations may be applied to spheres of different sizes by the following substitution:

$$a^3 \rightarrow \frac{1}{2}a_i\left(a_i^2 + a_j^2\right). \tag{B.9}$$

For overlapping beads the expressions are corrected simply by adding a difference of the respective generalized RPY expressions as follows:

$$\Delta\boldsymbol{D}_{ij}^{\mathrm{overlap}} = \boldsymbol{A}_{ij} - \boldsymbol{B}_{ij}, \tag{B.10}$$

where $\boldsymbol{B}_{ij}$ is given by Eq. 3.7a and $\boldsymbol{A}_{ij}$ is given either by Eq. 3.7b, or by Eq. 3.7c, depending on r_{ij}, a_i, and a_j (see whole Eq. 3.7 for details).

Appendix C

Resistance matrix scalar functions

Exact two-body resistance tensor $\boldsymbol{\xi}^{\mathrm{2B}}$ is expressed using dimensionless center-to-center separation s and the ratio of hydrodynamic radii λ:

$$s = \frac{2r}{a_1 + a_2}; \tag{C.1a}$$

$$\lambda = \frac{a_2}{a_1}, \tag{C.1b}$$

where r is distance between the particles of hydrodynamic radii a_1 and a_2. The formulas were obtained by Jeffrey & Onishi [90]. The translational part reads:

$$\boldsymbol{\xi}_{ij} = 6\pi\eta a_1 \left\{ X_{ij}^A(s,\lambda)\, \hat{\boldsymbol{r}}\hat{\boldsymbol{r}}^T + Y_{ij}^A(s,\lambda) \left[\delta_{ij}\boldsymbol{I} - \hat{\boldsymbol{r}}\hat{\boldsymbol{r}}^T \right] \right\}, \tag{C.2}$$

where η is dynamic viscosity, $\boldsymbol{r}$ is a vector pointing from particle 1 to particle 2, and $\hat{\boldsymbol{r}} = \boldsymbol{r}/r$. Equation C.2 involves a set of scalar resistance functions: X_{11}^A, X_{12}^A, X_{21}^A, X_{22}^A, Y_{11}^A, Y_{12}^A, Y_{21}^A and Y_{22}^A. It is important to mention that the paper by Jeffrey & Onishi [90] contains few mistakes, although not in expressions used here, which were spotted and corrected by Townsend [306], so one should be careful when referring to it.

Pertinent scalar functions read:

$$\begin{aligned} X_{11}^A(s,\lambda) = {} & g_1^X(\lambda) \cdot \left(1 - 4s^{-2}\right)^{-1} - g_2^X(\lambda) \cdot \ln\left(1 - 4s^{-2}\right) - \\ & g_3^X(\lambda) \cdot \left(1 - 4s^{-2}\right) \ln\left(1 - 4s^{-2}\right) + f_0^X(\lambda) - g_1^X(\lambda) + \\ & \sum_{\substack{m=2 \\ m \text{ even}}}^{\infty} \left[2^{-m} (1+\lambda)^{-m} \cdot f_m^X(\lambda) - g_1^X(\lambda) - 2m^{-1} \cdot g_2^X(\lambda) \right. \\ & \left. + 4m^{-1} \cdot m_1(m)^{-1} \cdot g_3^X(\lambda) \right] \left(\frac{2}{s}\right)^m; \end{aligned} \tag{C.3a}$$

$$X_{12}^{A}(s,\lambda) = -\Bigg\{2s^{-1}\cdot g_{1}^{X}(\lambda)\cdot\left(1-4s^{-2}\right)^{-1} + g_{2}^{X}(\lambda)\cdot\ln\frac{s+2}{s-2} + g_{3}^{X}(\lambda)\cdot\left(1-4s^{-2}\right)\ln\frac{s+2}{s-2} + 4g_{3}^{X}(\lambda)\cdot s^{-1} + \sum_{\substack{m=1\\ m\,\text{odd}}}^{\infty}\Big[2^{-m}\left(1+\lambda^{-1}\right)^{-m}\cdot f_{m}^{X}(\lambda) - g_{1}^{X}(\lambda) - 2m^{-1}\cdot g_{2}^{X}(\lambda) + 4m^{-1}\cdot m_{1}(m)^{-1}\cdot g_{3}^{X}(\lambda)\Big]\left(\frac{2}{s}\right)^{m}\Bigg\}, = l \quad \text{(C.3b)}$$

$$X_{22}^{A}(s,\lambda) = \lambda X_{11}^{A}\left(s,\frac{1}{\lambda}\right); \quad \text{(C.3c)}$$

$$Y_{11}^{A}(s,\lambda) = -g_{2}^{Y}(\lambda)\cdot\ln\left(1-4s^{-2}\right) - g_{3}^{Y}(\lambda)\cdot\left(1-4s^{-2}\right)\ln\left(1-4s^{-2}\right) + f_{0}^{Y}(\lambda) + \sum_{\substack{m=2\\ m\,\text{even}}}^{\infty}\Big[2^{-m}(1+\lambda)^{-m}\cdot f_{m}^{Y}(\lambda) - 2m^{-1}\cdot g_{2}^{Y}(\lambda) + 4m^{-1}\cdot m_{1}(m)^{-1}\cdot g_{3}^{Y}(\lambda)\Big]\left(\frac{2}{s}\right)^{m}; \quad \text{(C.4a)}$$

$$Y_{12}^{A}(s,\lambda) = -\Bigg\{g_{2}^{Y}(\lambda)\cdot\ln\frac{s+2}{s-2} + g_{3}^{Y}(\lambda)\cdot\left(1-4s^{-2}\right)\ln\frac{s+2}{s-2} + 4\cdot g_{3}^{Y}(\lambda)\cdot s^{-1} + \sum_{\substack{m=1\\ m\,\text{odd}}}^{\infty}\Big[2^{-m}(1+\lambda)^{-m}\cdot f_{m}(\lambda) - 2m^{-1}\cdot g_{2}^{Y}(\lambda) + 4m^{-1}\cdot m_{1}(m)^{-1}\cdot g_{3}^{Y}(\lambda)\Big]\left(\frac{2}{s}\right)^{m}\Bigg\}; \quad \text{(C.4b)}$$

$$Y_{22}^{A}(s,\lambda) = \lambda Y_{11}\left(s,\frac{1}{\lambda}\right). \quad \text{(C.4c)}$$

The functions use auxiliary expressions for m_1 (Eq. C.5), f_i^X (Eq. C.6), f_i^Y (Eq. C.7), g_i^X (Eq. C.8), and g_i^Y (Eq. C.9) polynomials, provided below:

$$m_{1}(m) = -2\delta_{m2} + (m-2)(1-\delta_{m2}), \quad \text{(C.5)}$$

$$f_{0}^{X}(\lambda) = 1, \quad \text{(C.6a)}$$

$$f_1^X(\lambda) = 3\lambda, \tag{C.6b}$$

$$f_2^X(\lambda) = 9\lambda, \tag{C.6c}$$

$$f_3^X(\lambda) = -4\lambda + 27\lambda^2 - 4\lambda^3, \tag{C.6d}$$

$$f_4^X(\lambda) = -24\lambda + 81\lambda^2 + 36\lambda^3, \tag{C.6e}$$

$$f_5^X(\lambda) = 72\lambda^2 + 243\lambda^3 + 72\lambda^4, \tag{C.6f}$$

$$f_6^X(\lambda) = 16\lambda + 108\lambda^2 + 281\lambda^3 + 648\lambda^4 + 144\lambda^5, \tag{C.6g}$$

$$f_7^X(\lambda) = 288\lambda^2 + 1620\lambda^3 + 1515\lambda^4 + 1620\lambda^5 + 288\lambda^6, \tag{C.6h}$$

$$f_8^X(\lambda) = 576\lambda^2 + 4848\lambda^3 + 5409\lambda^4 + 4524\lambda^5 + 3888\lambda^6 + 576\lambda^7, \tag{C.6i}$$

$$f_9^X(\lambda) = 1152\lambda^2 + 9072\lambda^3 + 14752\lambda^4 + 26163\lambda^5 + 14752\lambda^6 + 9072\lambda^7 + 1152\lambda^8, \tag{C.6j}$$

$$f_{10}^X(\lambda) = 2304\lambda^2 + 20736\lambda^3 + 42804\lambda^4 + 115849\lambda^5 + 76176\lambda^6 + 39264\lambda^7 + 20736\lambda^8 + 2304\lambda^9, \tag{C.6k}$$

$$f_{11}^X(\lambda) = 4608\lambda^2 + 46656\lambda^3 + 108912\lambda^4 + 269100\lambda^5 + 319899\lambda^6 + 269100\lambda^7 + 108912\lambda^8 + 46656\lambda^9 + 4608\lambda^{10}; \tag{C.6l}$$

$$f_0^Y(\lambda) = 1, \tag{C.7a}$$

$$f_1^Y(\lambda) = \frac{3}{2}\lambda, \tag{C.7b}$$

$$f_2^Y(\lambda) = \frac{9}{4}\lambda, \tag{C.7c}$$

$$f_3^Y(\lambda) = 2\lambda + \frac{27}{8}\lambda^2 + 2\lambda^3, \tag{C.7d}$$

$$f_4^Y(\lambda) = 6\lambda + \frac{81}{16}\lambda^2 + 18\lambda^3, \tag{C.7e}$$

$$f_5^Y(\lambda) = \frac{63}{2}\lambda^2 + \frac{243}{32}\lambda^3 + \frac{63}{2}\lambda^4, \tag{C.7f}$$

$$f_6^Y(\lambda) = 4\lambda + 54\lambda^2 + \frac{1241}{64}\lambda^3 + 81\lambda^4 + 72\lambda^5, \tag{C.7g}$$

$$f_7^Y(\lambda) = 144\lambda^2 + \frac{1053}{8}\lambda^3 + \frac{19083}{128}\lambda^4 + \frac{1053}{8}\lambda^5 + 144\lambda^6, \tag{C.7h}$$

$$f_8^Y(\lambda) = 279\lambda^2 + \frac{4261}{8}\lambda^3 + \frac{126369}{256}\lambda^4 - \frac{117}{8}\lambda^5 + 648\lambda^6 + 288\lambda^7, \tag{C.7i}$$

$$f_9^Y(\lambda) = 576\lambda^2 + 1134\lambda^3 + \frac{60443}{32}\lambda^4 + \frac{766179}{512}\lambda^5 + \frac{60443}{32}\lambda^6 + 1134\lambda^7 + 576\lambda^8, \tag{C.7j}$$

$$f_{10}^Y(\lambda) = 1152\lambda^2 + \frac{7857}{4}\lambda^3 + \frac{98487}{16}\lambda^4 + \frac{2744505}{128}\lambda^5 + \frac{67617}{8}\lambda^6 - \frac{351}{2}\lambda^7 + 3888\lambda^8 + 1152\lambda^9, \tag{C.7k}$$

$$f_{11}^Y(\lambda) = 2304\lambda^2 + 7128\lambda^3 + \frac{22071}{2}\lambda^4 + \frac{2744505}{128}\lambda^5 + \frac{95203835}{2048}\lambda^6 + \frac{2744505}{128}\lambda^7 + \frac{22071}{2}\lambda^8 + 7128\lambda^9 + 2304\lambda^{10}; \tag{C.7l}$$

$$g_1^X(\lambda) = 2\lambda^2(1+\lambda)^{-3}, \tag{C.8a}$$

$$g_2^X(\lambda) = \frac{1}{5}\lambda\left(1+7\lambda+\lambda^2\right)(1+\lambda)^{-3}, \tag{C.8b}$$

$$g_3^X(\lambda) = \frac{1}{42}\left(1+18\lambda-29\lambda^2+18\lambda^3+\lambda^4\right)(1+\lambda)^{-3}; \tag{C.8c}$$

$$g_2^Y(\lambda) = \frac{4}{15}\lambda\left(2+\lambda+2\lambda^2\right)(1+\lambda)^{-3}, \tag{C.9a}$$

$$g_3^Y(\lambda) = \frac{2}{375}\left(16-45\lambda+58\lambda^2-45\lambda^3+16\lambda^4\right)(1+\lambda)^{-3}. \tag{C.9b}$$

Recurrence formulas allowing for inclusion of further terms are available in the literature [90, 306]. In this Thesis, we include only the listed terms, and neglect the remaining ones.

Appendix D

Software

D.1 BD_BOX

We performed Brownian dynamics (BD) simulations reported in Sections 4.3–4.5, 5.2, and 5.3 using a custom version of the BD_BOX [307] package. Original BD_BOX was authored by Długosz [308]. Our customization included: (1) implementation of Henderson (Eq. A.7), Hamaker (Eq. A.8), and chain entanglement softened potential (CESP) (Eq. 4.16), and potentials describing dumbbell enzymes (Eqs. 5.1 and 5.2), (2) enabling performing Choleski decomposition every N steps, instead of every step, to reduce the computational cost, (3) allowing for overlaps between bonded beads. Furthermore, in Section 4.4, we also used another customized version in which attractive interactions only between Ficoll70 and dsDNA were calculated, and attractive Ficoll70-Ficoll70 and dsDNA-dsDNA interactions were ignored.

The original BD_BOX is accessible at `https://www.fuw.edu.pl/~mdlugosz/downloads.html`.

D.2 pyBrown

I developed a new, versatile pyBrown [298] software for BD and (F-version) Stokesian dynamics (SD) simulations and used it in Sections 4.2 and 6.3. The macromolecules are represented by beads and "molecules" composed of beads connected by harmonic bonds. In contrast to BD_BOX and other available open-source packages, apart from standard far-field hydrodynamic interactions treatment in generalized Rotne-Prager-Yamakawa (RPY) approximation (Section 3.2.1), pyBrown includes near-field hydrodynamic interactions *via* improved lubrication correction (Section 3.2.2) and allows for setting the frequency of Choleski decomposition in input file.

The code is written mainly in python3, but the most computationally demanding fragments, such as building Ewald-summated RPY diffusion matrix, are written in C programming language. Apart from pure BD simulations, pyBrown can classify trajectories into reactive and

nonreactive, which makes it possible to compute second-order reaction rate constants with the Northrup-Allison-McCammon (NAM) algorithm [297]. `pyBrown` also allows for user-defined potentials.

The `pyBrown` documentation and code are accessible at `https://tskora.github.io/pyBrown/`.

D.3 `pyBrown-tools`

To perform BD and SD trajectory analysis, I developed various tools and bundled them together into `pyBrown-tools` [309] package. These tools include:

1. `MSD.py` for computing time-averaged mean squared displacement (TAMSD) (Eq. A.14) and mean squared displacement (MSD) (Eq. A.15),
2. `RDF.py` for computing radial distribution function (RDF),
3. `RotDiff.py` for computing orientation autocorrelation (OA) (Eq. A.18) and mean squared angular displacement (MSAD),
4. `Lengths.py` for computing bead-bead separation histograms of dumbbell enzymes.

`MSD.py` and `RDF.py` use functions from `freud` [310] package for molecular dynamics (MD) trajectory analysis by Ramasubramani [311].

The `pyBrown-tools` code is accessible at `https://github.com/tskora/pyBrown-tools`, and the `freud` documentation and code are accessible at `https://freud.readthedocs.io/en/latest/index.html`.

D.4 `ExVol`

To compute excluded volume fraction ϕ_{ex} and activity coefficients γ using Monte Carlo (MC) integration, I developed `ExVol` [299] software. It performs random insertions of bead models into crowded boxes. The code is written in `python3`. Skeleton of the implementation of the algorithm is presented below:

```
1 def estimate_excluded_volume(seed, tracer, crowders,
    number_of_trials, box_size):
2     pseudorandom_number_generator =
          initialize_pseudorandom_number_generation(seed)
3     count = 0
4     for i in range(number_of_trials):
5         put_tracer_at_center(tracer)
```

```
6           rotation_matrix = Rotation.random(random_state =
                pseudorandom_number_generator).as_matrix()
7           translation_vector = pseudorandom_number_generator.rand
                (dimension)
8           translation_vector = translation_vector * box_size -
                box_size / 2
9           for t in tracer:
10              t.rotate(rotation_matrix)
11              t.translate(translation_vector)
12          if overlap_pbc( tracer, crowders, box_size ):
13              count += 1
14      return count / number_of_trials
```

The `ExVol` documentation and code is accessible at `https://tskora.github.io/ExVol/`.

D.5 PyGRPY

To compute hydrodynamic radii of rigid bead models, we used `stokesRadius` function from the `PyGRPY` [312] package authored by Waszkiewicz [313]. The `PyGRPY` is a `python` port of the original `Fortran GRPY` code by Zuk [181]. The `PyGRPY` code is accessible at `https://github.com/RadostW/PyGRPY`, and the `GRPY` is accessile at `https://github.com/pjzuk/GRPY`. [181]

Appendix E

Fluorescence correlation spectroscopy

Fluorescence correlation spectroscopy (FCS) is a versatile experimental method for studying the dynamics of macromolecules, *e.g.*, proteins, both *in vitro*, in dilute solutions or complex polymer mixtures, and *in vivo*, in biological cells or extracellular matrix [100, 315]. FCS allows for measuring the diffusion coefficients in a non-invasive way and is extremely sensitive, allowing for measurements of samples at nanomolar concentrations ($1\,\mathrm{nM}$ in $1\,\mathrm{fL}$ spot gives, on average, 0.6 molecules).

In FCS, laser illumination is used to excite the fluorophores in a very small (close to the diffraction limit, so femtoliter – $\mu\mathrm{m}^3$) focal volume, defined by a focused laser beam and a confocal aperture. To be studied with FCS, the molecules of interest have to be fluorescent or fluorescently tagged prior to the measurements. The fluorescence emission from the focal volume is registered as a function of time. However, the final output is not the intensity function $I(t)$ but the autocorrelation of fluorescence fluctuations $G(\tau)$:

$$G\left(\tau\right) = \frac{\langle I(t)I(t+\tau)\rangle}{\langle I(t)\rangle^2} - 1. \tag{E.1}$$

In that notation:

$$\langle I(t)\rangle = \frac{1}{T}\int_0^T I(t)dt, \tag{E.2}$$

is the mean fluorescence intensity and

$$\langle I(t)I(t+\tau)\rangle = \frac{1}{T-\tau}\int_0^{T-\tau} I(t)I(t+\tau)dt, \tag{E.3}$$

is the autocorrelation, *i.e.*, a convolution of the signal with itself.

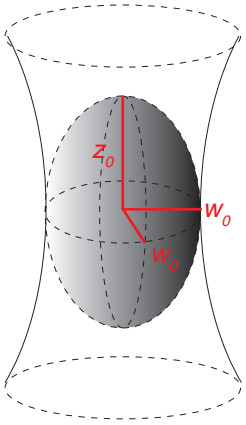

Figure E.1: **Scheme showing the illumination and focal volume in FCS measurement.** The focal volume is ellipsoidal, with axial half-length z_0 and planar half-length w_0. The ratio $\kappa = \frac{z_0}{w_0}$ characterizes the axial elongation.

E.1 Mathematical model

Some additional assumptions are needed to extract the diffusion coefficients from the raw FCS data. The assumptions are embodied in a specific model used to fit the autocorrelation function. For simplicity, the brightness profile $P(r)$ is assumed to be axial-elongated Gaussian:

$$P(r) = I_0 \exp\left[-2\left(x^2 + y^2\right)/w_0^2\right] \exp\left[-2z^2/z_0^2\right], \tag{E.4}$$

where I_0 is the maximal value of the fluorescence intensity, w_0 is the half-length of the focal plane, and $z_0 > w_0$ is the characteristic axial half-length (Fig. E.1). Position r is defined relative to the center of the focal volume. The characteristic spatial parameters w_0 and z_0 are defined in such a way that the brightness profile on the surface of the ellipsoid spanned by them is equal to $e^{-2} \approx 0.135$. Instead of z_0, it is common to use the ratio defined as follows:

$$\kappa = \frac{z_0}{w_0}. \tag{E.5}$$

Assuming that the only reason for intensity fluctuations is the Brownian motion of macromolecules, the autocorrelation function is expressed in the following way [315]:

$$G_D(\tau) = G_D(0)\left(1 + \frac{4D\tau}{w_0^2}\right)^{-1}\left(1 + \frac{4D\tau}{\kappa^2 w_0^2}\right)^{-1/2}, \tag{E.6}$$

where D is diffusion coefficient, or equivalently:

$$G_D(\tau) = G_D(0)\left(1 + \frac{\tau}{\tau_D}\right)^{-1}\left(1 + \frac{1}{\kappa^2}\frac{\tau}{\tau_D}\right)^{-1/2}, \tag{E.7}$$

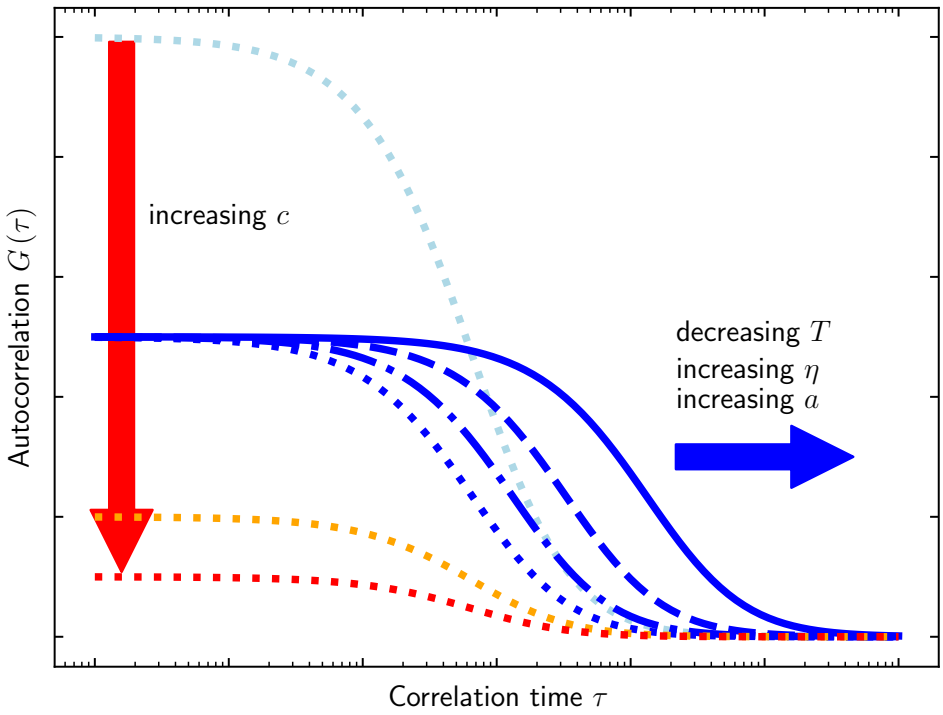

Figure E.2: **Schematic plot showing the behavior of intensity fluctuation autocorrelation function with varying conditions.** The autocorrelation is scaled down upon increasing the concentration (c) of fluorescent macromolecules (dotted lines, concentration grows from light-blue to red), and shifted right (in the direction of higher correlation time) with the decrease of diffusion coefficient (blue lines). The decrease may be due to decreasing temperature (T), increasing viscosity (η), or increasing hydrodynamic radius (a). Note that the x-axis is in a logarithmic scale.

by introducing a diffusion time τ_D:

$$\tau_D = \frac{w_0^2}{4D}. \tag{E.8}$$

The value of τ_D is obtained by a least-square fit of Eq. E.7 to the experimental autocorrelation function $G(\tau)$. Furthermore, the concentration c may be obtained from the relation [315]:

$$G_D(0) = \frac{1}{N} = \frac{1}{cV_{\text{eff}}} = \frac{1}{c\pi^{3/2}\kappa w_0^3}, \tag{E.9}$$

provided that the w_0 and κ are known. N denotes the mean number of fluorescent tracers in the focal spot of effective volume $V_{\text{eff}} = \pi^{3/2}\kappa w_0^3$.

Figure E.2 shows a summary of the behavior of autocorrelation function upon changes in concentration, temperature, viscosity, and hydrodynamic radius of a diffusing macromolecule (Eqs. 2.10 and E.9). FCS measurements are calibrated using fluorophores of known diffusion coefficients. Upon fitting the autocorrelation to the Eq. E.7, and using definition from Eq. E.8, the details of focal volume's shape (w_0, κ) are obtained.

E.2 Intersystem crossing

In principle, the fluctuations in intensity may originate not only from the Brownian motion but also from the photophysical processes and reactions in an excited state. Among these, the most prominent is the intersystem crossing: singlet-triplet transition, which makes the macromolecule fluorescently inactive due to the spin selection rule. It results in an apparent decrease of fluorescence intensity, which may well be misinterpreted as an enhanced diffusivity [217]. If the intersystem crossing timescale is significantly shorter than the diffusive one, the overall autocorrelation function may be written as a product [315]:

$$G(\tau) = G_D(\tau) G_T(\tau). \tag{E.10}$$

The part associated with the intersystem crossing reads:

$$G_T(\tau) = 1 + \frac{\bar{T}}{1-\bar{T}} \exp\left[-\tau/\tau_T\right], \tag{E.11}$$

where $\bar{T}$ is the fraction of macromolecules in the triplet state, and τ_T is the singlet-triplet relaxation time. $G_D(\tau)$ is given by Eq. E.7.

E.3 Experimental details

The FCS results presented in Section 4.3 were obtained by our collaborators from RWTH Aachen University and published along with our computational results [127]. Detailed technical description of the sample preparation and experimental setup are gathered in the Supporting Information to ref. [127]. Here only the most important information is summarized.

In the diffusion measurements, fluorescently-tagged tetrameric Streptavidin labelled with Alexa 647 was used as the tracer in nanomolar concentration regime. The protein was dissolved in aqueous buffer at $\mathrm{pH} = 7.5$ with various concentrations of crowders: Ficoll70 and $16\,\mathrm{nm}$-long (48 base pair) dsDNA. The calculated autocorrelation curves were fitted with Eq. E.10. Diffusion coefficient values presented in Tables E.1–E.4 are averaged over five independent measurements. When both numerator and denominator are burdened with uncertainties, σ_D and σ_{D_0} respectively, these propagate and result with the uncertainty of their ratio:

$$\sigma_{\frac{D}{D_0}} = \frac{D}{D_0} \sqrt{\left(\frac{\sigma_D}{D}\right)^2 + \left(\frac{\sigma_{D_0}}{D_0}\right)^2}. \tag{E.12}$$

Table E.1: **Diffusion coefficients of Streptavidin within Ficoll70 solutions of different crowder occupied volume fractions ϕ_{occ} measured with FCS.**

ϕ_{occ} %	$D\ (\mathrm{nm^2\,\mu s^{-1}})$	$\sigma_D\ (\mathrm{nm^2\,\mu s^{-1}})$	$\frac{D}{D_0}$	$\sigma_{\frac{D}{D_0}}$
0	63.8	1.2	1	0
5	57.8	0.8	0.91	0.02
10	52	1.3	0.82	0.02
20	41	3	0.65	0.05
35	23.0	1.1	0.360	0.018

Table E.2: **Diffusion coefficients of Streptavidin within dsDNA solutions of different crowder occupied volume fractions ϕ_{occ} measured with FCS.**

ϕ_{occ} %	$D\ (\mathrm{nm^2\,\mu s^{-1}})$	$\sigma_D\ (\mathrm{nm^2\,\mu s^{-1}})$	$\frac{D}{D_0}$	$\sigma_{\frac{D}{D_0}}$
1.25	50.0	0.6	0.784	0.017
2.5	36.4	0.5	0.570	0.013
5	25.8	0.7	0.404	0.013
10	4	1	0.056	0.016
15	3.9	0.4	0.062	0.006

Table E.3: **Diffusion coefficients of Streptavidin within dsDNA-Ficoll70 solutions of different molar fractions x_{dsDNA} and occupied volume fraction $\phi_{\mathrm{occ}} = 5\,\%$ measured with FCS.**

x_{dsDNA} %	$D\ (\mathrm{nm^2\,\mu s^{-1}})$	$\sigma_D\ (\mathrm{nm^2\,\mu s^{-1}})$	$\frac{D}{D_0}$	$\sigma_{\frac{D}{D_0}}$
0	57.8	0.8	0.91	0.02
25	25.0	0.6	0.392	0.012
50	22.6	1.4	0.35	0.02
75	20.4	1.4	0.32	0.02
100	25.8	0.6	0.404	0.012

Table E.4: **Diffusion coefficients of Streptavidin within dsDNA-Ficoll70 solutions of different molar fractions x_{dsDNA} and occupied volume fraction $\phi_{\mathrm{occ}} = 10\,\%$ measured with FCS.**

x_{dsDNA} %	$D\ (\mathrm{nm^2\,\mu s^{-1}})$	$\sigma_D\ (\mathrm{nm^2\,\mu s^{-1}})$	$\frac{D}{D_0}$	$\sigma_{\frac{D}{D_0}}$
0	52.0	1.3	0.82	0.02
25	23.3	0.4	0.364	0.009
50	17.5	0.4	0.275	0.009
75	7.4	0.6	0.115	0.009
100	3.6	1.0	0.056	0.016

Bibliography

1. Huang, B., Babcock, H. & Zhuang, X. Breaking the Diffraction Barrier: Super-Resolution Imaging of Cells. *Cell* **143,** 1047–1058 (2010).
2. Kwon, D. The secret lives of cells - as never seen before. *Nature* **598,** 558–560 (2021).
3. Albert, S., Wietrzynski, W., Lee, C. W., Schaffer, M., Beck, F., Schuller, J. M., Salomé, P. A., Plitzko, J. M., Baumeister, W. & Engel, B. D. Direct visualization of degradation microcompartments at the ER membrane. *Proceedings of the National Academy of Sciences* **117,** 1069–1080 (2020).
4. Mahamid, J., Pfeffer, S., Schaffer, M., Villa, E., Danev, R., Cuellar, L. K., Förster, F., Hyman, A. A., Plitzko, J. M. & Baumeister, W. Visualizing the molecular sociology at the HeLa cell nuclear periphery. *Science* **351,** 969–972 (2016).
5. Fulton, A. B. How Crowded Is the Cytoplasm? *Cell* **30,** 345–347 (1982).
6. Goodsell, D. S. Inside a living cell. *Trends in Biochemical Sciences* **16,** 203–206 (1991).
7. Goodsell, D. S. A Look Inside the Living Cell. *American Scientist* **80,** 457–465 (1992).
8. Ellis, R. J. Macromolecular crowding: obvious but underappreciated. *Trends in Biochemical Sciences* **26,** 597–604 (2001).
9. Zimmerman, S. B. & Trach, S. O. Estimation of macromolecule concentrations and excluded volume effects for the cytoplasm of *Escherichia coli*. *Journal of Molecular Biology* **222,** 599–620 (1991).
10. Skolnick, J. Perspective: On the importance of hydrodynamic interactions in the subcellular dynamics of macromolecules. *Journal of Chemical Physics* **145,** 100901 (2016).
11. Zimmerman, S. B. & Minton, A. P. Macromolecular Crowding: Biochemical, Biophysical, and Physiological Consequences. *Annual Review of Biophysics and Biomolecular Structure* **22,** 27–65 (1993).
12. Minton, A. P. Molecular crowding: Analysis of effects of high equilibria and rates in terms of volume exclusion. *Methods in Enzymology* **295,** 127–149 (1998).
13. Luby-Phelps, K. Cytoarchitecture and Physical Properties of Cytoplasm: Volume, Viscosity, Diffusion, Intracellular Surface Area. *International Review of Cytology* **192,** 189–221 (1999).
14. Zhou, H.-X., Rivas, G. & Minton, A. P. Macromolecular crowding and confinement: biochemical, biophysical, and potential physiological consequences. *Annual Review of Biophysics* **37,** 375–397 (2008).
15. Luby-Phelps, K. The physical chemistry of cytoplasm and its influence on cell function: an update. *Molecular Biology of the Cell* **24,** 2593–2596 (2013).

16. Kuznetsova, I. M., Turoverov, K. K. & Uversky, V. N. What Macromolecular Crowding Can Do to a Protein. *International Journal of Molecular Sciences* **15,** 23090–23140 (2014).

17. Minton, A. P. How can biochemical reactions within cells differ from those in test tubes? *Journal of Cell Science* **119,** 2863–2869 (2006).

18. Minton, A. P. How can biochemical reactions within cells differ from those in test tubes? *Journal of Cell Science* **128,** 1254 (2015).

19. Ross, J. L. The Dark Matter of Biology. *Biophysical Journal* **111,** 909–916 (2016).

20. Parry, B. R., Surovtsev, I. V., Cabeen, M. T., O'Hern, C. S., Dufresne, E. R. & Jacobs-Wagner, C. The Bacterial Cytoplasm Has Glass-like Properties and Is Fluidized by Metabolic Activity. *Cell* **156,** 183–194 (2014).

21. Nishizawa, K., Fujiwara, K., Ikenaga, M., Nakajo, N., Yanagisawa, M. & Mizuno, D. Universal glass-forming behavior of *in vitro* and *living* cytoplasm. *Scientific Reports* **7,** 15143 (2017).

22. Russell, B. *Dzieje zachodniej filozofii* pp. 685–686 (Aletheia, 2020).

23. Flammarion, C. *L'Atmosphère: Météorologie Populaire* p. 163 (1888).

24. Tomita, M. Whole-cell simulation: A grand challenge of the 21st century. *Trends in Biotechnology* **19,** 205–210 (2001).

25. Karr, J. R., Sanghvi, J. C., MacKlin, D. N., Gutschow, M. V., Jacobs, J. M., Bolival, B., Assad-Garcia, N., Glass, J. I. & Covert, M. W. A Whole-Cell Computational Model Predicts Phenotype from Genotype. *Cell* **150,** 389–401 (2012).

26. Feig, M. & Sugita, Y. Whole-Cell Models and Simulations in Molecular Detail. *Annual Review of Cell and Developmental Biology* **35,** 191–211 (2019).

27. Luthey-Schulten, Z. Integrating experiments, theory and simulations into whole-cell models. *Nature Methods* **18,** 446–447 (2021).

28. Maritan, M., Autin, L., Karr, J., Covert, M. W., Olson, A. J. & Goodsell, D. S. Building Structural Models of a Whole Mycoplasma Cell. *Journal of Molecular Biology* **434,** 167351 (2022).

29. Thornburg, Z. R., Bianchi, D. M., Brier, T. A., Gilbert, B. R., Earnest, T. M., Melo, M. C., Safronova, N., Sáenz, J. P., Cook, A. T., Wise, K. S., Hutchison III, C. A., Smith, H. O., Glass, J. I. & Luthey-Schulten, Z. Fundamental behaviors emerge from simulations of a living minimal cell. *Cell* **185,** 345–360 (2022).

30. Jumper, J., Evans, R., Pritzel, A., Green, T., Figurnov, M., Ronneberger, O., Tunyasuvunakool, K., Bates, R., Žídek, A., Potapenko, A., Bridgland, A., Meyer, C., Kohl, S. A. A., Ballard, A. J., Cowie, A., Romera-Paredes, B., Nikolov, S., Jain, R., Adler, J., Back, T., Petersen, S., Reiman, D., Clancy, E., Zielinski, M., Steinegger, M., Pacholska, M., Berghammer, T., Bodenstein, S., Silver, D., Vinyals, O., Senior, A. W., Kavukcuoglu, K., Kohli, P. & Hassabis, D. Highly accurate protein structure prediction with AlphaFold. *Nature* **596,** 583–589 (2021).

31. Berman, H. M., Westbrook, J., Feng, Z., Gilliland, G., Bhat, T. N., Weissig, H., Shindyalov, I. N. & Bourne, P. E. The Protein Data Bank. *Nucleic Acids Research* **28,** 235–242 (2000).

32. *Biophysical Society Celebrates 50 Years of the Protein Data Bank (PDB50)* `https://www.biophysics.org/meetings-events/special-sessions/protein-data-bank-50th-anniversary`.

33. Netz, R. R. & Eaton, W. A. Estimating computational limits on theoretical descriptions of biological cells. *Proceedings of the National Academy of Sciences* **118,** e2022753118 (2021).

34. Waldrop, M. M. The chips are down for Moore's law. *Nature News* **530,** 144–147 (2016).

35. Bicout, D. J. & Field, M. J. Stochastic Dynamics Simulations of Macromolecular Diffusion in a Model of the Cytoplasm of *Escherichia coli*. *The Journal of Physical Chemistry* **100,** 2489–2497 (1996).

36. Ando, T. & Skolnick, J. Crowding and hydrodynamic interactions likely dominate in vivo macromolecular motion. *Proceedings of the National Academy of Sciences* **107,** 18457–18462 (2010).

37. McGuffee, S. R. & Elcock, A. H. Diffusion, Crowding & Protein Stability in a Dynamic Molecular Model of the Bacterial Cytoplasm. *PLoS Computational Biology* **6,** e1000694 (2010).

38. Frembgen-Kesner, T. & Elcock, A. H. Computer simulations of the bacterial cytoplasm. *Biophysical Reviews* **5,** 109–119 (2013).

39. Brown, R. XXVII. A brief account of microscopical observations made in the months of June, July and August 1827, on the particles contained in the pollen of plants; and on the general existence of active molecules in organic and inorganic bodies. *The Philosophical Magazine* **4,** 161–173 (1828).

40. Einstein, A. Über die von der molekularkinetischen Theorie der Wärme geforderte Bewegung von in ruhenden Flüssigkeiten suspendierten Teilchen. *Annalen der Physik* **17,** 549–560 (1905).

41. Sutherland, W. LXXV. A dynamical theory of diffusion for non-electrolytes and the molecular mass of albumin. *Philosophical Magazine Series* **9,** 781–785 (1905).

42. Smoluchowski, M. Zur kinetischen Theorie der Brownschen Molekularbewegung und der Suspensionen. *Annalen der Physik* **326,** 756–780 (1906).

43. Frey, E. & Kroy, K. Brownian motion: A paradigm of soft matter and biological physics. *Annalen der Physik (Leipzig)* **14,** 20–50 (2005).

44. Renn, J. Einstein's invention of Brownian motion. *Annalen der Physik (Leipzig)* **14,** 23–37 (2005).

45. Sokolov, I. M. & Klafter, J. From diffusion to anomalous diffusion: A century after Einstein's Brownian motion. *Chaos* **15,** 026103 (2005).

46. Langevin, P. Sur la théorie du mouvement brownien. *Comptes Rendus de l'Académie des Sciences (Paris)* **146,** 530–533 (1908).

47. Stokes, G. G. On the effect of internal friction of fluids on the motion of pendulums. *Transactions of the Cambridge Philosophical Society* **9,** 8–106 (1850).

48. Feynman, R. P., Leighton, R. B. & Sands, M. *Feynmana Wykłady z Fizyki* pp. 244–247 (Polskie Wydawnictwo Naukowe, 2013).

49. Metzler, R., Jeon, J. H. & Cherstvy, A. G. Non-Brownian diffusion in lipid membranes: Experiments and simulations. *Biochimica et Biophysica Acta (BBA) - Biomembranes* **1858,** 2451–2467 (2016).

50. Golding, I. & Cox, E. C. Physical Nature of Bacterial Cytoplasm. *Physical Review Letters* **96,** 098102 (2006).

51. Klafter, J. & Sokolov, I. M. Anomalous diffusion spreads its wings. *Physics World* **18,** 29–32 (2005).

52. Sokolov, I. M. Models of anomalous diffusion in crowded environments. *Soft Matter* **8,** 9043–9052 (2012).

53. Höfling, F. & Franosch, T. Anomalous transport in the crowded world of biological cells. *Reports on Progress in Physics* **76,** 046602 (2013).

54. Metzler, R., Jeon, J. H., Cherstvy, A. G. & Barkai, E. Anomalous diffusion models and their properties: non-stationarity, non-ergodicity, and ageing at the centenary of single particle tracking. *Physical Chemistry Chemical Physics* **16,** 24128–24164 (2014).

55. Saxton, M. J. Anomalous diffusion due to binding: a Monte Carlo study. *Biophysical Journal* **70,** 1250–1262 (1996).

56. Saxton, M. J. Anomalous diffusion due to obstacles: a Monte Carlo study. *Biophysical Journal* **66,** 394–401 (1994).

57. Weiss, M., Elsner, M., Kartberg, F. & Nilsson, T. Anomalous Subdiffusion Is a Measure for Cytoplasmic Crowding in Living Cells. *Biophysical Journal* **87,** 3518–3524 (2004).

58. Klett, K., Cherstvy, A. G., Shin, J., Sokolov, I. M. & Metzler, R. Non-Gaussian, transiently anomalous, and ergodic self-diffusion of flexible dumbbells in crowded two-dimensional environments: Coupled translational and rotational motions. *Physical Review E* **104,** 064603 (2021).

59. Lang, P. R. & Liu, Y. in *Physics of Life* (eds Gomper, G., Dhont, J. K., Elgeti, J., Fahlke, C., Fedosov, D. A., Förster, S., Lettinga, M. P. & Offenhäusser, A.) pp. 489–504 (Forschungszentrum Jülich GmbH Zentralbibliothek, Verlag Jülich, 2018).

60. Sundararaj, S., Guo, A., Habibi-Nazhad, B., Rouani, M., Stothard, P., Ellison, M. & Wishart, D. S. The CyberCell Database (CCDB): a comprehensive, self-updating, relational database to coordinate and facilitate *in silico* modeling of *Escherichia coli*. *Nucleic Acids Research* **32,** D293–D295 (2004).

61. Milo, R., Jorgensen, P., Moran, U., Weber, G. & Springer, M. BioNumbers—the database of key numbers in molecular and cell biology. *Nucleic Acids Research* **38,** D750–D753 (2010).

62. Tabaka, M., Kalwarczyk, T., Szymanski, J., Hou, S. & Holyst, R. The effect of macromolecular crowding on mobility of biomolecules, association kinetics, and gene expression in living cells. *Frontiers in Physics* **2,** 54 (2014).

63. Gershon, N. D., Porter, K. R. & Trus, B. L. The cytoplasmic matrix: its volume and surface area and the diffusion of molecules through it. *Proceedings of the National Academy of Sciences* **82,** 5030–5034 (1985).

64. Heuser, J. Whatever happened to the 'microtrabecular concept'? *Biology of the Cell* **94,** 561–596 (2003).

65. Minton, A. P. Excluded Volume as a Determinant of Macromolecular Structure and Reactivity. *Biopolymers* **20,** 2093–2120 (1981).

66. Diestler, D. J. & Knapp, E. W. Statistical Mechanics of the Stability of Multivalent Ligand-Receptor Complexes. *The Journal of Physical Chemistry C* **114,** 5287–5304 (2010).

67. Reiss, H., Frisch, H. L. & Lebowitz, J. L. Statistical Mechanics of Rigid Spheres. *The Journal of Chemical Physics* **31,** 369–380 (1959).

68. Helfand, E., Reiss, H., Frisch, H. L. & Lebowitz, J. L. Scaled Particle Theory of Fluids. *The Journal of Chemical Physics* **33,** 1379–1385 (1960).

69. Lebowitz, J. L., Helfand, E. & Praestgaard, E. Scaled Particle Theory of Fluid Mixtures. *The Journal of Chemical Physics* **43,** 774–779 (1965).

70. Gibbons, R. M. The scaled particle theory for particles of arbitrary shape. *Molecular Physics* **17,** 81–86 (1969).

71. Graziano, G. A purely geometric derivation of the scaled particle theory formula for the work of cavity creation in a liquid. *Chemical Physics Letters* **440,** 221–223 (2007).

72. Schlick, T., Portillo-Ledesma, S., Myers, C. G., Beljak, L., Chen, J., Dakhel, S., Darling, D., Ghosh, S., Hall, J., Jan, M., Liang, E., Saju, S., Vohr, M., Wu, C., Xu, Y. & Xue, E. Biomolecular Modeling and Simulation: A Prospering Multidisciplinary Field. *Annual Review of Biophysics* **50,** 267–301 (2021).

73. Schlick, T. & Portillo-Ledesma, S. Biomolecular modeling thrives in the age of technology. *Nature Computational Science* **1,** 321–331 (2021).

74. Pedebos, C. & Khalid, S. Simulations of the spike: molecular dynamics and SARS-CoV-2. *Nature Reviews Microbiology* **20,** 192 (2022).

75. Ermak, D. L. & McCammon, J. A. Brownian dynamics with hydrodynamic interactions. *The Journal of Chemical Physics* **69,** 1352–1360 (1978).

76. Bidone, T. C., Skeeters, A. V., Oakes, P. W. & Voth, G. A. Multiscale model of integrin adhesion assembly. *PLOS Computational Biology* **15,** e1007077 (2019).

77. Długosz, M. & Trylska, J. Diffusion in crowded biological environments: applications of Brownian dynamics. *BMC Biophysics* **4,** 3 (2011).

78. Huber, G. A. & McCammon, J. A. Brownian Dynamics Simulations of Biological Molecules. *Trends in Chemistry* **1,** 727–738 (2019).

79. Muñiz-Chicharro, A., Votapka, L. W., Amaro, R. E. & Wade, R. C. Brownian dynamics simulations of biomolecular diffusional association processes. *WIREs Computational Molecular Science,* e1649 (2022).

80. Purcell, E. M. Life at low Reynolds number. *American Journal of Physics* **45,** 3–11 (1977).

81. Durlofsky, L., Brady, J. F. & Bossis, G. Dynamic simulation of hydrodynamically interacting particles. *Journal of Fluid Mechanics* **180,** 21–49 (1987).

82. Phillips, R. J., Brady, J. F. & Bossis, G. Hydrodynamic transport properties of hard-sphere dispersions. I. Suspensions of freely mobile particles. *The Physics of Fluids* **31,** 3462–3472 (1988).

83. Brady, J. F., Phillips, R. J. & Bossis, G. Dynamic simulation of hydrodynamically interacting suspensions. *Journal of Fluid Mechanics* **195,** 257–280 (1988).

84. Brady, J. F. & Bossis, G. Stokesian Dynamics. *Annual Review of Fluid Mechanics* **20,** 111–157 (1988).

85. Reichert, M. *Hydrodynamic Interactions in Colloidal and Biological Systems* PhD thesis (2006).

86. Rotne, J. & Prager, S. Variational Treatment of Hydrodynamic Interaction in Polymers. *The Journal of Chemical Physics* **50,** 4831–4837 (1969).

87. Yamakawa, H. Transport Properties of Polymer Chains in Dilute Solution: Hydrodynamic Interaction. *The Journal of Chemical Physics* **53,** 436–443 (1970).

88. De La Torre, J. G. & Bloomfield, V. A. Hydrodynamic properties of macromolecular complexes. I. Translation. *Biopolymers* **16,** 1747–1763 (1977).

89. Zuk, P. J., Wajnryb, E., Mizerski, K. A. & Szymczak, P. Rotne-Prager-Yamakawa approximation for different-sized particles in application to macromolecular bead models. *Journal of Fluid Mechanics* **741,** R5 (2014).

90. Jeffrey, D. J. & Onishi, Y. Calculation of the resistance and mobility functions for two unequal rigid spheres in low-Reynolds-number flow. *Journal of Fluid Mechanics* **139,** 261–290 (1984).

91. Cichocki, B., Ekiel-Jeżewska, M. L. & Wajnryb, E. Lubrication corrections for three-particle contribution to short-time self-diffusion coefficients in colloidal dispersions. *The Journal of Chemical Physics* **111,** 3265–3273 (1999).

92. Frenkel, D. & Smit, B. *Understanding molecular simulation: from algorithms to applications* pp. 23–27 (Academic Press, 2002).

93. Widom, B. Some Topics in the Theory of Fluids. *The Journal of Chemical Physics* **39,** 2808–2812 (1963).

94. Qin, S. & Zhou, H. X. Atomistic Modeling of Macromolecular Crowding Predicts Modest Increases in Protein Folding and Binding Stability. *Biophysical Journal* **97,** 12–19 (2009).

95. Qin, S., Minh, D. D., McCammon, J. A. & Zhou, H. X. Method to Predict Crowding Effects by Postprocessing Molecular Dynamics Trajectories: Application to the Flap Dynamics of HIV-1 Protease. *The Journal of Physical Chemistry Letters* **1,** 107–110 (2010).

96. Schavemaker, P. E., Boersma, A. J. & Poolman, B. How Important Is Protein Diffusion in Prokaryotes? *Frontiers in Molecular Biosciences* **5,** 93 (2018).

97. Soh, S., Byrska, M., Kandere-Grzybowska, K. & Grzybowski, B. A. Reaction-Diffusion Systems in Intracellular Molecular Transport and Control. *Angewandte Chemie - International Edition* **49,** 4170–4198 (2010).

98. Wojcieszyn, J. W., Schlegel, R. A., Wu, E.-S. & Jacobson, K. A. Diffusion of injected macromolecules within the cytoplasm of living cells. *Proceedings of the National Academy of Sciences* **78,** 4407–4410 (1981).

99. Lakowicz, J. R. *Principles of Fluorescence Spectroscopy* pp. 814–815 (Springer, 2010).

100. Lippincott-Schwartz, J., Snapp, E. & Kenworthy, A. Studying protein dynamics in living cells. *Nature Reviews Molecular Cell Biology* **2,** 444–456 (2001).

101. Wang, Y. L., Lanni, F., McNeil, P. L., Ware, B. R. & Taylor, D. L. Mobility of cytoplasmic and membrane-associated actin in living cells. *Proceedings of the National Academy of Sciences* **79,** 4660–4664 (1982).

102. Luby-Phelps, K., Taylor, D. L. & Lanni, F. Probing the structure of cytoplasm. *The Journal of Cell Biology* **102,** 2015–2022 (1986).

103. Luby-Phelps, K., Castle, P. E., Taylor, D. L. & Lanni, F. Hindered diffusion of inert tracer particles in the cytoplasm of mouse 3T3 cells. *Proceedings of the National Academy of Sciences* **84,** 4910–4913 (1987).

104. Seksek, O., Biwersi, J. & Verkman, A. S. Translational Diffusion of Macromolecule-Sized Solutes in Cytoplasm and Nucleus. *The Journal of Cell Biology* **138,** 131–142 (1997).

105. Swaminathan, R., Hoang, C. P. & Verkman, A. S. Photobleaching recovery and anisotropy decay of green fluorescent protein GFP-S65T in solution and cells: cytoplasmic viscosity probed by green fluorescent protein translational and rotational diffusion. *Biophysical Journal* **72,** 1900–1907 (1997).

106. Potma, E. O., De Boeij, W. P., Bosgraaf, L., Roelofs, J., Van Haastert, P. J. & Wiersma, D. A. Reduced Protein Diffusion Rate by Cytoskeleton in Vegetative and Polarized *Dictyostelium* Cells. *Biophysical Journal* **81,** 2010–2019 (2001).

107. Elowitz, M. B., Surette, M. G., Wolf, P. E., Stock, J. B. & Leibler, S. Protein mobility in the cytoplasm of *Escherichia coli*. *Journal of Bacteriology* **181,** 197–203 (1999).

108. Nenninger, A., Mastroianni, G. & Mullineaux, C. W. Size Dependence of Protein Diffusion in the Cytoplasm of Escherichia coli. *Journal of Bacteriology* **192,** 4535–4540 (2010).

109. Kumar, M., Mommer, M. S. & Sourjik, V. Mobility of Cytoplasmic, Membrane, and DNA-Binding Proteins in *Escherichia coli*. *Biophysical Journal* **98,** 552–559 (2010).

110. Mika, J. T., Van Den Bogaart, G., Veenhoff, L., Krasnikov, V. & Poolman, B. Molecular sieving properties of the cytoplasm of *Escherichia coli* and consequences of osmotic stress. *Molecular Microbiology* **77,** 200–207 (2010).

111. Mika, J. T. & Poolman, B. Macromolecule diffusion and confinement in prokaryotic cells. *Current Opinion in Biotechnology* **22,** 117–126 (2011).

112. Shen, H., Tauzin, L. J., Baiyasi, R., Wang, W., Moringo, N., Shuang, B. & Landes, C. F. Single Particle Tracking: From Theory to Biophysical Applications. *Chemical Reviews* **117,** 7331–7376 (2017).

113. Di Rienzo, C., Piazza, V., Gratton, E., Beltram, F. & Cardarelli, F. Probing short-range protein Brownian motion in the cytoplasm of living cells. *Nature Communications* **5,** 5891 (2014).

114. Etoc, F., Balloul, E., Vicario, C., Normanno, D., Liße, D., Sittner, A., Piehler, J., Dahan, M. & Coppey, M. Non-specific interactions govern cytosolic diffusion of nanosized objects in mammalian cells. *Nature Materials* **17,** 740–746 (2018).

115. Bellotto, N., Agudo-Canalejo, J., Colin, R., Golestanian, R., Malengo, G. & Sourjik, V. Dependence of diffusion in *Escherichia coli* cytoplasm on protein size, environmental conditions and cell growth. *eLife* **11,** e82654 (2022).

116. Konopka, M. C., Shkel, I. A., Cayley, S., Record, M. T. & Weisshaar, J. C. Crowding and Confinement Effects on Protein Diffusion In Vivo. *Journal of Bacteriology* **188,** 6115–6123 (2006).

117. Mullineaux, C. W., Nenninger, A., Ray, N. & Robinson, C. Diffusion of Green Fluorescent Protein in Three Cell Environments in *Escherichia Coli*. *Journal of Bacteriology* **188,** 3442–3448 (2006).

118. Van Den Bogaart, G., Hermans, N., Krasnikov, V. & Poolman, B. Protein mobility and diffusive barriers in *Escherichia coli*: consequences of osmotic stress. *Molecular Microbiology* **64,** 858–871 (2007).

119. Lukacs, G. L., Haggie, P., Seksek, O., Lechardeur, D., Freedman, N. & Verkman, A. S. Size-Dependent DNA Mobility in Cytoplasm and Nucleus. *Journal of Biological Chemistry* **275,** 1625–1629 (2000).

120. Lampo, T. J., Stylianidou, S., Backlund, M. P., Wiggins, P. A. & Spakowitz, A. J. Cytoplasmic RNA-Protein Particles Exhibit Non-Gaussian Subdiffusive Behavior. *Biophysical Journal* **112,** 532–542 (2017).

121. Sabri, A., Xu, X., Krapf, D. & Weiss, M. Elucidating the Origin of Heterogeneous Anomalous Diffusion in the Cytoplasm of Mammalian Cells. *Physical Review Letters* **125,** 058101 (2020).

122. Banks, D. S. & Fradin, C. Anomalous Diffusion of Proteins Due to Molecular Crowding. *Biophysical Journal* **89,** 2960–2971 (2005).

123. Wedel, M. J. A monument of inefficiency: The presumed course of the recurrent laryngeal nerve in sauropod dinosaurs. *Acta Palaeontologica Polonica* **57,** 251–256 (2012).

124. Soh, S., Banaszak, M., Kandere-Grzybowska, K. & Grzybowski, B. A. Why Cells Are Microscopic: A Transport-Time Perspective. *The Journal of Physical Chemistry Letters* **4,** 861–865 (2013).

125. Verkman, A. Solute and macromolecule diffusion in cellular aqueous compartments. *Trends in Biochemical Sciences* **27,** 27–33 (2002).

126. Junker, N. O., Vaghefikia, F., Albarghash, A., Höfig, H., Kempe, D., Walter, J., Otten, J., Pohl, M., Katranidis, A., Wiegand, S. & Fitter, J. Impact of Molecular Crowding on Translational Mobility and Conformational Properties of Biological Macromolecules. *The Journal of Physical Chemistry B* **123,** 4477–4486 (2019).

127. Skóra, T., Vaghefikia, F., Fitter, J. & Kondrat, S. Macromolecular Crowding: How Shape and Interactions Affect Diffusion. *The Journal of Physical Chemistry B* **124,** 7537–7543 (2020).

128. Li, C., Wang, Y. & Pielak, G. J. Translational and Rotational Diffusion of a Small Globular Protein under Crowded Conditions. *The Journal of Physical Chemistry B* **113,** 13390–13392 (2009).

129. Wang, Y., Li, C. & Pielak, G. J. Effects of Proteins on Protein Diffusion. *Journal of the American Chemical Society* **132,** 9392–9397 (2010).

130. Roosen-Runge, F., Hennig, M., Zhang, F., Jacobs, R. M. J., Sztucki, M., Schober, H., Seydel, T. & Schreiber, F. Protein self-diffusion in crowded solutions. *Proceedings of the National Academy of Sciences* **108,** 11815–11820 (2011).

131. Ridgway, D., Broderick, G., Lopez-Campistrous, A., Ru'aini, M., Winter, P., Hamilton, M., Boulanger, P., Kovalenko, A. & Ellison, M. J. Coarse-Grained Molecular Simulation of Diffusion and Reaction Kinetics in a Crowded Virtual Cytoplasm. *Biophysical Journal* **94,** 3748–3759 (2008).

132. Yu, I., Mori, T., Ando, T., Harada, R., Jung, J., Sugita, Y. & Feig, M. Biomolecular interactions modulate macromolecular structure and dynamics in atomistic model of a bacterial cytoplasm. *eLife* **5,** e19274 (2016).

133. Kalwarczyk, T., Ziębacz, N., Bielejewska, A., Zaboklicka, E., Koynov, K., Szymański, J., Wilk, A., Patkowski, A., Gapiński, J., Butt, H. J. & Hołyst, R. Comparative Analysis of Viscosity of Complex Liquids and Cytoplasm of Mammalian Cells at the Nanoscale. *Nano Letters* **11,** 2157–2163 (2011).

134. Kwapiszewska, K., Szczepański, K., Kalwarczyk, T., Michalska, B., Patalas-Krawczyk, P., Szymański, J., Andryszewski, T., Iwan, M., Duszyński, J. & Hołyst, R. Nanoscale Viscosity of Cytoplasm Is Conserved in Human Cell Lines. *The Journal of Physical Chemistry Letters* **11,** 6914–6920 (2020).

135. Saxton, M. J. Lateral diffusion in an archipelago. Distance dependence of the diffusion coefficient. *Biophysical Journal* **56,** 615–622 (1989).

136. Saxton, M. J. Lateral diffusion in an archipelago. The effect of mobile obstacles. *Biophysical Journal* **52,** 989–997 (1987).

137. Saxton, M. J. Lateral diffusion in a mixture of mobile and immobile particles. A Monte Carlo study. *Biophysical Journal* **58,** 1303–1306 (1990).

138. Saxton, M. J. Lateral diffusion and aggregation. A Monte Carlo study. *Biophysical Journal* **61,** 119–128 (1992).

139. Saxton, M. J. Lateral diffusion in an archipelago. Single-particle diffusion. *Biophysical Journal* **64,** 1766–1780 (1993).

140. Saxton, M. J. Lateral diffusion in an archipelago. Dependence on tracer size. *Biophysical Journal* **64,** 1053–1062 (1993).

141. Ellery, A. J., Baker, R. E. & Simpson, M. J. Calculating the Fickian diffusivity for a lattice-based random walk with agents and obstacles of different shapes and sizes. *Physical Biology* **12,** 066010 (2015).

142. Mercier, J. F. & Slater, G. W. Numerically exact diffusion coefficients for lattice systems with periodic boundary conditions. II. Numerical approach and applications. *The Journal of Chemical Physics* **110,** 6057–6065 (1999).

143. Mercier, J. F., Slater, G. W. & Guo, H. L. Numerically exact diffusion coefficients for lattice systems with periodic boundary conditions. I. Theory. *The Journal of Chemical Physics* **110,** 6050–6056 (1999).

144. Hanna, S., Hess, W. & Klein, R. Self-diffusion of spherical Brownian particles with hard-core interaction. *Physica A: Statistical Mechanics and its Applications* **111,** 181–199 (1982).

145. Muramatsu, N. & Minton, A. P. Tracer diffusion of globular proteins in concentrated protein solutions. *Proceedings of the National Academy of Sciences* **85,** 2984–2988 (1988).

146. Han, J. & Herzfeld, J. Macromolecular diffusion in crowded solutions. *Biophysical Journal* **65,** 1155–1161 (1993).

147. Cichocki, B. & Felderhof, B. U. Long-time self-diffusion coefficient and zero-frequency viscosity of dilute suspensions of spherical Brownian particles. *The Journal of Chemical Physics* **89,** 3705–3709 (1988).

148. Tokuyama, M. & Oppenheim, I. Dynamics of hard-sphere suspensions. *Physical Review E* **50,** R16 (1994).

149. Ostrowska, N. *Effects of macromolecular crowding on the activity and dynamics of the NS3/4A protease from the hepatitis C virus. The synergy between experiments and molecular dynamics simulations* PhD thesis (2022).

150. Laurent, T. C., Björk, I., Pietruszkiewicz, A. & Persson, H. On the interaction between polysaccharides and other macromolecules: II. The transport of globular particles through hyaluronic acid solutions. *Biochimica et Biophysica Acta* **78,** 351–359 (1963).

151. Jamieson, A. M., Southwick, J. G. & Blackwell, J. Dynamical behavior of xanthan polysaccharide in solution. *Journal of Polymer Science: Polymer Physics Edition* **20,** 1513–1524 (1982).

152. Szymański, J., Patkowski, A., Wilk, A., Garstecki, P. & Hołyst, R. Diffusion and Viscosity in a Crowded Environment: from Nano- to Macroscale. *The Journal of Physical Chemistry B* **110,** 25593–25597 (2006).

153. Hołyst, R., Bielejewska, A., Szymański, J., Wilk, A., Patkowski, A., Gapiński, J., Żywociński, A., Kalwarczyk, T., Kalwarczyk, E., Tabaka, M., Ziębacz, N. & Wieczorek, S. A. Scaling form of viscosity at all length-scales in poly(ethylene glycol) solutions studied by fluorescence correlation spectroscopy and capillary electrophoresis. *Physical Chemistry Chemical Physics* **11,** 9025–9032 (2009).

154. Agasty, A., Wisniewska, A., Kalwarczyk, T., Koynov, K. & Hołyst, R. Macroscopic Viscosity of Polymer Solutions from the Nanoscale Analysis. *ACS Applied Polymer Materials* **3,** 2813–2822 (2021).

155. Phillies, G. D., Ullmann, G. S., Ullmann, K. & Lin, T. H. Phenomenological scaling laws for "semidilute" macromolecule solutions from light scattering by optical probe particles. *The Journal of Chemical Physics* **82,** 5242–5246 (1985).

156. Dauty, E. & Verkman, A. S. Molecular crowding reduces to a similar extent the diffusion of small solutes and macromolecules: measurement by fluorescence correlation spectroscopy. *Journal of Molecular Recognition* **17,** 441–447 (2004).

157. Cukier, R. I. Diffusion of Brownian Spheres in Semidilute Polymer Solutions. *Macromolecules* **17,** 252–255 (1984).

158. Spitzer, J. J. & Poolman, B. Electrochemical structure of the crowded cytoplasm. *Trends in Biochemical Sciences* **30,** 536–541 (2005).

159. Schavemaker, P. E., Śmigiel, W. M. & Poolman, B. Ribosome surface properties may impose limits on the nature of the cytoplasmic proteome. *eLife* **6,** e30084 (2017).

160. Nawrocki, G., Wang, P. H., Yu, I., Sugita, Y. & Feig, M. Slow-Down in Diffusion in Crowded Protein Solutions Correlates with Transient Cluster Formation. *The Journal of Physical Chemistry B* **121,** 11072–11084 (2017).

161. Welty, R. S. *Effects of Macromolecular Crowding on Diffusion* Master thesis 2013.

162. Kalwarczyk, T., Tabaka, M. & Hołyst, R. Biologistics—Diffusion coefficients for complete proteome of *Escherichia coli*. *Bioinformatics* **28,** 2971–2978 (2012).

163. Tabaka, M., Kalwarczyk, T. & Hołyst, R. Quantitative influence of macromolecular crowding on gene regulation kinetics. *Nucleic Acids Research* **42,** 727–738 (2014).

164. Wisniewska, A., Sozanski, K., Kalwarczyk, T., Kedra-Krolik, K. & Hołyst, R. Scaling Equation for Viscosity of Polymer Mixtures in Solutions with Application to Diffusion of Molecular Probes. *Macromolecules* **50,** 4555–4561 (2017).

165. Szczepański, K., Kwapiszewska, K. & Hołyst, R. Stability of cytoplasmic nanoviscosity during cell cycle of HeLa cells synchronized with Aphidicolin. *Scientific Reports* **9,** 16486 (2019).

166. Kwapiszewska, K., Kalwarczyk, T., Michalska, B., Szczepański, K., Szymański, J., Patalas-Krawczyk, P., Andryszewski, T., Iwan, M., Duszyński, J. & Hołyst, R. Determination of oligomerization state of Drp1 protein in living cells at nanomolar concentrations. *Scientific Reports* **9,** 5906 (2019).

167. Bubak, G., Kwapiszewska, K., Kalwarczyk, T., Bielec, K., Andryszewski, T., Iwan, M., Bubak, S. & Hołyst, R. Quantifying Nanoscale Viscosity and Structures of Living Cells Nucleus from Mobility Measurements. *The Journal of Physical Chemistry Letters* **12,** 294–301 (2021).

168. Kasza, K. E., Rowat, A. C., Liu, J., Angelini, T. E., Brangwynne, C. P., Koenderink, G. H. & Weitz, D. A. The cell as a material. *Current Opinion in Cell Biology* **19,** 101–107 (2007).

169. Xiang, Y., Surovtsev, I. V., Chang, Y., Govers, S. K., Parry, B. R., Liu, J. & Jacobs-Wagner, C. Interconnecting solvent quality, transcription, and chromosome folding in *Escherichia coli*. *Cell* **184,** 3626–3642 (2021).

170. Modesti, G., Zimmermann, B., Börsch, M., Herrmann, A. & Saalwächter, K. Diffusion in Model Networks as Studied by NMR and Fluorescence Correlation Spectroscopy. *Macromolecules* **42,** 4681–4689 (2009).

171. Parrish, E., Caporizzo, M. A. & Composto, R. J. Network confinement and heterogeneity slows nanoparticle diffusion in polymer gels. *The Journal of Chemical Physics* **146,** 203318 (2017).

172. Godec, A., Bauer, M. & Metzler, R. Collective dynamics effect transient subdiffusion of inert tracers in flexible gel networks. *New Journal of Physics* **16,** 092002 (2014).

173. Cho, H. W., Kim, H., Sung, B. J. & Kim, J. S. Tracer Diffusion in Tightly-Meshed Homogeneous Polymer Networks: A Brownian Dynamics Simulation Study. *Polymers* **12,** 2067 (2020).

174. Vagias, A., Košovan, P., Koynov, K., Holm, C., Butt, H. J. & Fytas, G. Dynamics in Stimuli-Responsive Poly(N-isopropylacrylamide) Hydrogel Layers As Revealed by Fluorescence Correlation Spectroscopy. *Macromolecules* **47,** 5303–5312 (2014).

175. Vagias, A., Sergelen, K., Koynov, K., Košovan, P., Dostalek, J., Jonas, U., Knoll, W. & Fytas, G. Diffusion and Permeation of Labeled IgG in Grafted Hydrogels. *Macromolecules* **50,** 4770–4779 (2017).

176. Blanco, P. M., Via, M., Garcés, J. L., Madurga, S. & Mas, F. Brownian Dynamics Computational Model of Protein Diffusion in Crowded Media with Dextran Macromolecules as Obstacles. *Entropy* **19,** 105 (2017).

177. Löwdin, P.-O. O. Some comments on the present situation of quantum chemistry in view of the discussions at the Dubrovnik workshop on the electronic structure of molecules. *Pure and Applied Chemistry* **61,** 2185–2194 (1989).

178. Henderson, D., Duh, D.-M., Chu, X. & Wasan, D. An Expression for the Dispersion Force between Colloidal Particles. *Journal of Colloid and Interface Science* **185,** 265–268 (1997).

179. Levin, Y. Electrostatic correlations: from plasma to biology. *Reports on Progress in Physics* **65,** 1577–1632 (2002).

180. Cichocki, B., Rubin, M., Niedzwiecka, A. & Szymczak, P. Diffusion coefficients of elastic macromolecules. *Journal of Fluid Mechanics* **878,** R3 (2019).

181. Zuk, P. J., Cichocki, B. & Szymczak, P. Intrinsic viscosity of macromolecules within the generalized Rotne–Prager–Yamakawa approximation. *Journal of Fluid Mechanics* **822,** R2 (2017).

182. Zuk, P. J., Cichocki, B. & Szymczak, P. GRPY: An Accurate Bead Method for Calculation of Hydrodynamic Properties of Rigid Biomacromolecules. *Biophysical Journal* **115,** 782–800 (2018).

183. Frembgen-Kesner, T. & Elcock, A. H. Striking Effects of Hydrodynamic Interactions on the Simulated Diffusion and Folding of Proteins. *Journal of Chemical Theory and Computation* **5,** 242–256 (2009).

184. Iniesta, A. & García de la Torre, J. A second-order algorithm for the simulation of the Brownian dynamics of macromolecular models. *The Journal of Chemical Physics* **92,** 2015–2018 (1990).

185. Balbo, J., Mereghetti, P., Herten, D.-P. & Wade, R. C. The Shape of Protein Crowders is a Major Determinant of Protein Diffusion. *Biophysical Journal* **104,** 1576–1584 (2013).

186. Kondrat, S., Zimmermann, O., Wiechert, W. & von Lieres, E. The effect of composition on diffusion of macromolecules in a crowded environment. *Physical Biology* **12,** 046003 (2015).

187. Blanco, P. M., Garcés, J. L., Madurga, S. & Mas, F. Macromolecular diffusion in crowded media beyond the hard-sphere model. *Soft Matter* **14,** 3105–3114 (2018).

188. Słyk, E., Skóra, T. & Kondrat, S. How macromolecules softness affects diffusion under crowding. *Soft Matter* **18,** 5366–5370 (2022).

189. Noro, M. G. & Frenkel, D. Extended corresponding-states behavior for particles with variable range attractions. *The Journal of Chemical Physics* **113,** 2941–2944 (2000).

190. Saphire, E. O., Parren, P. W., Pantophlet, R., Zwick, M. B., Morris, G. M., Rudd, P. M., Dwek, R. A., Stanfield, R. L., Burton, D. R. & Wilson, I. A. Crystal Structure of a Neutralizing Human IgG Against HIV-1: A Template for Vaccine Design. *Science* **293,** 1155–1159 (2001).

191. Sehnal, D., Bittrich, S., Deshpande, M., Svobodová, R., Berka, K., Bazgier, V., Velankar, S., Burley, S. K., Koča, J. & Rose, A. S. Mol* Viewer: modern web app for 3D visualization and analysis of large biomolecular structures. *Nucleic Acids Research* **49,** W431–W437 (2021).

192. Bongini, L., Fanelli, D., Piazza, F., De Los Rios, P., Sandin, S. & Skoglund, U. Freezing immunoglobulins to see them move. *Proceedings of the National Academy of Sciences* **101,** 6466–6471 (2004).

193. Fang, X., Kruse, K., Lu, T. & Wang, J. Nonequilibrium physics in biology. *Reviews of Modern Physics* **91,** 045004 (2019).

194. Losa, J., Leupold, S., Alonso-Martinez, D., Vainikka, P., Thallmair, S., Tych, K. M., Marrink, S. J. & Heinemann, M. Perspective: a stirring role for metabolism in cells. *Molecular Systems Biology* **18,** e10822 (2022).

195. Li, B., Dou, S.-X., Yuan, J.-W., Liu, Y.-R., Li, W., Ye, F., Wang, P.-Y. & Li, H. Intracellular transport is accelerated in early apoptotic cells. *Proceedings of the National Academy of Sciences* **115,** 12118–12123 (2018).

196. Feng, M. & Gilson, M. K. Enhanced Diffusion and Chemotaxis of Enzymes. *Annual Review of Biophysics* **49,** 87–105 (2020).

197. Pressé, S. A thermodynamic perspective on enhanced enzyme diffusion. *Proceedings of the National Academy of Sciences* **117,** 32189–32191 (2020).

198. Ghosh, S., Somasundar, A. & Sen, A. Enzymes as Active Matter. *Annual Review of Condensed Matter Physics* **12,** 177–200 (2021).

199. Zhao, X., Dey, K. K., Jeganathan, S., Butler, P. J., Córdova-Figueroa, U. M. & Sen, A. Enhanced Diffusion of Passive Tracers in Active Enzyme Solutions. *Nano Letters* **17,** 4807–4812 (2017).

200. Zhang, Y., Armstrong, M. J., Bassir Kazeruni, N. M. & Hess, H. Aldolase Does Not Show Enhanced Diffusion in Dynamic Light Scattering Experiments. *Nano Letters* **18,** 8025–8029 (2018).

201. Günther, J. P., Majer, G. & Fischer, P. Absolute diffusion measurements of active enzyme solutions by NMR. *The Journal of Chemical Physics* **150,** 124201 (2019).

202. Kondrat, S. & Popescu, M. N. Brownian dynamics assessment of enhanced diffusion exhibited by 'fluctuating-dumbbell enzymes'. *Physical Chemistry Chemical Physics* **21,** 18811–18815 (2019).

203. Börsch, M., Turina, P., Eggeling, C., Fries, J. R., Seidel, C. A., Labahn, A. & Gräber, P. Conformational changes of the H^+-ATPase from *Escherichia coli* upon nucleotide binding detected by single molecule fluorescence. *FEBS Letters* **437,** 251–254 (1998).

204. Yu, H., Jo, K., Kounovsky, K. L., Pablo, J. J. & Schwartz, D. C. Molecular Propulsion: Chemical Sensing and Chemotaxis of DNA Driven by RNA Polymerase. *Journal of the American Chemical Society* **131,** 5722–5723 (2009).

205. Muddana, H. S., Sengupta, S., Mallouk, T. E., Sen, A. & Butler, P. J. Substrate Catalysis Enhances Single-Enzyme Diffusion. *Journal of the American Chemical Society* **132,** 2110–2111 (2010).

206. Sengupta, S., Dey, K. K., Muddana, H. S., Tabouillot, T., Ibele, M. E., Butler, P. J. & Sen, A. Enzyme Molecules as Nanomotors. *Journal of the American Chemical Society* **135,** 1406–1414 (2013).

207. Sengupta, S., Spiering, M. M., Dey, K. K., Duan, W., Patra, D., Butler, P. J., Astumian, R. D., Benkovic, S. J. & Sen, A. DNA Polymerase as a Molecular Motor and Pump. *ACS Nano* **8,** 2410–2418 (2014).

208. Riedel, C., Gabizon, R., Wilson, C. A., Hamadani, K., Tsekouras, K., Marqusee, S., Pressé, S. & Bustamante, C. The heat released during catalytic turnover enhances the diffusion of an enzyme. *Nature* **517,** 227–230 (2015).

209. Illien, P., Zhao, X., Dey, K. K., Butler, P. J., Sen, A. & Golestanian, R. Exothermicity Is Not a Necessary Condition for Enhanced Diffusion of Enzymes. *Nano Letters* **17,** 4415–4420 (2017).

210. Jee, A.-Y., Cho, Y.-K., Granick, S. & Tlusty, T. Catalytic enzymes are active matter. *Proceedings of the National Academy of Sciences* **115,** E10812–E10821 (2018).

211. Jee, A.-Y., Dutta, S., Cho, Y.-K., Tlusty, T. & Granick, S. Enzyme leaps fuel antichemotaxis. *Proceedings of the National Academy of Sciences* **115,** 14–18 (2018).

212. Zhao, X., Palacci, H., Yadav, V., Spiering, M. M., Gilson, M. K., Butler, P. J., Hess, H., Benkovic, S. J. & Sen, A. Substrate-driven chemotactic assembly in an enzyme cascade. *Nature Chemistry* **10,** 311–317 (2018).

213. Xu, M., Ross, J. L., Valdez, L. & Sen, A. Direct Single Molecule Imaging of Enhanced Enzyme Diffusion. *Physical Review Letters* **123,** 128101 (2019).

214. Jee, A. Y., Tlusty, T. & Granick, S. Master curve of boosted diffusion for 10 catalytic enzymes. *Proceedings of the National Academy of Sciences* **117,** 29435–29441 (2020).

215. Mathies, J. C. & Goodman, E. D. The Diffusion Coefficient and Molecular Weight of Alkaline Phosphatase. *Journal of the American Chemical Society* **75,** 6061–6062 (1953).

216. Bai, X. & Wolynes, P. G. On the hydrodynamics of swimming enzymes. *The Journal of Chemical Physics* **143,** 165101 (2015).

217. Günther, J. P., Börsch, M. & Fischer, P. Diffusion Measurements of Swimming Enzymes with Fluorescence Correlation Spectroscopy. *Accounts of Chemical Research* **51,** 1911–1920 (2018).

218. Jee, A. Y., Chen, K., Tlusty, T., Zhao, J. & Granick, S. Enhanced Diffusion and Oligomeric Enzyme Dissociation. *Journal of the American Chemical Society* **141,** 20062–20068 (2019).

219. Golestanian, R. Enhanced Diffusion of Enzymes that Catalyze Exothermic Reactions. *Physical Review Letters* **115,** 108102 (2015).

220. Golestanian, R., Liverpool, T. B. & Ajdari, A. Propulsion of a Molecular Machine by Asymmetric Distribution of Reaction Products. *Physical Review Letters* **94,** 220801 (2005).

221. Astumian, R. D. Trajectory and Cycle-Based Thermodynamics and Kinetics of Molecular Machines: The Importance of Microscopic Reversibility. *Accounts of Chemical Research* **51,** 2653–2661 (2018).

222. Böttcher, B., Bertsche, I., Reuter, R. & Gräber, P. Direct visualisation of conformational changes in EF_0F_1 by electron microscopy. *Journal of Molecular Biology* **296,** 449–457 (2000).

223. Oyama, N., Kawasaki, T., Mizuno, H. & Ikeda, A. Glassy dynamics of a model of bacterial cytoplasm with metabolic activities. *Physical Review Research* **1,** 032038(R) (2019).

224. Illien, P., Adeleke-Larodo, T. & Golestanian, R. Diffusion of an enzyme: The role of fluctuation-induced hydrodynamic coupling. *Europhysics Letters* **119,** 40002 (2017).

225. Michaelis, L. & Menten, M. L. Die Kinetik der Invertinwirkung. *Biochemische Zeitschrift* **49** (1913).

226. Skóra, T., Popescu, M. N. & Kondrat, S. Conformation-changing enzymes and macromolecular crowding. *Physical Chemistry Chemical Physics* **23,** 9065–9069 (2021).

227. Häusler, E., Domagalski, P., Ottens, M. & Bardow, A. Microfluidic diffusion measurements: The optimal H-cell. *Chemical Engineering Science* **72,** 45–50 (2012).

228. Yu, M., Silva, T. C., van Opstal, A., Romeijn, S., Every, H. A., Jiskoot, W., Witkamp, G. J. & Ottens, M. The Investigation of Protein Diffusion via H-Cell Microfluidics. *Biophysical Journal* **116,** 595–609 (2019).

229. Frentrup, H., Avendaño, C., Horsch, M., Salih, A. & Müller, E. A. Transport diffusivities of fluids in nanopores by non-equilibrium molecular dynamics simulation. *Molecular Simulation* **38,** 540–553 (2012).

230. Kondrat, S. *Physics and modelling of intracellular diffusion* (preprint) 2018. `https://arxiv.org/abs/1810.05496`.

231. Chang, A., Jeske, L., Ulbrich, S., Hofmann, J., Koblitz, J., Schomburg, I., Neumann-Schaal, M., Jahn, D. & Schomburg, D. BRENDA, the ELIXIR core data resource in 2021: new developments and updates. *Nucleic Acids Research* **49,** D498–D508 (2021).

232. Behe, M. J. & Englander, S. W. Sickle hemoglobin gelation. Reaction order and critical nucleus size. *Biophysical Journal* **23,** 129–145 (1978).

233. Benesch, R. E., Benesch, R., Edalji, R. & Kwong, S. Intermolecular effects in the polymerization of hemoglobin S. *Biochemical and Biophysical Research Communications* **81,** 1307–1312 (1978).

234. Sunshine, H. R., Hofrichter, J. & Eaton, W. A. Gelation of sickle cell hemoglobin in mixtures with normal adult and fetal hemoglobins. *Journal of Molecular Biology* **133,** 435–467 (1979).

235. Zimmerman, S. B. & Trach, S. O. Effects of macromolecular crowding on the association of *E.coli* ribosomal particles. *Nucleic Acids Research* **16,** 6309–6326 (1988).

236. Rivas, G., Fernandez, J. A. & Minton, A. P. Direct Observation of the Self-Association of Dilute Proteins in the Presence of Inert Macromolecules at High Concentration via Tracer Sedimentation Equilibrium: Theory, Experiment, and Biological Significance. *Biochemistry* **38,** 9379–9388 (1999).

237. Minton, A. P. Implications of macromolecular crowding for protein assembly. *Current Opinion in Structural Biology* **10,** 34–39 (2000).

238. Cheung, M. S., Klimov, D. & Thirumalai, D. Molecular crowding enhances native state stability and refolding rates of globular proteins. *Proceedings of the National Academy of Sciences* **102,** 4753–4758 (2005).

239. Minton, A. P. Models for Excluded Volume Interaction Between an Unfolded Protein and Rigid Macromolecular Cosolutes: Macromolecular Crowding and Protein Stability Revisited. *Biophysical Journal* **88,** 971–985 (2005).

240. Minton, A. P. Influence of macromolecular crowding upon the stability and state of association of proteins: Predictions and observations. *Journal of Pharmaceutical Sciences* **94,** 1668–1675 (2005).

241. Snoussi, K. & Halle, B. Protein Self-Association Induced by Macromolecular Crowding: A Quantitative Analysis by Magnetic Relaxation Dispersion. *Biophysical Journal* **88,** 2855–2866 (2005).

242. Stagg, L., Zhang, S. Q., Cheung, M. S. & Wittung-Stafshede, P. Molecular crowding enhances native structure and stability of α/β protein flavodoxin. *Proceedings of the National Academy of Sciences* **104,** 18976–18981 (2007).

243. Dhar, A., Samiotakis, A., Ebbinghaus, S., Nienhaus, L., Homouz, D., Gruebele, M. & Cheung, M. S. Structure, function, and folding of phosphoglycerate kinase are strongly perturbed by macromolecular crowding. *Proceedings of the National Academy of Sciences* **107,** 17586–17591 (2010).

244. Magno, A., Caflisch, A. & Pellarin, R. Crowding Effects on Amyloid Aggregation Kinetics. *The Journal of Physical Chemistry Letters* **1,** 3027–3032 (2010).

245. Gasic, A. G., Boob, M. M., Prigozhin, M. B., Homouz, D., Daugherty, C. M., Gruebele, M. & Cheung, M. S. Critical Phenomena in the Temperature-Pressure-Crowding Phase Diagram of a Protein. *Physical Review X* **9,** 041035 (2019).

246. Gomez, D., Huber, K. & Klumpp, S. On Protein Folding in Crowded Conditions. *The Journal of Physical Chemistry Letters* **10,** 7650–7656 (2019).

247. Heo, L., Sugita, Y. & Feig, M. Protein assembly and crowding simulations. *Current Opinion in Structural Biology* **73,** 102340 (2022).

248. Zhou, H. X. & Dill, K. A. Stabilization of Proteins in Confined Spaces. *Biochemistry* **40,** 11289–11293 (2001).

249. Hall, D. & Minton, A. P. Macromolecular crowding: Qualitative and semiquantitative successes, quantitative challenges. *Biochimica et Biophysica Acta - Proteins and Proteomics* **1649,** 127–139 (2003).

250. Rivas, G. & Minton, A. P. Macromolecular Crowding *In Vitro*, *In Vivo*, and In Between. *Trends in Biochemical Sciences* **41,** 970–981 (2016).

251. Homchaudhuri, L., Sarma, N. & Swaminathan, R. Effect of crowding by dextrans and Ficolls on the rate of alkaline phosphatase–catalyzed hydrolysis: A size-dependent investigation. *Biopolymers* **83,** 477–486 (2006).

252. Norris, M. G. & Malys, N. What is the true enzyme kinetics in the biological system? An investigation of macromolecular crowding effect upon enzyme kinetics of glucose-6-phosphate dehydrogenase. *Biochemical and Biophysical Research Communications* **405,** 388–392 (2011).

253. Balcells, C., Pastor, I., Vilaseca, E., Madurga, S., Cascante, M. & Mas, F. Macromolecular Crowding Effect upon *in Vitro* Enzyme Kinetics: Mixed Activation-Diffusion Control of the Oxidation of NADH by Pyruvate Catalyzed by Lactate Dehydrogenase. *The Journal of Physical Chemistry B* **118,** 4062–4068 (2014).

254. Pastor, I., Pitulice, L., Balcells, C., Vilaseca, E., Madurga, S., Isvoran, A., Cascante, M. & Mas, F. Effect of crowding by Dextrans in enzymatic reactions. *Biophysical Chemistry* **185,** 8–13 (2014).

255. Maximova, K., Wojtczak, J. & Trylska, J. Enzymatic activity of human immunodeficiency virus type 1 protease in crowded solutions. *European Biophysics Journal* **48,** 685–689 (2019).

256. Minton, A. P. Water Loss in Aging Erythrocytes Provides a Clue to a General Mechanism of Cellular Senescence. *Biophysical Journal* **119,** 2039–2044 (2020).

257. Alric, B., Formosa-Dague, C., Dague, E., Holt, L. J. & Delarue, M. Macromolecular crowding limits growth under pressure. *Nature Physics* **18,** 411–416 (2022).

258. Hatters, D. M., Minton, A. P. & Howlett, G. J. Macromolecular Crowding Accelerates Amyloid Formation by Human Apolipoprotein C-II*. *Journal of Biological Chemistry* **277,** 7824–7830 (2002).

259. Shtilerman, M. D., Ding, T. T. & Lansbury, P. T. Molecular Crowding Accelerates Fibrillization of α-synuclein: Could an Increase in the Cytoplasmic Protein Concentration Induce Parkinson's Disease? *Biochemistry* **41,** 3855–3860 (2002).

260. Sharp, K. A. Analysis of the size dependence of macromolecular crowding shows that smaller is better. *Proceedings of the National Academy of Sciences* **112,** 7990–7995 (2015).

261. Senske, M., Törk, L., Born, B., Havenith, M., Herrmann, C. & Ebbinghaus, S. Protein Stabilization by Macromolecular Crowding through Enthalpy Rather Than Entropy. *Journal of the American Chemical Society* **136,** 9036–9041 (2014).

262. Elcock, A. H. Models of macromolecular crowding effects and the need for quantitative comparisons with experiment. *Current Opinion in Structural Biology* **20,** 196–206 (2010).

263. Wirth, A. J. & Gruebele, M. Quinary protein structure and the consequences of crowding in living cells: Leaving the test-tube behind. *BioEssays* **35,** 984–993 (2013).

264. Hyman, A. A., Weber, C. A. & Jülicher, F. Liquid-Liquid Phase Separation in Biology. *Annual Review of Cell and Developmental Biology* **30,** 39–58 (2014).

265. Brangwynne, C. P., Tompa, P. & Pappu, R. V. Polymer physics of intracellular phase transitions. *Nature Physics* **11,** 899–904 (2015).

266. Boeynaems, S., Alberti, S., Fawzi, N. L., Mittag, T., Polymenidou, M., Rousseau, F., Schymkowitz, J., Shorter, J., Wolozin, B., Van Den Bosch, L., Tompa, P. & Fuxreiter, M. Protein Phase Separation: A New Phase in Cell Biology. *Trends in Cell Biology* **28,** 420–435 (2018).

267. Dolgin, E. Cell biology's new phase. *Nature* **555,** 300–302 (2018).

268. Minton, A. P. Simple Calculation of Phase Diagrams for Liquid-Liquid Phase Separation in Solutions of Two Macromolecular Solute Species. *The Journal of Physical Chemistry B* **124,** 2363–2370 (2020).

269. Minh, D. D., Chang, C. E., Trylska, J., Tozzini, V. & McCammon, J. A. The Influence of Macromolecular Crowding on HIV-1 Protease Internal Dynamics. *Journal of the American Chemical Society* **128,** 6006–6007 (2006).

270. Ackers, G. K., Doyle, M. L., Myers, D. & Daugherty, M. A. Molecular Code for Cooperativity in Hemoglobin. *Science* **255,** 54–63 (1992).

271. Eaton, W. A., Henry, E. R., Hofrichter, J. & Mozzarelli, A. Is cooperative oxygen binding by hemoglobin really understood? *Nature Structural Biology* **6,** 351–358 (1999).

272. Yang, D., Kroe-Barrett, R., Singh, S., Roberts, C. J. & Laue, T. M. IgG cooperativity–Is there allostery? Implications for antibody functions and therapeutic antibody development. *mAbs* **9,** 1231–1252 (2017).

273. Li, P., Banjade, S., Cheng, H. C., Kim, S., Chen, B., Guo, L., Llaguno, M., Hollingsworth, J. V., King, D. S., Banani, S. F., Russo, P. S., Jiang, Q. X., Nixon, B. T. & Rosen, M. K. Phase transitions in the assembly of multivalent signalling proteins. *Nature* **483,** 336–340 (2012).

274. Borcherds, W., Bremer, A., Borgia, M. B. & Mittag, T. How do intrinsically disordered protein regions encode a driving force for liquid–liquid phase separation? *Current Opinion in Structural Biology* **67,** 41–50 (2021).

275. Hunter, C. A. & Anderson, H. L. What is Cooperativity? *Angewandte Chemie - International Edition* **48,** 7488–7499 (2009).

276. Ercolani, G. & Schiaffino, L. Allosteric, Chelate, and Interannular Cooperativity: A Mise au Point. *Angewandte Chemie - International Edition* **50,** 1762–1768 (2011).

277. Janssen, M., Stenmark, H. & Carlson, A. Divalent ligand-monovalent molecule binding. *Soft Matter* **17,** 5375–5383 (2021).

278. Shuker, S. B., Hajduk, P. J., Meadows, R. P. & Fesik, S. W. Discovering High-Affinity Ligands for Proteins: SAR by NMR. *Science* **274,** 1531–1534 (1996).

279. Mack, E. T., Snyder, P. W., Perez-Castillejos, R. & Whitesides, G. M. Using Covalent Dimers of Human Carbonic Anhydrase II To Model Bivalency in Immunoglobulins. *Journal of the American Chemical Society* **133,** 11701–11715 (2011).

280. Whitty, A. Cooperativity and biological complexity. *Nature Chemical Biology* **4,** 435–439 (2008).

281. Mangel, W. F., Lin, B. & Ramakrishnan, V. Characterization of an Extremely Large, Ligand-Induced Conformational Change in Plasminogen. *Science* **248,** 69–73 (1990).

282. Tsytlonok, M., Hemmen, K., Hamilton, G., Kolimi, N., Felekyan, S., Seidel, C. A., Tompa, P. & Sanabria, H. Specific Conformational Dynamics and Expansion Underpin a Multi-Step Mechanism for Specific Binding of p27 with Cdk2/Cyclin A. *Journal of Molecular Biology* **432,** 2998–3017 (2020).

283. Pickover, C. A., McKay, D. B., Engelman, D. M. & Steitz, T. A. Substrate binding closes the cleft between the domains of yeast phosphoglycerate kinase. *Journal of Biological Chemistry* **254,** 11323–11329 (1979).

284. Kumar, S. A., Murthy, N. S. & Krakow, J. S. Ligand-induced change in the radius of gyration of cAMP receptor protein from *Escherichia coli*. *FEBS Letters* **109,** 121–124 (1980).

285. Newcomer, M. E., Lewis, B. A. & Quiocho, F. A. The radius of gyration of L-arabinose-binding protein decreases upon binding of ligand. *Journal of Biological Chemistry* **256,** 13218–13222 (1981).

286. Dumas, C. & Janin, J. Conformational changes in arginine kinase upon ligand binding seen by small-angle X-ray scattering. *FEBS Letters* **153,** 128–130 (1983).

287. Olah, G. A., Trakhanov, S., Trewhella, J. & Quiocho, F. A. Leucine/isoleucine/valine-binding protein contracts upon binding of ligand. *Journal of Biological Chemistry* **268,** 16241–16247 (1993).

288. Taylor, T. C. & Andersson, I. Structural transitions during activation and ligand binding in hexadecameric Rubisco inferred from the crystal structure of the activated unliganded spinach enzyme. *Nature Structural Biology* **3,** 95–101 (1996).

289. Sevvana, M., Vijayan, V., Zweckstetter, M., Reinelt, S., Madden, D. R., Herbst-Irmer, R., Sheldrick, G. M., Bott, M., Griesinger, C. & Becker, S. A Ligand-Induced Switch in the Periplasmic Domain of Sensor Histidine Kinase CitA. *Journal of Molecular Biology* **377,** 512–523 (2008).

290. Salvi, M., Schomburg, B., Giller, K., Graf, S., Unden, G., Becker, S., Lange, A. & Griesinger, C. Sensory domain contraction in histidine kinase CitA triggers transmembrane signaling in the membrane-bound sensor. *Proceedings of the National Academy of Sciences* **114,** 3115–3120 (2017).

291. Ghobadi, S., Ashrafi-Kooshk, M. R., Mahdiuni, H. & Khodarahmi, R. Enhancement of intrinsic fluorescence of human carbonic anhydrase II upon topiramate binding: Some evidence for drug-induced molecular contraction of the protein. *International Journal of Biological Macromolecules* **108,** 240–249 (2018).

292. Cheng, R. *Conformational dynamics of an unfolded biopolymer: theory and simulation* PhD thesis (2012).

293. Chen, M. & Lin, K. Y. Universal amplitude ratios for three-dimensional self-avoiding walks. *Journal of Physics A: Mathematical and General* **35,** 1501–1508 (2002).

294. Rubinstein, M. & Colby, R. H. *Polymer Physics* pp. 102–104 (Oxford University Press, 2003).

295. Grimaldo, M., Lopez, H., Beck, C., Roosen-Runge, F., Moulin, M., Devos, J. M., Laux, V., Härtlein, M., Da Vela, S., Schweins, R., Mariani, A., Zhang, F., Barrat, J.-L., Oettel, M., Forsyth, V. T., Seydel, T. & Schreiber, F. Protein Short-Time Diffusion in a Naturally Crowded Environment. *The Journal of Physical Chemistry Letters* **10,** 1709–1715 (2019).

296. Geyer, T. Many-particle Brownian and Langevin Dynamics Simulations with the Browmove package. *BMC Biophysics* **4,** 1–20 (2011).

297. Northrup, S. H., Allison, S. A. & McCammon, J. A. Brownian dynamics simulation of diffusion-influenced bimolecular reactions. *The Journal of Chemical Physics* **80,** 1517–1524 (1984).

298. Skóra, T. & Kondrat, S. *pyBrown* `https://tskora.github.io/pyBrown/`.

299. Skóra, T. *ExVol* `https://tskora.github.io/ExVol/`.

300. Hamaker, H. C. The London-van der Waals attraction between spherical particles. *Physica* **4,** 1058–1072 (1937).

301. Czarnecki, J. & Dabroś, T. Attenuation of the van der Waals attraction energy in the particlesemi-infinite medium system due to the roughness of the particle surface. *Journal of Colloid and Interface Science* **78,** 25–30 (1980).

302. Roth, C. M., Neal, B. L. & Lenhoff, A. M. Van der Waals interactions involving proteins. *Biophysical Journal* **70,** 977–987 (1996).

303. Kharazmi, A. & Priezjev, N. V. Molecular Dynamics Simulations of the Rotational and Translational Diffusion of a Janus Rod-Shaped Nanoparticle. *The Journal of Physical Chemistry B* **121,** 7133–7139 (2017).

304. Smith, E. R., Snook, I. K. & Van Megen, W. Hydrodynamic interactions in Brownian dynamics. *Physica A: Statistical Mechanics and its Applications* **143,** 441–467 (1987).

305. Beenakker, C. W. J. Ewald sum of the Rotne–Prager tensor. *The Journal of Chemical Physics* **85,** 1581–1582 (1986).

306. Townsend, A. K. *Generating, from scratch, the near-field asymptotic forms of scalar resistance functions for two unequal rigid spheres in low-Reynolds-number flow* (preprint) 2018. `https://arxiv.org/abs/1802.08226`.

307. Długosz, M. *BD_BOX* `https://www.fuw.edu.pl/~mdlugosz/downloads.html`.

308. Długosz, M., Zieliński, P. & Trylska, J. Brownian dynamics simulations on CPU and GPU with BD_BOX. *Journal of Computational Chemistry* **32,** 2734–2744 (2011).

309. Skóra, T. *pyBrown-tools* https://github.com/tskora/pyBrown-tools.

310. Ramasubramani, V. *FREUD* https://freud.readthedocs.io/en/latest/index.html.

311. Ramasubramani, V., Dice, B. D., Harper, E. S., Spellings, M. P., Anderson, J. A. & Glotzer, S. C. freud: A software suite for high throughput analysis of particle simulation data. *Computer Physics Communications* **254,** 107275 (2020).

312. Waszkiewicz, R. *PyGRPY* https://github.com/RadostW/PyGRPY.

313. Waszkiewicz, R., Bartczak, M., Kolasa, K. & Lisicki, M. *Pychastic: Precise Brownian Dynamics using Taylor-Itō integrators in Python* (preprint) 2022. https://arxiv.org/abs/2209.04332.

314. Zuk, P. *GRPY* https://github.com/pjzuk/GRPY.

315. Lakowicz, J. R. *Principles of Fluorescence Spectroscopy* pp. 798–840 (Springer, 2010).

Institute of Physical Chemistry
Polish Academy of Sciences

Kasprzaka 44/52
01-224 Warsaw, Poland

www.ichf.edu.pl